

Development and Performance Studies of Silicon Radiation Detectors

By

Arvind Singh

Enrolment No. PHYS01201204006

Bhabha Atomic Research Centre, Mumbai, India

*A thesis submitted to the
Board of Studies in Physical Sciences*

*In partial fulfilment of requirements
for the Degree of*

DOCTOR OF PHILOSOPHY

of

HOMI BHABHA NATIONAL INSTITUTE



July, 2019

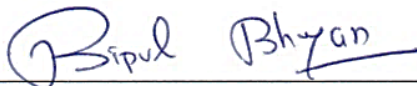
Homi Bhabha National Institute

Recommendation of the Viva Voce Committee

As members of the Viva Voce Committee, we certify that we have read the dissertation prepared by Shri Arvind Singh entitled "Development and Performance Studies of Silicon Radiation Detectors" and recommended that it may be accepted as fulfilling the dissertation requirement for the award of Degree of Doctor of Philosophy.


Date: July 15, 2019
Chairman- Dr. S. C. Gadkari


Date: 15/07/2019
Guide- Dr. Anita V. Topkar


Date: 15/07/2019
External Examiner- Prof. Bipul Bhuyan


Date: 15/7/19
Member-1- Dr. S. Santra


Date: 15/7/19
Member-2- Prof. Rajiv Dusane

Final approval and acceptance of this dissertation is contingent upon the candidate's submission of the final copies of the dissertation to HBNI.

I hereby certify that I have read this dissertation prepared under my direction and recommend that it may be accepted as fulfilling the dissertation requirement.

Date: 15-07-2019

Place: Mumbai



Dr. Anita V. Topkar
(Guide)

STATEMENT BY AUTHOR

This dissertation has been submitted in partial fulfilment of requirements for an advanced degree at Homi Bhabha National Institute (HBNI) and is deposited in the Library to be made available to borrowers under rules of the HBNI.

Brief quotations from this dissertation are allowable without special permission, provided that accurate acknowledgement of source is made. Requests for permission for extended quotation from or reproduction of this manuscript in whole or in part may be granted by the Competent Authority of HBNI when in his or her judgment the proposed use of the material is in the interests of scholarship. In all other instances, however, permission must be obtained from the author.



(Arvind Singh)

DECLARATION

I, hereby declare that the investigation presented in the thesis has been carried out by me. The work is original and has not been submitted earlier as a whole or in part for a degree / diploma at this or any other Institution/University.

A handwritten signature in blue ink that reads "Arvind Singh". The signature is written in a cursive style with a horizontal line underneath the name.

(Arvind Singh)

List of publications arising from the thesis

Journal

1. “Performance Study of Thin Epitaxial Silicon PIN Detectors for Thermal Neutron Measurements with Improved n/γ Discrimination”, **Arvind Singh**, S. Desai, A. Kumar and A. Topkar, *Nucl. Instr. and Meth. A.*, **2018**, 890, 28–34.
2. “Development, prototyping and characterization of double sided silicon strip detectors”, A. Topkar, **Arvind Singh**, B. Aggarwal, A. Kumar, A. Kumar, L.V. Murali Krishna, *Nucl. Instr. and Meth. A.*, **2016**, 834, 205-210.
3. “Performance study of an Integrated ΔE –E Silicon Detector Telescope using the Lohengrin Fission Fragment Separator at ILL, Grenoble”, **Arvind Singh**, A. Topkar, U. Köster, P. K. Mukhopadhyay, and C. K. Pithawa, *IEEE Transaction on Nuclear Science*, **2015**, 62, 264-271.
4. “Development of Integrated ΔE -E Silicon Detector Telescope using Silicon Planar Technology”, Anita Topkar, **Arvind Singh**, S. Santra, P. K. Mukhopadhyay, A. Chatterjee, R.K. Choudhury, C.K. Pithawa, *Nucl. Instr. and Meth. A.*, **2011**, 654, 330-335.

Conferences

1. “Performance Study of Indigenously Developed Double Sided Silicon Strip Detector With Charged Particles”, **Arvind Singh**, K. Mahata, A. Shrivastava, K. Ramachandran, V. V. Parkar, S. K. Pandit, S. Gupta, P. Patale, B. Aggarwal, and A. Topkar, *Proceedings of the DAE Symp. on Nucl. Phys.* **2017**, 62, 1044-1045.
2. “Thin epitaxial silicon PIN detectors for thermal neutron detection with improved gamma(γ) discrimination”, **Arvind Singh** and A. Topkar, *AIP Conf. Proc.*, **2016**, 1731, 060022-1–060022-3.
3. “Development of Double Sided Silicon Strip Detectors”, A. Topkar, **Arvind Singh**, B. Aggarwal, A. Kumar, A. Kumar, C. K. Pithawa, *Proceedings of the DAE Symp. on Nucl. Phys.*, **2013**, 58, 856-857.
4. “Development of Large Area Two-Dimensional Position Sensitive Silicon Strip Detectors”, A. Topkar, **Arvind Singh**, B. Aggarwal, A. Kumar, A.

Kumar, M. Krishna L.V. and C. K. Pithawa, *Proceedings of the NSNI held in BARC-2013*.

5. "Performance of integrated ΔE -E silicon detector telescope with light charged particles and fission fragments", **Arvind Singh**, S. Santra, Anita Topkar, K. Mahata, P K Rath, A Parihari, P.K. Mukhopadhyay, A. Chatterjee, C.K. Pithawa, *Proceedings of the DAE Symp. on Nucl. Phys.*, **2012**, 57.

(Arvind Singh)

Dedicated

To

My Parents

ACKNOWLEDGEMENTS

First and foremost, I would like to express my sincere gratitude to my guide, Prof. Anita V. Topkar, Electronic Division, Bhabha Atomic Research Centre (BARC), Mumbai, for his luminous guidance, constant support, motivation, constructive criticism and valuable advices. I deeply appreciate her positivity, true enthusiasm and engagement in all the research projects that have led to considerable output in the form of this thesis. I am thankful to Shri Debasis Das, Director, Electronics & Instrumentation Group, and Smt. Anita Behere, Head, Electronics Division, BARC for their support and encouragement. I extend my gratitude to Prof. D. S. Patil, Prof. S. C. Gadkari and Prof. A. Chatterjee, as doctoral committee chairmen, for their valuable advises and scientific/technical inputs. Thanks are due to Dr. S. Santra, Nuclear Physics Division, BARC and Prof. Rajiv O. Dusane, Indian Institute of Technology Bombay, Mumbai whose useful suggestions as doctoral committee members have been very helpful.

My thanks are also attributable to Dr. Ulli Köster, Institut Laue-Langevin, Grenoble, France, Dr. Aradhana Shrivastava and Dr. K. Mahata, Nuclear Physics Division, and Dr. S. Desai, Solid State Physics Division, BARC for their immense support in carrying out detector performance experiments and analysing the resulting data. Special thanks to my friends and colleagues, Bharti Aggarwal, Amit Kumar, Arvind Kumar, Soumyajit Chakrawarti and Sebin Philip who directly or indirectly have helped me in achieving my goals. I take the opportunity to sincerely thank all my colleagues of Electronics Division, for helping me in several different ways.

Last but not the least, I would like to express my love and gratitude to my parents and all the family members for being supportive in my endeavour and extending encouragement throughout my life.

CONTENTS

	Page No.
Synopsis.....	xii
List of figures.....	xxii
List of tables.....	xxv
Chapter 1.....	1

INTRODUCTION

Chapter 2.....	5
----------------	---

RADIATION DETECTORS

2.1. Introduction	5
2.2. Interaction of radiation with matter.....	6
2.2.1. Charged particles	6
2.2.2. Photons	8
2.2.3. Neutrons.....	11
2.3. Simplified detector model	12
2.4. Types of detectors	14
2.4.1. Gas detectors.....	14
2.4.2. Track detectors	16
2.4.3. Solid state detectors	17
2.4.4. Miscellaneous detector types.....	19
2.5. General characteristics of detectors.....	20
2.5.1. Statistical noise	20
2.5.2. Energy resolution.....	22
2.5.3. Response time	25
2.5.4. Dead time.....	26
2.5.5. Detector efficiency	26
2.5.6. Radiation damage in detectors.....	27
2.6. Silicon as a radiation detector	28
Chapter 3.....	31

SILICON DETECTORS: DEVICE STRUCTURE, FABRICATION SCHEME AND CHARACTERIZATION SETUP

3.1. Introduction	31
3.2. Basic semiconductor structures	32
3.2.1. The p–n junction diode	32

3.2.2. Semiconductor metal junction: Schottky barrier and Ohmic contact.....	36
3.2.3. The N ⁻ N ⁺ or P ⁻ P ⁺ structures	38
3.2.4. Silicon PIN or P ⁺ N ⁻ N ⁺ structure: PIN diode detector	39
3.3. Various types of silicon detectors	42
3.3.1. Diffused junction detectors.....	42
3.3.2. Surface barrier detectors (SSB)	42
3.3.3. PIN configuration-based detectors	42
3.3.4. Strip detectors	43
3.3.5. Particle identification: ΔE -E detector	44
3.3.6. Semiconductor based thermal neutron detector.....	46
3.4. Basic fabrication steps of PIN diode-based detectors.	48
3.4.1. Oxidation	49
3.4.2. Photolithography	49
3.4.3. Ion implantation.....	50
3.4.4. Annealing.....	50
3.4.5. Metallization.....	50
3.4.6. Charge collection and measurement.....	51
3.5. Characterization of detectors.....	52
3.5.1. Static characterization of silicon detectors	52
3.5.2. Dynamic characterization of silicon detectors.....	57
Chapter 4.....	69
DEVELOPMENT AND CHARACTERIZATION OF INTEGRATED ΔE-E DETECTOR TELESCOPE	
4.1. Introduction	69
4.2. Detector design and fabrication process.....	70
4.3. Detector characterization.....	74
4.4. Results and discussion.....	78
4.4.1. Static characterization.....	78
4.4.2. Alpha response of the detectors	81
4.4.3. The performance of the ΔE -E detector as a particle telescope for different charged particles.....	83
4.4.4. Performance evaluation for fission fragments and corresponding energy calibration	88
4.5. Conclusion.....	100

Chapter 5.....	101
DEVELOPMENT OF DOUBLE SIDED SILICON STRIP DETECTORS	
5.1. Introduction	101
5.2. Basic design considerations	102
5.2.1. Detector geometrical parameters	102
5.2.2. Wafer and design parameters	103
5.2.3. Considerations for back side (N ⁺ strip side) configuration: N ⁺ strip isolation.....	104
5.2.4. Mask design.....	106
5.3. Detector fabrication process.....	109
5.4. Results and discussion.....	111
5.4.1. Detector process and device simulation study.....	111
5.4.2. Evaluation of detector performance by static characterization	116
5.4.3. Evaluation of detector performance by dynamic characterization	122
5.4.4. 2-D image and position resolution.....	129
5.4.5. Inter-strip cross-talk measurement	132
5.5. Conclusions	133
Chapter 6.....	135
THIN EPITAXIAL SILICON PIN DETECTORS FOR THERMAL NEUTRON MEASUREMENTS WITH IMPROVED n/γ DISCRIMINATION	
6.1. Introduction	135
6.2. Experimental	137
6.2.1. Simulation study	137
6.2.2. Fabrication of pin detectors	138
6.2.3. Characterization of pin detectors.....	141
6.3. Results and Discussion.....	141
6.3.1. Optimization of the parameters using simulation studies.....	141
6.3.2. Static characterization.....	144
6.3.3. Response of the detectors to the charged particles.	146
6.3.4. Gamma sensitivity of the detectors.	147
6.3.5. Thermal neutron response of the detectors.....	149
6.4. Conclusions	155
Chapter 7.....	157
SUMMARY	
Appendix A.....	159

A.1. Energy gap: direct and indirect band gap	161
A.2. Intrinsic semiconductors and extrinsic semiconductors	165
A.3. Generation & recombination of charge carriers	168
A.4. Carrier transport	172
References.....	175

SYNOPSIS

Radiation detectors or particle detectors are devices that identify the passage of any radiation and measures the associated characteristic parameters like energy or charge of the radiation. The detection of radiation is essential for numerous reasons including a few as environment safety, personal protection, power regulation in nuclear reactors, determining dose limits for medical use of radiation, baggage scanning, calibration of radioactive isotopes, etc.. Apart from these, the maximum requirements of the nuclear radiation detectors arise in the nuclear and particle physics experiments which are performed to answer some of the fundamental questions of the natural nuclear behavior. The experiments in nuclear and particle physics involve the detection of primary radiation/particle and that of the product particles, if any. Each experiment is intended to target some specific characteristics of a particular kind of radiation/particle, necessitating the requirement of the specially designed and well characterized nuclear detectors fulfilling the requirements of the experiments. The working principal of the radiation detectors depends on the interaction of nuclear radiation with active medium of the detector. Based on the state of the active medium, the detectors can be broadly classified into three categories: (i) gas detectors, (ii) track (liquid state) detectors (iii) solid state detectors. The solid state detectors can be further categorized as scintillator detectors and semiconductor detectors. Gas detectors such as GM counters, proportional chamber or ^3He neutron detector counts the passage of the radiation and sometimes differentiate them on the basis of their energy. The track detectors (e.g. emulsion plates) are also capable to record the track of the indicant radiation or the charged particle. On the other hand, solid state detectors such as semiconductor detectors, scintillator detectors, etc., can be used to achieve all these objectives including counting as well as determination of energy/charge/track of the radiation or the radioactive particles.

Among all these detectors, silicon-based semiconductor detectors possess several unique advantages such as cost effectiveness, rugged, small in size, high energy and position

resolution, fast time response, low power requirement, high stopping power, high efficiency, batch processing with low cost and better uniformity. A high level of segmentation such that strips, microstrips, pixels can be done for one-dimensional (1-D) and two-dimensional (2-D) position sensing. These advantages of silicon-based semiconductor detectors emerge as a result of physics governing the properties of semiconductors and the associated phenomenon. In semiconductor detectors, a semiconductor material such as a silicon or germanium crystal constitutes the active medium. One such device is p-n junction diode where the passage of the radiation is determined through radiation driven creation of charge carriers (electrons and electron-deficient sites called holes). The migration of these charge carriers gives rise to a current pulse which is collected under the influence of a voltage maintained across the junction. Several important parameters of semi-conductor detectors like doping, depletion width, bias voltage, etc., determines different performance parameters of the detector. With all these advantages and scope for the tunability of the detector performance, the development of specific semiconductor detectors with optimized characteristic parameters is still an area of prime interest. Though various types of detectors have been developed and reported, the design and fabrication process details are only superficially given. Actual design and process are not disclosed in published papers. In this thesis, the design, simulation, fabrication process development, characterization and the performance evaluation of three different kind of semiconductor detectors or more precisely silicon based semiconductor detectors have been presented.

(i) ΔE -E detector telescope: These detectors are used not only for determining the particle energy but also for charged particle identification. A novel methodology overcoming the drawbacks of the conventional ΔE -E detector is adapted for developing these detectors where the ΔE and E detectors are integrated back to back on the same silicon wafer. The monolithic detectors developed in this work are based on a totally new device design and fabrication

process. The detectors are demonstrated successfully identifying the light charge particles as well as a wide range of heavy fission fragments.

(ii) Double sided silicon detectors: The prototype double sided silicon strip detectors are developed for the use in GASPARD Experiment at the upcoming SPIRAL2 facility at GANIL, France. These detectors are designed to have precise position sensing of the charged particles and are shown remarkably doing so without any inter-strip crosstalk. These detectors have large size, higher number of strips and hence better position resolution than those available commercially.

(iii) Thin thermal neutron detectors: An innovative approach of using thin epitaxial silicon PIN detector with optimized thickness for thermal neutron detection has been presented and significant improvement in n/γ discrimination has been achieved by this method.

The entire work carried out has been described in seven Chapters in this thesis. Chapter 1 describes the motivation, objective and scope of the thesis. At the end of the chapter, a layout of the thesis is presented.

Chapter 2 provides a general introduction to the working principals of the different radiation detectors, their limitations and applicability and particular details of the semiconductor detectors (in particular silicon based detectors). Based on the active materials, the detectors can be broadly classified as gas detectors, liquid state detector or solid state detectors. While on the basis of the detecting signals, detectors were also classified as electrical or optical. Among all these detectors, solid state detectors, particularly, semiconductor detectors possess a prominent place due to their several unique advantages. Being the main course of this thesis, the advantages of the semiconductor detectors over the others along with the basic principles of the solid state physics governing the working of semiconductor detectors particularly silicon based radiation detectors are detailed in this Chapter. The capability of a detector is measured in terms of various characteristic parameters such as efficiency,

sensitivity, resolution, dead time, etc. The usefulness of all these parameters for different types of detectors along with their suitability for detection of specific kind of radiation is also discussed.

The properties and suitability of silicon as an active material of radiation detectors, basic detector structure, different types of silicon detectors and the fabrication process technology used for the fabrication of silicon detectors are described in Chapter 3. The proper and objective characterization of the developed detectors is an essential requirement for the successful utilization of them. In general, the detector characterization is termed as static and dynamic characterization in which former deals with the study of the inbuilt properties (e. g, leakage current, bias voltage, electronic noise, etc.) while the later demonstrate the capability of the registering the incident radiation. In Chapter 3, the various techniques, required experimental setups and the facilities used for both kinds of characterization purposes have been presented. All the detectors were examined for their current-voltage (I-V) and capacitance-voltage (C-V) profiles in order to determine the leakage current, full depletion voltage, capacitance and breakdown voltage, etc.. The basic energy resolution was investigated using dual energy alpha source $^{238}\text{Pu}+^{239}\text{Pu}$. The specific experiments on various particle accelerator/reactor facilities were carried out to evaluate the performance of the detectors for specific experiments. For examples, the suitability of the $\Delta E-E$ silicon detector for identifying heavy fission fragments was examined at Lohengrin Fission Fragment Separator at ILL, Grenoble, France whereas the position sensing of the double sided strip detector was determined in the experiments performed at Pelletron LINAC Facility, TIFR, Mumbai. The description and the comparative potential competence of all the majorly used facilities (FOTIA, BARC; Pelletron, TIFR; detector testing facility, Dhruva reactor, BARC and Lohengrin ILL, France) are presented in this chapter.

Chapter 4 describes the development of an integrated ΔE -E silicon detector telescope using silicon planar technology. ΔE -E detector telescopes are being used for particle identification and energy measurements in nuclear physics experiments for many years. However, it is a challenging task to get a robust, large area thin ΔE detector with a good uniformity. The conventional ΔE -E detectors are known to suffer several limitations as they are fragile, difficult to handle and quite expensive due to production methods involving silicon etching. To overcome these problems, in this work, a novel ΔE -E detector has been developed where the ΔE and E detectors are integrated back to back on the same silicon wafer by using a custom developed fabrication process, adapted from bipolar silicon integrated circuit technology. The technology developed is based on standard integrated circuit technology and involves double sided wafer processing. The ΔE and E detectors have been realized in a PIN configuration with a common buried N-type layer. The detectors with ΔE thicknesses of 10, 15 and 25 μm , and E detector with a thickness of 300 μm have been fabricated and tested for energy resolution as well as for charged particle identification using $^{238}\text{Pu}+^{239}\text{Pu}$ dual alpha source and 12 MeV ^7Li ion beam on carbon target. The results of these experiments demonstrate that the integrated detector telescope clearly separates the charged particles, such as alpha particles, protons and ^7Li . Due to good energy resolution of the E detector, discrete alpha groups corresponding to well-known states of ^{15}N populated during the reaction could also be clearly identified.

The further experiments performed to characterize the ΔE -E detector telescope for fission fragments are described. The detector with the ΔE detector of thickness of 10 μm and E detector of thickness 300 μm has been calibrated for light and heavy ions in terms of nuclear charge, energy and channel number using Lohengrin Fission Fragment Separator at ILL, Grenoble, France. Lohengrin provides the facility to select mass number, charge state as well as the energy of the particles produced as fission fragments. In these characterization experiments,

the detectors were successfully demonstrated for the identification of fission fragments having mass in the range of 75 to 110 and energy range 70 MeV to 110 MeV. In order to cover the full mass range and energy range of fission fragments from ^{235}U , the detectors (of different active areas i.e. 50 mm^2 & 100 mm^2) of lower ΔE thickness $\sim 7\text{ }\mu\text{m}$ were developed. These experiments helped in developing the better understanding of mechanisms dominating the pulse height defect in our telescope. The detector response was precisely characterized by a nuclear charge dependent approach, which differs from the usual mass-dependent characterization. Overall, the results demonstrate the suitability of the integrated detector for identification of fission fragments and their energy measurement.

In Chapter 5, an overview of the design of double sided silicon strip detectors, their fabrication process, simulation results and characterization results are presented. The tracking devices having fast and highly precise position sensing of the charged particle are of prime importance in particle and nuclear physics experiments. For this purpose, we have developed double sided silicon strip detectors with orthogonal strips on opposite faces satisfying both the requirements. Though these kinds of detectors are commercially available, the process details of fabrication are not published anywhere. The specifications of this prototype detector were configured based on the requirements of GASPARD Experiment (in collaboration with NPD, BARC) at the upcoming SPIRAL2 facility at GANIL, France. Double sided DC-coupled silicon strip detectors were designed to have geometry of $65\text{ mm} \times 65\text{ mm}$ with 64 P^+ strips on the front side and 64 N^+ strips on the back side with a pitch of 0.9 mm. These detectors were fabricated using a twelve mask layer process involving double sided wafer processing technology. Semiconductor process and device simulations were carried out in order to theoretically estimate the impact of important design and process parameters on the breakdown voltage of detectors. The performance of the prototype detectors has been initially studied using static characterization tests and using an alpha source. The results show quite low leakage

current of few nA (nanoampere) per strip and capacitance about 25 pF. The observed energy resolution is ~50 keV and ~60 keV respectively for the P⁺ and N⁺ strips which is estimated from the FWHM obtained by fitting the alpha peaks acquired using a ²⁴¹Am alpha source. In order to obtain the 2-D position resolution of the detector, a mask based on the geometrical parameters of the detector was fabricated and the detector was covered with a mask during experiments with an ion source. The 2-D image obtained shows a position resolution of about 1 mm. The characterization results demonstrate that the detectors have good uniformity over the detector area of about 40 cm². In order to study the response of these detectors for a wide range of particles and energy, detectors were further characterized in different particle beams with different target at Pelletron accelerator facility, TIFR in collaboration with NPD, BARC. ⁷Li beam of 30 MeV on targets ⁹³Nb and ¹⁹⁷Au were used for detector response study. Different contributions from elastic scattering of ⁷Li, quasi elastic scattering of ⁷Li, alpha, proton, deuteron and triton (due to break up of ⁷Li) were recorded. Data analysis showed the detector is responding well to all the reaction products obtained by different targets. The data acquired has been analysed to obtain energy resolution. Experiments with alpha source and charged particle beams show that each strip is capable of notifying the passage of the particles, individually and uniformly without any inter-strip crosstalk.

Now a days, there is an increased demand of neutron detectors for security applications requiring detection of special nuclear materials (SNMs) to prevent proliferation and illegitimate trafficking, various physics experiments ranging from studies of nuclear reaction to exploring lattice structure in condensed matter, and for monitoring neutron beams, etc. Traditionally, ³He and BF₃ gas filled detectors are being used for such applications due their high efficiencies. However, these detectors suffer from certain issues such global shortage of ³He, toxicity of BF₃, portability, etc. Therefore, in recent years, there has been a significant interest in the development of semiconductor based thermal neutron detectors as an alternative to these gas

filled detectors. A novel approach of using thin epitaxial silicon PIN detectors for thermal neutron measurements with improved n/γ discrimination has been presented in Chapter 6. Monte Carlo simulations were carried out to show that there is a significant reduction in the gamma sensitivity for thin detectors with the thickness of 10-25 μm compared to a detector of thickness of 300 μm . Epitaxial PIN silicon detectors with the thickness of 10 μm , 15 μm and 25 μm were fabricated using a custom process. The detectors exhibited low leakage currents of a few nA. The gamma sensitivity of the detectors was experimentally studied using a 33 μCi , 662 keV, ^{137}Cs source. Considering the count rates, compared to a 300 μm thick detector, the gamma sensitivity of the 10 μm , 15 μm and 25 μm thick detectors was reduced by factors of 1874, 187 and 18 respectively. The detector performance for thermal neutrons was subsequently investigated with a thermal neutron beam using an enriched ^{10}B film as a neutron converter layer. The thermal neutron spectra for all three detectors exhibited three distinct regions corresponding to the ^4He and ^7Li charge products released in the ^{10}B -n reaction. The thermal neutron response of thin detectors with 10 μm and 25 μm thicknesses showed significant reduction in the gamma sensitivity compared to that observed for the 300 μm thick detector. Considering the total count rate obtained for thermal neutrons with a ^{10}B converter film, the count rate without the converter layer were about 4 %, 7 % and 36 % for detectors with thicknesses of 10 μm , 25 μm and 300 μm respectively. The detector with 10 μm thickness showed negligible gamma sensitivity of 4 CPS, but higher electronic noise and reduced pulse heights. The detector with 25 μm thickness demonstrated the best performance with respect to electronic noise, thermal neutron response and gamma discrimination.

Chapter 7 summarizes the findings of the thesis. The main contribution of the thesis highlighted below:

- A novel silicon detector telescope with integrated ΔE and E detectors on the same wafer has been developed using double sided wafer processing technology, which is quite

complex compared to the technology utilized for developing standard integrated circuits. The results of the tests carried out to evaluate the performance of the detector could successfully demonstrate the identification of the charged particles as well as wide range of fission fragments.

- Double sided 64 strip detectors having geometrical area $65 \text{ mm} \times 65 \text{ mm}$ have been designed and fabricated. The characterization results show that the detectors have very low strip leakage current and notably high uniformity. It has been shown that the detectors are applicable for successful position sensing of charged particles in terms of X and Y coordinates without any inter-strip cross talk.
- The thin epitaxial silicon PIN detectors are developed for thermal neutron detection using a converter layer. Monte Carlo simulations showed that there is a significant reduction in the gamma sensitivity for thin detectors with the thickness of 10-25 μm compared to a detector of thickness of 300 μm . The experimental results showed the best performance with significant suppression in gamma sensitivity for the 25 μm thick detector compared to those having smaller and higher thicknesses.

To conclude, this thesis demonstrates the development and utilization of three different kinds of semiconductor detectors ($\Delta E-E$ detector telescope, double sided silicon strip detector, thin epitaxial silicon PIN detector). The thesis involves innovative technological developments of the semiconductor detectors, along with simulation studies to optimize the design parameters. The present work also elaborates various characterization methods essential for precise performance evaluation as well as for establishing feedback mechanism for the design improvement.

LIST OF FIGURES

Figure 2.1. Basic schematic circuit for pulse mode operation of a detector using simplified detector model.....	13
Figure 2.2. Position localization in proportional counters using the charge-division method.....	15
Figure 2.3. Pulse height distribution of a hypothetical detector for a mono-energetic beam of particle/radiation [49].....	23
Figure 3.1. Energy band diagram of n-p junction in unbiased condition. E_C , E_i , E_F , and E_V are the bottom energy level of conduction band, intrinsic energy level, Fermi level and top energy level of conduction band, respectively.....	33
Figure 3.2. The distribution of the space charge $\rho(x)$, electric potential $\phi(x)$ and electric field $E(x)$ in the depletion region across p-n junction.....	34
Figure 3.3. Typical energy band diagram of metal and semiconductor. $e\chi_m$, $e\chi_s$ and $e\phi_s$ represent the work function of metal, electron affinity of semiconductor and work function of semiconductor respectively.....	37
Figure 3.4. Energy band diagram of a metal semiconductor junction [62].	37
Figure 3.5. Energy band diagram before and after formation of $N^- N^+$ junction.	38
Figure 3.6 Graphical representation of the variation of charge density, potential and electric field in the depletion region of an almost fully depleted PIN diode.....	40
Figure 3.7. Schematic of ΔE -E detector for the particle identification.....	46
Figure 3.8. Schematic representation of basic steps used for the fabrication of PIN diode based detectors [22].	51
Figure 3.9. Formation of detector signal due to separation of electron-hole pairs by applied electric field in the depletion region of the detector [22].....	52
Figure 3.10. Block diagram of electronic setup for I-V characterization.	54
Figure 3.11. Laboratory setup for static characterization.	54
Figure 3.12. Screen shot of control software user interface.	55
Figure 3.13. Circuit diagram of auto-balancing bridge impedance measurement method.....	56
Figure 3.14 Screen shot of control software user interface.	57
Figure 3.15. A simplified block diagram of the setup used for the dynamic characterization.....	58
Figure 3.16. Experimental set up used for detector characterization with alpha source.	58
Figure 3.17. Pulse height spectra of α -particles by a silicon detector.	59
Figure 3.18 6 MV folded tandem ion accelerator facility at BARC [82,83].	60
Figure 3.19. Three dimensional schematic view of LOHENGRIN fission fragment separator, at Institut Laue Langevin [85,86].....	62
Figure 3.20. Schematic diagram showing working principle of LOHENGRIN fission fragment separator, at Institut Laue Langevin [84].....	63
Figure 3.21. Detector mounting jig with goniometer.	64
Figure 3.22. BARC-TIFR Pelletron-LINAC Facility [87].	66
Figure 3.23. Scattering chamber at BARC-TIFR Pelletron-LINAC Facility [88].	67
Figure 4.1. (a) Schematic cross section and (b) Top view of ΔE -E detector.....	71
Figure 4.2. Schematic representation of fabrication steps used for integrated telescope.	73
Figure 4.3. Top (ΔE detector) and bottom (E detector) side of packaged detector.	74

Figure 4.4. Schematic of experimental setup used to evaluate the detector performance as particle telescope at FOTIA.	75
Figure 4.5. The electronic setup used for processing of signals from ΔE and E detectors.	75
Figure 4.6. Typical reverse I-V characteristics E detectors of area 100 mm ² and 50 mm ²	79
Figure 4.7. Typical reverse I-V characteristics of ΔE detector of area 100 mm ²	79
Figure 4.8. C-V characteristics and 1/C ² -V plot of the E detector of area 100 mm ²	80
Figure 4.9. C-V characteristic of ΔE detectors of different thicknesses.	81
Figure 4.10. Alpha (²³⁸ Pu + ²³⁹ Pu) response of E detector of area 100 mm ² at a bias voltage of 60 V.	81
Figure 4.11. Alpha (²³⁸ Pu + ²³⁹ Pu) response of ΔE detector (area 100 mm ²) of thickness 10 μ m at bias voltage of 6 V.	82
Figure 4.12. Alpha (²³⁸ Pu + ²³⁹ Pu) response of ΔE detector (area 100 mm ²) of thickness 25 μ m at bias voltage of 6 V.	82
Figure 4.13. Two-dimensional (2-D) spectrum recorded by the integrated detector at FOTIA for the reaction of 12 MeV ⁷ Li beam on ¹² C target.	84
Figure 4.14. Projection of alpha bands containing discrete peaks of alpha particles corresponding to different excited states of ¹⁵ N* which are identified and labeled.	85
Figure 4.15. Typical one-dimensional (1-D) histograms of elastic and alpha particles detected by E and ΔE detectors comparing their energy resolutions, elastically scattered ⁷ Li particles as detected by; (a) ΔE and (b) E detectors and alpha particles as detected by (c) ΔE and (d) E detectors.	86
Figure 4.16. Two-dimensional spectrum recorded by the integrated detector for fission fragment measurements in ¹⁹ F + ²⁰⁹ Bi reaction.	87
Figure 4.17. One-dimensional spectrum recorded by the ΔE detector of the integrated detector for fission fragment measurements in ¹⁹ F + ²⁰⁹ Bi reaction.	88
Figure 4.18. Alpha energy histogram for the E detector with thickness of 300 μ m used for the estimation of the energy resolution with 4.7 MeV alpha particles.	89
Figure 4.19. Histogram for the ΔE detector of thickness 10 μ m used for determination of the energy resolution with 90 MeV, A 90 fission fragments.	89
Figure 4.20. Two-dimensional spectrum showing the ΔE signal vs. E _T for a fixed value of A/q = 5 and A/E _T = 1 MeV/nucleon. ΔE detector thickness ~ 10 μ m.	90
Figure 4.21. Plot of ΔE versus E _T for fission fragments of different mass, nuclear charge and energy demonstrating the Z separation of the telescope. ΔE detector thickness ~ 10 μ m.	91
Figure 4.22 (a) Plot between total energy measured by the integrated detector (E _T) vs energy E selected by the Lohengrin fission fragment separator for different fission fragments, ΔE Detector thickness ~10 μ m. (b) The data have been shifted vertically for clear (Z ~ 34) \times 1, (Z ~ 36) \times 1.2, (Z ~ 38) \times 1.4, (Z ~ 40) \times 1.6, (Z ~ 42) \times 1.8, (Z ~ 53) \times 1.0. The solid lines show fits to the data using linear relations.	92
Figure 4.23. Energy resolution of integrated detector for fission fragments of different energies and charge.	96
Figure 4.24. Typical 2-D spectra obtained from several set of measurements identifying fission fragments from A= 80 to A= 148.	97
Figure 4.25. Typical 2-D spectra obtained from several set of measurements identifying fission fragments from A= 80 to A= 148.	98

Figure 5.1. Basic representation of DSSD.....	103
Figure 5.2. Schematic representation of (a) charge accumulation layer at the interface of SiO ₂ , (b) N ⁺ strip isolation using P ⁺ spray and (c) N ⁺ strip isolation using P ⁺ stop method.	105
Figure 5.3. Mask layout representing all layers.....	107
Figure 5.4. Magnified mask view	108
Figure 5.5. P ⁺ side of the wafer with double sided silicon strip detector in centre and test structures. (b) N ⁺ side of the wafer with silicon strip detector in the centre and test structures.	110
Figure 5.6. (a) P ⁺ side of the diced DSSD and, (b) N ⁺ side of the diced DSSD.....	111
Figure 5.7. Double sided silicon detector packaged in transmission mode on PCB with 68 pin SMD connectors for connecting P ⁺ and N ⁺ strips to readout circuit.	111
Figure 5.8. Comparison of breakdown voltage of the pad detector for different boron implantation energies of 30 keV, 50 keV and 80 keV. The detector is simulated without metal overhang.....	113
Figure 5.9. Comparison of breakdown voltage of the pad detector for different boron implantation energies of 30 keV, 50 keV and 80 keV. Metal overhang is 10 μm for all the cases.....	114
Figure 5.10. Comparison of breakdown voltage of the pad detector for metal overhang of 0/10 μm/15 μm. Boron implantation energy 50 keV.....	115
Figure 5.11. Comparison of breakdown voltage of the pad detector for field oxide thicknesses from 0.35 to 0.75 μm at 50 keV boron implantation energy and 10 μm metal overhang.	115
Figure 5.12. The block diagram of the electronic setup used to measure I-V characteristic.	116
Figure 5.13. Leakage current variation of all 64 strips with reverse voltage for a detector from first batch. Different curves are showing leakage current variation of different strips.	117
Figure 5.14. Leakage current variation of strips for a detector from first fabrication batch at 100 V reverse voltage.	118
Figure 5.15. Leakage current variation of all 64 strips with reverse voltage for a detector from final fabrication batch. Different curves are showing leakage current variation of different strips.....	119
Figure 5.16. Leakage current variation of strips for a detector from final fabrication batch at 100 V reverse voltage.	119
Figure 5.17. Leakage current variation of strips of a baby strip test structure from final fabrication batch.....	120
Figure 5.18. C-V and 1/C ² -V plots of a strip.	121
Figure 5.19. C-V characteristics of all 64 P ⁺ strips of a double-sided strip detector.....	121
Figure 5.20. Variation of capacitance of P ⁺ strips at 100 V reverse voltage.	122
Figure 5.21. Alpha response of pad detector from the P ⁺ side injection.....	123
Figure 5.22. Alpha response of the pad detector from N ⁺ side injection.....	123
Figure 5.23. 1-D histograms of some of the P ⁺ side strips showing alpha particle response.....	125
Figure 5.24. Alpha histogram of one of the P ⁺ strip fitted with a Gaussian function.....	126
Figure 5.25. 1-D histogram of some of the N ⁺ side strips showing alpha particle response.	126
Figure 5.26. Alpha histogram of one of the N ⁺ strip, fitted with Gaussian function.....	127

Figure 5.27. The counts recorded in each strip of the detector from (a) front side and (b) back side, when ${}^7\text{Li}$ beam of energy 30 MeV is incident on the gold target of thickness 500 mg/cm^2 .	129
Figure 5.28. Detector with a mask having 9 circular holes mounted in scattering chamber.	130
Figure 5.29. 2-D image of mask obtained by the detector.	131
Figure 5.30. (a) The mask designed with a diagonal line opening of 1 mm and holes of diameter 0.7 mm with a gap of 1.5 mm and (b) corresponding image detected by the detector.	132
Figure 5.31. The two hit events showing hits in the neighbouring strips and random hits.	133
Figure 6.1. Schematic cross section of fabricated detectors, (a) Standard thick PIN detector, (b) Thin PIN detector.	140
Figure 6.2. Simulated gamma spectra for silicon detectors with different thicknesses.	143
Figure 6.3. Electric field variation along the depth of a silicon PIN detector at a 5 V reverse bias for different detector thicknesses.	144
Figure 6.4. Typical I–V and C–V characteristics of a thin PIN detector with thickness of 25 μm , detector area of 50 mm^2 .	145
Figure 6.5. Typical I–V and C–V characteristics of a standard PIN detector with thickness of 300 μm , detector area of 100 mm^2 .	146
Figure 6.6. Alpha spectra obtained using a dual alpha source (${}^{238+239}\text{Pu}$) for PIN detectors of different thicknesses. Thin detectors were biased at 5 V and 300 μm thick detector was biased at 60 V.	147
Figure 6.7. Gamma spectra obtained with a ${}^{137}\text{Cs}$ source for PIN detectors of different thicknesses. All detectors were operated at 5 V bias voltage.	148
Figure 6.8. Spectra obtained with a thermal neutron beam using a 10 μm thick detector showing response (i) without a ${}^{10}\text{B}$ film, (ii) with a Cd filter, and (iii) with a ${}^{10}\text{B}$ film.	150
Figure 6.9. Spectra obtained with a thermal neutron beam using a 25 μm thick detector showing response (i) without a ${}^{10}\text{B}$ film, (ii) with a Cd filter and (iii) with a ${}^{10}\text{B}$ film.	151
Figure 6.10. Spectra obtained with a thermal neutron beam using a 300 μm thick detector showing response (i) without a ${}^{10}\text{B}$ film, (ii) with a Cd filter and (iii) with a ${}^{10}\text{B}$ film.	151
Figure 6.11 Comparison of count rates obtained with or without a ${}^{10}\text{B}$ film for detectors with thicknesses of; 1 – 10 μm , 2 - 25 μm , 3 - 300 μm .	154
Figure A.1. Basic E-k Band diagram.	160
Figure A.2. Energy band diagram of (a) Indirect and (e.g. silicon) and (b) direct band gap (e.g. GaAs) semiconductors.	161
Figure A.3. Intrinsic semiconductor; (a) Schematic band diagram, (b) Density of states, (c) Fermi distribution function, (d) Carrier concentration.	162
Figure A.4. Ionization energy of various impurities in silicon [61]. For levels above the mid line, the energy is measured from EC and for those below the mid line, energy is measured from EV. Acceptor and donor levels are shown in red and violet, respectively.	164
Figure A.5. Energy band diagrams of intrinsic, n-type and p-type semiconductors.	165
Figure A.6. Schematic band diagram, density of states, Fermi distribution function and carrier concentration of (a) n-type semiconductor, (b) p-type semiconductor [62].	166
Figure A.7. Typical energy band diagram presenting indirect recombination.	170

LIST OF TABLES

Table 4.1. Nuclear charge for corresponding mass numbers.....	78
Table 4.2. Comparison of actual energy set at Lohengrin and energy obtained using calibration equation for fission fragments of different charge and energies.	95
Table 6.1. Count rate obtained with a ^{137}Cs gamma source for detectors of different thicknesses	149

Chapter 1

INTRODUCTION

Nuclear and particle physics experiments require several types of radiation detectors for the detection of the radiation/sub-atomic particles, their energy and position measurements, as well as even for their identification [1]–[6]. Among all the different kind of detectors, silicon radiation detectors have achieved maximum scientific attention due to their several unique advantages such as high signal to noise ratio, fast response, high energy resolution, etc. [7]–[12]. Also using photolithographic technique, it is possible to segment the detector in to strip, microstrip and pixels for one-dimensional (1-D) and two-dimensional (2-D) position sensing [13], [14]. Hence compact arrays involving several thousand detectors can be built using these detectors. This has opened up ways for the utilization of these detectors not only in physics experiments but also in medicine, security and space science [15]–[18].

A p-n junction diode in reverse biased mode formulates the basic structure of the silicon detectors, though several modifications in the design and the operation parameters are needed depending on the experimental requirements and for the improvement of the characteristic parameters (dead time, leakage current, resolution, efficiency etc.) [19]–[23]. The most importance advantage of the silicon detectors is the well-established and advanced fabrication technology available for fabrication of the detectors of different geometries and specifications [22], [24]–[28].

Several different kind of silicon detectors, for example charge coupled devices, silicon resistive pad detectors and one-dimensional (1-D) / two-dimensional (2-D) strip/micro-strip detectors have been developed by various researchers using a technology derived from standard IC fabrication technology [14], [29]–[34]. One of the crucial concerns in this regard is the size of

these detectors, which is significantly large compared to present micro-electronic devices, presenting a challenge to fabricate large area silicon detectors with almost similar size as that of the silicon wafers [35], [36]. In addition to this, the detectors fabrication process should also be designed not only to achieve excellent initial quality but also to restrict the degradation of the detector, even after receiving heavy flux of the radiation [37], [38]. The developed detectors are required to be evaluated for various general as well as application specific characteristics. The general characterization includes static characterization examining performance of the silicon device in terms of parameters such as leakage current, breakdown voltage and capacitance etc. The fabricated detectors are also tested (known as dynamic characterization) for their required performance i.e. their ability to indicating the passage of different charged particles, fission fragments, photons and/or neutrons, energy measurements, as well as the identification of the charge state of the incident particles. The detectors designed particularly for physics experiments usually operates in an environment containing a combined flux of different particles such as neutrons, photons and other charged particles. Sometimes, it is also desirable to make detectors sensitive only to a certain kind of particles and suppressing the contributions from other sources.

The detectors for building a specific experiment are required to be designed and fabricated to meet the experimental requirements in terms of energy resolution, position sensing, coverage and charged particle identification. This thesis presents design, development, characterization and successful demonstration of three different types of silicon detectors [39]–[42]:

- i) Integrated ΔE -E detectors
- ii) Double sided strip detectors
- iii) Thin PIN detectors

- i) *The Integrated ΔE -E detectors*: A detector telescope comprising a thin and a thick detector, known as ΔE -E detector is used for charged particle identification by recording the energy losses in two adjacent detectors i.e. ΔE and E detectors. The conventional ΔE detectors fabricated by mechanical polishing and chemical etching of silicon wafers suffer several limitations such as fragile, non-uniform, difficult to handle, quite expensive, etc. [43], [44]. The fabrication process also puts constraints on the size and thickness of the detectors. To overcome these drawbacks of conventional ΔE detector, in the present work, an integrated ΔE -E detector (with two detectors integrated back to back on the same silicon wafer) has been designed and developed. The successful application of the detectors for identifying the light charged particles as well as a wide range of heavy fission fragments has been demonstrated [39], [42].
- ii) *Double sided silicon strip detectors*: The prototype double sided silicon strip detectors have been designed and developed as per the specifications required for the GASPARD Experiment at the upcoming SPIRAL2 facility at GANIL, France. These detectors have been demonstrated to have the required position sensing of the charged particles without any significant inter-strip crosstalk [41].
- iii) *Thin PIN detectors for thermal neutron detection*: For improved n/γ discrimination, an innovative approach of using thin epitaxial silicon PIN detector in combination with a ^{10}B converter layer for thermal neutron measurements has been demonstrated. The thin PIN detectors required for the experiments were designed and developed using a custom process [42].

The thesis is organized in seven Chapters where the first (present) chapter introduces the basic aim of the work carried out and the structure of the thesis.

Chapter 2 presents an overview involving the basics of the interaction of radiation with matter, different types of the detectors used for detecting these radiations and some of the concepts of the semi-conductor physics, important from the point of view of silicon detector fabrication and its performance.

In Chapter 3, a brief description of various silicon detectors, their fabrication technology, process steps and characterization methodologies as well as various national and international facilities used for the characterization of the detectors in the present work has been provided.

Chapters 4, 5 and 6 are dedicated for the development and performance evaluation of the ΔE -E detectors, double sided silicon strip detectors (DSSD) and thin PIN detectors, respectively. The three detectors have been shown to achieve expected specifications and performance.

The chapter 7 summarizes the findings of the thesis and presents a future outlook.

Chapter 2

RADIATION DETECTORS

2.1. Introduction

The silicon detectors are being increasingly used in mega science international experimental facilities (CMS, ATLAS, ALICE at LHC etc.) for research in nuclear and particle physics experiments [4], [6], [45]–[48]. The development of the detectors for these experimental facilities resulted in spin off technologies for space science, medical imaging, security applications, etc. The operation of silicon detector is based on the interaction of the radiation with silicon resulting in the generation of low energy charge carriers (electrons and positive-ions) [1]. These charge carriers are collected by the measurements electronics to detect the presence of radiation and further measurements of position, energy, etc.

In general, the radiation detectors are classified in many types such as gas detectors (Geiger–Müller (GM) counters, proportional counters), track detectors (emulsions, liquid state detectors), solid state detectors (semiconductor detectors, inorganic or organic scintillators) [49]. Each of these detectors has advantages as well as limitations and the suitability of a detector is governed by the requirements of the application. Semiconductor detectors are known for their compact sizes, ability of precise position determination with high speed readout, real time detection, precise simultaneous measurement of position as well as energy and the possibility to fabricate several detectors along with required readout electronics on the same wafer [50].

In this chapter, a brief introduction on interaction of radiation particularly for charged particles, photons and neutrons with matter has been presented. A basic detector model, different types

of detectors and the crucial parameters used to evaluate the performance of a detector system have also been discussed. Some of the concepts of semiconductor physics, particularly important for realizing an optimized semiconductor detector are described in the end of the chapter.

2.2. Interaction of radiation with matter

The radiation, originating from the radioactive nucleus/ radiation source propagates in the medium and interacts with other matter along its path. It is the interaction of radiation with external matter, which enables the observation of the radiation and determination of the nature of the nuclear transitions, occurring prior and after the emission of the radiation. The operation of radiation detectors, designed for detecting the radiations requires active and prominent interaction of the detector material (atomic electrons/nuclei) with the incident radiation, directly or indirectly. The interaction of radiation with matter majorly depends on the type of radiation and is discussed in the subsequent sub sections for different kind of incident particles/radiation [49].

2.2.1. Charged particles

The charged particles interact with atomic electrons and nuclei present in the detector material, mainly via Coulomb interaction and gradually lose their energy till fully stopped. The process of passage of charged particles in the medium can thus be visualized as a series of line segments between the scattering events, where the trajectory of the path is decided by the kinematics of these scattering events. The scattering involves elastic and inelastic scattering, both primarily with atomic electrons leading to excitation and ionization of the atom and hence causing the creation of the charges in the medium.

The charged particle-matter interaction is usually described in terms of an important parameter, known as the stopping power (S) of the material which accounts for the rate $(-dE/dx)$ at which charged particles lose energy dE as they travel through a distance dx in the material. In general, the stopping power comprises two contributions: the electronic stopping power due to the interaction with the atomic electrons of the material and the nuclear stopping power, arising from the interaction of charged particle with material nuclei. However, since the contribution of the nuclear term is very small, the stopping power can be approximated to electronic contribution [49].

$$-\frac{dE}{dx} = S_{\text{nuclear}} + S_{\text{electronic}} \approx S_{\text{electronic}} \quad (2.1)$$

The Bethe-Bloch formula provides the mathematical formulation to the stopping power (in units of MeV/cm) and can be expressed as [1], [51]:

$$-\left\langle \frac{dE}{dx} \right\rangle = Kz^2 \frac{Z}{A} \frac{1}{\beta^2} \left[\frac{1}{2} \ln \frac{2m_e c^2 \beta^2 \gamma^2 T_{\text{max}}}{I^2} - \beta^2 - \frac{\delta(\beta\gamma)}{2} \right] \quad (2.2)$$

where,

A: atomic mass of the absorber

$$K/A = \frac{4\pi N_A r_e^2 m_e c^2}{A} = 0.307075 \text{ MeV g}^{-1} \text{ cm}^2, \text{ for } A = 1 \text{ g mol}^{-1}$$

z: atomic number of incident particle

Z: atomic number of absorber.

T_{max} : maximum transferable energy

I: material dependent characteristic ionization constant

$\delta(\beta\gamma)$: density effect correction

x: mass thickness ($= \rho \times s$, s is the path-length, traversed in the medium while ρ is the mass density of the medium).

$\beta=v/c$, where v and c are the particle speed and the speed of light in vacuum, respectively.

The above equation describes the dependence of S on kinetic energy of the incident particle, atomic number, and mass number of the medium. The equation shows that the range (the depth in the medium where the energy of the incident particle becomes almost zero) of the heavy charged particles is less than that of light particles of same kinetic energy. The formula also suggests that materials having atoms of higher Z offers a lower range and hence may act as better shields as well as better detector medium for registering high energy charged particles.

A charged particle when it passes through a material with a speed ϑ greater than the phase velocity of light $\vartheta_{em}(= c/n, n$ is refractive index) in that medium, the radiation emitted is known as Cherenkov radiation. It can be illustrated with the help of quantum mechanics. The molecules of the medium get excited when a charged particle moves inside a polarizable medium, and return back to their ground state by re-emitting some photons (electromagnetic radiation). This emitted electromagnetic radiation (waves) move out spherically at the phase velocity for the medium. If the particle moves faster than the light speed $\frac{c}{n} < \vartheta < c$, the emitted waves add up constructively leading to a coherent radiation at angle θ with respect to the particle direction, known as Cherenkov radiation. The angle of the photons with respect to the charged particle direction depends on the velocity of the charged particle. In particle physics, the Cherenkov radiation is used frequently in particle identification detectors (PID).

2.2.2. Photons

The photons (energy quanta) do not lose energy systematically in the medium rather they interact in a discrete manner [52]. Unlike charged particles, photons being massless and charge

less are not subjected to long-range Coulomb force, nor even short-range nuclear forces. As a result, it is the intensity of the photon beam which decreases as the photons interact while the energy of all the non-interacting photons remains constant. The intensity (I) of the photon beam at a distance x covered by the photons in the medium of density ρ can be expressed as:

$$I(x) = I_0 e^{-\mu\rho x} \quad (2.3)$$

Where I_0 is the initial intensity at $x = 0$ (at the surface) and μ (cm^2/gm) is the mass attenuation coefficient which mostly depends on the properties of the medium and energy of the photon. In general, the photons (x-rays and gamma rays) interact with the matter primarily in following three ways, and hence thereby knocking out the electrons:

a. Photoelectric effect

In the photoelectric interaction, the photon transfers all its energy to a bound electron, causing ejection of the electron from the atom. The electron being charged particle rapidly loses its energy to the medium. Hence the entire energy transfer process takes place in two steps, (i) transfer of photon energy to the bound electron, making it free and (ii) transfer of energy of the emitted electron to nearby matter. The ejected electron moves relatively short distance from its original location and therefore, whole energy is deposited in the matter close to the site of the photoelectric interaction.

The maximum kinetic energy (K.E.) of the ejected electron is given by:

$$(\text{K. E.})_{\text{max}} = h\nu - W \quad (2.4)$$

where h is Planck constant, ν is the frequency of the incident photon and W is the work function of the material. The interaction cross section (φ) for photoelectric effect varies with the atomic number (Z) of absorber material and energy of the photon (E_γ) approximately as [1], [49]:

$$\varphi \propto \frac{Z^n}{E_\gamma^{3.5}} \quad (2.5)$$

where n varies between 4 and 5. This implies that higher the Z of the absorber, higher will be the probability of photon interaction with the absorbing medium through photo electric effect.

b. Compton scattering

In Compton interaction, the incoming photon is absorbed by the free electron and a photon is produced with reduced energy and leaves the site of the interaction in a direction different from that of the original photon. The electron also moves in the appropriate direction to conserve the momentum. The change in wavelength of the photon ($\lambda_f - \lambda_i$, where λ_i and λ_f are the wavelength of photons in initial and final stages, respectively) and hence, in energy, depends only on the scattering angle (θ) and can be expressed as:

$$\lambda_f - \lambda_i = \frac{h}{m_e c} (1 - \cos \theta) \quad (2.6)$$

where, h is Planck's constant, m_e is the rest mass of electron and c is the speed of light in vacuum. This process is significant in some cases because the material within the primary x-ray beam becomes a secondary radiation source. Unlike the photo electric effect which shows peaks in the energy spectrum, Compton scattering constitutes a superimposed background. The Compton scattering cross section (σ) varies with Z^2 , suggesting that the Compton scattering is also more probable in higher Z material but less probable compare to photo electric effect [51].

c. Pair production

This process is the direct conversion of the radiation into matter where the most energetic photons ($E_\gamma > 1.02 \text{ MeV}$) create matter-antimatter pair of electrons ($m_e \sim 0.511 \text{ MeV}$) usually in the vicinity of an atomic nucleus. These pair of electron-positron induces a cascade of secondary electrons. The probability of pair production in photon-matter interactions increases with photon energy and increases approximately as the square of atomic number of the nearby atom.

2.2.3. Neutrons

The neutrons ($m_n \sim 940\text{MeV}$) being nuclear particles with zero charge do not interact with atomic electrons, but rather interacts with the atomic nuclei. The nuclear forces governing these interactions are very short range, therefore, a very few neutrons passing through the vicinity of the nuclei can interact (approximately 10^{-6} times weaker adsorption compare to charged particles). The free neutrons are usually unstable and undergo beta decay with a lifetime of approximately 15 minutes. The interaction of the neutrons with nuclei very much depends on the neutron energies, based on which neutrons are characterized in following categories:

High energy neutrons: $E_n > 100 \text{ MeV}$

Fast neutrons: $100 \text{ keV} < E_n < 10 \text{ MeV}$

Epithermal neutrons: $0.1 \text{ eV} < E_n < 100 \text{ keV}$

Thermal/ slow neutron: $E_n = 25 \text{ meV}$

Cold/ ultra-cold neutrons: $E_n < 25 \text{ meV}$

The slow or thermal neutrons usually undergo slow diffusion, elastic scattering, and nuclear capture, while epithermal neutrons also cause nuclear excitation, in addition to above process. On the other hand, fast neutrons interact via elastic, inelastic scattering, and energetically favorable various nuclear reactions. All these processes give rise to emission of secondary charged particles which are in most of the cases heavy charged particles or high energy gamma rays, which further interacts with the detector medium, through mechanisms described above. Following are a few examples where neutrons undergo nuclear interaction to generate secondary charged particles (alpha, proton etc.) and/or photons.



The neutron interaction cross section in general varies with $E^{-1/2}$.

2.3. Simplified detector model

When a single particle or quantum of radiation is incident on the detector, a charge Q is generated in the detector due to the interaction between the radiation and the material of the detector. This charge is collected by applying an electric field. The charge collection time ranges from few nanoseconds to few milliseconds, depending on the detector system. The charge collection time depends on the mobility of charge carriers in the detector material and the average distance travelled by the carrier before collection at the electrodes [49], [53], [54].

If t_c is the charge collection time and $i(t)$ is the current at time t in the circuit then charge Q can be given as:

$$\int_0^{t_c} i(t)dt = Q \quad (2.10)$$

In real situations, detector faces a flux of radiation instead of a single particle. The rate of interaction of the incident flux decides the mode of the operation of the detector. There are three modes of detector operation:

- a. Current mode
- b. MSV (Mean Square Voltage) mode
- c. Pulse mode

Current mode operation is used when event rates are high. MSV (Mean Square Voltage) mode is used for enhancing the difference between types of radiation. Detectors are used in this mode primarily for nuclear reactor instrumentation for measuring neutrons in high gamma background. Measurements of individual radiation quanta (radiation spectroscopy) is being done by using detectors operated in pulse mode. This mode is practical and efficient in the case of low rate of interactions. The pulse mode is briefly discussed in this section, the detectors are mostly operated in pulse mode in the present thesis.

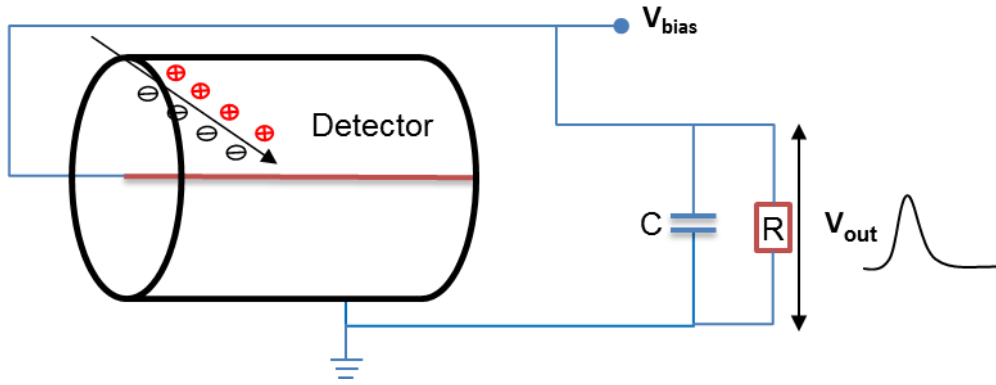


Figure 2.1. Basic schematic circuit for pulse mode operation of a detector using simplified detector model.

Figure 2.1 shows the simple schematic circuit used in pulse mode. R is the input resistance of the circuit and C represents the equivalent capacitance of both the detector and the measuring circuit. The potential difference (V_{out}) across the load resistance is the pulse voltage. The time constant of the circuit is $\tau = RC$. There are two extreme cases to be considered in pulse mode [1]:

Case 1: Small RC ($\tau \ll t_c$),

In this configuration, the current flowing through the resistance (R) is essentially equal to the instantaneous value of the current flowing in the detector. It is used in high event rates situation when timing information is required with accuracy.

Case 2: Large RC ($\tau \gg t_c$)

In this configuration, a small current flow through R during the charge collection time and the detector current is integrated on the capacitance. Long tail voltage pulse due to capacitor discharge appears at the output. If the time between pulses is large enough, the capacitance will discharge through the resistance, returning the voltage across R to zero. This configuration is the most commonly used for accurate energy measurements. The magnitude (V_{max}) of the maximum voltage provides the pulse height and is equal to Q (the total charge) divided by the capacitance C .

2.4. Types of detectors

In general, a detector utilizes the interaction of radiation with its active medium and registers the resulting signal for indicating the passage of the radiation. The detectors can thus be classified based on the manner of interaction of radiation with active medium, physical state of their active medium, and the form of the output signal. The interaction of the radiation with active medium either ionizes the molecules of the medium to give rise to a current pulse, or produces light flashes from the excitation of the molecules or leaves their signature in the form of a track. According to these, the detectors are classified as ionization detectors, scintillation detectors and track detectors. The detectors are also classified based on the output signal as: electronic detectors and optical detectors where the former produces an electronic signal while later produce an optical signal to indicate the passage of the radiation/particle. The GM counter, p-n junction diode, ^3He detectors are the example of electronic detectors whereas scintillator detectors or spark chambers are the example of optical detectors. From the perspectives of the present thesis, a brief detail on the detectors, classified on the basis of the state of active medium is presented below. According to the active medium, the detectors are mainly of following types:

2.4.1. Gas detectors

In these detectors, a suitable gas (mostly inert) is chosen to serve as an active material. The incident radiation/particle beam interacts with the gas molecules to create electron-ion pairs through different mechanism, as described in previous sections. The charge carriers are collected between two electrodes by applying a suitable voltage. A typical schematic of the gas detectors and formation of voltage signal pulse is shown in Figure 2.1. The detector characteristics and capabilities depend majorly on the applied voltage and hence, three different kinds of gas detectors can be formed depending on the region of the operating voltage.

a. Ionization Chamber

These detectors only utilize the primary ionization created by the incident radiation in the active gas and does not involve the gas multiplication mechanisms as the operating voltage is kept sufficiently low.

b. Proportional Counter

These detectors operate in the proportional (intermediate) range of the operating voltage where the output signal is proportional to the energy of the incident radiation. Hence, the detector is widely utilized for measuring energy levels of incident radiation, (e.g. X-ray radiation dose). Proportional counters (as well as Photo multiplier tubes, scintillator rods and silicon strip detectors) in some configurations are capable of sensing the position of an event taking place within the detector volume. Charge division method, utilized for position sensing in proportional tubes is discussed in this section. The anode wire of the proportional tube is fabricated such that it has measurable resistance per unit length (R/L) and both the ends of the anode wire are connected to the different amplifiers. The collected charge in an event is divided between the amplifiers connected at ends of the wire in a proportion (as illustrated in Figure 2.2) that is related to the position of the interaction. A proportional position signal pulse is obtained by dividing the output of an amplifier by summed signal.

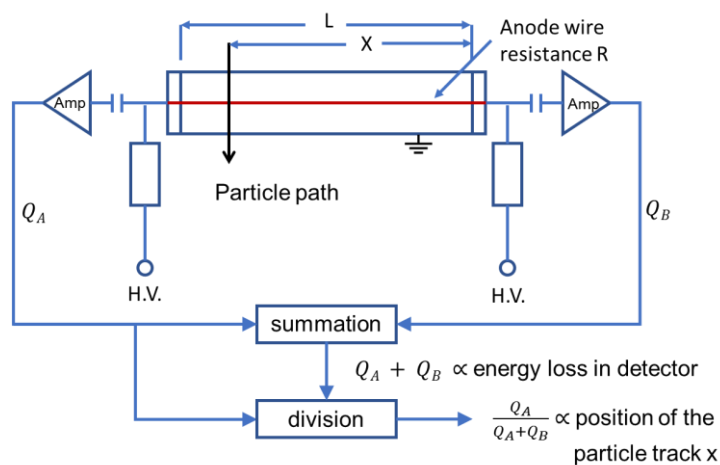


Figure 2.2. Position localization in proportional counters using the charge-division method.

If the track of incident radiation extends for some distance along the length of the tube, then many avalanches will also be distributed along the anode and only an average position can be deduced.

Instead of single anode wire, multiple anode wires are used between two parallel cathode plates to cover large surface area in multiwire proportional counter. The avalanche created by the interaction is collected by the nearest anode wire will produce large negative pulse in comparison to the small positive pulse appears on neighboring anode wires. The signals obtained from the preamplifiers connected to each anode wire indicate the position of the event in terms of the position of the anode wire (one-dimensional position sensing). The position resolution is limited by the finest spacing between the wires i.e. 1 or 2 mm. The number of preamplifiers can be reduced by deploying the charge division method in which all anode wires can be interconnected by using resistors and signals from the end preamplifiers can be treated as shown in the Figure 2.2. In order to make a 2-dimensional position sensitive proportional counter, the cathode can also be fabricated in the form of isolated wires or strips.

c. Geiger-Müller Counter

The Geiger-Müller detector mostly use as a counter when operated in Plateau region (Geiger-Müller region) of operating voltage resulting in the complete avalanche in the active medium, leading to a considerably amplified detection pulse. However, this makes counter insensitive to the incident radiation energy and hence the detector can only act as counter.

Therefore, the gas detectors are capable of not only counting the particles but also measuring their energies depending on the operating voltage. However, these detectors are very bulky and require high bias voltage.

2.4.2. Track detectors

In this kind of detectors, the active medium is usually in liquid state. The examples of these detectors are bubble chamber, emulsions, etc. These detectors have the capabilities to track the path of the incident radiation in addition to counting and measuring the energy of the particles.

2.4.3. Solid state detectors

These detectors comprise some solid material such as scintillating crystal or semi-conducting material as active medium. However, the term ‘solid-state detector’, is mostly used for semiconductor detectors where a semiconductor device such as p-n junction produces a current pulse due to generation of electron-hole pairs, when a particle of ionizing radiation traverses it. Being the main course of this thesis, the fabrication, working principal and advantages of silicon based detectors will be discussed in detail in the later sections of this Chapter and in Chapter 3. Scintillation, germanium and diamond detectors are discussed briefly in this section.

a. Scintillation detectors

The energy deposited by radiation in scintillators is converted in to visible light and is detected by photo sensors.

Types of inorganic scintillators: Alkali halide: NaI(Tl), CsI(Tl), CsI(Na), LiI(Ei) Other slow Inorganics: BGO, CdWO₄, ZnS(Ag) Cerium-Activated Fast Inorganics: GSO, YAP, YAG, LSO, LuAP, LaBr₃

Types of organic scintillators: Anthracene, Stilbene, plastic scintillators and liquid scintillators

The inorganic scintillators are known to provide the best light output and linearity, but their response time is relatively slow. Organic scintillators are relatively faster but have low light yield. The choice of scintillator detector mostly depends on the application. For example, sodium iodide detectors doped with thallium (NaI [TI]) and other high Z-value inorganic scintillating crystals with high density (BGO, CdWO₄, GSO etc.) of are used for γ - and X-ray

detection. Bismuth germanate (BGO) is one of the best scintillator crystal for γ -ray counting applications, due to its high density (7.13 g/cm^3) and atomic number (83) of bismuth component. These scintillator crystals are known to be mechanically robust, non-hygroscopic, having virtually almost no afterglow emissions, and no cleavage planes, enabling its easy machining into different shapes and geometries [49]. The BGO has very high photo cross-section for γ -ray absorption providing high probability per unit volume for photoelectric absorption of gamma radiation. Therefore, these crystals are found to have applications requiring high photo cross-section such as PET scanners or high detection efficiency such as Compton suppression spectrometers.

b. Germanium detectors

The Germanium being a semiconductor also offers similar detector scope as that of the silicon with almost similar working principals and applications. In comparison to silicon detectors where the thickness cannot be greater than a few millimeter, germanium can have a much larger depleted, sensitive thickness up to centimeters. This leads to its effective utilization as a total absorption detector for gamma rays having energies up to a few MeV. The depletion region is extended by creating high-purity germanium detectors (HPGe) in a PIN configuration. The utilization of these detectors is restricted due to the requirement of liquid nitrogen temperatures for their operation to produce efficient spectroscopic data. This is due to the smaller band gap of the Ge ($\sim 0.7 \text{ eV}$) which results in high currents due to thermal generation of carriers.

c. Diamond Detectors

Recently, diamond has been found to be an excellent material for detector applications. Diamond detectors have many similarities with silicon detectors. It is a semiconductor with a large band gap (5.45 eV) which offer significant advantages over silicon in terms of very low leakage currents at room temperature. Diamond is a radiation hard material and the diamond

detectors give fast signal response due to the high electron and hole mobility. At present the detector substrates are much more expensive and are more difficult to manufacture in the form of single crystals (detector grade). Procrystalline diamonds offers lower cost but results in reduced signal amplitude due the recombination of charge carriers at the grain boundaries.

2.4.4. Miscellaneous detector types

2.4.4.1. Micro-channel plate (MCP)

A micro-channel plate (MCP) is a planar component which is used for the detection of single particles (electrons, ions and neutrons) as well as low intensity impinging radiation (ultraviolet radiation and X-rays). This works similar to an electron multiplier, which intensifies signal from the particle/radiation by the multiplication of electrons via secondary emission. However, unlike secondary electron multiplier, a micro-channel plate detector has million separate independent channels, each channel acting as independent electron multiplier as a result it can additionally provide spatial resolution. An MCP consists of several very-small diameter glass channels fused together and sliced in a thin plate, in a two-dimensional periodic array. A single particle enters a channel and emits a secondary electron from the channel wall which are accelerated by an electric field. These secondary electrons move along parabolic trajectories until they hit the channel surface, causing further generation of the more secondary electrons. The process is repeated several times resulting into a cloud of several thousand electrons, finally existing from the rear of the plate. If two or more MCPs are connected in series, a single input event will result in to a pulse of about 10^8 or even more electrons at the output.

2.4.4.2. Chemical dosimeters

Chemical dosimeters are based on a quantitative measurement of chemical changes of a material after the completion of the radiation induced reactions. Liquid aqueous systems or solid materials are commonly used as chemical dosimeters. The liquid material based

dosimeters are i) Fricke dosimeter which use ferrous- ferric sulfate system and ii) Ceric Sulphate (Ceric- Cerous) dosimeters which makes use of the reduction of ceric sulphate (ceric ions are reduced to cerous) by Radiation . Many aromatic compounds such as benzene and benzoic acid undergo hydroxylation on irradiation in aqueous solution and the amount of product formed can be related to the dose. The dosimeters based on solids are based thermo-luminescence or phosphorescence. If the heat is used as an exciting agent, the phenomenon is known as thermo-luminescence and the material is called a thermo-luminescent (TL) material. These materials when used for dosimetry are known as thermo-luminescent dosimeter (TLD). Most commonly used TLD in medical applications because of their tissue equivalence are LiF:Mg,Ti, LiF:Mg,Cu,P and Li₂B₄O₇:Mn,. Other TLDs, used because of their high sensitivity, are CaSO₄:Dy, Al₂O₃:C and CaF₂:Mn. If the exciting agent is light, the phenomenon is referred to as optically stimulated luminescence (OSL). OSL has been demonstrated for a number of natural materials such as quartz and feldspar, or synthetic materials such as porcelain.

2.5. General characteristics of detectors

Usually a single detector cannot perfectly serve for all the possible applications with full satisfaction. As per the requirement of a given application, detectors and/or complex detector systems are designed to follow several criteria. The performance of a detector is evaluated in terms of some general characteristics common to all types of detectors, discussed above. Some of these characteristics like energy resolution, statistical noise, and detection efficiency etc., used to determine the suitability of a detector for an experiment / application in known surroundings are discussed below:

2.5.1. Statistical noise

The generation of charge carriers by the incident radiation in the detector medium is a statistical process [49]. The number of charge carriers is a discrete quantity and randomly fluctuates from event to event even when the deposited energy in the detector volume is the same. This discrete nature and random fluctuations in total generated charge (Q) give rise to the statistical noise. The formation of charge Q in detectors by the deposition of the energy can be considered as the Poisson process. If the N is average total number of charge carriers generated then the statistical fluctuation (standard deviation) can be given as \sqrt{N} . If the statistical noise is the only source of fluctuation in the signal, then the response function will be Gaussian with N being a large number.

The Gaussian function G(H) with average pulse height H_0 and standard deviation σ can be given as (Figure 2.3).

$$G(H) = \frac{A}{\sigma\sqrt{2\pi}} \exp\left[-\frac{(H - H_0)^2}{2\sigma^2}\right] \quad (2.11)$$

By definition, the full width at half maxima (FWHM)

$$\frac{1}{2}G(H_0) = G(H_0) \exp\left[-\frac{(FWHM/2)^2}{2\sigma^2}\right] \quad (2.12)$$

$$\ln \frac{1}{2} = \left[-\frac{(FWHM/2)^2}{2\sigma^2}\right] \quad (2.13)$$

$$\left(\frac{FWHM}{2}\right)^2 = -2\sigma^2 \ln 0.5 = 2\sigma^2 \ln 2 \quad (2.14)$$

$$FWHM = 2\sqrt{2\ln 2} \sigma = 2.355\sigma$$

The average pulse height H_0 is proportional to N, $H_0 = KN$, where K is the proportionality constant. The standard deviation (σ) of the peak in the pulse height spectrum is $K\sqrt{N}$ and the

FWHM is $2.355 K\sqrt{N}$. A limiting resolution R due to only statistical fluctuation in the number of charge carriers is thus given by:

$$R_{\text{poisson limit}} = \frac{\text{FWHM}}{H_0} = \frac{2.355 K\sqrt{N}}{KN} = \frac{2.355}{\sqrt{N}} \quad (2.15)$$

2.5.2. Energy resolution

This parameter is important for the detectors that need to measure the energy of the radiation in addition to simply counting the flux. Under the assumption that only single energy is recorded by a hypothetical detector, the resulting differential pulse height distribution is depicted in Figure 2.3. Theoretically, for a beam of mono-energetic particles, the distribution should be a delta function, but due to statistical fluctuations involved in excitation and ionization processes as well as other fluctuations arising from drift in operating conditions, random and electronic noise, etc., one observes a Gaussian like peak, as shown in Figure 2.3 [49].

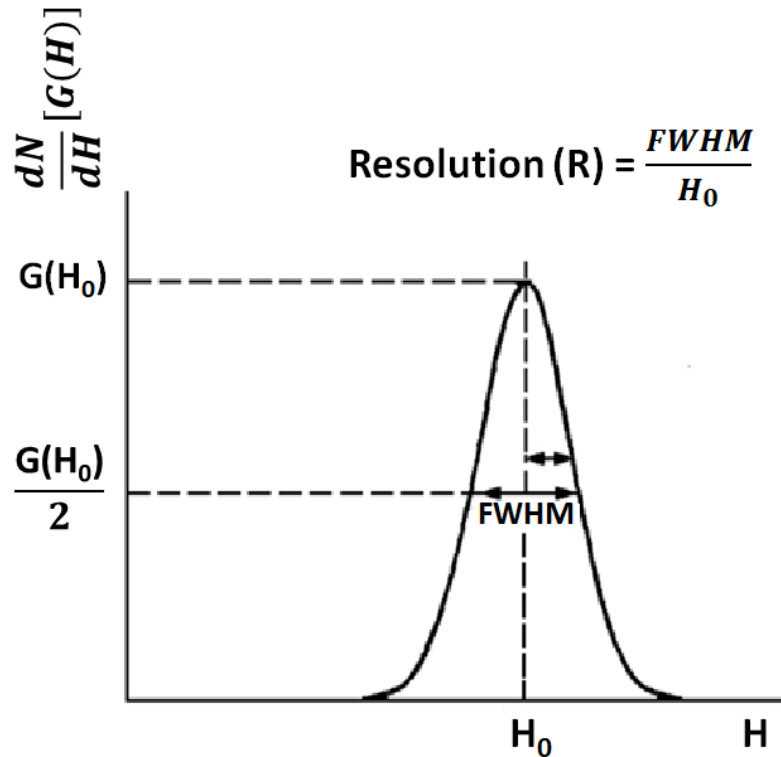


Figure 2.3. Pulse height distribution of a hypothetical detector for a mono-energetic beam of particle/radiation [49].

The energy resolution is defined by:

$$\text{Resolution (R)} = \frac{\text{FWHM}}{H_0} \quad (2.16)$$

Resolution represents the ability of the detector to distinguish between two radiations having nearby energies. In fact, the radiation with energy closer than the detector resolution cannot be separately identified; rather, the energy spectrum may be misleading by showing a single peak with broader FWHM. The average energy needed to produce an ionization event is a constant depending only on the detector material. This implies that the average number of ionizations and hence total charge collected increase with the deposited energy. Since the number of ionization are fluctuating according to Poissonian distribution, the relative resolution ($\Delta E/E$) scales as $E^{1/2}$ ($R_{\text{poisson limit}}$).

In the situation of fixed energy deposition in the detector, the variance in the Poisson statistics is imposed by an upper bound. In his pioneer works, Ugo Fano observed that the variance of the number of ionizations is found to be two or three times smaller than if this number were governed by a Poisson distribution. He assumed that the variance in the number of charge carriers is [55], [56]

$$\sigma_N^2 = (N - \langle N \rangle)^2 = F \langle N \rangle$$

where $\langle N \rangle$ is the average number of ion pairs produced by ionizing radiation for a fixed energy loss E . The factor F is named the Fano factor. It accounts for the interdependence of ionization events (such as energy dependence of ionization cross sections, phonon exchange of energy), which causes variance reduction in comparison with the Poisson statistics. So the value of the Fano factor is less than unity for semiconductor detectors.

The Fano factor is introduced in order to quantify the departure of the observed statistical fluctuation in the number of charge carriers from pure Poisson statistics.

$$F = \frac{\text{observed variance } N}{\text{Poisson predicted variance}} \quad (2.17)$$

The energy resolution for the charged particle in a semiconductor detector is dependent on several components and it can be expressed as:

$$\text{Resolution (R)} = 2.35 \sqrt{\frac{F}{J}} = 2.35 \sqrt{\frac{Fw}{E}} \quad (2.18)$$

where, w is the average energy for the electron-hole creation, E is the total energy of the incident particle and $J=E/w$.

For a 5 MeV alpha particle, the intrinsic resolution expected for silicon is therefore $R \sim 0.07\%$ or 3.5 keV. Typical measured resolutions are nearly 14-15 keV which signifies that

contribution from other sources contributes significantly in determining the resolution of the detector.

If there are several symmetric and independent sources of fluctuation present, the statistical theory predicts that the overall response function will always tend towards a Gaussian shape, even if the individual sources are characterized by distributions of different shape [49]. Then the total resolution is:

$$(\text{FWHM})_{\text{total}} = (\delta_i^2 + \delta_l^2 + \delta_{nc}^2 + \delta_r^2 + \delta_p^2 + \delta_{el}^2)^{1/2}$$

where, the individual δ 's are the contributions to the total energy spread from different sources in the FWHM.

δ_i is the contribution due to the statistics of the ionization process.

δ_l is the contribution due to detector leakage current noise.

δ_w is the energy drift contribution introduced at the detector window.

δ_{nc} is the energy drift contribution or straggling spread from nuclear collision within the detector.

δ_r is the contribution by the electron-hole recombination process. This component contributes significantly in case of heavy ions where the intense ionization plasma exists along the tracks.

δ_p = the contribution by position or range effects in the detector. It may become significant in a coaxial germanium detector and position-sensitive detector but can also arise due to field heterogeneity near the edge of the conventional detector.

δ_{el} = the electronic span due to front end electronics.

Except, δ_{el} , all other noise contributions arise from the detection process of the detector.

2.5.3. Response time

The response time is defined as the time interval between the arrival of the radiation in the detector medium and the formation of an output signal, in response to the radiation. The formation of the signal in very short time scale and with a fast rising pulse enables the marking of some important event in the time scale. This response time is particularly important if the timing information is crucial for the objectives of the experiments under study. In addition, response time of a detector is also critical for the measurements like time of flight measurements or drift time measurements.

2.5.4. Dead time

Every detector takes a minimum and finite time to process the energy/radiation deposition to give rise a measurable output signal. The detector is usually not able to record any subsequent signal or a part of it in this time. Therefore, the dead time of a detector is defined as the time after each event during which the system is not able to register another event. Depending on the objectives of the experiments, type of the detector, rate of the emission of the radiation/particles and its interaction with the detector medium, the dead time can be an important parameter. If the detector has a large dead time i.e. it is insensitive to other events for a larger time, many of the subsequent events remained un-registered. On the other hand, if the detector is sensitive to additional events during the readout period these events may pile-up and distort the signal. In experiments, where the incoming particle flux is quite high, the dead time can be significantly reduced by designing the detector with a high granularity such that the occupancy per detector cell is reasonably small. The pile-up of the events can be eliminated by shaping the detector signal to reduce the shaping time which is however limited by the inherent detector noise.

2.5.5. Detector efficiency

The detector efficiency is defined in two ways, namely absolute efficiency and intrinsic efficiency [1].

The absolute efficiency can be defined as:

$$\epsilon_{\text{abs}} = \frac{\text{number of pulses recorded}}{\text{number of radiation quanta emitted by source}} \quad (2.19)$$

This depends on the detector properties and geometrical configuration of the detector system.

The intrinsic efficiency is defined as:

$$\epsilon_{\text{int}} = \frac{\text{number of pulses recorded}}{\text{number of radiation quanta incident on the detector}} \quad (2.20)$$

The intrinsic efficiency mildly depends on the geometry that is why much more convenient to tabulate. This depends on the detector material, type and energy of the radiation and thickness of the detector in the direction of incident radiation. For radiation sources of low intensity, the detection efficiency is particularly important so as to decide the total time needed to record enough pulses for good statistical accuracy in the measurement.

Based on the energy deposited by a radiation, the detection efficiency is further subdivided into two categories: total efficiency and peak efficiency. The total efficiency is defined as the probability that a quantum of radiation incident on detector produces a pulse, regardless of energy of quantum and hence pulse size. On the other hand, the peak efficiency provides the probability that the quantum will deposit all its initial energy in the detector. However, almost always the quantum of radiation deposit only part of its energy and then escape from the detector, therefore, total efficiency is generally greater than the peak efficiency.

2.5.6. Radiation damage in detectors

Radiation damage in the detectors occurs on exposure to ionizing and non-ionizing radiation. Exposure to ionizing radiation results in accumulation of free charges which can alter the detecting medium properties and hence the characteristics of the detector. Prolonged exposure

or receiving high total ionization dose (TID) results in surface damage due to accumulation of charge. Non-ionizing radiation can displace atoms from their lattice sites and termed as displacement damage dose (DDD) effect or also non-ionizing energy loss (NIEL) effect. Silicon detectors are sensitive to both DDD and TID effects. In case of silicon detectors, the charge generated due to TID can get trapped at the silicon and oxide interface, can result in increase of detector noise and breakdown voltage. The DDD can damage the crystalline structure, can produce trap centers and high DDD ($> 10^{13}$ hadrons/cm²) can change the doping concentration which may results in type inversion [57]. Gas detectors are also sensitive to TID and ageing effect in gas detectors [58] can start from 10^{11} MIP/mm². On the other hand, the effects of TID and DDD are different in scintillating crystal calorimeters, depending on scintillating material. In case of inorganic scintillating crystals, the ionizing radiation produce color centers which may absorb scintillation light, and hence reduces the light yield. TID of even a few Gy can induce color centers in inorganic scintillators, and the scintillation centers can in some cases be completely or partially damaged. DDD, in particular low energy neutrons may cause severe damage to the organic scintillators. The low energy neutrons interact with hydrogen atoms and modify the molecular roto vibrational levels and therefore the scintillation processes.

2.6. Silicon as a radiation detector

Earlier in this chapter, different types of detectors were discussed. There are different types of semiconductor materials which can be used for the detection of radiation depending on the interaction of radiation with the material and the energy of the incident radiation. Among all, silicon is the most investigated and successfully deployed semiconductor material for radiation detectors due to following unique advantages [21], [22]:

- i) Small band gap (1.12 eV at room temperature): Due to small band gap, a large number of $e^- h$ pairs are generated as compared to gas detectors. The average energy required for the generation of $1e^- h$ pair is only 3.6 eV, which is much lower than the energy required (30 eV) for the creation of e^- ion pair in gases.
- ii) Compactness: Being solid, small size is sufficient for the full energy depositing of charged particles in most of the experiments.
- iii) High energy and position resolution: Generation of large number of $e^- h$ pairs on interaction with radiation leads to good statistics and results in good energy resolution. Fabrication technology suitable for fine pixels leads to good position resolution.
- iv) Fast time response: The mobilities of electron and holes in silicon are $\mu_e = 1400 \text{ cm}^2/\text{V}$ and $\mu_p = 450 \text{ cm}^2/\text{V}$, respectively. Due to high mobilities, both the charge carriers in a standard $300\mu\text{m}$ silicon detector can be collected within a few nanoseconds, resulting in fast time response.
- v) Low power requirement
- vi) High stopping power
- vii) High efficiency
- viii) High level of segmentation in the form of strips, microstrips and pixels is possible for one-dimensional and two-dimensional position sensing.
- ix) Batch processing is possible which results in low cost, better uniformity of the detector.

With all these advantages and scope for the tunability of the detector performance, the development of specific silicon-based radiation detectors with optimized characteristic parameters is still an area of prime interest of research.

At room temperature, the number of free charge carriers even in the intrinsic silicon is several orders higher than the number of charge carriers generated by any incident radiation in the given thickness of the silicon. This problem can be solved by cooling the detector at cryogenic

temperatures or by making depletion volume i.e. reversed biased p-n junction. Former solution is not very practical in terms of compactness. Therefore later (p-n junction diode in reversed biased mode) formulates the basic structure of the silicon detectors. The next Chapter elaborates on the different silicon device based structures suitable for detector purpose, fabrication methodologies, characterization techniques and different facilities used for the detector characterization.

Chapter 3

SILICON DETECTORS: DEVICE STRUCTURE, FABRICATION SCHEME AND CHARACTERIZATION SETUP

3.1. Introduction

The basic mechanism behind the working of all the radiation detectors is the interaction of the radiation with the detector medium to produce a measurable signal. In the case of semiconductor detectors, this interaction leads to the formation of the charge (electron-hole pairs) carriers, which are thereby collected by the subsequent electronics to create a current pulse indicating the passage of the radiation/charged particle. Unequivocally, the signal produced by the incident radiation should be much larger than the surrounding noise (high signal to noise ratio). These necessitate two contradictory requirements: (i) low band gap so that the smallest energy particle can be detected with an adequate signal magnitude and (ii) large band gap so that thermal energy and/or surrounding noise should not contribute the actual signal. The ideal band gap, stratifying both the above conditions is therefore considered to be about 6 eV. The diamond has a band gap of about 5.5 eV [59] and can serve the purpose but it is too costly for the large area detectors. It also produces a lower signal due to high mean energy for electron-hole pair creation (~13 eV) [60]. Silicon, on the other hand, though much cheaper, has lower band gap. However, simple calculations using formulae described in Chapter 2, show that it has a much larger number of thermally generated electron-hole pairs compared to the actual signal. This problem is resolved by using the p-n junction diode (instead of intrinsic silicon) in the reverse bias mode and the active area for the detection is obtained in the depletion region where there are almost no free charge carriers present at room

temperatures. Several modifications in the simple form of the p-n junction diode are required in order to increase the depletion width and to suit for the different applications. This chapter details the basic device structures used for silicon detectors [22], [49], [61], [62], modifications required to improve their functioning as radiation detectors, their fabrication schemes and subsequent characterization methodologies.

3.2. Basic semiconductor structures

3.2.1. The p–n junction diode

Basic electronic structure for most of the silicon detectors is a p-n junction. The p-n junction is formed in a single crystal semiconductor by starting with a wafer of p-type or n-type and then doped with n-type impurity in the case of p-type base wafer or with p-type impurity in the case of n-type base wafer. Initially, during the formation of junction, electrons diffuse in to p-region and holes in to n-region (due to concentration gradient) leaving behind the positive and negative space charge regions, respectively. The extent of space charge is called depletion region. This space charge creates an electric field which opposes further diffusion of the electrons and holes. Due to this electric field, a potential is developed known as built in potential (V_{bi}). This process is described in the Figure 3.1 with the help of energy band diagram for n-p junction. If the doping levels are equal on both sides of the junction, the depletion region extends equal distances into both sides. Usually, however, for silicon detectors there is a difference in the doping levels on one side of the junction compared with the other. For example, if doping concentration in p-type region is higher than that of donor atom concentration in the n-type, the holes diffusing across the junction will tend to travel a greater distance into the n-type region before recombining with electrons. In this case, the depletion region would extend farther into the n side as shown in Figure 3.2. along with the resultant profile for space charge $\rho(x)$, electric potential $\phi(x)$ and electric field $E(x)$.

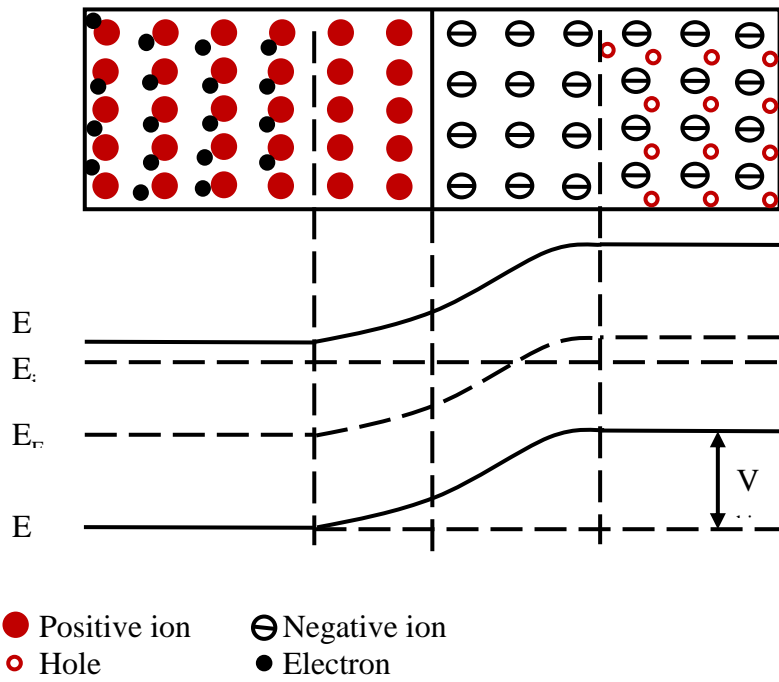


Figure 3.1. Energy band diagram of n-p junction in unbiased condition. E_C , E_i , E_F , and E_V are the bottom energy level of conduction band, intrinsic energy level, Fermi level and top energy level of conduction band, respectively.

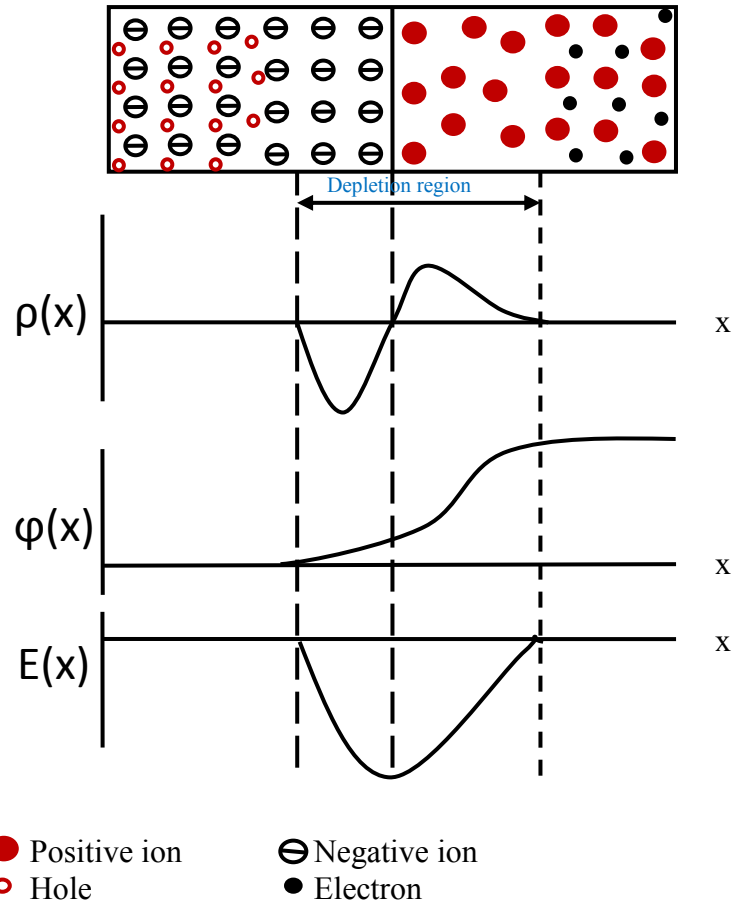


Figure 3.2. The distribution of the space charge $\rho(x)$, electric potential $\phi(x)$ and electric field $E(x)$ in the depletion region across p-n junction.

If the charge density distribution $\rho(x)$ is known, then built in potential, electric field and depletion region can be determined from Poisson's equation,

$$\frac{d^2\phi}{dx^2} = -\frac{\rho}{\epsilon} \quad (3.1)$$

where ϵ is the permittivity of the medium (silicon).

For simplicity, it is assumed that the charge is uniformly distributed about the p-n junction. If x_n and x_p denotes the extent of depletion region on the n side and p side respectively, then

$$\rho(x) = \begin{cases} eN_D, & 0 < x < x_n \\ -eN_A, & -x_p < x < 0 \end{cases} \quad (3.2)$$

As the semiconductor is neutral,

$$N_A x_p = N_D x_n \quad (3.3)$$

Integrating equation (3.1) and applying boundary conditions, the electric field can be given as

$$\frac{d\phi}{dx} = \begin{cases} -\frac{eN_D}{\epsilon}(x - x_n), & 0 < x < x_n \\ \frac{eN_D}{\epsilon}(x + x_p), & x_p < x < 0 \end{cases} \quad (3.4)$$

By integrating (3.4) and applying boundary conditions, the built-in potential V_{bi} can be obtained.

$$V_{bi} = \frac{e}{2\epsilon} (N_D x_n^2 + N_A x_p^2) \quad (3.5)$$

Again using (3.2)

$$x_n = \left(\frac{2\epsilon V_{bi}}{eN_D(1 + N_D/N_A)} \right)^{1/2}, \quad x_p = \left(\frac{2\epsilon V_{bi}}{eN_A(1 + N_A/N_D)} \right)^{1/2} \quad (3.6)$$

$$d = x_n + x_p = \left(\frac{2\epsilon(N_A + N_D)}{e N_A N_D} V_{bi} \right)^{1/2} \quad (3.7)$$

Where d is the total width of depletion region. If p-region is much heavily doped with respect to n-region (as in the case of detectors) then the depletion region is extended almost entirely in the p-region (if $N_A \gg N_D$, then $x_n \gg x_p$).

Then, the total width of depletion region

$$d \cong x_n = \left(\frac{2\varepsilon V_{bi}}{eN_D} \right)^{1/2} \quad (3.8)$$

$$d \cong (2\varepsilon\rho_n\mu_n V_{bi})^{1/2} \quad (3.9)$$

The built-in potential can be calculated from the difference in the intrinsic levels of the p-region and n-regions using equations described in Section 2.6 (equations (A.11), (A.17)) and (2.41)].

$$n_n n_p = N_D N_A = n_i^2 e^{\frac{E_i^p - E_i^n}{k_B T}} \quad (3.10)$$

$$V_{bi} = \frac{1}{q} (E_i^p - E_i^n) = \frac{k_B T}{q} \ln \frac{N_A N_D}{n_i^2} \quad (3.11)$$

3.2.2. Semiconductor metal junction: Schottky barrier and Ohmic contact

The contact electrodes for semiconductor devices are usually provided by the metals, therefore, it is very important to understand the contact mechanism between metal and semiconductor [22]. The energy band diagrams for metal, extrinsic semiconductor and that for their junction are represented in Figure 3.3 and Figure 3.4. When the metal comes in contact with the semiconductor, the contact may be Ohmic or Schottky junction.

The Schottky barrier is a metal-semiconductor contact with large barrier height. It has similar properties as p-n junction and works as a rectifying contact. When a metal and a semiconductor are brought in to contact, the Fermi levels get aligned (Figure 3.4) and a built-in potential $V_{bi} = \phi_m - \phi_s$ develops across the junction and the band bend near the junction. As shown in Figure 3.4, for a n-type semiconductor, barrier height ϕ_{Bn} may be written as,

$$\phi_{Bn} = \phi_m - \chi_s \quad (3.12)$$

Similarly, the barrier height can be calculated for a p-type semiconductor.

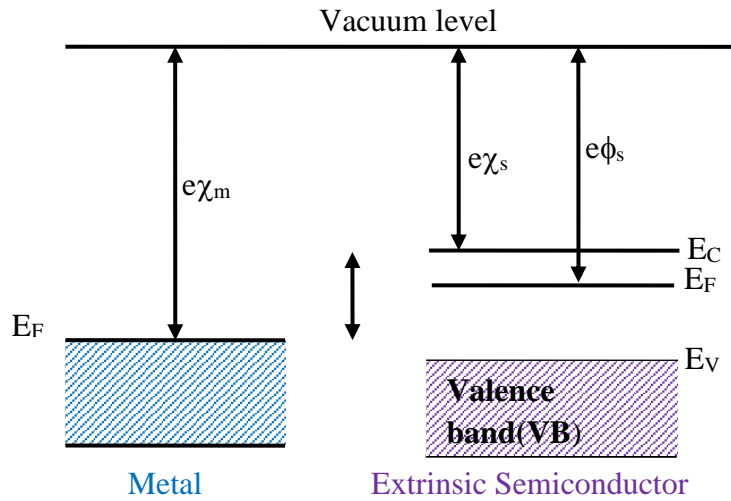


Figure 3.3. Typical energy band diagram of metal and semiconductor. $e\chi_m$, $e\chi_s$ and $e\phi_s$ represent the work function of metal, electron affinity of semiconductor and work function of semiconductor respectively.

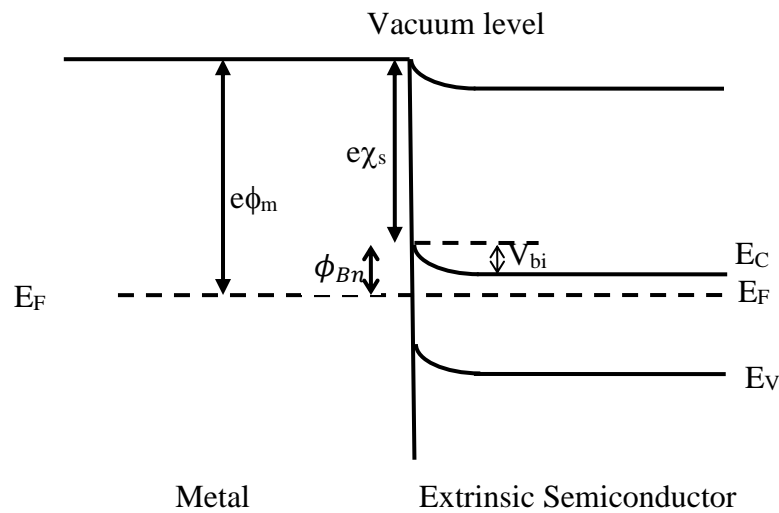


Figure 3.4. Energy band diagram of a metal semiconductor junction [62].

An Ohmic contact is defined as a metal-semiconductor contact that has a negligible contact resistance relative to the bulk or series resistance of the semiconductor. A satisfactory Ohmic contact should not significantly degrade device performance and can pass the required current with a voltage drop that is small compared with the drop across the active region of the device. If highly doped semiconductor ($\sim 10^{19} \text{ cm}^{-3}$) is put in contact with the metal, then the width of potential barrier may become so small that tunneling probability becomes sufficiently enough to form an Ohmic contact [22].

For making contacts in semiconductor detectors, a highly doped layer (N^+ or P^+) of same type of semiconductor is introduced at metal-semiconductor interface to make an Ohmic contact.

3.2.3. The $N^- N^+$ or $P^- P^+$ structures

Figure 3.5 shows an example of formation of junction between lightly doped n-type (N^-) silicon and highly doped n-type (N^+) silicon. When both are brought in to contact, the Fermi level lines up at thermal equilibrium. As there are always electrons available for conduction and due to the gradient in doping concentrations of N^- and N^+ region, a built-in potential develops which prevents the high leakage current.

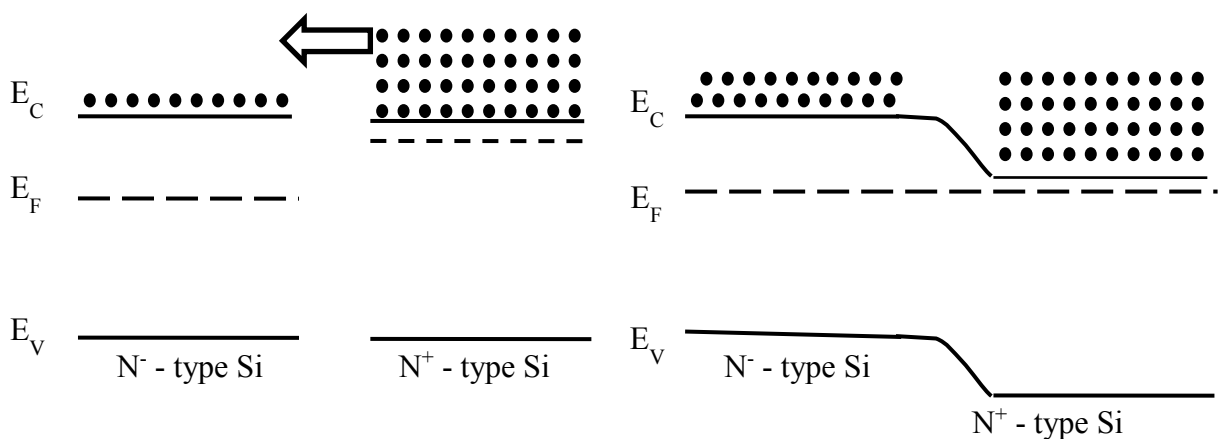


Figure 3.5. Energy band diagram before and after formation of $N^- N^+$ junction.

3.2.4. Silicon PIN or P⁺ N⁻ N⁺ structure: PIN diode detector

In most of the applications, it is preferred that the maximum or full energy of the incident radiation should be deposited in the depletion region of the detector volume, as the effective collection of charge generated by the energy deposited in the nondepleted region is not possible. This originates the need of large depletion width. The silicon PIN detectors consist of narrow highly doped p-region (P⁺-region), mildly doped n-region (N⁻ or I: high resistivity n-type wafer) and highly doped n-region (N⁺-region). As the equation (3.7) suggests that the depletion in this configuration will be fully extend in the N⁻ region. The reverse biasing of this P⁺ N⁻ junction by applying a reverse voltage V_R, further increases the width of depletion region. Hence the equation (3.7) can be written as,

$$d = x_n + x_p = \left(\frac{2\epsilon_{Si}(N_A + N_D)}{e N_A N_D} (V_{bi} + V_R) \right)^{1/2} \quad (3.13)$$

If D is the thickness of the detector, then the full depletion voltage V_{FD} can be given as,

$$V_{FD} = \frac{qD^2 N_D N_A}{2\epsilon_{Si}(N_A + N_D)} - V_{bi} \quad (3.14)$$

Here N_A ≫ N_D,

$$V_{FD} = \frac{qD^2 N_D}{2\epsilon_{Si}} - V_{bi} \quad (3.15)$$

The variation of charge density, potential and electric field in the depletion region of an almost fully depleted PIN diode is shown in Figure 3.6.

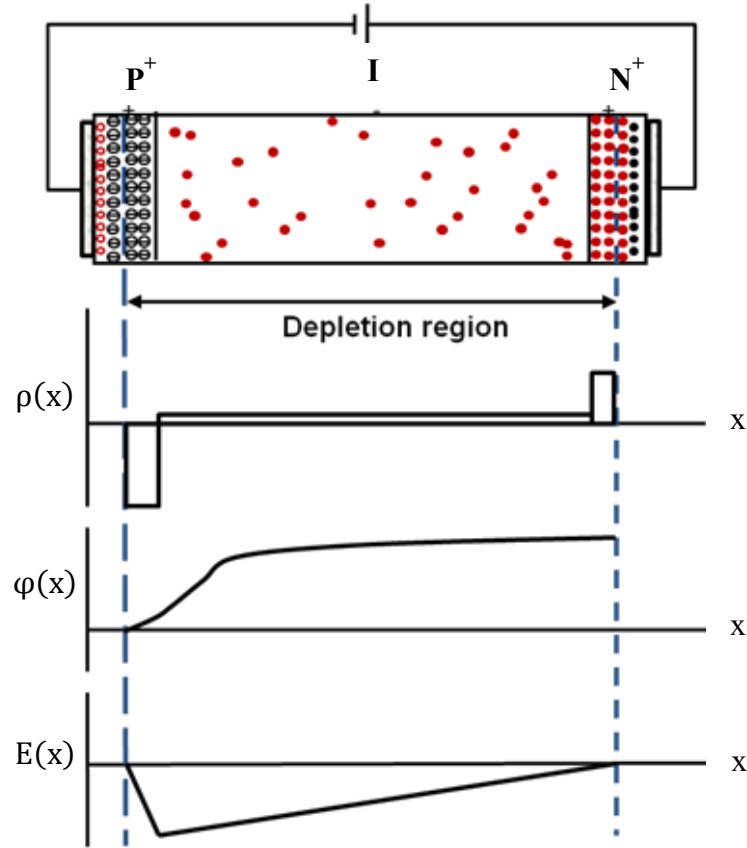


Figure 3.6 Graphical representation of the variation of charge density, potential and electric field in the depletion region of an almost fully depleted PIN diode.

3.2.4.1. Capacitance

The bulk capacitance per unit area of a PIN diode/PIN detector for depth of depletion region (d) with the help of equation (3.13) can be given as:

$$C_d = \frac{\epsilon_{Si}}{d} = \sqrt{\frac{\epsilon_{Si}^2}{\frac{2\epsilon_{Si}(N_A+N_D)}{e N_A N_D} (V_{bi} + V_R)}} \quad (3.16)$$

$$C_d = \sqrt{\frac{e\epsilon_{Si}N_D}{2(V_{bi} + V_R)}} \quad (3.17)$$

If the detector is fully depleted then there will be no further change in the capacitance.

$$C_{FD} = \frac{\epsilon_{Si}}{D} \quad (3.18)$$

This only depends on the geometry of the detector. Fully depleted detectors have low capacitance and hence, achieve good energy resolution due to low contribution in electrical noise.

3.2.4.2. Leakage current

The net current in unbiased condition of PIN diode is zero as the drift and diffusion currents balance each other at thermal equilibrium. In reversed biased condition, small leakage current due to minority charge carriers flows due to the increase in depletion width and barrier potential. The reverse leakage current for an ideal diode can be given as,

$$I = I_s \left(e^{\frac{qV}{k_B T}} - 1 \right) \quad (3.19)$$

Where $I_s = q \left(\frac{D_p p_n}{L_p} + \frac{D_n n_p}{L_n} \right)$ reverse saturation current, D_p and D_n are the diffusion coefficient for charge carriers, L_p and L_n are the diffusion lengths for the carriers, p_n and n_p are the minority carrier concentrations in P and N regions, respectively at thermal equilibrium.

3.2.4.3. Breakdown

When a sufficiently high reverse voltage is applied across the detector then the drift velocity no more remains linear with the electric field as kinetic energy of the charge carriers attains the values much higher than the thermal energies. This can lead to the breakdown of the p-n junction and results in the flow of large leakage currents through the junction. This voltage is known as breakdown voltage. The breakdown can take place mainly through two mechanisms, namely avalanche multiplication and quantum mechanical tunneling of carriers through the bandgap. Planar detectors have higher electric field at the junction edges which leads to early breakdown.

3.3. Various types of silicon detectors

Silicon is the most widely used semiconductor with wide availability and mature fabrication technology. The p-n diode or metal-semiconductor junction diode are basic device structures for the measurement of nuclear radiation. Most commonly used detector configurations are described below [49]:

3.3.1. Diffused junction detectors

These detectors are based on p-n junction configuration in which p-type impurity is diffused in to the n-type silicon substrate to form p-n junction. The doping concentration is made high to ensure the extension of depletion region into the n-side of the junction. The diffused p-type layer extended up to 2 μm of the depth and creates a dead layer for the incident radiation. Now a day's, the uses of these detectors are very limited due to the disadvantage of thick dead layer [1].

3.3.2. Surface barrier detectors (SSB)

These detectors are based on the metal-semiconductor rectifying junction or Schottky barrier as described previously. Usually n-type silicon with gold or p-type silicon with aluminium is used to make SSB. These detectors are fabricated by etching silicon surface followed by deposition a thin layer ($\sim 200 \text{ \AA}$) of gold by evaporation. These detectors are very prone to surface contamination and general environment [19], [21].

3.3.3. PIN configuration-based detectors

The most widely used silicon detectors are based on PIN ($\text{P}^+ \text{N}^- \text{N}^+$) configuration (as described in Section 3.2.4) and are being fabricated on silicon (111) wafers using silicon planar technology adopted from microelectronic technologies [15], [22]. These detectors are

more stable than SBB. The batch production of multiple detectors is possible starting with a large-area silicon wafer using planner technology, thus providing cost savings [63]. Other advantages of these detectors are as listed in Section 2.7.

3.3.4. Strip detectors

Silicon based position sensitive detectors provide high position resolution in comparison to any other detector. High level of implant segmentation is possible by the use of advance silicon fabrication technology. These detectors are being extensively used in high energy particle physics experiments [13], [14], [16] Fabrication of one dimensional position sensitive strip detector is done by the P⁺ implantation on one of the surface in the form of strips. Each strip works as an individual detector. The readout from each strip can determine the position of incident particle in one dimension (either x or y) and precision of position depends upon the gap between the strips and strip thickness. For the two-dimensional position sensing strip detectors, double sided wafer processing is implemented and the segmentation in the form of strips is done on the both sides (P⁺ side as well as N⁺ side). Strips on one side are made orthogonal to the other side strips. Main challenge comes in fabrication of isolated N⁺ side strips as the charge accumulation at the interface of silicon and SiO₂ creates interstrip conduction path between the N⁺ side strips. Few techniques such as p-stop and p-spray are being used to properly isolate the N⁺ side strips [64]. In p-stop method, P⁺ implantation between the N⁺ strips are carried out to break the conduction path, mostly by using three configurations namely atoll, common and atoll with common. This method increases the number of masks used to pattern the additional stop implantation [64]. On the other hand, the interstrip insulation can be achieved alternatively by the use of a uniform blanket ion implant performed on the silicon surface (p-spray). The use of this technique does not require an extra

mask as for the p-stop implant. The tuning of p-spray implant is very critical, repeatability and non-uniformity issues may be faced.

3.3.5. Particle identification: ΔE -E detector

The identification of charged particles to obtain relevant physics results is required in various experiments. The identification of charged particle can be achieved using a variety of techniques. All techniques depend on the measurement of the momentum and the velocity to determine the charged particle rest mass using $m_o = p/\beta c\gamma$ (where m_o is the rest mass, p is the momentum, $\gamma = \frac{1}{\sqrt{1-\beta^2}}$, β is the relativistic factor (v/c), v is particle velocity and c is speed of light) and therefore its identity. For this purpose, several methods, such as time of flight measurements, detection of Cherenkov radiation, pulse shape discrimination (PSD) method and specific energy loss measurement can be utilized [49], [65]. Among all these techniques, the specific energy loss technique which employed ΔE -E detector telescope is one of the most convenient techniques.

The basic formalism for this method lies in Bethe formula (equation (2.2)), according to which, for non-relativistic charged particles of mass m and charge ze , the specific energy loss, can be expressed as

$$\frac{dE}{dx} = C_1 \frac{mz^2}{E} \ln C_2 \frac{E}{m} \quad (3.20)$$

where C_1 and C_2 are constants. The product $E(dE/dX)$ is a logarithmic function of energy, showing mild dependence upon energy but directly related to the term mz^2 , that helps in the characterization of the particles involved. If incident radiation consists of a mixture of different particles whose energies do not vary by large extent, the product of the amplitude of the total energy (E) and the specific energy loss (dE/dx) will be unique for each particle. The

detector telescope for this technique, therefore, comprises two detectors namely, ΔE detector and E detector, measuring specific energy and total energy, respectively. Because the incident energy can be obtained by summing the pulse amplitudes from the ΔE and E detectors, simultaneous measurement of both mass and energy of each incident particles is therefore possible.

Thick gas detectors such as ionization chamber, proportional chamber or solid state detectors like silicon and germanium detectors work as E detector where the particle completely stops. Particle loses all of its energy in the bulk of the detector and generates charge carriers. The collection of charge carriers gives electrical signal the amplitude of which depends upon the total amount of deposited energy. The specific energy loss is measured in a thin detector, placed before the E detector. The detector has a thickness much less than the range of incident particles, so that the particle loses only a small fraction of its total energy. The number of charge carriers created within the thickness of Δt will simply be $(dE/dX) \Delta t/\epsilon$, where ϵ is the energy required to create one electron hole pair. So the measured signal directly gives specific energy loss which ultimately gives the identity of the particle.

In order to avoid stray counts in individual ΔE and E detectors, only those events are counted which occur in coincidence between the two detectors as shown in the Figure 3.7. Therefore, the detector telescope simultaneously measures a specific energy loss in ΔE detector and their rest energy in E detector. The performance of such detector strongly depends upon the uniformity of the detector over its area exposed to the incident particle beam. A slight variation in thickness influences in the energy resolution of the detector. If a semiconductor is used as a ΔE -detector, a thin semiconductor detector is difficult to handle because of the fragile nature. So transmission detectors are commonly supported with a thick silicon detector. Such ΔE -E detectors are also not very suitable for multi detector array system.

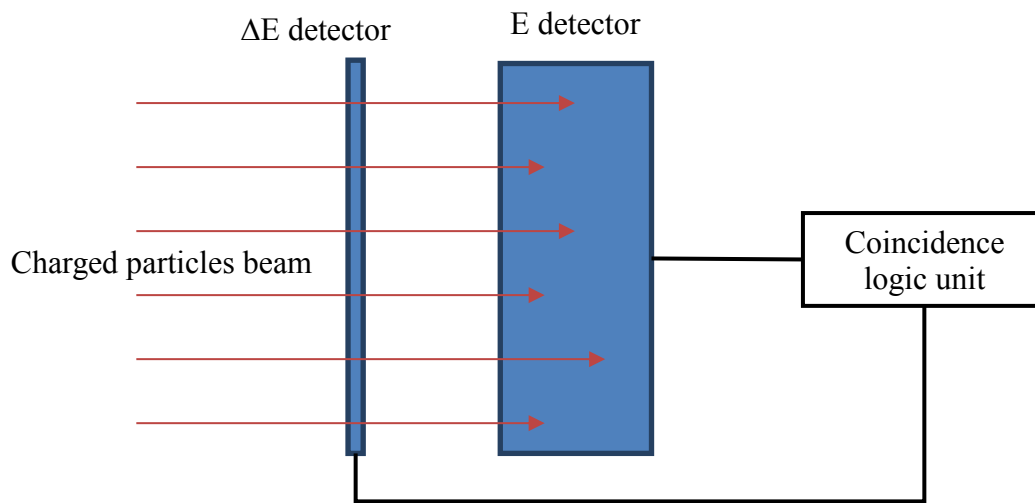


Figure 3.7. Schematic of ΔE -E detector for the particle identification.

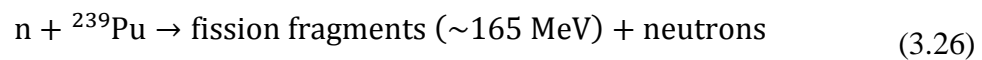
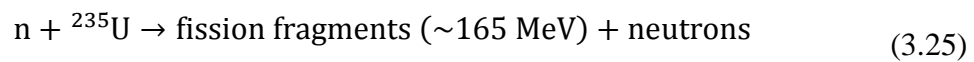
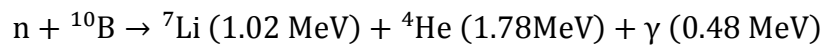
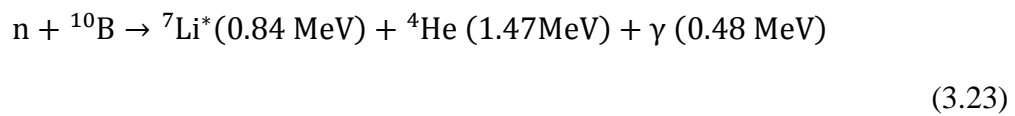
The integration of both detectors makes it more compact and easier to handle. In this thesis, a novel integrated ΔE -E detector telescopes in which both the detectors are fabricated on the same wafer for particle identification and energy measurement in physics experiments have been developed. These telescopes were successfully demonstrated to be useful for light charged particle, fission product identification and their energy measurements.

3.3.6. Semiconductor based thermal neutron detector

Detection of neutrons is important for many applications such as personnel and environmental safety, reactor control, medicine, and detection of illicit material. Being a non-ionizing particle, direct detection of neutron is not possible. Hence, the neutron detectors must rely on the indirect detection i.e. secondary charged particle detection, as described in Chapter 2. The incident neutron participates in a nuclear reaction to produce secondary charged particles and then detection of these charged particles indicates the presence of neutron. Various nuclear reactions are used for neutron detection, and these can be divided into absorptive and

scattering reactions [49]. Absorptive reactions are (n, α), (n, p), (n, γ), or (n, fission) [66]. In scattering reaction, the detection of knocked-out proton facilitates the neutron detection.

The common reactions which are utilized in detection of neutrons are:



There are various neutron detectors, among those gas proportional counters and ionization chambers, scintillation detectors and solid state semiconductor detectors are most important. In gas detectors (filled with ${}^3\text{He}$ or BF_3), striking neutron produces secondary charged particles (equations (3.21) and (3.23)) and these charged particles deposit their energy in the detector volume to give rise to the signal as described in the Chapter 2. These detectors have some disadvantages like bulky in size, requirement of high bias voltage, shortage of ${}^3\text{He}$, toxic nature of BF_3 . There are some common scintillators such as Li glass, ZnS (Ag)-LiF which are also utilized for neutron detection. But due to the use of photo multiplier tubes, the detector design becomes bulky and also faces the problem of γ -neutron separation.

Among all other available thermal neutron detectors, silicon based thermal neutron detectors can provide compact and economical detectors for neutron detection and imaging application

[67]–[70]. Commonly used conversion materials for silicon based thermal neutron detectors are boron and lithium. The boron is most preferable due to the high thermal neutron cross section of 3800 barn and it interacts with a neutron by $^{10}\text{B} (n, \alpha) ^7\text{Li}$ nuclear reaction. ^{157}Gd could also be a convertor material neutron detection due to its extremely high neutron capture cross section (255,000 barns) but its suitability for certain applications remains debatable due to low energy of internal conversion electrons and high gamma background [71], [72]. In this thesis, an innovative approach of using thin epitaxial silicon PIN detector with a ^{10}B converter layer for thermal neutron measurements has been demonstrated in Chapter 6.

3.4. Basic fabrication steps of PIN diode-based detectors.

The fabrication of PIN diode-based detector is based on standard semiconductor fabrication technology [22]. For fabrication of standard detectors, a high value of resistivity (3 to 5 K Ω -cm) is required for the full depletion of the detector (thickness of 300 μm) at reverse bias of 50 to 100 V. In addition, a uniform radial and axial resistivity distribution across the ingot is also essential for the large area detectors and batch production [73]. Wafers from ingot grown from Float zone (FZ) method are exclusively used for standard detector applications due to their high purity and low radial resistivity variation (RRV). For pulse shape analysis applications, resistivity variation (RV) or resistivity non-uniformity of the silicon should be as minimum as possible. Signals collected from areas of a detector having different resistivity show variation in pulse shape (eg. different rise time), thus degrading the performance of the detector [74]. This issue could be solved up to some extent by using Neutron transmuted doped (NTD) and Preferred Float Zone (PFZ) wafer. The Neutron Transmutation Doped Float Zone Silicon wafer has the lowest resistivity variation ($\pm 3\%$ to $\pm 10\%$) of any crystalline silicon product on the market. These wafers are offered in the widest range of resistivities. PFZ single crystal silicon has the lowest resistivity variations ($\pm 10\%$ to $\pm 20\%$) of the in-situ

doped float zone products available and the dopant distribution is uniform throughout the length of the ingot. The rate of the energy loss by a charged particle in a crystalline material is dependent on the orientation of its path with respect to the crystal axes. On average, the energy lost by a particle travelling parallel to the crystal plane is lower than that for particles traversing in some arbitrary direction. As a result, these channeled particles have better penetration depth in the medium. The effect is particularly important for thin and totally depleted detectors, as the amount of the energy deposited varies significantly in this case with changes in the crystal orientation with respect to particle direction. This effect of channeling can be minimized by fabricating the detectors from silicon cut so that the (111) crystal orientation is perpendicular to the wafer surface. The recorded pulse height can be affected and hence the resolution by the channeling even when the particle is fully stopped within the active volume. Also, since the probability of the nuclear collisions is less for channeled particles, the pulse height defect for heavy ions may be reduced [75]. The fabrication steps are briefed in following sections and presented schematically in Figure 3.8.

3.4.1. Oxidation

Chemically cleaned and mildly doped N^- wafers (highly pure) are thermally oxidized at temperature about 1000°C by placing in quartz tube in oxygen environment to form thin layer of SiO_2 on the wafer surface. Si is consumed from the wafer surface to form SiO_2 .

3.4.2. Photolithography

Device patterns for various layers comprising the detector are generated on mask plates. The oxidized wafer is covered by a photo resist and then illuminated through patterned mask plate. Thus, the pattern is transferred to photo resist. Photoresists are classified as positive and negative. For positive resists, the exposed regions become more soluble and thus more easily removed in the development process. For negative resists, the exposed regions become less

soluble, and the patterns formed in the negative resist are the reverse of the mask patterns. After development of photo resist, SiO₂ is etched from the diode area for ion implantation.

3.4.3. Ion implantation

In this process, an accelerated beam of desired impurity ions (usually boron for P⁺ implant and phosphorous for N⁺) is directed onto the semiconductor surface. The penetration depth of the ions inside the wafer depends upon the dopant impurity and imparted energy. Only uncovered region of silicon gets implanted as in covered regions and the implant is stopped by the SiO₂ layer. The back side of wafer is fully implanted with phosphorous for creating a N⁺ layer.

3.4.4. Annealing

While implantation collisions take place between impurity atoms and lattice, most of this lattice damage can be recovered by the process called annealing. It also helps in proper settlement of impurity atoms in the lattice. In this process, wafer is heated up to 1000⁰C for short duration of time to prevent further in-diffusion.

3.4.5. Metallization

In order to make the contact to the detector, Al is deposited (by sputtering) followed by sintering about 500⁰C for better contact (Ohmic).

The edges of the diode are considered to be most delicate regions of the detector structure. When the detector is biased, high electric fields are generated in some regions leading to more probable electrical breakdown. Various types of detector designs have been invented and successfully implemented to take care this problem. Some of the examples are guard rings

[76], the partial compensation of accumulation layer by implantation [77]–[79], metal overhangs [80], etc .

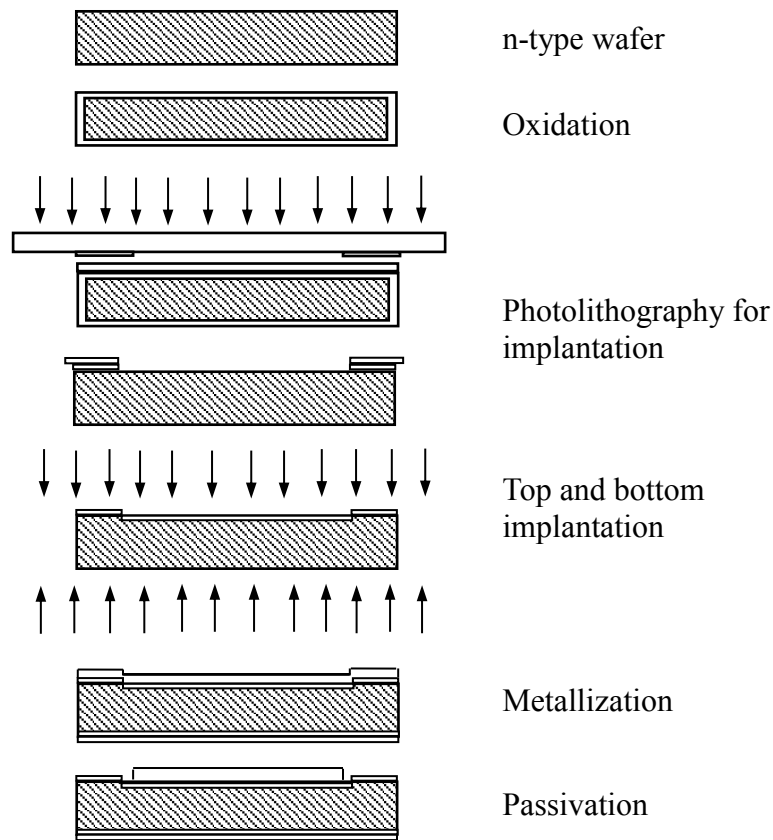


Figure 3.8. Schematic representation of basic steps used for the fabrication of PIN diode based detectors [22].

3.4.6. Charge collection and measurement

In the detector, the electron–hole pairs created in the space-charge region are separated by the applied electric field which drift towards the respective electrodes. As shown in Figure 3.9, holes will go to the P^+ junction while electrons will move towards the backside N^+ electrode. It is important to mention here that the detector will show signal even before the arrival of the charges at the electrodes. The electrons and holes will induce different charges on the electrodes, due to their different distances as well as mobilities (Figure 3.9). If a total charge q is induced by the hole then it will be divided between the top and bottom surface electrodes

in the ratio of the inverse of distances. A simple calculation will thus provide a charge induced by hole equal to $q (d-x_h)/d$ on the top and $q x_h/d$ on the bottom electrodes. The addition of charge induced by the electron gives the total induced charge as $q (x_e-x_h)/d$. where x_e , x_h , and d represents the distance of generated hole from the top, distance of electron from the top and thickness of the detector as shown in Figure 3.9.

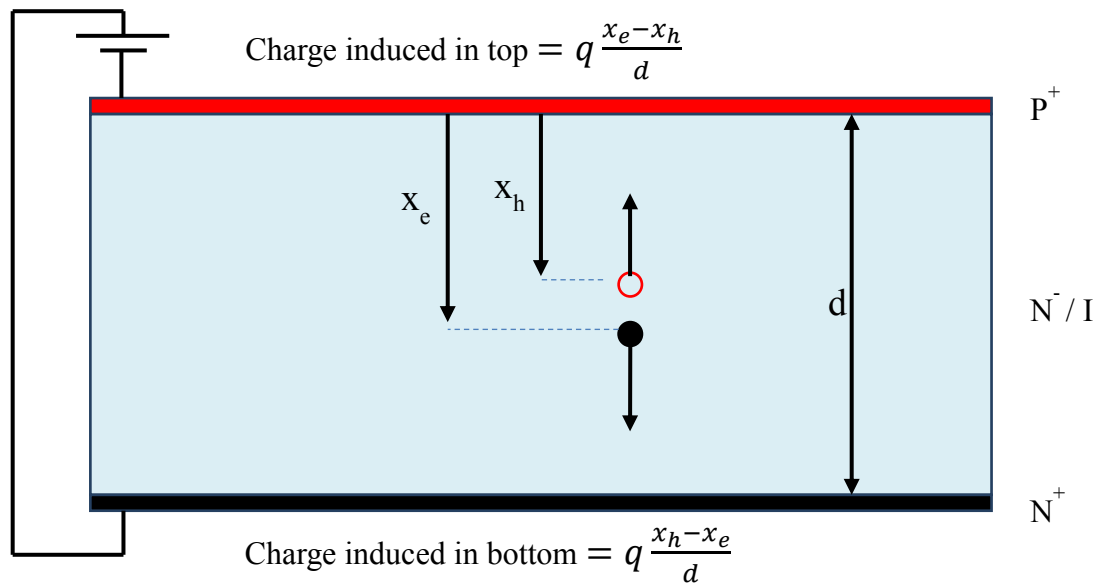


Figure 3.9. Formation of detector signal due to separation of electron-hole pairs by applied electric field in the depletion region of the detector [22].

3.5. Characterization of detectors

3.5.1. Static characterization of silicon detectors

Static characterization is carried out to evaluate the performance of the silicon detectors in terms of current-voltage (I-V) and capacitance-voltage (C-V) characteristics to obtain various electrical parameters of the detectors such as leakage current, full depletion voltage and breakdown voltage.

3.5.1.1. Current-Voltage (I-V) characterization

I-V characteristics are obtained by measuring the current flow in the diode as a function of applied voltage. The reverse I-V characteristics curves are very useful for calculating the breakdown voltage, leakage current and stability analysis. The laboratory setup used for this purpose in the present work is shown in Figure 3.10.

Figure 3.10 shows the block diagram of automated PC based characterization setup used in the present work. This setup consists of PC, picoammeter with voltage source, prober station (for wafer label characterization) and a light shield arrangement (for characterization of packaged detectors) for mounting the detectors inside. The picoammeter is controlled by PC through a software program. The control panel, used for I-V test, named as “Auto IV Measurement”, contains several features (Figure 3.12) as mentioned below:

- i. Setting up minimum reverse bias voltage (start voltage)
- ii. Setting up maximum reverse bias voltage (voltage)
- iii. Setting up number of steps,
- iv. Setting up current limit,
- v. File path to save the data, output file name and soft keys like run, run continuously, stop and pause to operate.

The picoammeter operates in following sequence as per the command given:

- i. Setting up minimum reverse bias voltage
- ii. Waiting for specified settling time (speed)
- iii. Calculation of leakage current at given voltage
- iv. Increase the level of bias voltage as per step size given
- v. Repeat the above given steps till the end voltage
- vi. Saving of output file and memory and plotting IV characteristics.

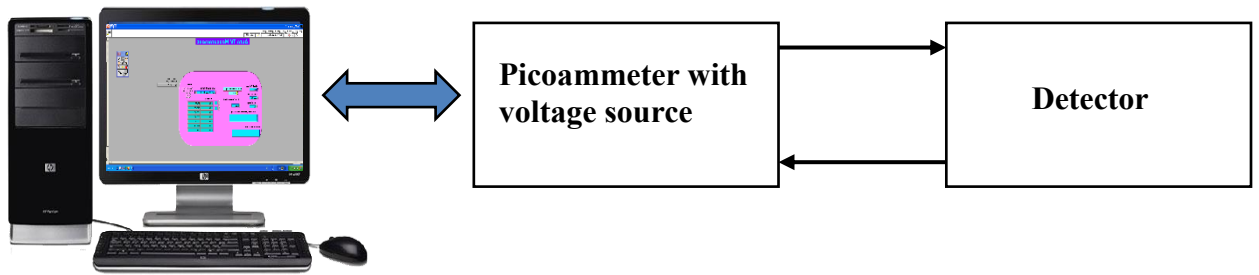


Figure 3.10. Block diagram of electronic setup for I-V characterization.

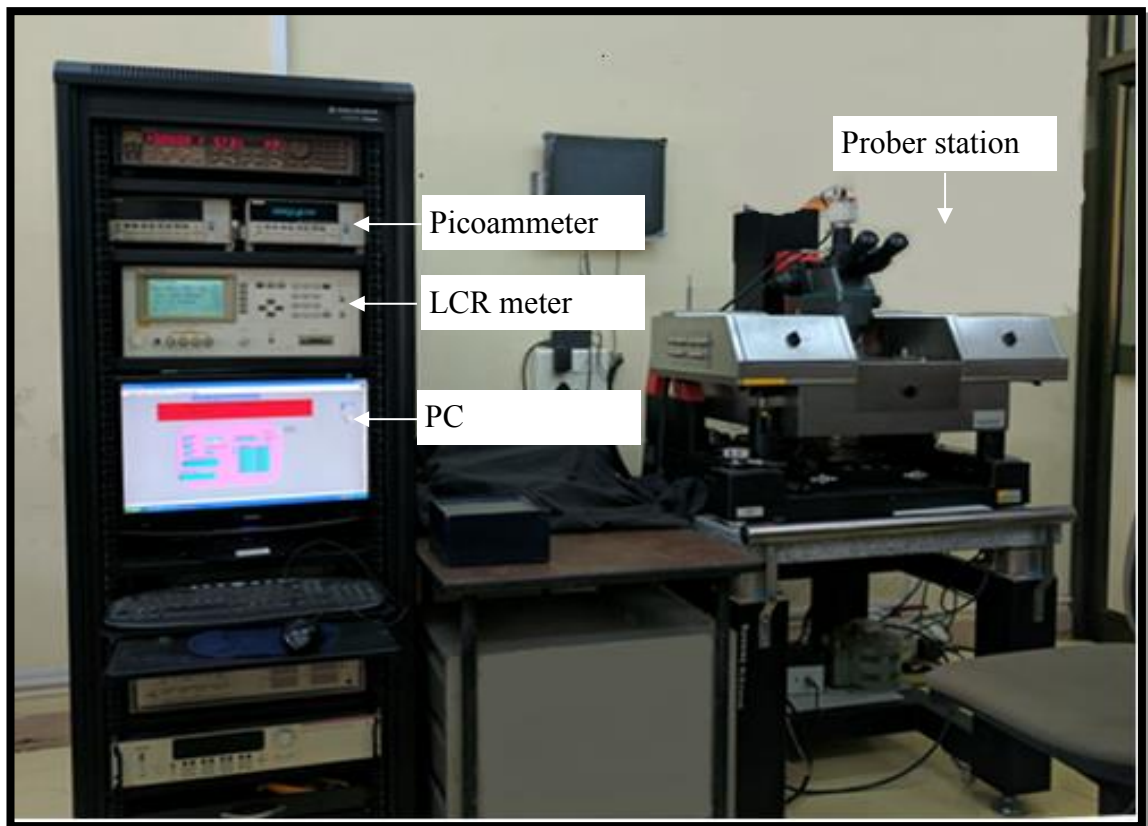


Figure 3.11. Laboratory setup for static characterization.

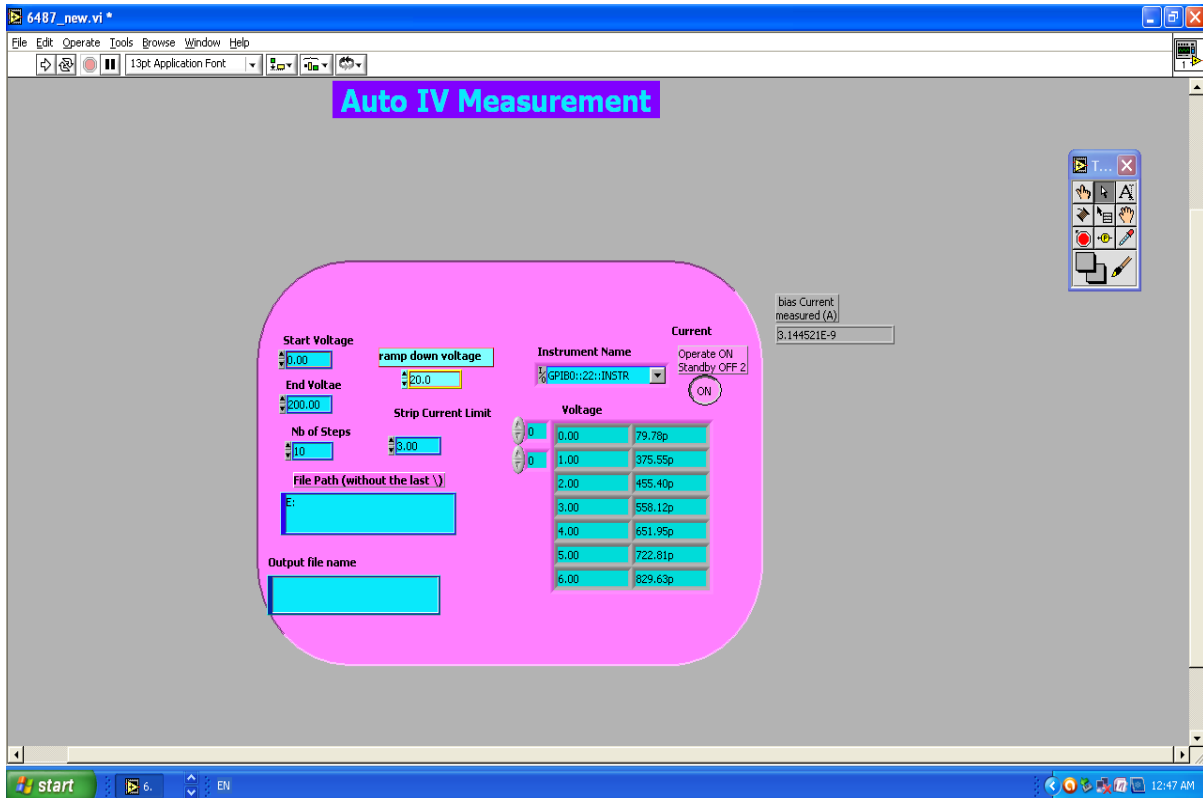


Figure 3.12. Screen shot of control software user interface.

3.5.1.2. Capacitance-Voltage (C-V) characterization

Capacitance-voltage profiling is a technique for characterizing semiconductor materials and devices. The capacitance is measured and plotted as a function of applied voltage. The depletion region with its ionized charges inside behaves like a capacitor. By varying the voltage applied to the junction it is possible to vary the depletion width (equation (3.13)). The dependence of the depletion width upon the applied voltage provides information on the semiconductor's internal characteristics, such as its doping profile, full depletion voltage and electrically active defect densities (Section 3.2.4).

In the present work, the capacitance-voltage characteristics were measured using a LCR meter, an electronic test equipment used to measure the inductance (L), capacitance (C), and resistance (R) of a component. In the simpler versions of this instrument, the true values of these quantities are not measured, rather the impedance is measured internally and converted

for display to the corresponding capacitance or inductance value. The auto-balancing bridge method is commonly used up to 110 MHz. The complex impedance of the device under test (DUT) can be measured with a measurement circuit consisting of a signal source and a circuit to measure the vectors (magnitude and phase angle) of the signal voltage or current, respectively. The current I_x balances with the current I_r which flows through the range resistor (R_r), by operation of the I-V converter (Figure 3.13). The potential at the low point is maintained at zero volt (thus called a virtual ground). The impedance (Z_x) of the DUT can be calculated from using the voltage measured at the High terminal (V_x) and across R_r (V_r) as shown below.

$$\frac{V_x}{Z_x} = I_x = I_r = \frac{V_r}{R_r} \rightarrow Z_x = \frac{V_x}{I_x} = R_r \frac{V_x}{V_r} \quad (3.27)$$

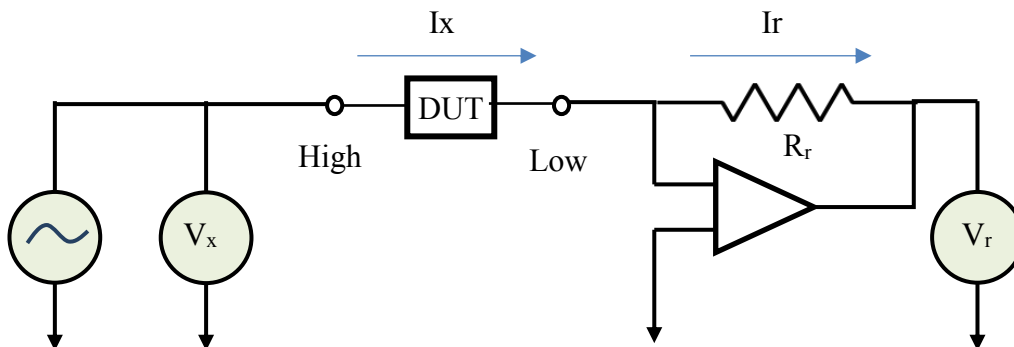


Figure 3.13. Circuit diagram of auto-balancing bridge impedance measurement method.

The LCR meter is controlled by using an automated program through computer. The screen shot of control software user interface which provides several options during the measurement is shown in Figure 3.14.

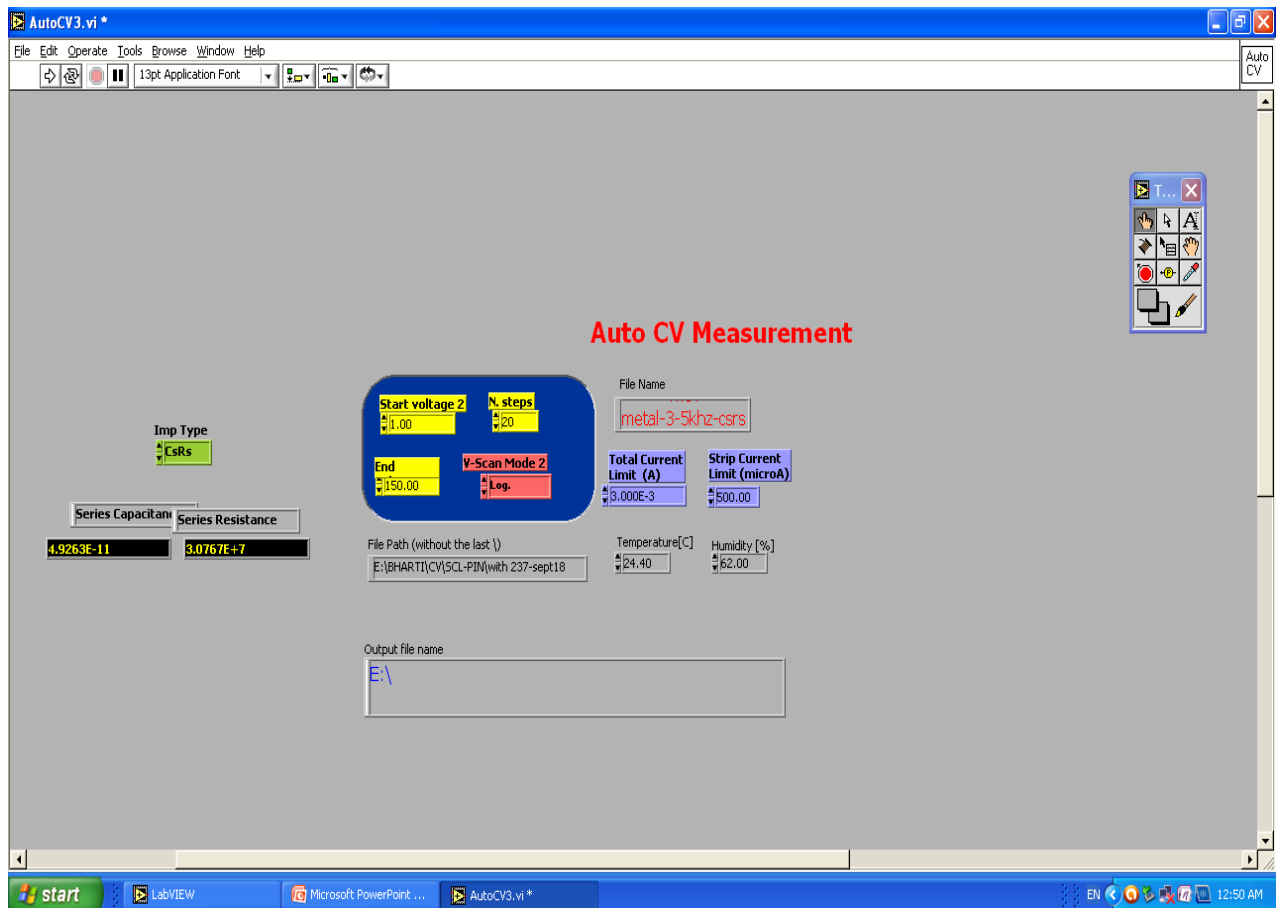


Figure 3.14 Screen shot of control software user interface.

3.5.2. Dynamic characterization of silicon detectors

Dynamic characterization of the silicon detectors is carried out to ensure the performance of the fabricated device as detector (i.e. capability of the device to detect the desired particles and to obtain the associated properties (e.g. energy, charge state, life time etc.) correctly. As a first step, the detector is always characterized using an alpha source which provides the energy calibration and an estimate of the energy resolution. In the present work, other characterization experiments with different incident beams (e.g. ${}^7\text{Li}$, ${}^{12}\text{C}$, fission fragments etc.) are performed to examine the detector response, as per the objectives for which the detector was designed.

3.5.2.1. Detector initial characterization with alpha source

Main objective of the pulse height spectroscopy (PHS) using alpha source is to test the performance of the detector. The schematic block diagram and the experimental setup for the pulse height spectroscopy using alpha source are shown in the Figure 3.15 and Figure 3.16, respectively.

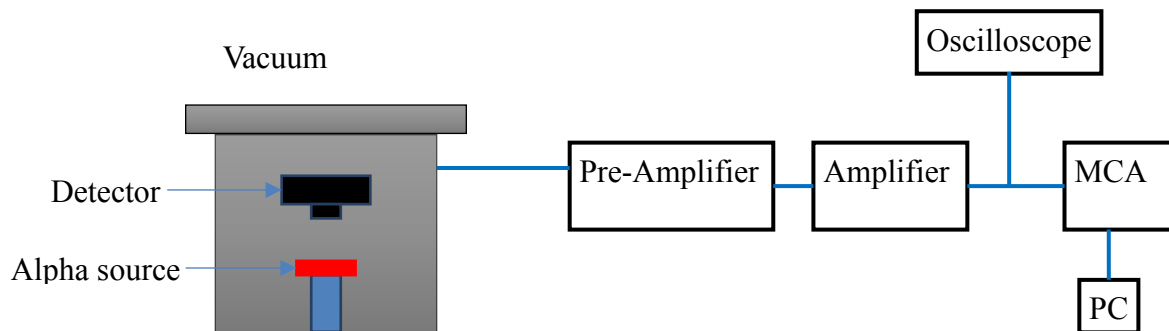


Figure 3.15. A simplified block diagram of the setup used for the dynamic characterization.

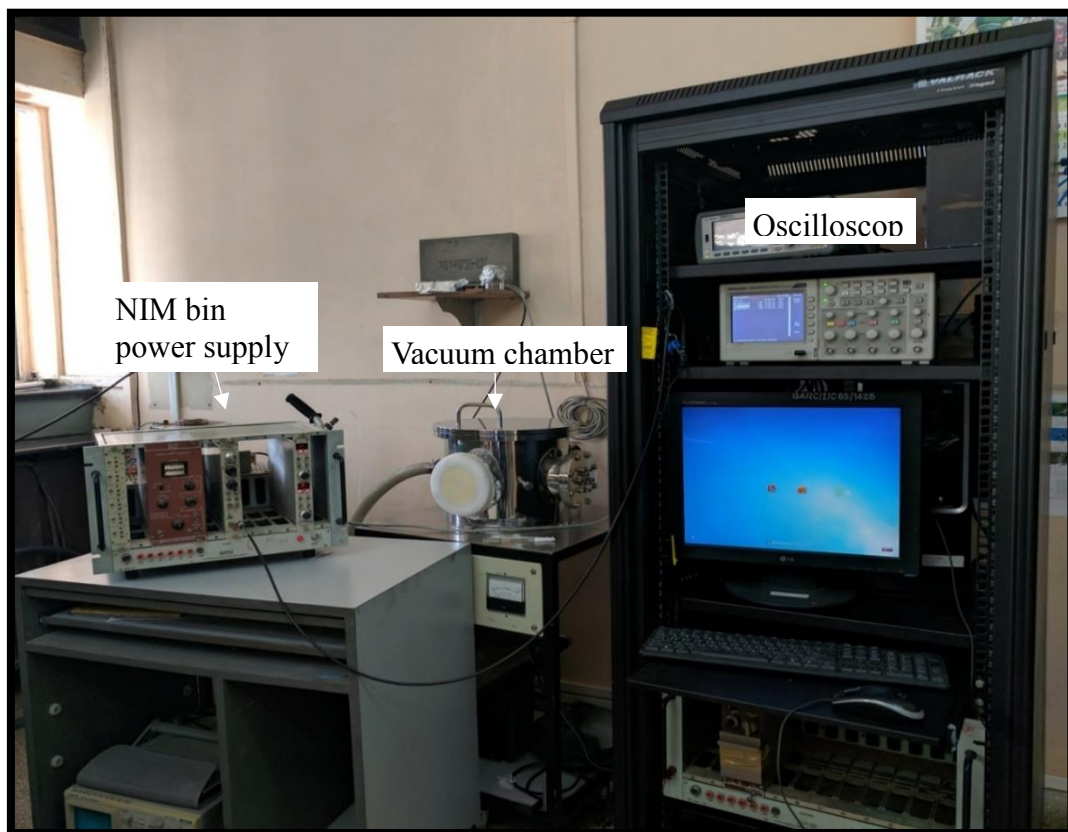


Figure 3.16. Experimental set up used for detector characterization with alpha source.

The measurement of detector with the α -particles is done inside a vacuum chamber with pressure 10^{-2} mbar (as shown in the Figure 3.15) to provide a smooth path to the charge particle for interaction with detector without losing its energy due to collision with the particles of the medium. When α -particle passes through the detector medium it creates electron-hole pairs. These charge carriers collected using applied electric field generate electrical signal. Usually this electrical signal is weak, so it is fed into the charge sensitive pre-amplifier to amplify and to convert the signal in to proportional voltage pulse. To reduce the capacitive noise and distortion in detectors signal, preamplifier should be connected as close to the detector as possible. To further amplify the signal, it is fed onto the amplifier. The output of amplifier is visualized on an oscilloscope. The amplified signal is also fed into the multichannel analyzer (MCA) which gives the pulse height histogram for the α -particles with the help of computer.

The response of a typical PIN detector for α -particles is shown in the Figure 3.17. The PHS shows three peaks corresponding to the α -particles of three different energies at 5.396 MeV, 5.456 MeV and 5.499 MeV. Energy resolution of the detector calculated from the PHS is approximately 30 keV at 5.499 MeV.

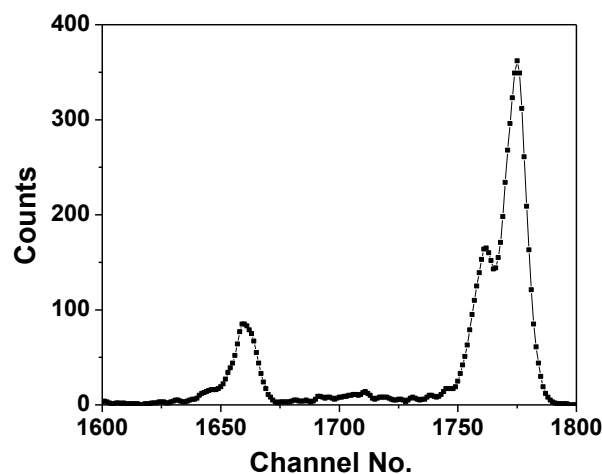


Figure 3.17. Pulse height spectra of α -particles by a silicon detector.

3.5.2.2. In beam characterization

In beam characterization finally proves the detector performance in actual experiments. In the present thesis, in beam experiments are performed at following facilities which provide different charged particles.

a. *Folded Tandem Ion Accelerator (FOTIA) in BARC*

Folded Tandem Ion Accelerator (FOTIA) is a facility which produces low energy as well as high energy ion beams up to $A=40$ and energy up to 66 MeV (Figure 3.18)[81]. The accelerator consists of several components including a high voltage column section, two accelerating tubes, 20° -electrostatic deflector, three dipole magnets, a foil/gas stripper, several electrostatic and magnetic focusing and steering components, precision double slits,

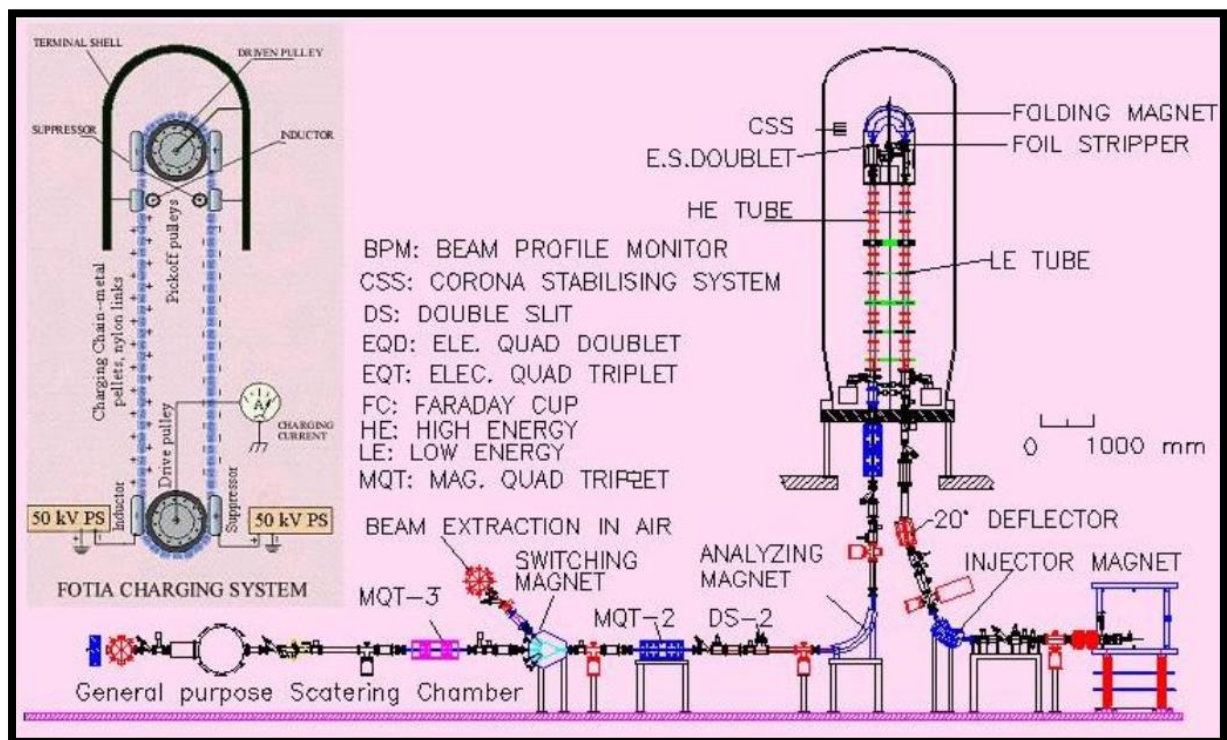


Figure 3.18 6 MV folded tandem ion accelerator facility at BARC [82], [83].

monitoring and control devices, SF₆ gas handling system etc. In FOTTA, a beam of negative ions is pre-accelerated up to 150 keV and is injected into the low energy accelerating tube through a combination of a 70° -magnet ($ME/q^2=12$, $R=40$ cm) and a 20° -electrostatic deflector. These negative ions strike to a stripper and the electrons of these accelerated negative ions get stripped off and positive ions with desired charge state thus produced are selected with a 180°-magnet ($ME/q^2=10$, $R=30.5$ cm). The beam is finally bent into the high energy accelerating tube. The beams in the high energy tubes are focused using magnetic quadrupole triplet and finally analyzed by a 90°-magnet ($ME/q^2=50$, $R=75$ cm) and are transported to the experimental set up through various beam handling components.

b. LOHENGRIN fission fragment separator, at Institut Laue Langevin (ILL)

LOHENGRIN at Institut Laue Langevin (ILL), Grenoble, France is a high-resolution recoil mass spectrometer (Figure 3.19, Figure 3.20) which is popularly used to study the characteristics (the mass, kinetic energy and charge distribution) of the alluring isotopes originated during the fission process [84], [85]. The instrument also facilitates the detection of γ -rays, conversion electrons, β -rays and delayed neutrons, and coincidences between these particles.

In this facility, the fission products are generated by placing a fissile isotope target, in an environment of thermal neutrons (flux 5.3×10^{14} n cm⁻² s⁻¹) near the core of the reactor. The isotopes thus produced are selected by a combination of electric and magnetic fields aligned perpendicular to each other and thus having focusing in the plane of deflection (Figure 3.20). The combination of these two fields enables the separation of the different ions (even though their velocity may be similar) according to their mass/charge (A/q) state, each following a characteristic parabolic path at the exit slit of the spectrometer.

The appropriate choice of the filed parameters, the particles of desired A/q value can be deflected in to an exit slit of about 72 cm, as the energy dispersion in the direction along each parabola appears in about 7.2 cm for about 1% energy difference while the mass dispersion extends in about 3.24 cm, perpendicular to parabola, for 1% difference in mass. To account the distribution width (14 MeV) of fission products, approximately 100 cm stretch of the parabola is illuminated by one type of the mass at the exit slit. Overall, mass resolving powers

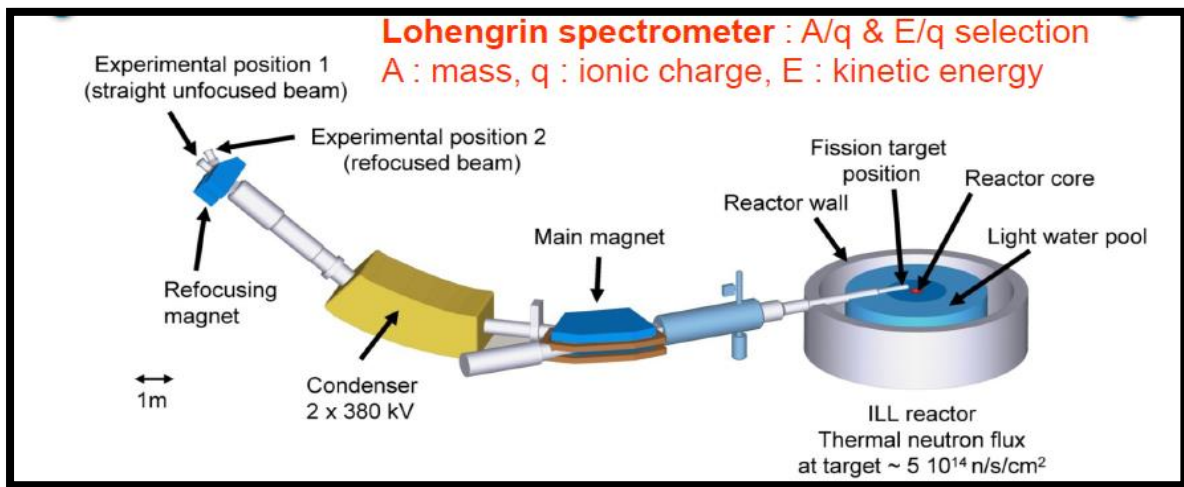


Figure 3.19. Three dimensional schematic view of LOHENGRIN fission fragment separator, at Institut Laue Langevin [85], [86].

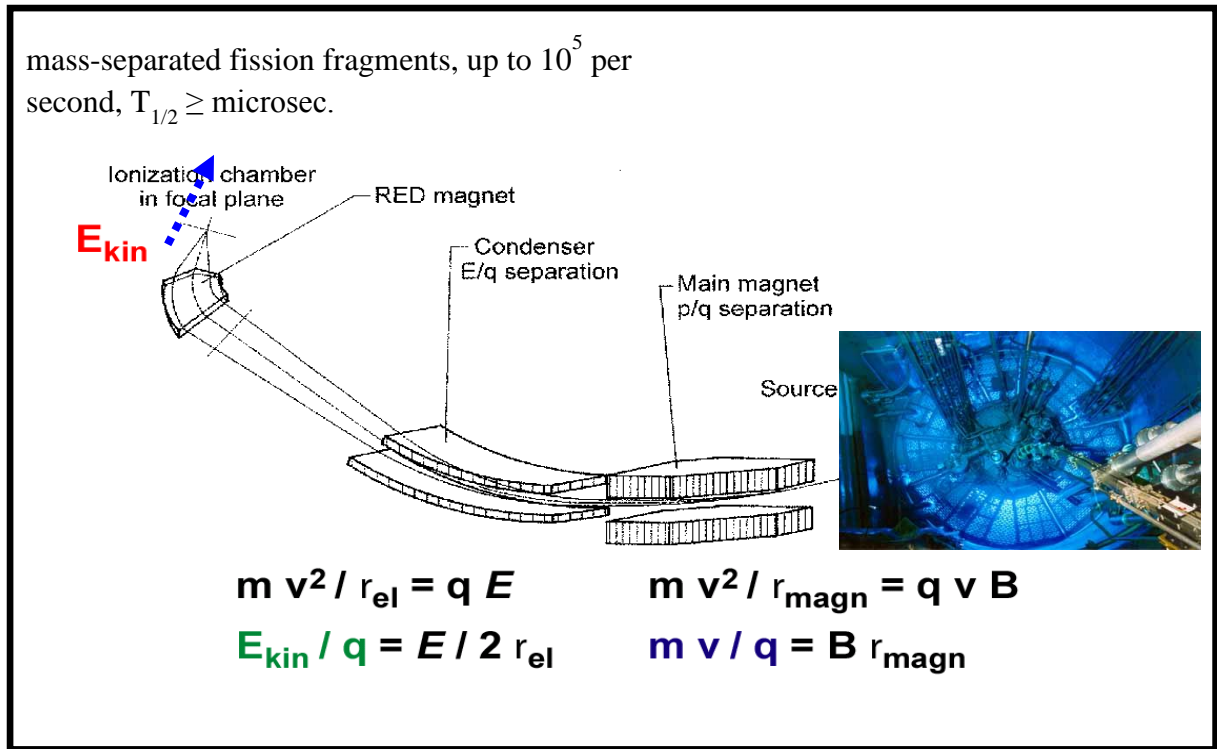


Figure 3.20. Schematic diagram showing working principle of LOHENGRIN fission fragment separator, at Institut Laue Langevin [84].

up to $A/\Delta A = 1500$ while energy resolution values $E/\Delta E$ between 100 to 1000, can be achieved by suitable settings of target size and collimator settings. The spectrometer facilitates installation of different required instruments/detectors (e.g. ionization chambers, surface barrier detectors, Si and Ge detectors, plastic scintillators and long counters for delayed neutrons) for various object-oriented investigations. Majorly, studies examine the spectroscopic properties (spins, parities, magnetic moments, life time, etc.) of exotic neutron-rich nuclei and fission processes (mass, kinetic energy and nuclear charge distributions of products, kinematics of delayed neutrons etc.) are primarily of interest using this spectrometer. In the present thesis, we have utilized the fission fragments produced at this facility to characterize the capabilities of our ΔE -E detector. During the experiments a custom

made vacuum compatible detector holder with goniometer arrangement was used to mount the detector as shown in Figure 3.21.



Figure 3.21. Detector mounting jig with goniometer.

c. Pelletron Accelerator at Tata Institute of Fundamental research (TIFR)

Pelletron at Tata Institute of Fundamental research (TIFR), Mumbai is also a tandem accelerator facility which is capable of reaching 14 MV on the terminal [87]. The accelerator (Figure 3.22) consists of a cesium sputter ion source producing negative ions, which are initially accelerated to low energies (150-250 keV) in a short horizontal section. These ions are bent through 90° into the vertical accelerating column using an injector magnet for further enhancing its energy. The ions are accelerated by electrostatic attraction produced by a high voltage positively terminal placed at the center of the column. The high electric potential at the terminal is obtained by continuously transferring charge to the terminal using chain of

steel pellets, giving name Pelletron. The negative ions are converted in heavy positive ions by passing them through a carbon foil or a small gas volume. The terminal voltage and the type of ion decides the average charge on the ions. The resulting positive ions then enter in second stage of the acceleration where the positive voltage of the terminal repel these ions. As a result, the energy acquired by a positive ion having charge (n) electronic units will be (n+1) times of terminal voltage. The accelerated beams from proton to uranium ions with varying charges can be produced, not only continuous, but also with the pulsed beams of duration 1 ns having separation widths ranging between 100 ns to 1.6 ms. The experiments to test double sided silicon strip detectors are performed in the scattering chamber (Figure 3.23) at 150° beam line of Pelletron facility.

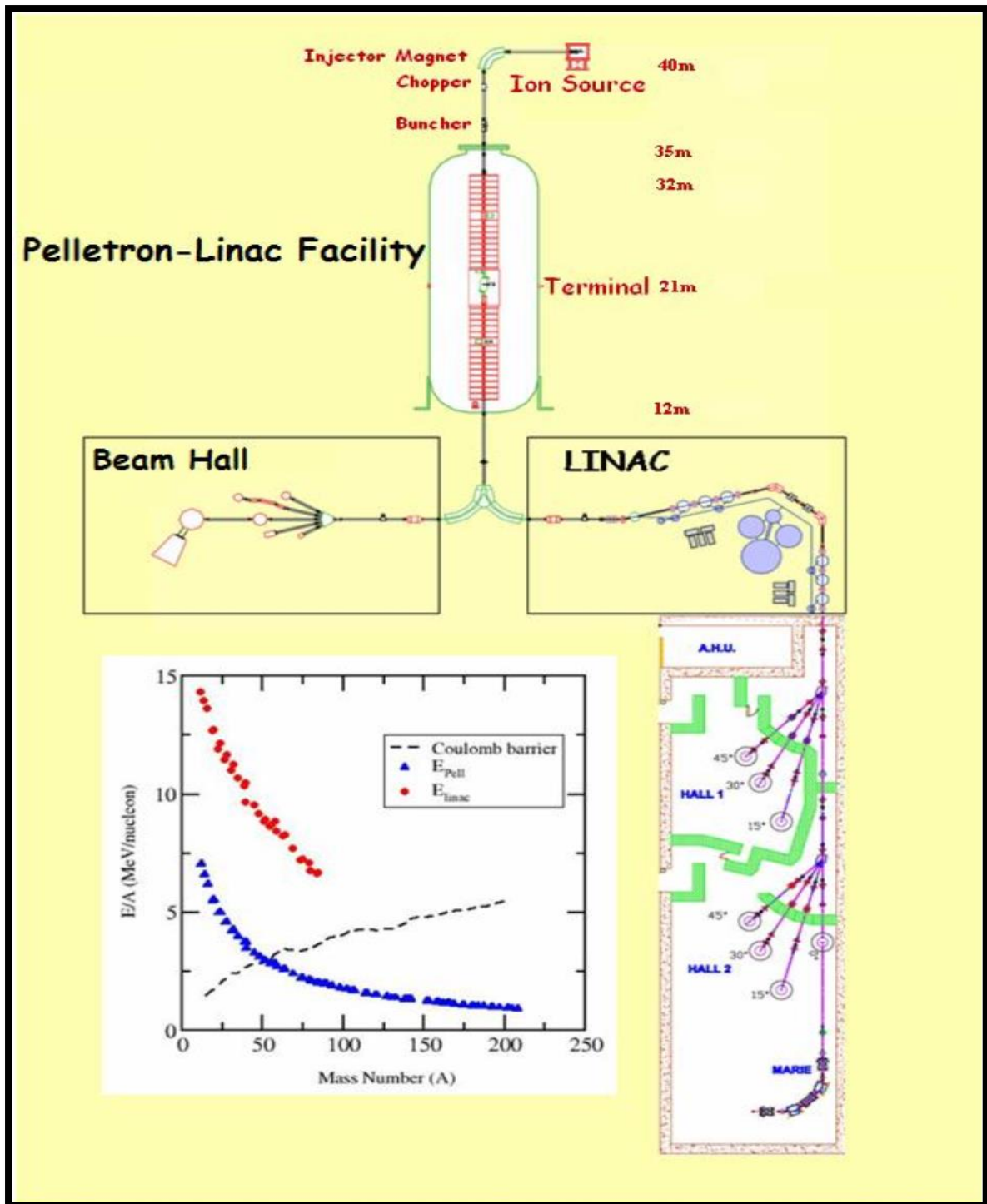


Figure 3.22. BARC-TIFR Pelletron-LINAC Facility [87].



Figure 3.23. Scattering chamber at BARC-TIFR Pelletron-LINAC Facility [88].

d. Test Facility for Neutron Detectors at Dhruva, Reactor, BARC

The experiments for the neutron detection using thin silicon detectors developed in the present work were performed at Multi-purpose facility available at the Guide Tube Laboratory (G2), Dhruva Reactor, BARC [89]. Dhruva is a research reactor at BARC producing about 1.4×10^{14} n / cm² -s at the core. These neutrons are brought to the guide tube hall using total external reflection inside the Ni coated guides and the flux at the sample position (detector in this case) is about 10^6 n / cm² -s. The facility comprises a BeO filter which provides all the neutrons having wave length more than 4.2 Å corresponding to the energies about 5.1 meV (a wide range of the energy spectrum). Since neutrons do not interact directly with silicon, therefore, a suitable converter layer (¹⁰B in this case) is placed before the detector. In some of our earlier experiments, the detectors were coated with a thin layer of the boron carbide using hot wire vapor deposition [65-67]. A neutron beam of diameter 30 mm is incident on the detectors.

The gamma background is about 1 R/h at 90 MW thermal power of Dhruva reactor. The subsequent electronics to collect the spectra is similar to that discussed in Section 3.5.2.1.

In the following Chapters (4-6) of this thesis, the development of the three different silicon based detectors, (i) integrated ΔE -E detector, (ii) double sided strip detector and (iii) thin PIN detectors, their fabrication and successful characterization are presented.

Chapter 4

DEVELOPMENT AND CHARACTERIZATION OF INTEGRATED ΔE -E DETECTOR TELESCOPE

4.1. Introduction

Identification of the unknown sub-atomic particles originated as out product of any nuclear reaction is essential in addition to their energy measurements in several experiments. As discussed in Chapter 3, detector telescopes comprising two detectors (ΔE and E detectors) are being utilized since many years. The conventional ΔE detectors in the desired thickness range (10–25 μm) are usually fabricated by mechanical polishing and chemical etching of silicon wafers. These detectors suffer several limitations such as fragile nature, non-uniformity in thickness, difficulty in handling and high costs due to production methods of silicon etching [43]. Moreover, it is very difficult to arrange these detectors in a multi detector array system of compact geometry [44]. All these issues can be overcome by physically integrating ΔE and E detectors by fabricating both the detectors on the same wafer.

Different techniques have been employed to obtain integrated ΔE -E detectors. The E and ΔE detectors have been integrated by using wafer bonding technology with cobalt silicide as an intermediate metallic layer between the two detectors [90]. The implantation of the boron ions of high energy (~ 1 MeV) has been utilized to create a very thin ΔE detector (1 μm). Such implantation creates a buried P^+ region which thereby giving rise to an integrated $\text{N}^+ - \text{N}^- - \text{P}^+ - \text{N}^- - \text{N}^+$ detector [91]. Method of quasi-selective epitaxial growth has been utilized by A. J. Kordyasz, et al., to create a detector with the Schottky configuration with buried P^+ region between the two integrated ΔE and E detectors [92]. It may be pointed out here that the wafer bonding and high energy boron implantation are not the standard processes usually utilized in

integrated circuit (IC) technology. Moreover, the implantation technique can only be used for a limited thickness of the ΔE detector, because of the constraints on the available energies for the ion implanters. In the present thesis, an integrated silicon detector telescope having both ΔE and E detectors integrated on the same wafer has been developed.

This integrated detector was realized by fabricating an epitaxial silicon layer for a thin ΔE detector on the top of the E detector in a PIN configuration with a common buried N^+ layer. The technology developed is more in line with standard silicon integrated circuit technology and is suitable for fabrication of large area ΔE detectors with thickness in the range of a few micrometers (μm) to a few tens of micrometers (μm). The total detector thickness being more than $300 \mu m$, the detector is rugged to handle as well as suitable for using in a multi-detector system consisting of an array of detectors. The performance of the integrated ΔE -E detector was examined for light charged particles as well as for heavy fission fragments. The prominently seen pulse height defect in semiconductor detectors (unlike gas detectors) was studied. The design, fabrication and characterization of this detector are presented in this Chapter [39], [40].

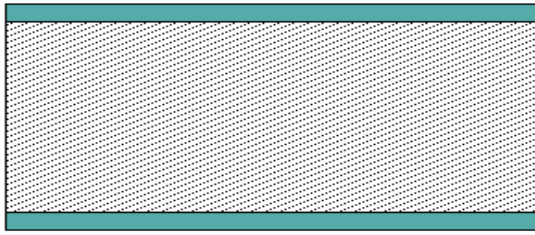
4.2. Detector design and fabrication process

The schematic cross section of ΔE -E detector is shown in Figure 4.1. The integrated ΔE -E detector comprises two PIN detectors, a thin ΔE detector on the front side of the wafer and an E detector on the backside of the wafer. A common N^+ layer was created as a buried layer between the two detectors and the contact to buried layer was brought to the front side using a heavily doped N^+ ring. The breakdown voltage of the PIN detectors was improved by incorporating two guard rings and metal overhang over the active P^+ implanted regions.

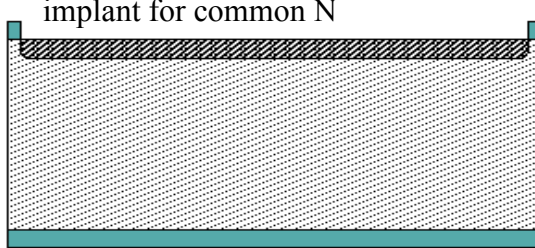
the front and backside of the wafer at 70 keV energy to obtain P⁺ doped active regions with a junction depth was about 0.4 μm. The contacts were opened to the active P⁺ regions on both sides of the wafer and to the common N⁺ ring contact on the front side of the wafer. Aluminium contact electrodes of 0.3 μm thickness were provided outside the active area to prevent additional dead layer to the detector. The post metallization anneal was performed at 450° C, for 30 min in nitrogen environment. Phosphosilicate glass (PSG) was used as a passivation material to protect the chip from ambient. The PSG layer was removed in the pad region for carrying out wire bonding using aluminum wires. Since the fabrication technology involved double-sided wafer processing, a double-sided aligner was used for alignment and patterning of various layers. The P⁺ implanted layer and the buried N⁺ contact layer are the dominant dead layers. Hence, the process parameters were optimized to minimize the thickness of these dead layers. The simplified process sequence used for the fabrication of integrated detector is schematically shown in Figure 4.2 (a) to (h).

The detector chips were mounted in specially designed PCB packages in transmission mount and the wire bonding of the front side ΔE and backside E detectors was performed. The front and back side of the final packaged detector is as shown in Figure 4.3.

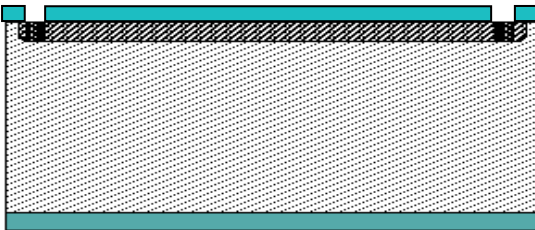
a. Initial oxidation



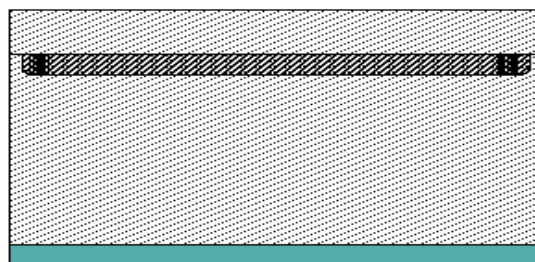
b. Buried layer Lithography and Sb ion implant for common N⁺



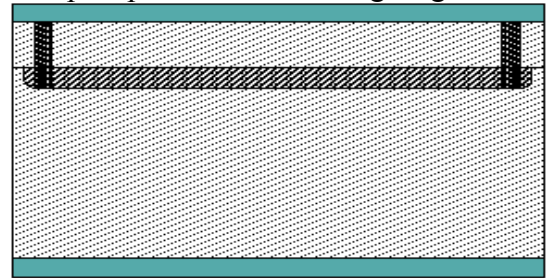
c. Phosphorous implantation for N⁺ contact ring



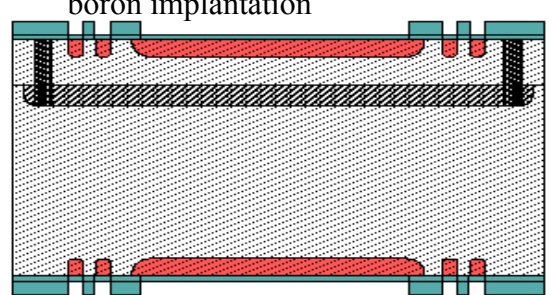
d. Epitaxial silicon layer deposition (10-25μm)



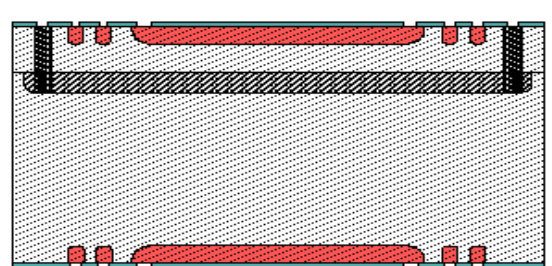
e. Lithography and then diffusion of phosphorous for N⁺ Plug/ring



f. Lithography and then front and back boron implantation



g. Lithography for contact opening



h. Al metallization, deposition of BPSG and contact pad opening

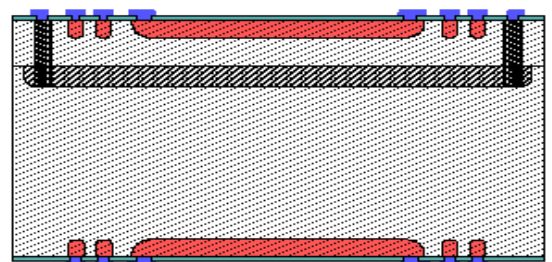


Figure 4.2. Schematic representation of fabrication steps used for integrated telescope.

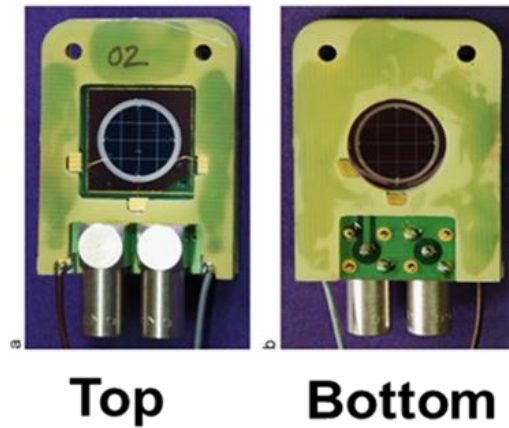


Figure 4.3. Top (ΔE detector) and bottom (E detector) side of packaged detector.

4.3. Detector characterization

The fabricated detectors were evaluated by static and dynamic characterizations. The static characterization was carried out as described in Chapter 3 and the corresponding parameters (leakage current and capacitance) were obtained at different reverse bias voltages. The energy resolution of the detectors was evaluated by studying the alpha response using a dual alpha ($^{238}\text{Pu} + ^{239}\text{Pu}$) source of activity about 4300 Bq. A test setup as detailed in Chapter 3 comprising charge sensitive amplifier, high voltage power supply and a MCA were used for the measurements. The detectors were placed in a vacuum chamber and then sample to detector distance was adjusted to collect the maximum count rate without making compromise with the energy resolution. The source was first placed in front of the P^+ side of the E detector to record its alpha spectrum and to obtain the energy resolution. Same procedure has been repeated for ΔE detector.

The performance of the detectors as particle telescope has been tested at FOTIA (Folded Tandem Ion Accelerator) facility, BARC which is described in Chapter 3. For this purpose, a 12 MeV $^7\text{Li}^+$ beam was made incident on carbon (^{12}C) target. A self-supporting ^{12}C carbon target of thickness about $50 \mu\text{g}/\text{cm}^2$, prepared by vacuum evaporation was used for this purpose. The reaction products were detected by ΔE -E detector, placed at a forward angle ($\theta_{\text{Lab}} = 20^\circ$,

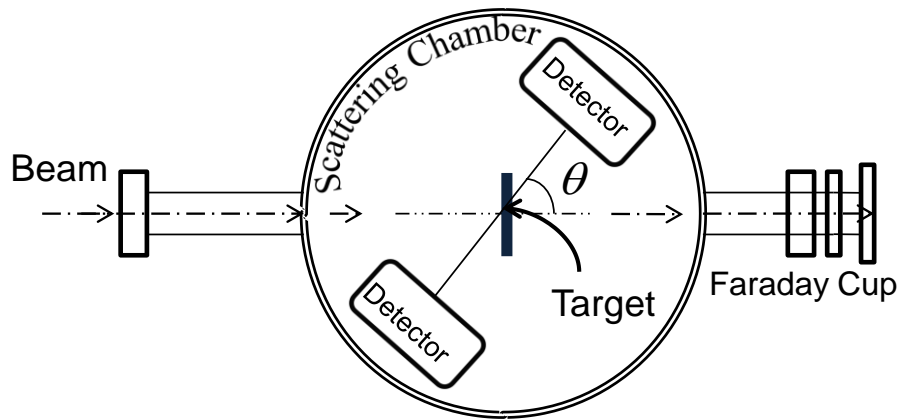
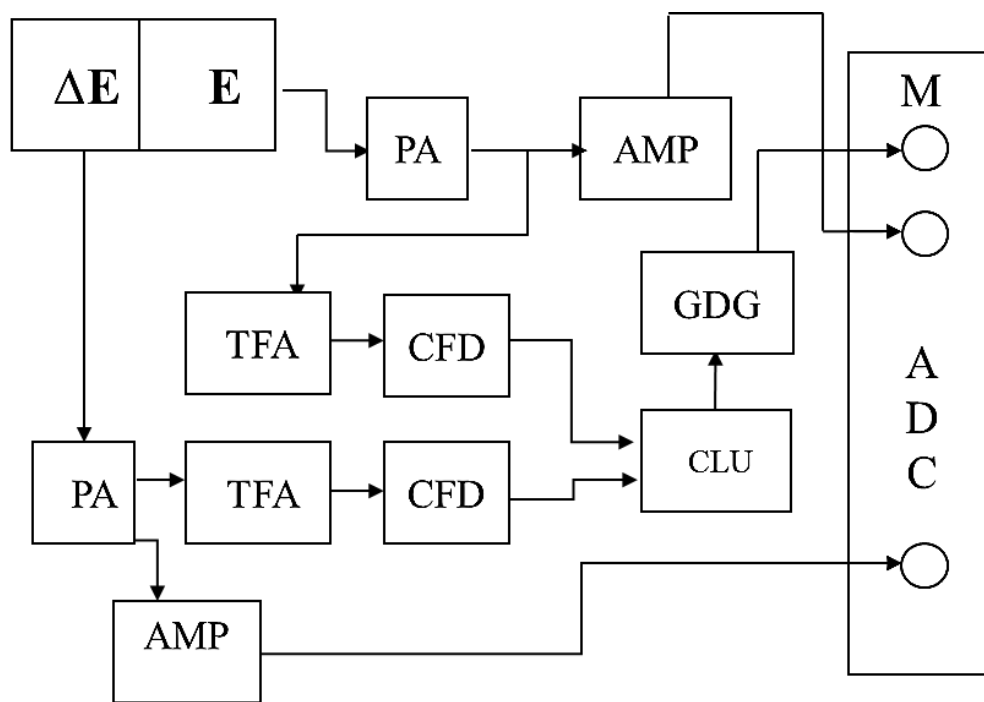


Figure 4.4. Schematic of experimental setup used to evaluate the detector performance as particle telescope at FOTIA.



PA- Pre-amplifier **CLU** - Coincidence logic unit
TFA- Timing filter amplifier **GDG** - Gate and delay generator
M - Master gate **ADC** - A to D convertor
AMP – Amplifier **CFD** - Constant fraction Discriminator

Figure 4.5. The electronic setup used for processing of signals from ΔE and E detectors.

for high count rates and higher energies of the projectile like particles) on a movable arm inside a standard 80 cm diameter general purpose scattering chamber. The telescope with a 5 mm diameter collimator resulted in an angular spread of $\pm 1.5^\circ$ and consequently kinematic broadening of the elastic peak up to 120 keV. The resulting detector pulses were processed by standard electronic protocol. The schematic of the experimental setup and electronics used is shown in Figure 4.4.

The experiments have also been performed to check the capability of the ΔE -E detectors to separate the charged particles and fission fragments. The ΔE -E detector with ΔE thickness of 10 μm has been used in typical charged particle measurement setup using ^{19}F beam from BARC-TIFR Pelletron accelerator facility. In these experiments, a self-supporting Bi target of 800 $\mu\text{g}/\text{cm}^2$ thickness was used. The events occurred in the $^{19}\text{F} + ^{209}\text{Bi}$ reaction at a bombarding energy of 44.8 MeV were recorded by the detector kept at 151° and 131° respectively.

The performance evaluation and energy calibration of the detectors for heavy fission fragments with higher Z of varying energies were carried out at the Lohengrin fission fragment separator, Institut Laue Langevin, Grenoble, France. The Lohengrin facility separates the fission fragments produced in thermal neutron-induced ^{235}U fission according to their mass A and kinetic energy E over ionic charge q. A combination of a magnetic sector field and a cylinder condenser acting as electrostatic deflector is used for this purpose. The ion beam arrives in the focal plane quasi-parallel ($< 2^\circ$ angular divergence) dispersed according to kinetic energy along the focal line (A/q-line) while the A/q-dispersion is perpendicular to it.

A target of enriched $^{235}\text{UO}_2$ was placed near the core of reactor interacts with the out-coming neutrons from the reactor to produce the fission fragments. For an integer value of A/q, a beam with several mass numbers A, each with a kinetic energy E (proportional to A) was incident on the detector surface. In addition to these heavy fission fragments, light charged particles/ions

are also produced from the ternary fission and, protons and alphas from (n, p) and (n, α) reactions.

Two detectors of active area 100 and 50 mm² with ΔE thickness of 10 μm were tested for fission fragment identification. During the experiments, the detectors were mounted using a custom-made arrangement in the vacuum chamber of the fission fragment separator (Figure 3.21). The electronic setup for the detector and the data acquisition system, comprised of charge sensitive preamplifiers (Ortec 142A), spectroscopy amplifiers (Ortec572, shaping time 2 s), ADCs (FAST 8072T), and a FAST MPA-3 multiparameter multichannel analyzer system. The signals were recorded in coincident manner in the ΔE and E detectors. The gains of spectroscopy amplifiers in the ΔE and E channels were 50 and 500 for fission fragments and for alphas, respectively.

All measurements were performed at room temperature. It may be added here that the dead time was not an issue as the count rates were less than 100 cps, and the shaping time was 2 μs . The fission fragments of mass numbers from 80 to 136 with kinetic energies from 35 to 110 MeV were tested with the detectors in various scans. Each scan comprised several runs with varying energy in steps of 5 MeV while keeping mass number and charge state constant, ensuring the availability of various fission fragments with varying energy for complete characterization of the detector. Every mass separated by Lohengrin contains several isobars that are produced with different fission yields. For the following analysis, the average nuclear charge as given by the JEFF3.1 fission yield database [11] has been used for each mass as tabulated in Table 4.1.

Thermal-neutron-induced fission shows a quite narrow isobaric yield distribution: $-\sigma_z \cong 0.53$ when the relative isobaric fission yields are described by a Gaussian distribution [12]. Therefore, the fission yield of all masses in this study is dominated by a single isobar that

represents 48% to 88% of the respective mass yield. Thus, the nuclear charge dispersion of the calibration masses can be neglected to first-order, and the mean Z can be used. The detector was further characterized by the measurement of the energy resolution of ΔE and E detectors. For energy resolution measurements of the E detector, the telescope was placed from the back side so that the incident beam is faced by the E detector. For the energy resolution measurements of the ΔE detector, the telescope was placed such that the beam was incident from the front side. The ΔE detector angle was optimized so that incident particles lose their entire energy in the ΔE detector. For the E detector, the incident beams used were alpha particles of two energies 4.7 MeV and 11 MeV and $A=90$ at 90 MeV, respectively. Since 4.7 MeV and 11 MeV alpha particles do not deposit their full energy in the ΔE detector, the energy resolution was experimentally measured only for $A=90$ fragments at 90 MeV. For full energy deposition, the ΔE detector was placed at an angle of 450 with an incident beam of $A=90$.

Table 4.1. Nuclear charge for corresponding mass numbers.

Mass Number (A)	Nuclear charge (Z)	Mass Number (A)	Nuclear charge (Z)
80	32	105	42
85	34.1	110	43.3
90	35.9	130	50.2
95	38.1	132	51.3
100	39.9	136	52.8

4.4. Results and discussion

4.4.1. Static characterization

The typical reverse I-V characteristics as obtained by measuring the current for the applied voltage varying from 0 to 80 V for E-detector and 0 to 10 V for ΔE detector respectively, are shown in the Figure 4.6 and Figure 4.7. As can be seen, the detectors show very low leakage currents in the range of a few nA.

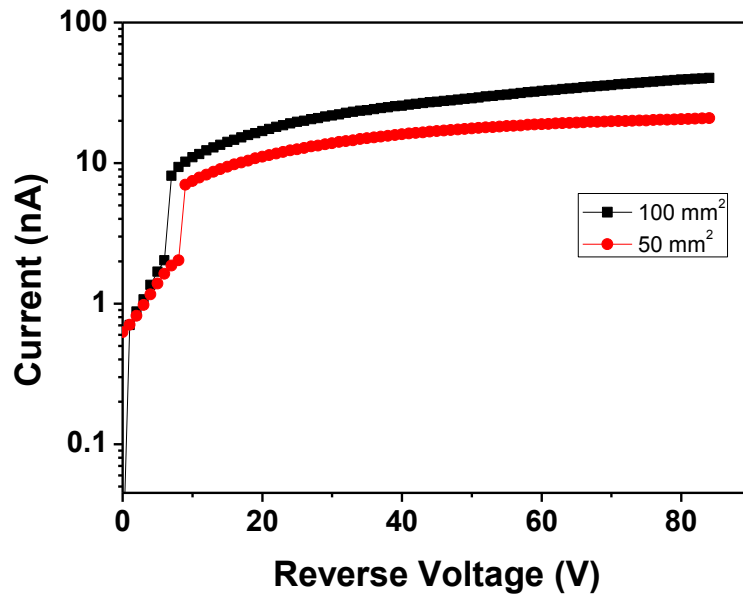


Figure 4.6. Typical reverse I-V characteristics E detectors of area 100 mm² and 50 mm².

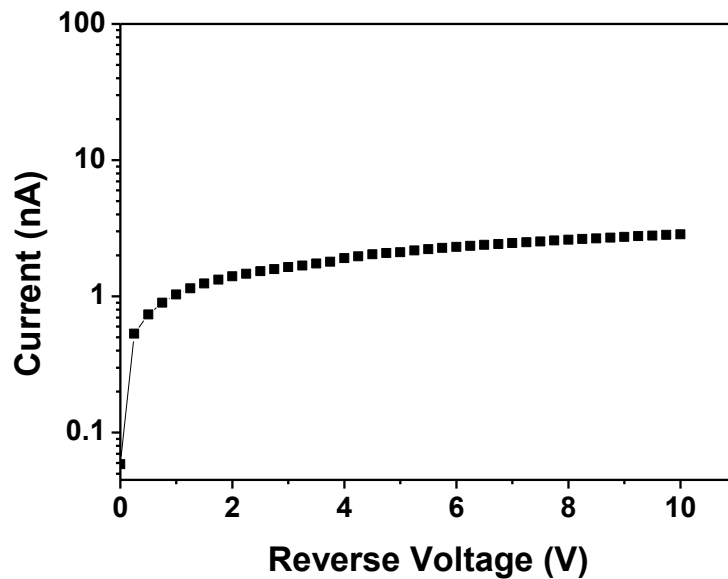


Figure 4.7. Typical reverse I-V characteristics of ΔE detector of area 100 mm².

The typical capacitance-voltage (C-V) characteristics of E and ΔE detectors are presented in Figure 4.8 and Figure 4.9 respectively. The ΔE and E detectors show expected capacitance behaviour where the capacitance of the PIN detector decreases with reverse bias voltage as the depletion region width increases and reaches a saturation (full depletion). The full depletion voltage is estimated from $1/C^2$ versus V plots and is found to be about 60 V for the E detector. The ΔE detector is fabricated in an epitaxial layer, deposited without doping and therefore epitaxial layer is expected to have high resistivity. At no bias condition, the depletion region of an N type substrate (resistivity about 3 k Ω -cm) is about 20 μm . Therefore, the detector is anticipated to be fully depleted even at zero bias. However, there is out diffusion of antimony from the buried N⁺ layer during the process of epitaxial deposition causing some changes in the doping. The experimental value of the full depletion voltage of ΔE detector obtained from C-V data is about 6 V. The C-V characteristics of ΔE detectors with different thicknesses are shown in Figure 4.9. The capacitances of the ΔE detectors of thicknesses 10-25 μm are much higher than the capacitance of E detector which is as expected due to the smaller depletion widths of the ΔE detectors (Section 3.2.4).

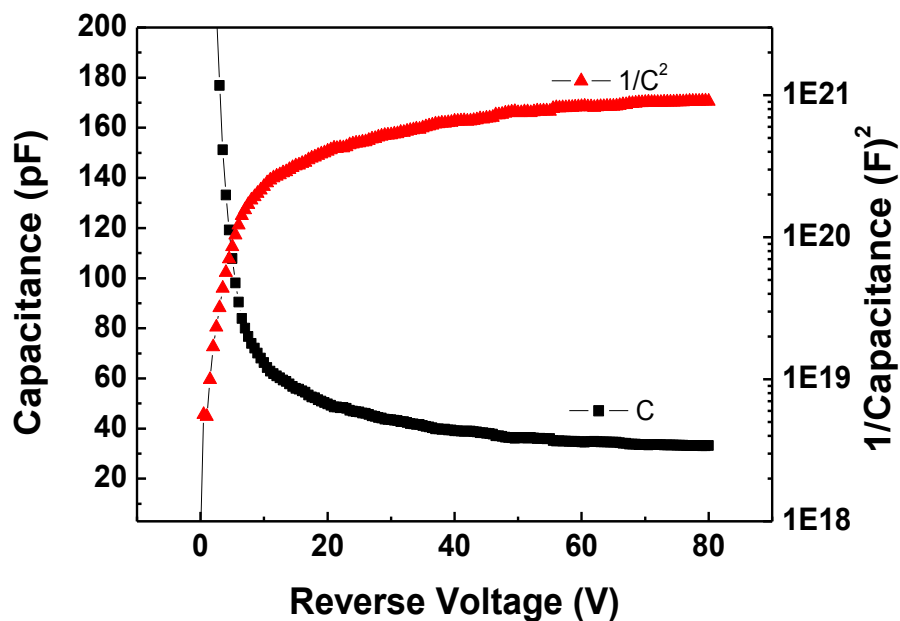


Figure 4.8. C-V characteristics and $1/C^2$ -V plot of the E detector of area 100 mm².

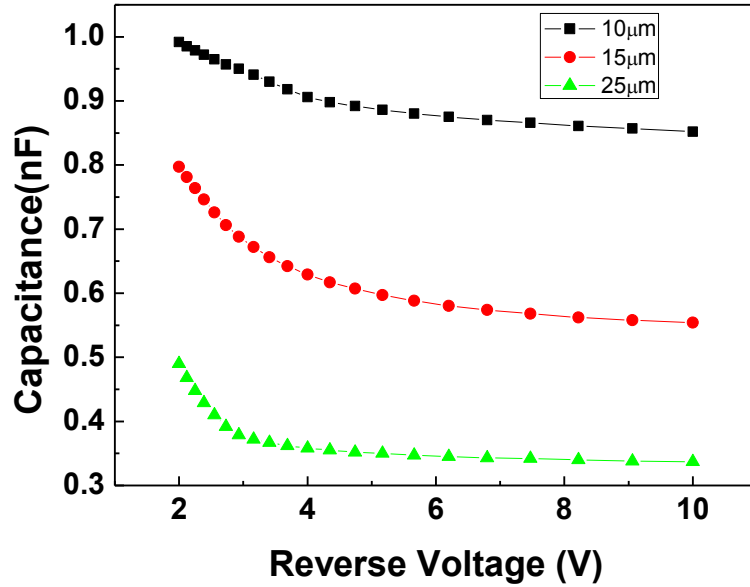


Figure 4.9. C-V characteristic of ΔE detectors of different thicknesses.

4.4.2. Alpha response of the detectors

The histograms of E and ΔE detectors are obtained using a dual energy alpha source are depicted in Figure 4.10-4.12. The detector area is 100 mm^2 and thicknesses of ΔE detectors are $10 \text{ }\mu\text{m}$ and $25 \text{ }\mu\text{m}$.

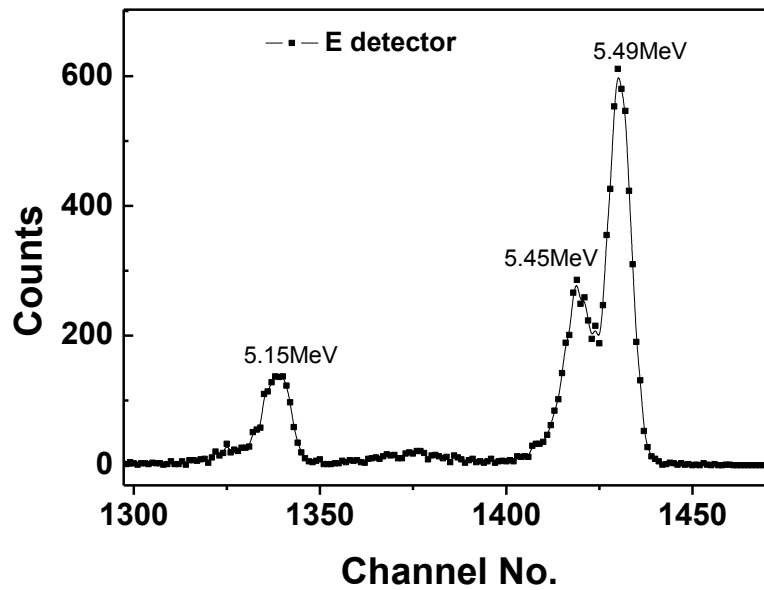


Figure 4.10. Alpha ($^{238}\text{Pu} + ^{239}\text{Pu}$) response of E detector of area 100 mm^2 at a bias voltage of 60 V.

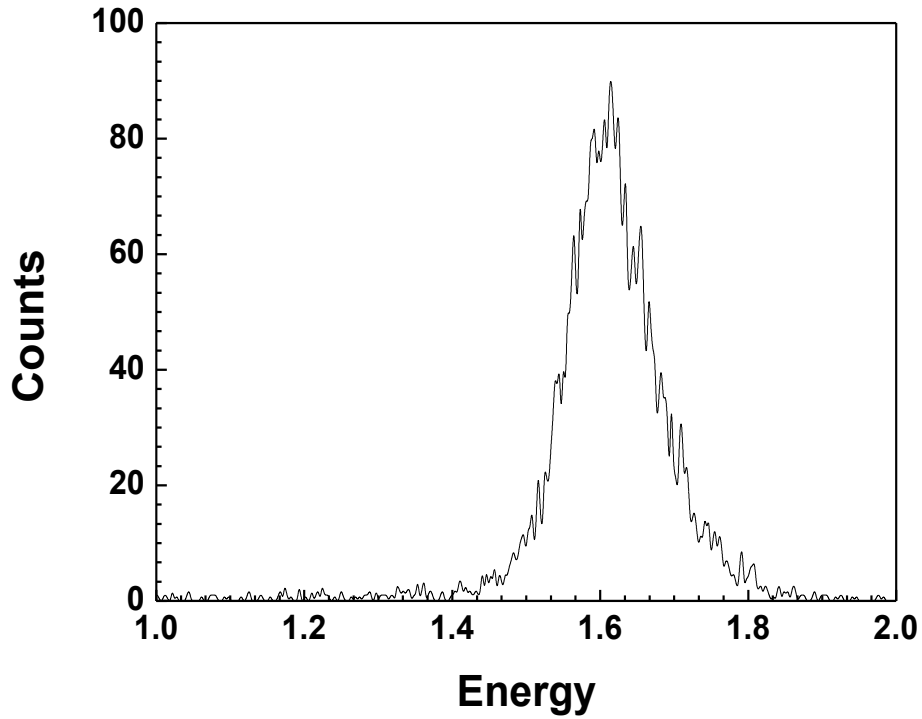


Figure 4.11. Alpha ($^{238}\text{Pu} + ^{239}\text{Pu}$) response of ΔE detector (area 100 mm^2) of thickness $10 \mu\text{m}$ at bias voltage of 6 V.

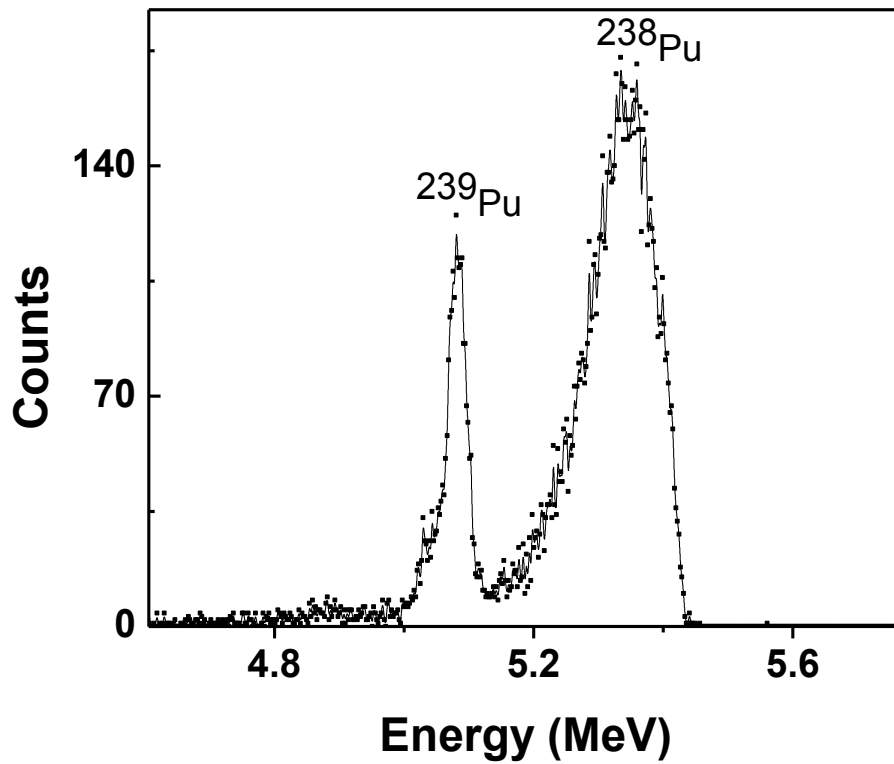


Figure 4.12. Alpha ($^{238}\text{Pu} + ^{239}\text{Pu}$) response of ΔE detector (area 100 mm^2) of thickness $25 \mu\text{m}$ at bias voltage of 6 V.

The E detector is found to have a very good energy resolution of 20 keV for alpha particles of 5.499 MeV (0.36%), while ΔE detector of thickness 10 μm gives a broad peak (Figure 4.11) and is not able to resolve the alphas of energy 5.15 and 5.499 MeV.

The estimated range of the 5.0 MeV alpha particles is about 22 μm as a result of which the alpha particles from the source could only deposit a part of their energies in 10 μm thick ΔE detector. The calculations carried out using SRIM software, show that the alpha particles having energies 5.1 and 5.499 MeV can deposit only 1.53 and 1.47 MeV energies, respectively in 10 μm thick detector. Since the estimated energy difference in the deposited energies is very low (~ 70 keV) to distinguish between the two alphas, a broad peak is experimentally observed (Fig. 4.12). Moreover, the resolution of the thin ΔE detector is expected to be inferior to that of the thick E detector because of the higher capacitance and energy straggling. If the thickness of the ΔE detector is increased up to 25 μm , the detector is found to be able to register at least two peaks as shown in Figure 4.12.

Since 5.15 MeV alphas are stopped in ΔE detector while 5.499 MeV are transmitted, it is not possible to determine the resolution for the ΔE detector accurately. Therefore, the energy resolution of ΔE detectors has been estimated by tilting the detector at an angle using a goniometer to provide larger path to charged particles for full energy deposition, as discussed later.

4.4.3. The performance of the ΔE -E detector as a particle telescope for different charged particles

The performance of the integrated ΔE -E detector for light charged particles as evaluated at FOTIA, BARC and Pelletron Accelerator, TIFR (Section 3.6.3) are discussed in this section.

Figure 4.13 shows the two-dimensional (2-D) spectrum obtained by plotting ΔE and E signals for 12 MeV ${}^7\text{Li}$ beam on ${}^{12}\text{C}$ target. It can be observed from this figure that the reaction products like ${}^7\text{Li}$, alpha and proton are detected as well as separated from each other.

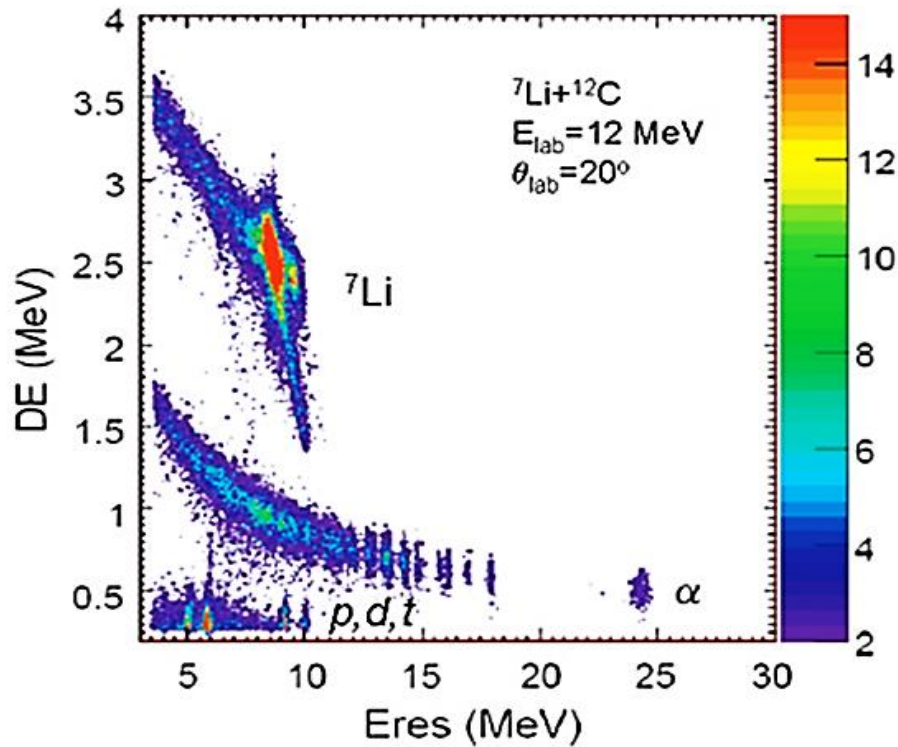


Figure 4.13. Two-dimensional (2-D) spectrum recorded by the integrated detector at FOTIA for the reaction of 12 MeV ${}^7\text{Li}$ beam on ${}^{12}\text{C}$ target.

Since the thickness of the ΔE detector was only 10 μm , particles with $Z=1$ have a small pulse height and are not clearly separated from the noise. The elastic scattering of ${}^7\text{Li}$ particles with the target results in the most intense groups present in the band of ${}^7\text{Li}$. Another ${}^7\text{Li}$ group adjacent to intense ${}^7\text{Li}$ group but at a higher E channel corresponds to the elastic scattering from a higher Z target impurity. The energy loss calculations along with the energy calibration using a standard alpha source are utilized for the identifications of different particles and their energies.

The one-dimensional (1-D) projection of alpha particles, as depicted in Figure 4.14 clearly shows the discrete alpha groups corresponding to well-known states of ${}^{15}\text{N}$. The levels

identified in ^{15}N originates due to triton transfer mechanism as well as from the decay of ^{19}F compound nucleus. These results are comparable to those observed by others using physically separated E and ΔE detectors as a telescope [93]. The rightmost peak in the alpha spectrum represents the alpha particles arising from the reaction $^1\text{H}(^7\text{Li},\alpha)\alpha$, where the hydrogen exists as impurity in the target. The resolutions of the ΔE and E detectors are compared in Figure 4.15 where the typical 1-D projection spectra corresponding to the elastic peak and one of the discrete alpha groups are plotted. From the 1-D histogram of elastically scattered ^7Li particles as detected by ΔE and E detectors (Figure 4.15 (a) and (b)), the energy resolution values (FWHM) are obtained to be 129 keV and 155 keV, respectively for the ΔE and E detectors. In addition to the intrinsic detector resolution, these values also include contributions from kinematic broadening due to large solid angle, energy straggling due to finite target thickness, noise due to electronics setup etc. The energy resolution obtained from the alpha peak, as

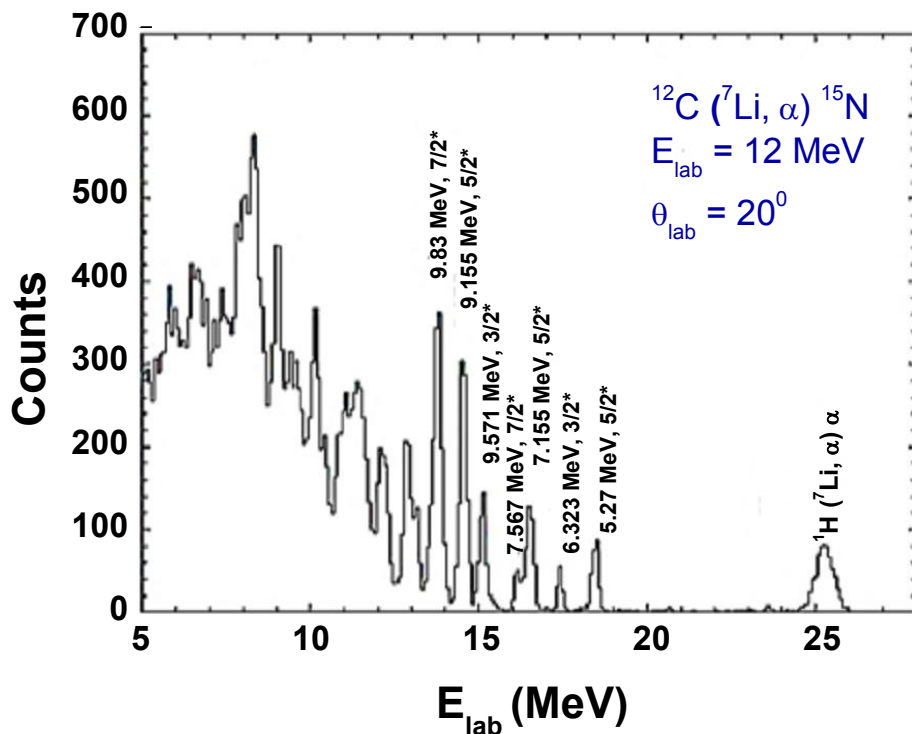


Figure 4.14. Projection of alpha bands containing discrete peaks of alpha particles corresponding to different excited states of $^{15}\text{N}^*$ which are identified and labeled.

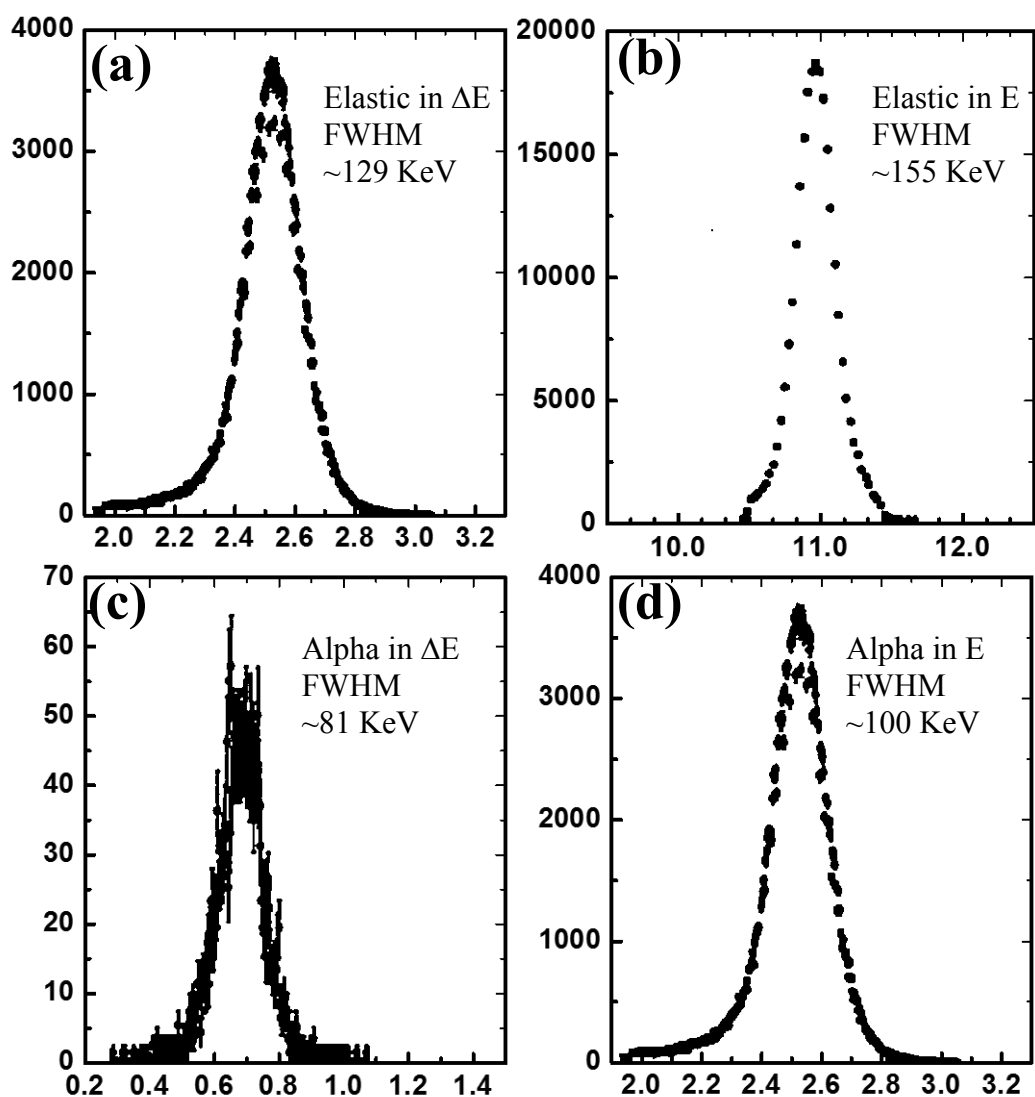


Figure 4.15. Typical one-dimensional (1-D) histograms of elastic and alpha particles detected by E and ΔE detectors comparing their energy resolutions, elastically scattered ${}^7\text{Li}$ particles as detected by; (a) ΔE and (b) E detectors and alpha particles as detected by (c) ΔE and (d) E detectors.

shown in Figure 4.15 (c) and (d), was found to be 81 and 100 keV. The results thus obtained suggest that the energy resolution for ΔE detector is not inferior to that of the E detector as far as the particle discrimination is concerned.

A typical 2-D (ΔE -E) spectrum for the reaction products of the reaction ${}^{19}\text{F}+{}^{209}\text{Bi}$ as measured at Pelletron facility by the ΔE -E detector of area 100 mm^2 and with ΔE thickness of $10\mu\text{m}$ is

shown in Figure 4.16. Figure 4.17 represents the corresponding 1-D spectrum recorded by the ΔE detector. It can be observed that the events of fission are widely separated from those for elastic and direct reaction channels. Projectile like fragments of different Z (such as F, O, N, C) are also clearly separated from each other showing the quality and capability of the detectors to separate fission fragments from the other charged particles.

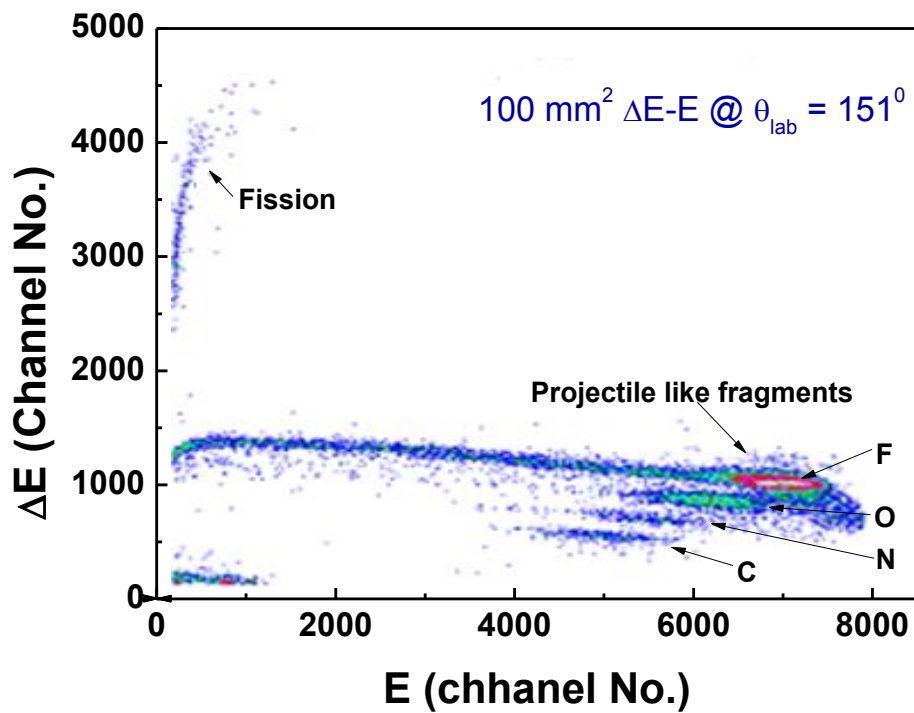


Figure 4.16. Two-dimensional spectrum recorded by the integrated detector for fission fragment measurements in $^{19}\text{F} + ^{209}\text{Bi}$ reaction.

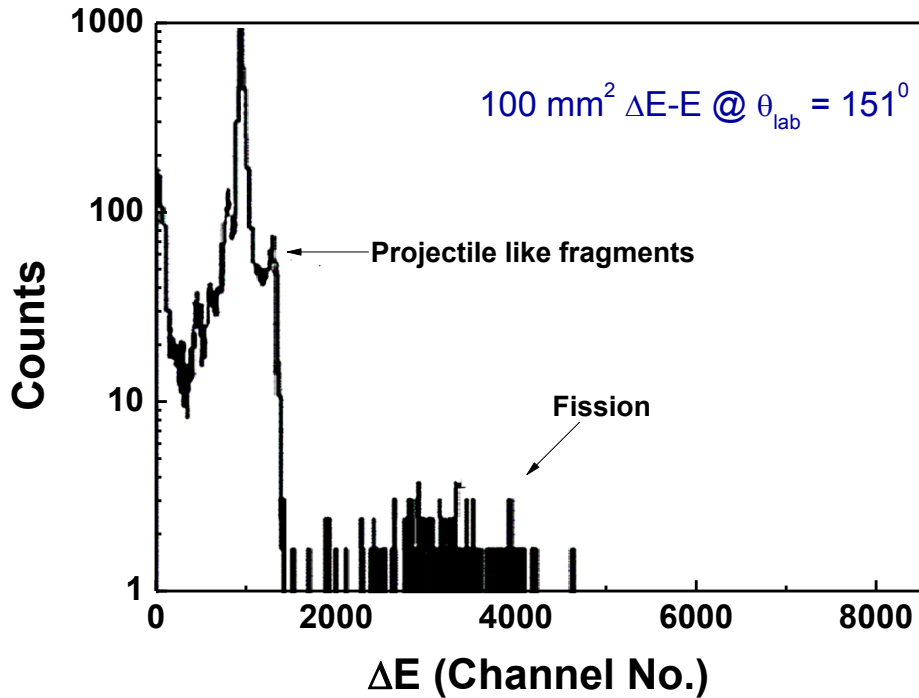


Figure 4.17. One-dimensional spectrum recorded by the ΔE detector of the integrated detector for fission fragment measurements in $^{19}\text{F} + ^{209}\text{Bi}$ reaction.

4.4.4. Performance evaluation for fission fragments and corresponding energy calibration

The performance evaluation of the integrated ΔE -E detector for fission fragments as carried out at Lohengrin facility (Section 3.6.3) is described in this section.

Figure 4.18 shows the histogram obtained for the E detector for 4.7 MeV alpha particles obtained from the double neutron capture event ($^{59}\text{Ni} (n, \alpha)$ reactions) in the nickel cover foil of the target. The Gaussian fit to the spectrum gives an energy resolution of about 0.7 %. Figure 4.19 shows a histogram obtained with the ΔE detector using 90 MeV, $A=90$ fragments incident at an angle of 45° with respect to the detector surface using goniometer to get full deposition in the detector. The energy resolution was about 1.3% for the ΔE detector obtained from the FWHM by fitting this spectrum to a Gaussian.

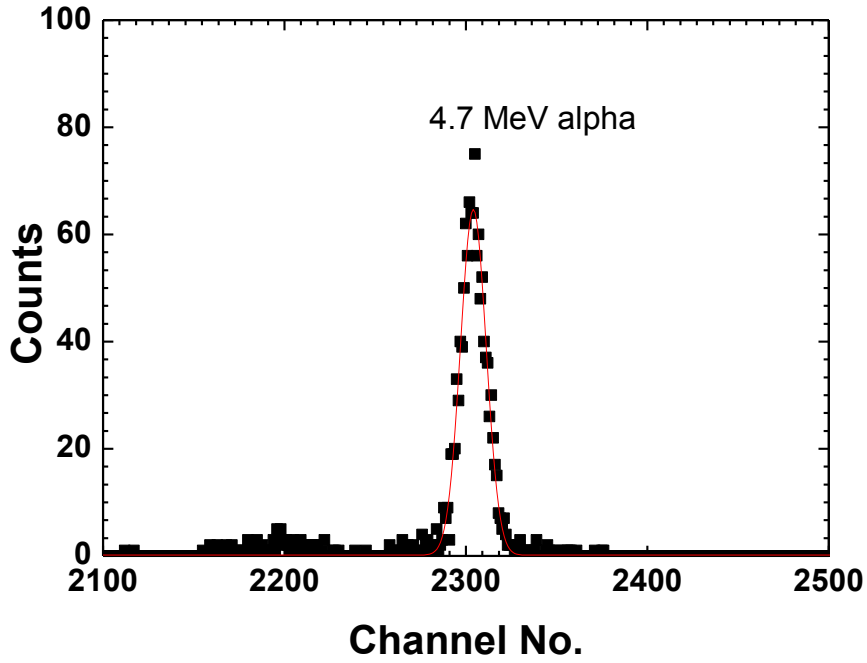


Figure 4.18. Alpha energy histogram for the E detector with thickness of 300 μm used for the estimation of the energy resolution with 4.7 MeV alpha particles.

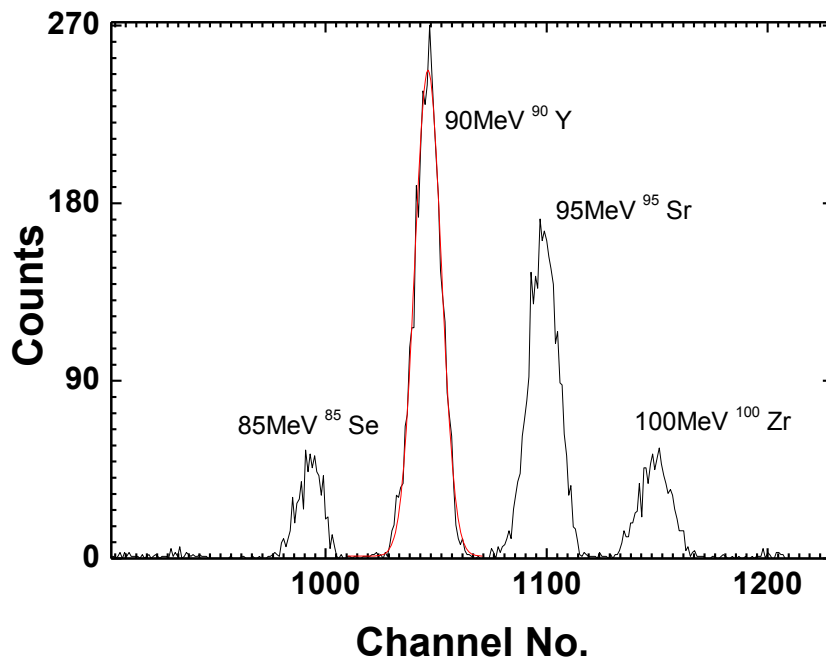


Figure 4.19. Histogram for the ΔE detector of thickness 10 μm used for determination of the energy resolution with 90 MeV, A 90 fission fragments.

Figure 4.20 represents one of the typical 2-D spectrum showing five different fission fragments of different energies recorded by the ΔE -E detector for a particular A/q ratio ($A/q = 5$) and energy ($A/E_T = 1$ MeV/nucleon where $E_T = E + \Delta E$). Several such spectra have been recorded in various runs to obtain the data for different fission fragments. Figure 4.21 shows the corresponding one-dimensional plots [ΔE (in terms of channel numbers) vs. $E + \Delta E$ (total energy E_T)] for a fixed value of A/E_T . Each such fission fragment is expected to appear in the form of a discrete spot in this plot (for a fixed A/E_T) at a particular ΔE - E_T corresponding to its respective mass numbers (Figure 4.20). It is important to note here that there may exist several fission fragments of different mass numbers and energies but having the same A/E_T ratio. It is clear from the spectrum that the detector telescope is capable of distinguishing each fission fragment (mass numbers $A = 85, 90, 95, 100$ and 105 and 136). Each fission fragment is represented by a separate curve in the plot and hence can be easily identified even for varying A/E_T .

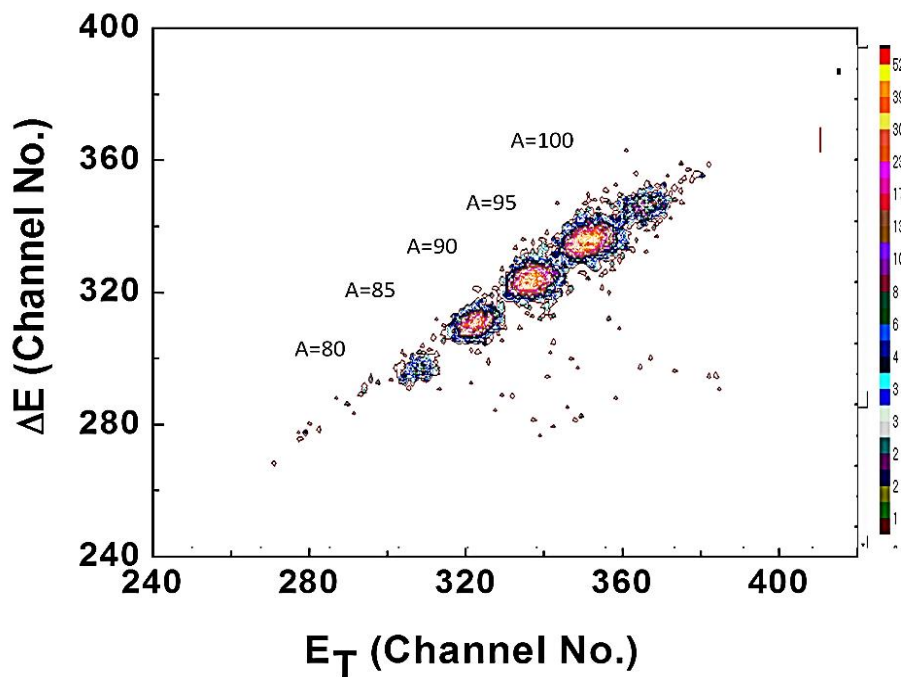


Figure 4.20. Two-dimensional spectrum showing the ΔE signal vs. E_T for a fixed value of $A/q = 5$ and $A/E_T = 1$ MeV/nucleon. ΔE detector thickness $\sim 10 \mu\text{m}$.

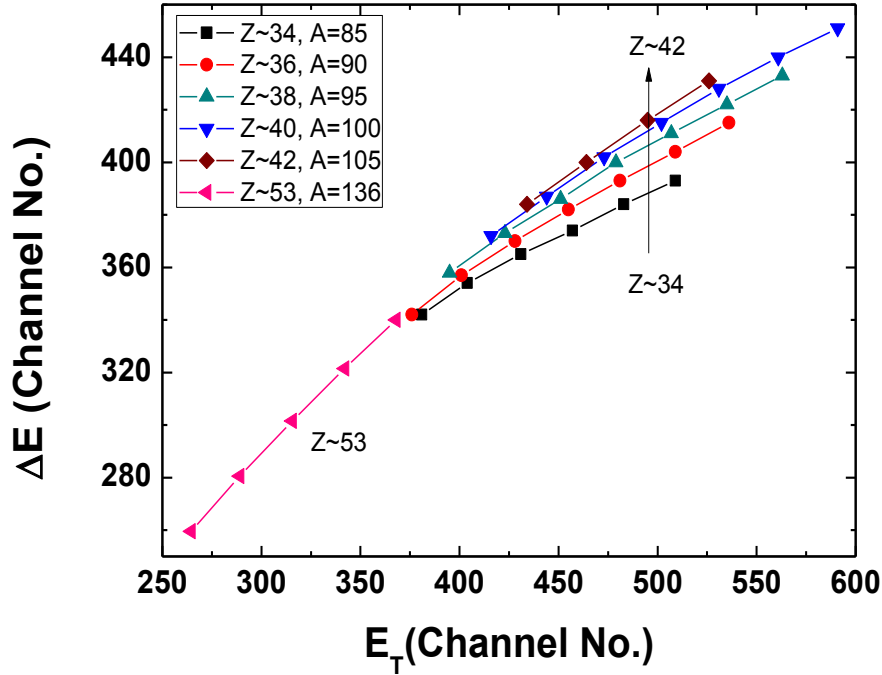


Figure 4.21. Plot of ΔE versus E_T for fission fragments of different mass, nuclear charge and energy demonstrating the Z separation of the telescope. ΔE detector thickness $\sim 10 \mu\text{m}$.

The calibration of the channels in terms of energy of the incident particles is required to use any detector in an experiment. For a detector, typically a linear relation (equation (4.1)) is being utilized for the energy calibration by considering linear charge calibration by the detector and neglecting the nonlinearities of processing electronics.

$$E = BX + C \quad (4.1)$$

where, E is the energy, X is the channel number, and B and C are constants. However, the energy calibration is not straight forward due to pulse height defect in silicon detectors which is much more prominent when dealing with fission fragments. The pulse height defect is more in heavy charged particles compared to lighter charged particles. The total pulse height defect in a detector comprises of energy loss in the detector entrance window, non-ionization energy loss and recombination loss due to plasma effects. Hence, the energy calibration applicable for lighter particles such as alphas cannot be applied directly to measure energies of fission fragments. The constants B and C in equation (4.1) are no more independent of the mass of

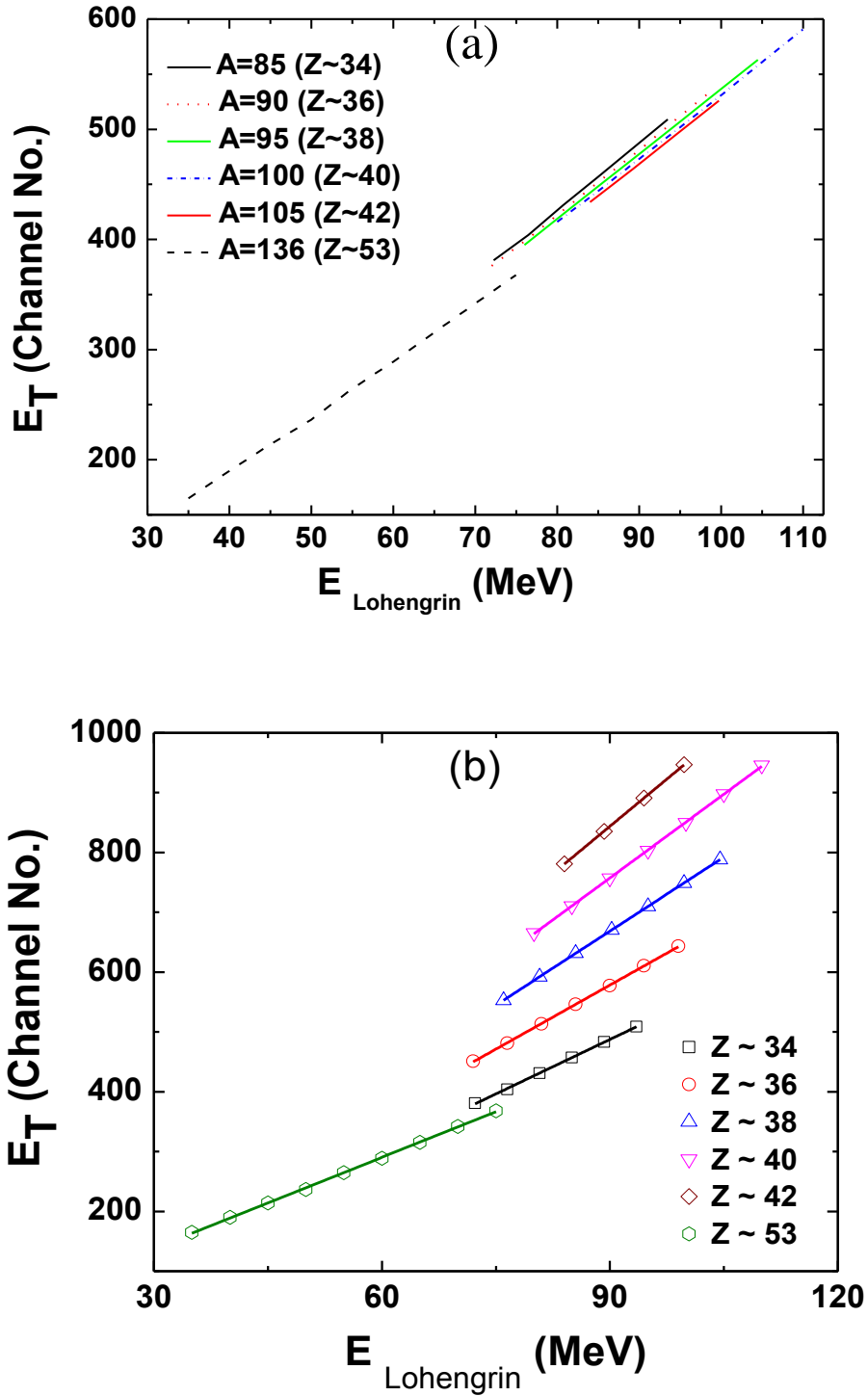


Figure 4.22 (a) Plot between total energy measured by the integrated detector (E_T) vs energy E selected by the Lohengrin fission fragment separator for different fission fragments, ΔE Detector thickness ~ 10 μm . (b) The data have been shifted vertically for clear ($Z \sim 34$) $\times 1$, ($Z \sim 36$) $\times 1.2$, ($Z \sim 38$) $\times 1.4$, ($Z \sim 40$) $\times 1.6$, ($Z \sim 42$) $\times 1.8$, ($Z \sim 53$) $\times 1.0$. The solid lines show fits to the data using linear relations.

particles. Various methods for energy calibration of silicon detectors for heavy charged particles have been reported earlier. Schmitt et al. demonstrated that the constants B and C are

linearly dependent on the mass of $^{79,81}\text{Br}$ and ^{127}I in the 30-130 MeV range [94]. From this study, a general expression for a particle of mass M and energy E can be given as

$$E = (b + b'M) X + (c + c'M) \quad (1.1)$$

where b , b' , c and c' are constants and are characteristics of a detector. The study of Schmitt, et al. [94] was further extended by Weissenberger, et al. [95], for a broad range of fission fragment masses and energies and universal constants characteristics of a particular detector type (ORTEC F series) were obtained. The method of calibration for silicon detectors by Weissenberger, et al., was used in other experiments also [96].

In the present work, a calibration equation has been generated for the integrated detector in terms of E_T (corresponding to channel No X) and actual energy set at Lohengrin from the data acquired at Lohengrin. Incident beams of medium mass fission fragments ($A=85$ to 105 and $A=136$), dominated by a single isobar, namely ^{85}Se , ^{90}Kr , ^{95}Sr , ^{100}Zr , ^{105}Mo and ^{136}I respectively have been utilized for this purpose. This set of calibration isotopes can serve to precisely determine the Z dependence of the detector response. The total energy resolution of the detector was obtained by plotting the relations between set energy of the incident particles and measured channel number corresponding to the total energy (E_T) in Figure 4.22 (a). The data for different Z values has been shifted vertically for clarity in presentation in Figure 4.22 (b).

The set energy and total measured energy (E_T) are observed to follow approximately linear relation for the various fission fragments. These plots have been analyzed using following Z dependent relation:

$$E(E_T, Z) = B(Z) E_T + C(Z) \quad (1.2)$$

where, $B(Z)$ and $C(Z)$ are constants which depend on the nuclear charge, E represents the total energy, while E_T denotes corresponding channel number X . The above relation is inspired by the mass dependent formulae [95], but the original mass dependence here is replaced by the more physical nuclear charge dependence.

The pulse height defect mainly arises from the energy lost in the dead layers and recombination effects, particularly important in the case of high ionization density. It is clear from Bethe formula (equation (2.2)) that both of these effects are strongly dependent on nuclear charge (Z). When only usual neutron-rich fission fragments are considered, a strong correlation between A and Z is observed and hence a mass dependent relation can also work efficiently. However, the Z dependent version is more appropriate for easier translation of the obtained parameters to stable or neutron-deficient ions [97].

The constants B and C are also Z dependent and approximately vary linearly in Z .

$$B(Z) = b + b'Z \quad (1.3)$$

$$C(Z) = c + c'Z \quad (1.4)$$

Using equations (4.3), (4.4) and (4.5), the total energy E is

$$E = b E_T + b'E_T Z + c'Z + c \quad (1.5)$$

The fitting of the experimental data using these linear relation yields following values of the constants (b , b' , c and c') in MeV. The total root-mean-square deviation (RMSD) of the data is about 0.282.

$$b = 0.1053 \pm 0.0089, \quad b' = 0.0017 \pm 0.00021$$

$$c = 22.6 \pm 3.68, \quad c' = -0.356 \pm 0.09$$

The comparison of the actual values of the total energy of fission fragments set by Lohengrin and that obtained from the calibration equation is depicted in Table 4.2. It is evident from the table that the values of the total energy obtained using the fitted constants are in excellent agreement with those set during the experiments for a wide range of fission product energies suggesting the validity of this calibration method for use in further experiments.

Table 4.2. Comparison of actual energy set at Lohengrin and energy obtained using calibration equation for fission fragments of different charge and energies.

Z	Set Energy (with standard deviation)	Fitted Energy (with standard deviation)	% Deviation (In average value)	Z	Set Energy (with standard deviation)	Fitted Energy (with standard deviation)	% Deviation (In average value)	Z	Set Energy (with standard deviation)	Fitted Energy (with standard deviation)	% Deviation (In average value)
~34	72.2 ± 0.3	72.5 ± 0.6	0.41	~38	76.0 ± 0.3	76.1 ± 0.5	0.13	~53	35.0 ± 0.1	35.9 ± 0.5	2.57
	76.5 ± 0.3	76.3 ± 0.6	0.26		80.7 ± 0.3	80.8 ± 0.6	0.12		40.0 ± 0.1	40.8 ± 0.5	2.0
	80.8 ± 0.3	80.7 ± 0.6	0.12		85.5 ± 0.3	85.6 ± 0.7	0.11		45.0 ± 0.1	45.4 ± 0.5	0.89
	85.0 ± 0.3	84.9 ± 0.6	0.12		90.2 ± 0.4	90.3 ± 0.7	0.11		50.0 ± 0.1	49.8 ± 0.5	0.40
	89.2 ± 0.4	89.1 ± 0.6	0.11		95.0 ± 0.4	95.1 ± 0.7	0.10		55.0 ± 0.2	55.3 ± 0.6	0.54
	93.5 ± 0.4	93.4 ± 0.6	0.11		99.7 ± 0.4	99.8 ± 0.7	0.10		60.0 ± 0.2	60.0 ± 0.7	0.0
~36	72.0 ± 0.3	72.2 ± 0.5	0.28	~40	104.5 ± 0.4	104.6 ± 0.8	0.05	65.0 ± 0.2	65.2 ± 0.8	0.30	
	76.5 ± 0.3	76.4 ± 0.6	0.13		80.0 ± 0.3	80.2 ± 0.6	0.25	70.0 ± 0.2	70.3 ± 0.9	0.43	
	81.0 ± 0.3	80.8 ± 0.6	0.25		85.0 ± 0.3	85.1 ± 0.6	0.12	75.0 ± 0.2	75.4 ± 0.9	0.53	
	85.5 ± 0.3	85.3 ± 0.7	0.23		90.0 ± 0.4	90.1 ± 0.6	0.11				
	90.0 ± 0.4	89.6 ± 0.7	0.44		95.0 ± 0.4	95.1 ± 0.6	0.10				
	94.5 ± 0.4	94.3 ± 0.7	0.21		100.0 ± 0.4	100.1 ± 0.6	0.10				
	99.0 ± 0.4	98.8 ± 0.7	0.20		105.0 ± 0.4	105.3 ± 0.6	0.28				
				110.0 ± 0.4	110.5 ± 0.7	0.45					

The energy resolution of the integrated detector for various fission fragments at different energies has also been estimated from the experimental data. The energy resolution of about 1.5-1.85 MeV has been observed for the light fission fragments in the energy range 75-100 MeV while a resolution in the range 1.3-2.4 MeV has been obtained for the heavy fission fragments ($Z=53$) in the energy range 45-75 MeV (Figure 4.23). In thermal neutron induced fission of ^{235}U , light fission fragments ($32 < Z < 43$) have typically kinetic energies of 85–110 MeV and heavy fission fragments ($50 < Z < 58$) have kinetic energies of 50–75 MeV. $Z= 53$ belongs to the group of heavy fission fragments. Pulse height defect is more prominent in heavy fission fragments due to higher atomic number and lower kinetic energy in comparison to light fission fragments. The energy lost in dead layers will also be more for $Z=53$. These factors will be responsible for the poor energy resolution. The resolution obtained from these

measurements is comparable to that observed for silicon surface barrier (SSB) detectors. The SSB detectors has been shown to have an energy resolution of about 1.1-1.5 MeV for lighter fission fragments (mass $A=80-100$) at 90MeV and an energy resolution of about 1.6-1.8 MeV for heavier fission fragments (mass $A=130-140$) at 60MeV [95].

From the experiments at Lohengrin, it has been realized that a thinner ΔE detector with thickness approximately in the range of 4-6 μm will be more appropriate for heavier fission fragments ($A > 130$). Several spectra were further recorded in the second run of the experiments using thinner ΔE detector, covering a wide range of fission fragments, $A = 80$ to 148 (Figure 4.24 and Figure 4.25). The detectors were found to be showing an excellent performance in identify the entire range of the fission fragments.

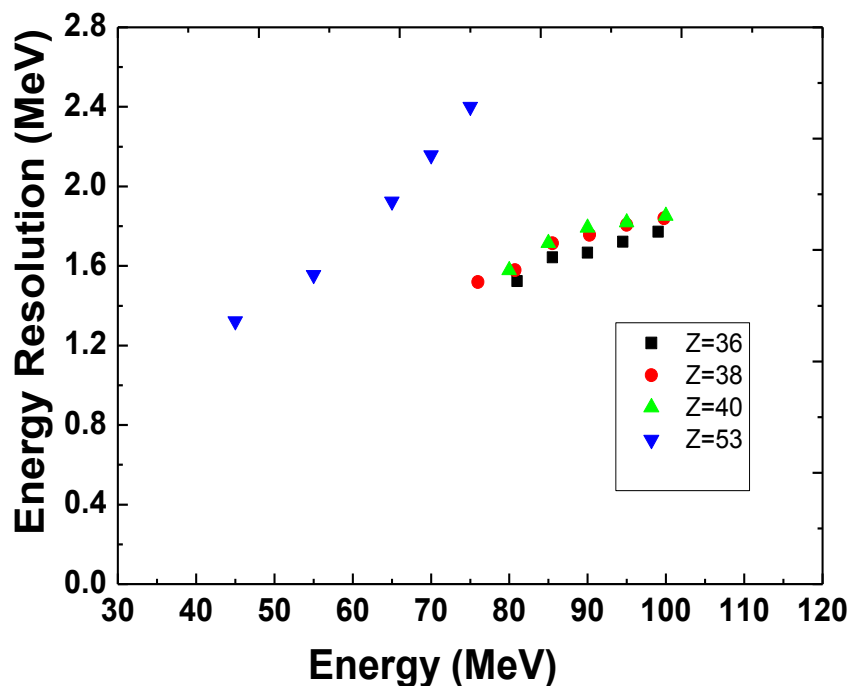


Figure 4.23. Energy resolution of integrated detector for fission fragments of different energies and charge.

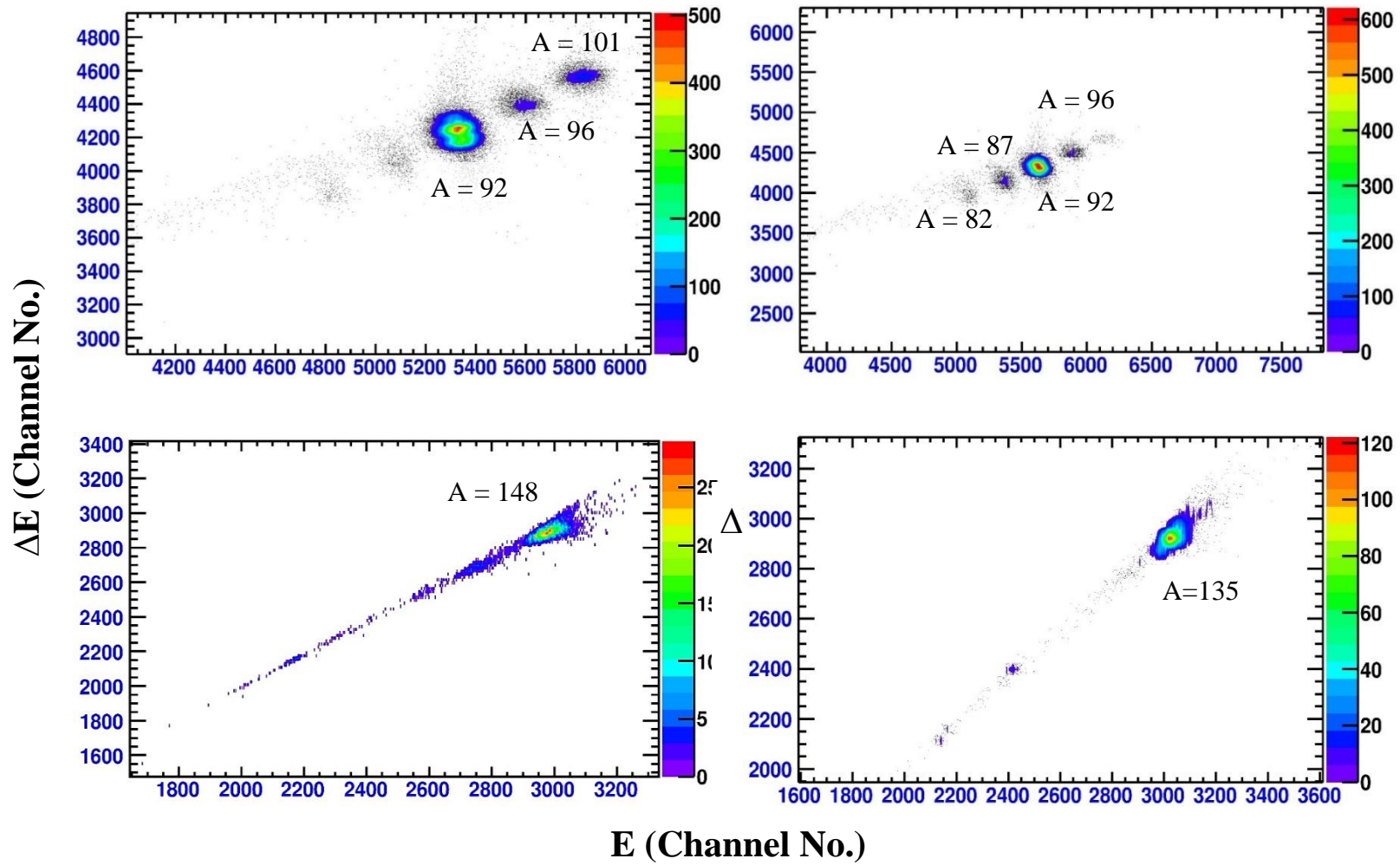


Figure 4.24. Typical 2-D spectra obtained from several set of measurements identifying fission fragments from $A = 80$ to $A = 148$.

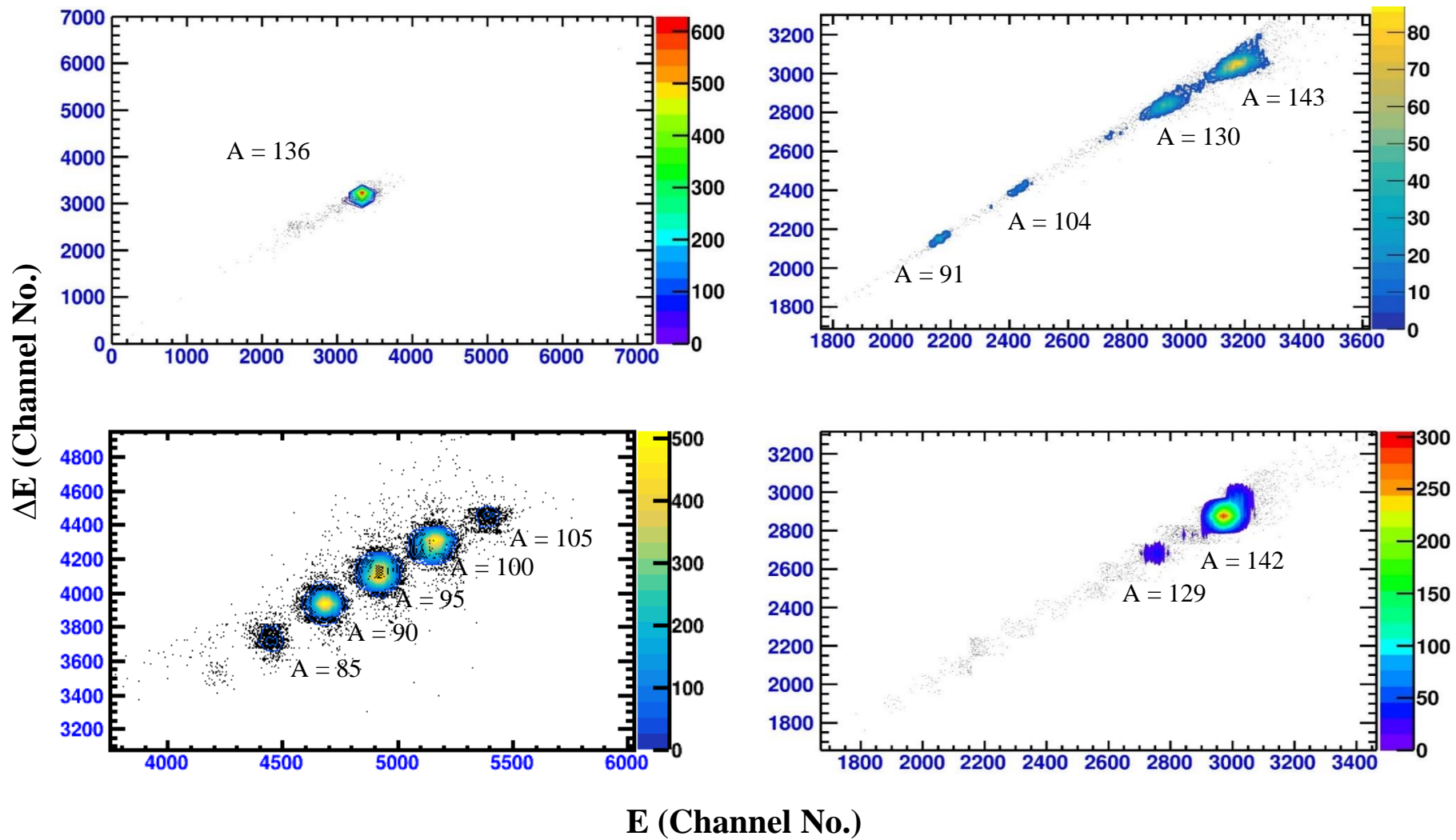


Figure 4.25. Typical 2-D spectra obtained from several set of measurements identifying fission fragments from $A= 80$ to $A= 148$.

The best ever reported nuclear charge resolving power of a 8 μ m thick ΔE Si detector was reported as $Z/DZ=43$ for 100 MeV fission products [98]. However, the total energy was defined by the LOHENGRIN separator and no residual energy measurement was performed, i.e. dead layers on the backside of the detector were of no concern. Moreover, to assure optimum homogeneity, the beam had to be collimated to a tiny area of 1 to 2 mm² in the center of the detector which resulted in low acceptance. Other separated or integrated Si telescopes were mainly tested with lighter ions. Kordyasz, et al., tested their Si detector telescope with fission products but did not quote the obtained Z resolution [92].

The detailed investigations of the fission process often targets full separation of neighboring Z (i.e. $dZ \gg 1$). In order to meet this challenging aim, the solid angle and overall efficiency both have to be compromised. The fission process is also frequently used as efficient production mechanism for nuclear spectroscopy of neutron-rich nuclei. Recently, a powerful gamma detector array has been utilized to study the excited states of fission products from ²³⁵U(n,f) and ²⁴¹Pu(n,f) respectively at ILL [99]. The prompt gamma rays are emitted from many excited states of over 300 different nuclides that are populated in fission. Still, individual gamma rays of strongly populated fission products can be identified and singled out via triple coincidences. However, in the case of weakly produced nuclides, when the gamma ray energies are low or when no or few exploitable transitions are yet known, the method reaches to its limits. In such situation, the combination with an additional identification method can serve the purpose by restricting the number of nuclides and thus cleaning up the gamma spectra considerably. Even a crude measurement of A and/or Z of one of the fragments could help, but for this purpose large solid angle coverage, and hence, high detection efficiency is more important than ultimate Z resolution. Thus, a compact telescope would be extremely useful for such experiments, even if its nuclear charge resolution reaches only $dZ \gg 2-3$.

4.5. Conclusion

A novel detector with integrated E and ΔE (monolithic) detector based on a totally new device design and fabrication process has been realized using double sided wafer-processing technology. The detector is demonstrated to clearly identify light charged particles (e.g. protons, alpha and lithium) and heavy fission fragments ($A \sim 80-140$). The results are equally comparable to those obtained with physically separate ΔE and E detectors. A new charge dependent approach for the energy calibration of these detectors for fission fragments is also presented.

Chapter 5

DEVELOPMENT OF DOUBLE SIDED SILICON STRIP DETECTORS

5.1. Introduction

The nuclear and particle physics experiments, medical imaging as well as scanning instruments sometimes require fast and highly precise tracking devices with accurate position sensing. The double sided silicon strip detectors (DSSD) with orthogonal strips on opposite faces satisfying both the above requirements are being increasingly used for these purposes due to their ability to provide the position information of radiation in two dimensions. As described in Section 3.4, these detectors are fabricated using well-established silicon planar technology, which allows fine detector segmentation in the form of strips, microstrips or pixels and large-scale production of detectors with good uniformity at lower costs. A spatial resolution of few microns can be easily realized using such segmented detectors. DSSDs are the extension of single sided strip detectors. In single sided strip detectors, segmentation in the form of strips is done only on junction side of the detector to obtain 1-dimensional position information [100]. While in DSSDs, additional segmentation in the form of N^+ strips on the Ohmic side is done to obtain two-dimensional position sensing.

In recent years, there is growing interest in using DSSDs for particle identification using pulse shape discrimination (PSD) techniques for upcoming detector arrays such as GASPARD [101] and FAZIA [73], [102]. The detectors are used for PSD applications when mounted facing the incident particle flux from Ohmic (back) side. In comparison to the standard ΔE -E telescopic technique, this approach reduces the complexity as well as the costs due to lesser number of detectors, and also overcomes many of the performance limitations arising from the use of

conventional ΔE detectors in terms of thickness, active area, uniformity, etc. The main challenges in fabricating the DSSDs arise due to the complexity of processing involving a large number of processing steps with double sided wafer processing. Single sided silicon strip detectors with 32-strips were developed at BARC, India for the Preshower of the Compact Muon Solenoid detector at Large Hydron Collider [103]. As a continuation, the development of large area ($\sim 40 \text{ cm}^2$) double sided DC coupled silicon strip detectors for use with PSD technique for particle identification was carried out [41]. An overview of the design, fabrication, characterization and performance evaluation of these detectors developed in the present work are described in this Chapter [41], [104], [105].

5.2. Basic design considerations

In the present work, the development of large area ($\sim 40 \text{ cm}^2$) DSSD was carried out as per the requirement of nuclear physics experiments in India and for the GASPARD Experiment at the upcoming SPIRAL2 facility at GANIL, France. Basic detector design considerations are described in subsequent subsections.

5.2.1. Detector geometrical parameters

The detectors were designed to have 64 P^+ strips on the front side (junction side) with pitch of 0.9 mm and 64 N^+ strips on the back side (Ohmic side) with pitch of 0.9 mm. Strips on one side are designed to be orthogonal to the other side of the strips as shown in Figure 5.1. With this orthogonal arrangement, two-dimensional measurement can be obtained from a single detector. Each strip is having a length of 60 mm. The active area of DSSD is 60 mm x 60 mm. As per the requirement of geometry, calculations were made for deciding the design parameters for the mask.

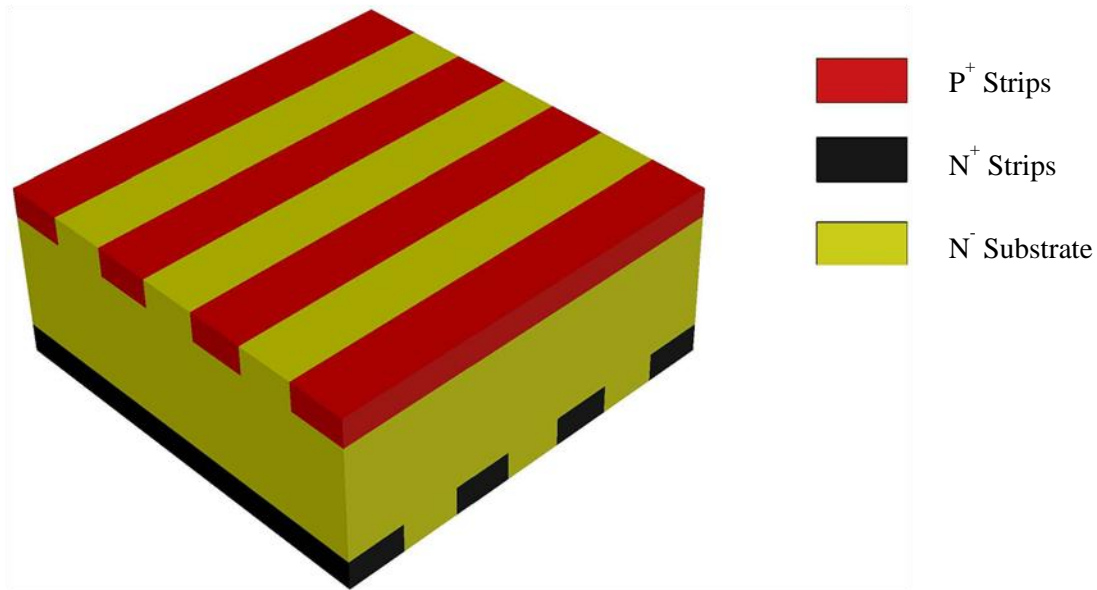


Figure 5.1. Basic representation of DSSD.

5.2.2. Wafer and design parameters

The optimization of fabrication process and selection of substrate wafer is important to minimize the capacitance, leakage current and hence the noise. Moreover, a very uniform electric field in the bulk of the detector is essentially required for the identification of the charged particles using PSD technique. This requirement can be met by using silicon wafers with neutron transmutation doping (NTD) having doping accuracy better than 5% for detector fabrication. However, in the present work, the standard high resistivity wafers were used for the development of prototype for reducing the cost. Detector grade, N-type FZ wafers with thickness of $300 \pm 20 \mu\text{m}$ were selected for the fabrication of the detectors. The $\langle 111 \rangle$ orientation of wafer were chosen to prevent possibility of channeling as well as to increase the probability of generation of the electron-hole pairs, due to high atomic density of this plane.

It may be mentioned here that more the resistivity of wafer, less is the full depletion voltage and lower is the capacitance for a particular bias voltage (Section 3.2.4). In order to keep lower full depletion voltage, for the PIN configuration of the detectors, the resistivity of the wafer

was chosen to be 3-5 k Ω cm. Double sided polished wafer were used for double sided processing. The selected wafers were having carrier life time of a few ms which is suitable for keeping leakage currents low. The detectors fabricated using wafers with higher life time are expected to have lower leakage current due to lower density of defects at which generation-recombination occur.

5.2.3. Considerations for back side (N⁺ strip side) configuration: N⁺ strip isolation

The isolation of the both sides of strips from each other is not straight forward. Simply providing N⁺ and P⁺ strips as shown in the Figure 5.2 does not solve the problem of electrical isolation due to the build of an electron accumulation layer near the surface (Figure 5.2 (a)). This layer provides the conduction path between the N⁺ strips resulting in reduced interstrip resistance. Few techniques (Figures 5.2 (b) and (c)) such as p-stop and p-spray are being used to isolate the N⁺ side strips properly, as discussed in Section 3.3.4. In p spray method, global P⁺ implantation close to the silicon surface compensates for the electron accumulation. In this method, the implantation dose is very critical as high concentrations may lead to early breakdown [22]. In p-stop method, P⁺ implantations between the N⁺ strips are carried out to break the conduction path. It can be done using three configurations namely atoll, common and atoll with common. This method increases the number of masks used to pattern the additional stop implantation. Atoll and common configuration provide better isolation therefore, the isolation between the N side strips was provided by atoll and common types of isolation [106]. In atoll isolation, each n-type strip is surrounded by a ring-shaped p-type implant which provides isolation to each strip from adjacent strips. For common type of isolation, n-type strips are embedded in a p-type implanted area covering the whole sensor except at small regions around the strips. The interstrip gap between the strips on the P side was 40 μm . However, for

incorporating the P⁺ isolation between the strips on N side, the interstrip gap on the N side was increased to 180 μm.

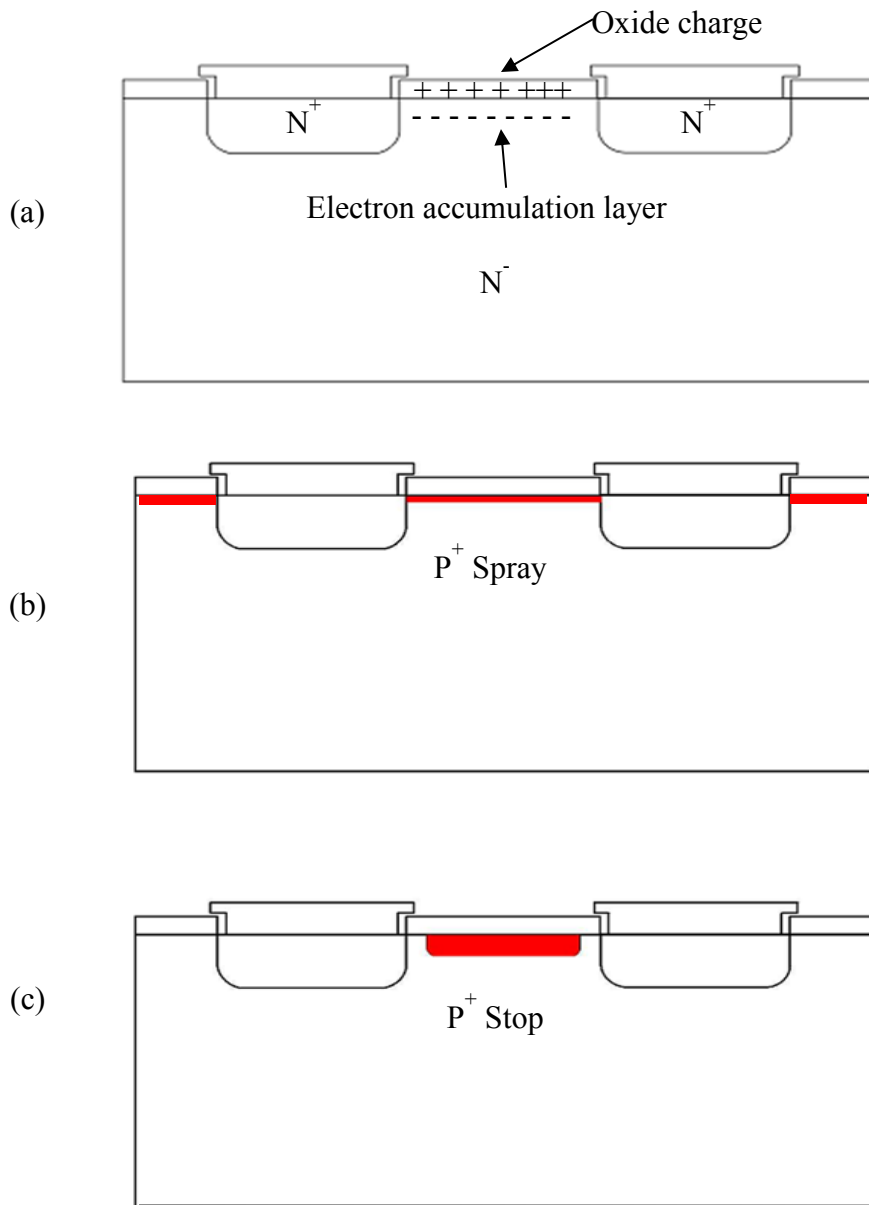


Figure 5.2. Schematic representation of (a) charge accumulation layer at the interface of SiO₂, (b) N⁺ strip isolation using P⁺ spray and (c) N⁺ strip isolation using P⁺ stop method.

One of the other important concern is to minimize the dead layer of the detector surface facing the charged particles as it causes significant energy loss for heavy charged particles and reduces minimum energy threshold for a particular charged particle. Such reduction of dead layer necessitates shallow junctions and puts a severe limitation on realization of higher breakdown

voltage. Standard design techniques such as floating field guard rings and metal overhang over the strips were incorporated in order to improve the strip breakdown voltage [107]. Semiconductor and process device simulations were performed to investigate the field distribution in the device for identification of high electric field regions, causing the breakdown. The simulation study was done by varying important design and process parameters. The results of this simulation study are discussed in the Section 5.4 of this Chapter. The detector was mounted on the PCB package in transmission mode with the support at the edges. The scribe line was designed to facilitate such mounting of detectors during packaging. Phosphorous doped N^+ layer was provided on the front side along the detector edges for making front side contact to the N^+ region. A number of test structures such single element PIN pad detectors, single and double sided baby strip detectors, etc. were designed along with the main detector to evaluate the P and N side processing quality during the fabrication. The design was implemented for a twelve-layer mask fabrication process.

5.2.4. Mask design

The following structures (Figure 5.3 and 5.4) were designed for the mask:

a. Main detector

The main detector has active area 60 mm x 60 mm with five P^+ guardrings. It is having total 64 P^+ implanted strips on the front side having width 890 micron with a gap of 40 μm between the strips and 64 N^+ implanted strips right-angled to the front side strips on the back side with a gap of 180 μm between the strips. An atoll and common P^+ stop structure were used for N^+ strip isolation. The P^+ and N^+ strips were designed with metal overhang. Front side N^+ implant at the detector edge was provided for taking N^+ contact while characterizing the front side.

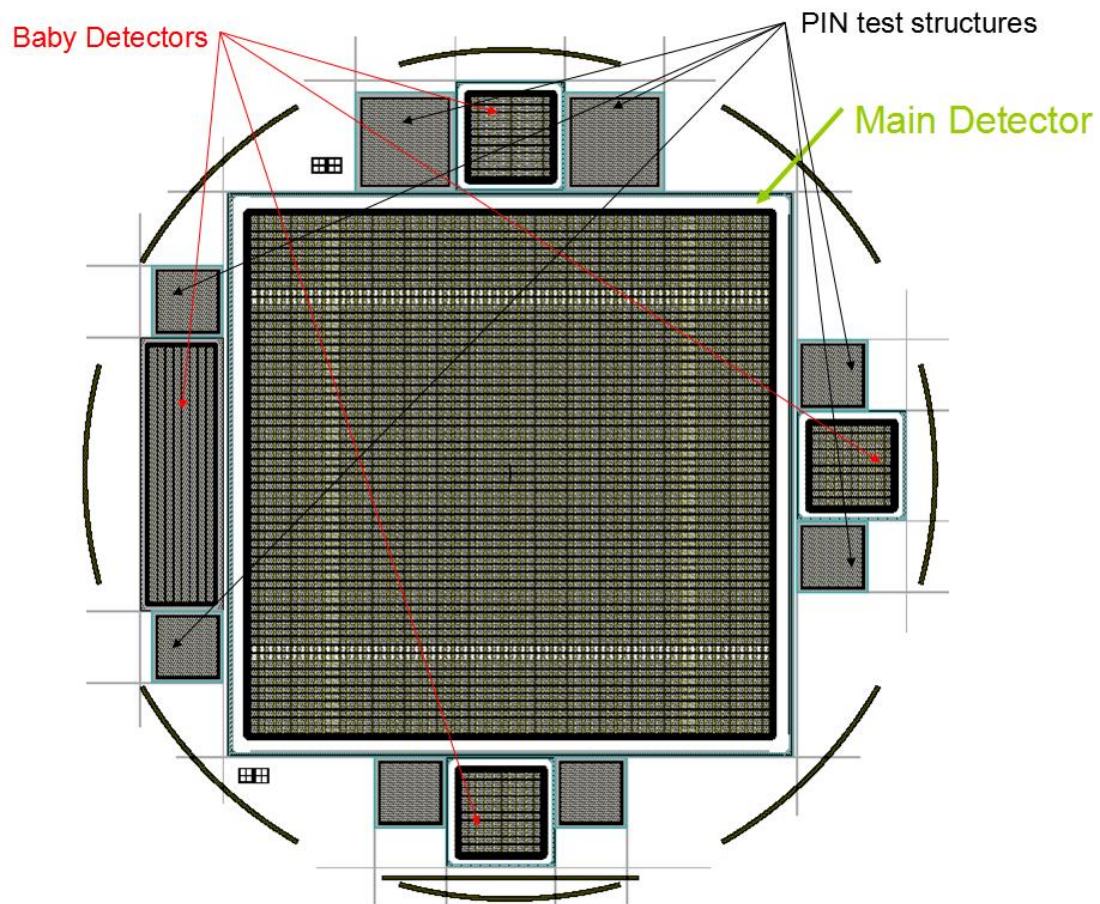


Figure 5.3. Mask layout representing all layers.

b. PIN test structures

PIN test structures of active area 10 mm x 10 mm and 7 mm x 7 mm were incorporated to verify the front side processing of the wafer.

c. Single sided baby strip detector

Single sided baby strip detector was designed for verifying the processing steps of front side P⁺ strip detector.

d. Double sided baby strip detectors

Double sided baby strip detectors of three different configuration as atoll, common, and atoll along with common were designed to compare these three configurations for N side strip isolation.

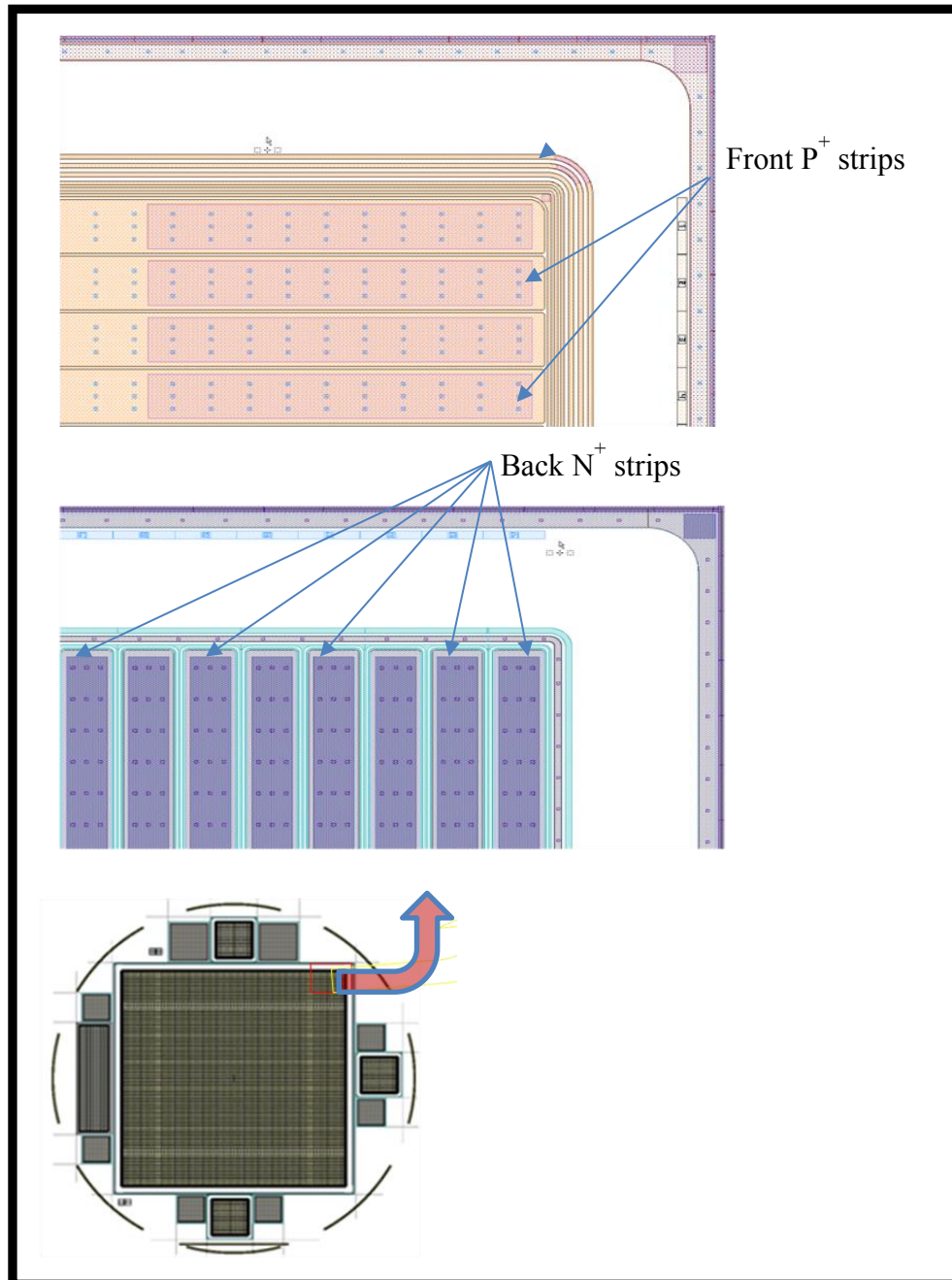


Figure 5.4. Magnified mask view

5.3. Detector fabrication process

The detector was fabricated using double sided wafer processing. The fabrication process has following process steps.

- (a) High resistivity, <111>, N type, FZ, double sided polished wafers of thickness 300 μm as substrate wafers.
- (b) Growth of field oxide using pyrogenic oxidation.
- (c) Back P⁺ lithography for P⁺ (Boron) back implant and implant annealing followed by drive-in.
- (d) Back N⁺ lithography for N⁺ back implant and implant annealing followed by drive-in.
- (e) Front N⁺ lithography for N⁺ front implant and implant annealing followed by drive-in.
- (f) Front P⁺ lithography, P⁺ front implant and implant annealing followed by drive-in.
- (g) P⁺ /N⁺ front and N⁺/P⁺ back contact opening.
- (h) Metallization on front and back side and lithography on front and back side.
- (i) Annealing after metallization.
- (j) Passivation and passivation opening on front and back side for bonding pads.

The field oxidation (a few thousand Å) was done using pyrogenic oxidation method due to its higher growth rate and low thermal budget in comparison with dry oxidation. Thin screen oxidation was carried out using dry oxidation process to maintain uniform implantation. The wafers were cleaned using standard RCA cleaning process before each processing step to remove organic and metallic contaminants. The initial process parameters were based on the

simulation results. The fabrication process was further optimised in consequent batches to achieve the desired breakdown voltage (about 1.5 times the full depletion voltage) and energy resolution (about 30 keV for 5.5 MeV alpha particle) of individual strips. The processed wafer (the P⁺ side and N⁺ side of the fabricated detector) is shown in Figure 5.5. The diced DSSD is depicted in Figure 5.6. A PCB Package for the detector packaging was designed according to future application of these detectors. It contained one main PCB with 64 bonding pads for P⁺ strips, 64 bonding pads for N⁺ strips, two 68 pin connectors and two cover PCBs for bond wire protection. The diced detector chip was mounted on this package and the front P⁺ and back N⁺ strips were wire bonded using 25 μ m diameter aluminum wire to the PCB pads. The final connections from the strips were brought to two 68 pin miniature SMD connectors. The photograph of the packaged detector is shown in Figure 5.7.

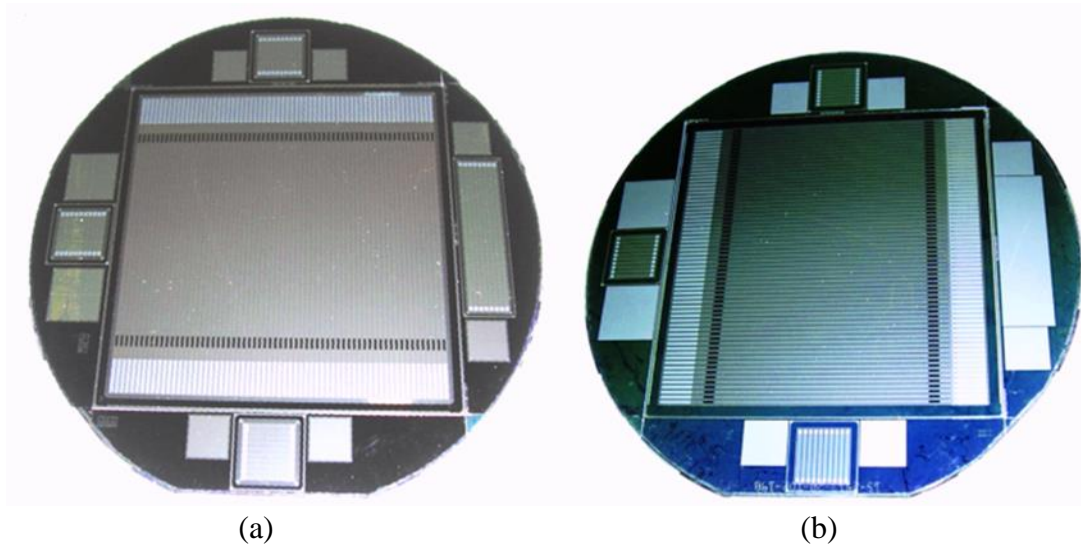
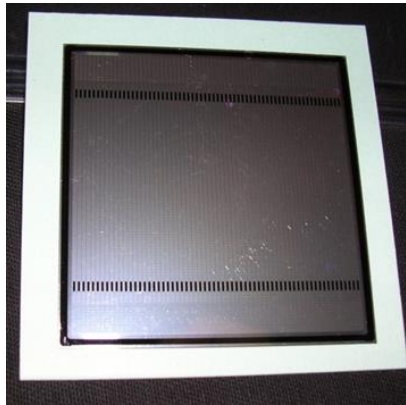
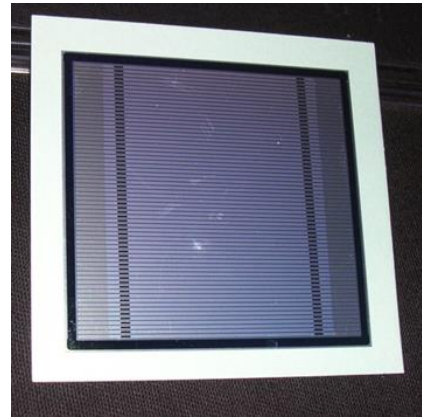


Figure 5.5. P⁺ side of the wafer with double sided silicon strip detector in centre and test structures. (b) N⁺ side of the wafer with silicon strip detector in the centre and test structures.



(a)



(b)

Figure 5.6. (a) P⁺ side of the diced DSSD and, (b) N⁺ side of the diced DSSD.

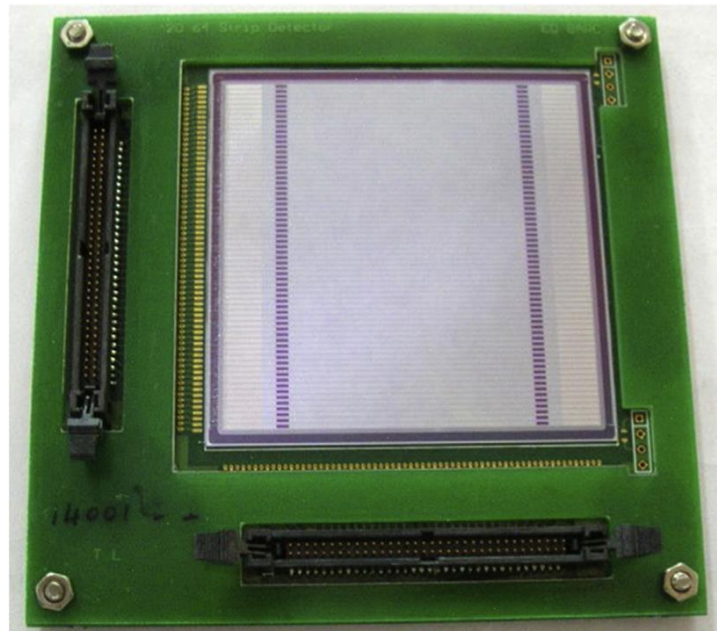


Figure 5.7. Double sided silicon detector packaged in transmission mode on PCB with 68 pin SMD connectors for connecting P⁺ and N⁺ strips to readout circuit.

5.4. Results and discussion

5.4.1. Detector process and device simulation study

As mentioned earlier, device and process simulations were carried out for the theoretical estimation of the breakdown voltage with respect to the different design and process

parameters. The front P⁺ strips form P⁺/N junctions and back side N⁺ strips form Ohmic contact with the N type substrate wafer. The electric fields are found to be maximum at the P⁺/N junctions and hence deciding the breakdown voltage of the detector. The two-dimensional (2-D) simulations of a single PIN pad structure were carried out by simulating the process flow for the front side of the wafer using a commercial process simulator. All process steps such as pyrogenic or dry oxide, boron and phosphorous implantation, annealing after implantation, Al deposition and etching, etc were simulated to generate a 2-D model (cross section) representing the pad detector. The 2-D model thus obtained was subsequently simulated in the device simulator to obtain various physical parameters such as electric fields, potential distribution, impact ionization region, leakage current, etc., for the pad detector. The theoretical breakdown voltage of the detector was calculated from the simulated reverse I-V characteristics. The impact of important parameters such as P⁺ implant energy, metal overhang and field oxide thickness over the junction, etc., was also examined during the simulations for improving the breakdown voltage. The simulated variation of breakdown voltage with boron implant energies of 30 keV, 50 keV and 80 keV for no metal overhang is depicted in Figure 5.8. As expected, lower implant energies reduce the breakdown voltage due to shallower junctions. The P⁺/N junction breaks down at the junction curvature due to higher electric fields at these locations. However, as can be seen in Figure 5.9, the theoretical breakdown voltage can be significantly increased by using metal overhang. Irrespective of boron implant energy, the junction breaks down at the same voltage (Figure 5.9). For 50 keV boron implant energy, the reverse I-V characteristics are plotted for no overhang and for metal overhang of 10 μm and 15 μm (Figure 5.10). The breakdown voltage is observed to be increasing from about 650 V to 1075 V for 10 μm metal overhang, and to 1170 V for 15 μm overhang. The effect of field oxide thickness on breakdown voltage was also examined for 50 keV implantation energy for oxides with thicknesses 0.35 μm, 0.5 μm and 0.75 μm (Figure 5.11). By increasing the field oxide thickness,

the electric field at the junction at the surface is reduced and consequently, the improvement in the breakdown voltage is observed. Overall, the improvement in the breakdown voltage can be obtained by deeper junctions, using metal overhanging over the oxide and by increasing the oxide thickness. It may be mentioned here that the deeper junctions also increase the dead layer for charged particles increasing the low energy threshold of the measurement in nuclear physics experiments and this deteriorates the energy resolution for charged particles due to energy straggling in the dead layer.

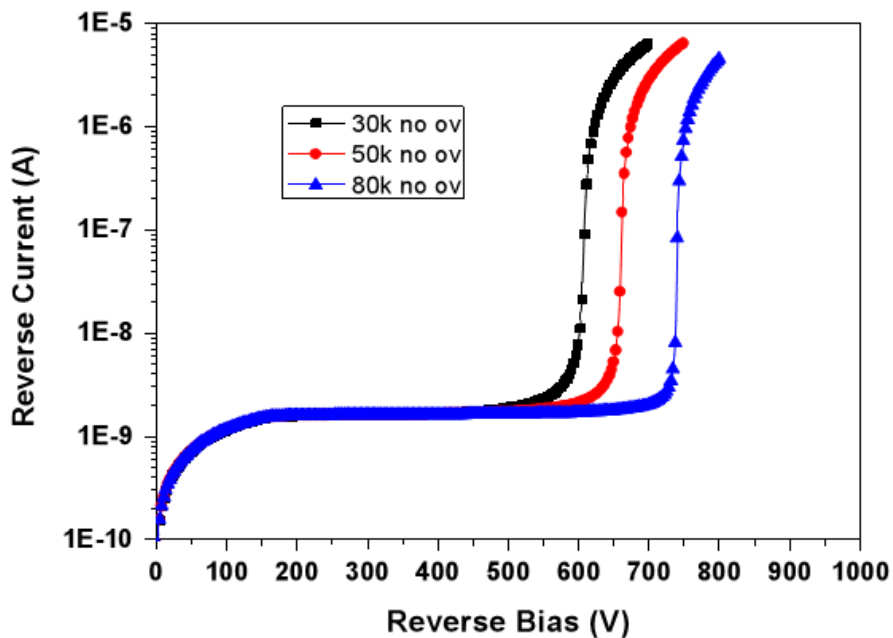


Figure 5.8. Comparison of breakdown voltage of the pad detector for different boron implantation energies of 30 keV, 50 keV and 80 keV. The detector is simulated without metal overhang.

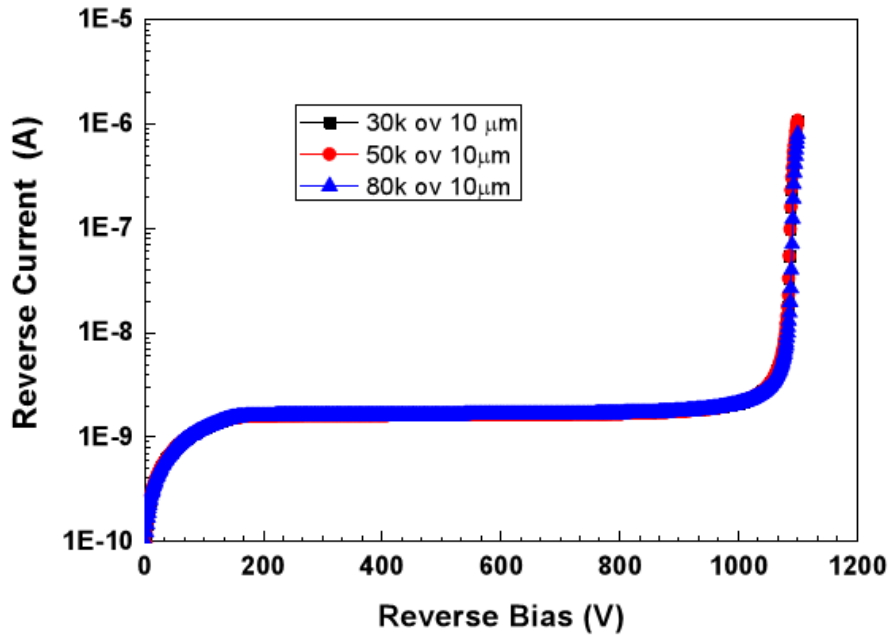


Figure 5.9. Comparison of breakdown voltage of the pad detector for different boron implantation energies of 30 keV, 50 keV and 80 keV. Metal overhang is 10 μm for all the cases.

The actual breakdown voltages (as discussed in the later sections of the Chapter) are observed much lower than theoretical breakdown voltages due to presence of defects in either the virgin wafer or those generated during processing of wafers. Hence, simulation results, though have been useful for finalizing the initial process parameters but further tuning of process parameters was done based on the performance of fabricated detectors. The prototype development was carried out targeting for a full depletion voltage and breakdown voltage of about 70 V and 100 V respectively. The detectors with i) field oxide thickness of 0.35 μm or above, ii) 50 to 80 keV boron implantation energy, and iii) metal overhang of 10 μm or more, were theoretically observed to have breakdown voltages exceeding 1000 V (Figures 5.8-5.11).

Based on the simulation results, the design and fabrication parameters were finalized as i) field oxide thickness of 0.35 μm to reduce the thermal budget, ii) metal overhang of 5 μm considering the spacing of 40 μm between P⁺ strips, and iii) 80 keV implant energy for boron considering implanter capability at the foundry.

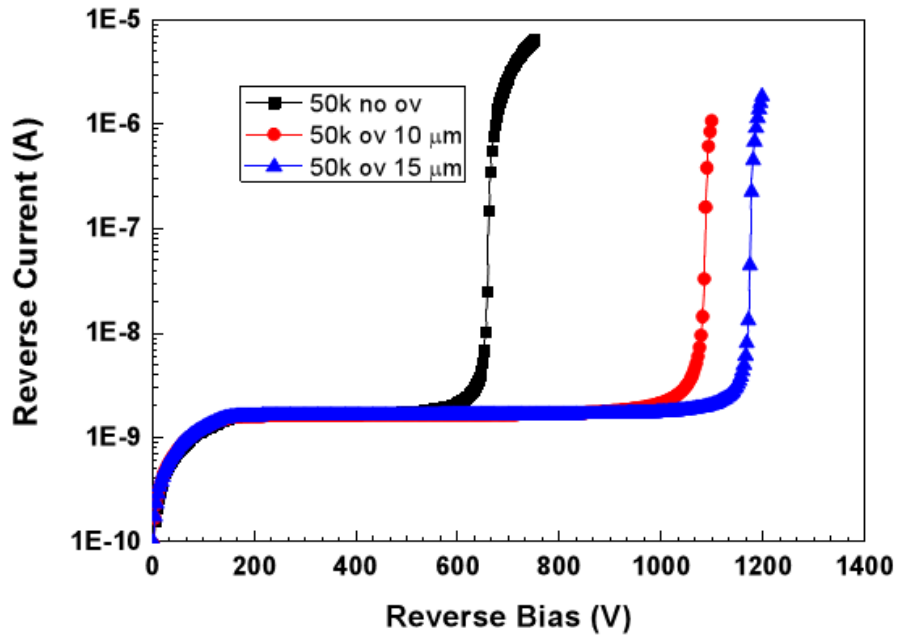


Figure 5.10. Comparison of breakdown voltage of the pad detector for metal overhang of 0/10 μm /15 μm . Boron implantation energy 50 keV.

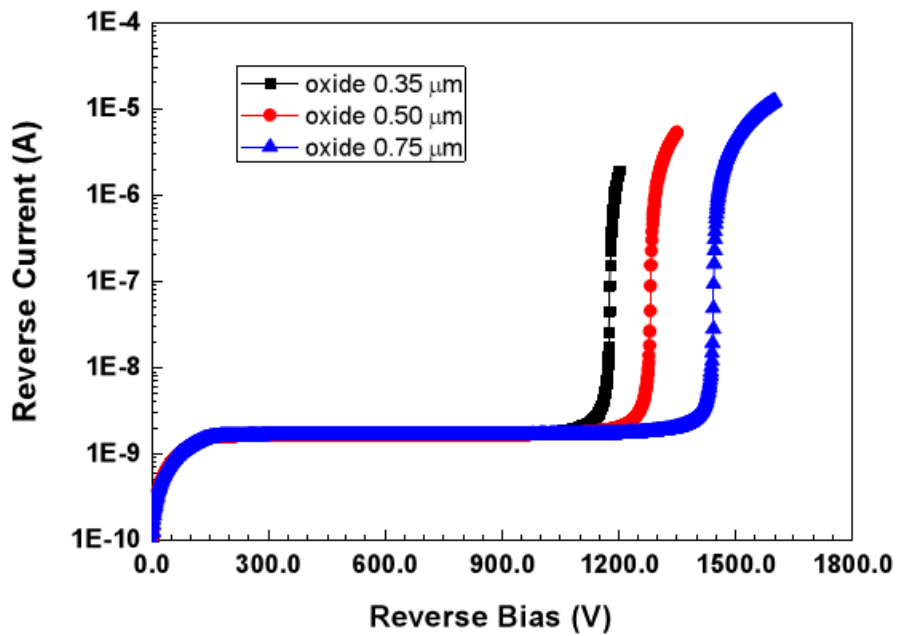


Figure 5.11. Comparison of breakdown voltage of the pad detector for field oxide thicknesses from 0.35 to 0.75 μm at 50 keV boron implantation energy and 10 μm metal overhang.

5.4.2. Evaluation of detector performance by static characterization

In order to verify the wafer fabrication process, I-V and C-V measurements of 7 mm × 7 mm and 10 mm x 10 mm PIN test structures were carried out. To estimate the energy resolution of the P⁺ and the N⁺ strips of the detector, the alpha response of 7 mm x 7 mm PIN test structure was measured as the area of individual strip and the 7mm x 7mm PIN test structure is nearly same. To evaluate the performance of the DSSD in terms of static characterization, a probe jig having two rows of spring loaded pins for simultaneous measurement of 64 strips of the detector was designed and fabricated. The I-V characteristics were used to verify the quality of the detector. Low leakage currents ascertain good quality of detectors and breakdown voltage gives upper limit on the operating voltage of detectors. The full depletion voltage for the detector which determines the operating voltage is estimated from the C-V data. The Same I-V and C-V setups as discussed in Chapter 3 with additional programmable multiplexer and probe jig were used for the static characterization. The instruments were interfaced through GPIB with the computer for automated measurement. The I-V setup is shown in the Figure 5.12

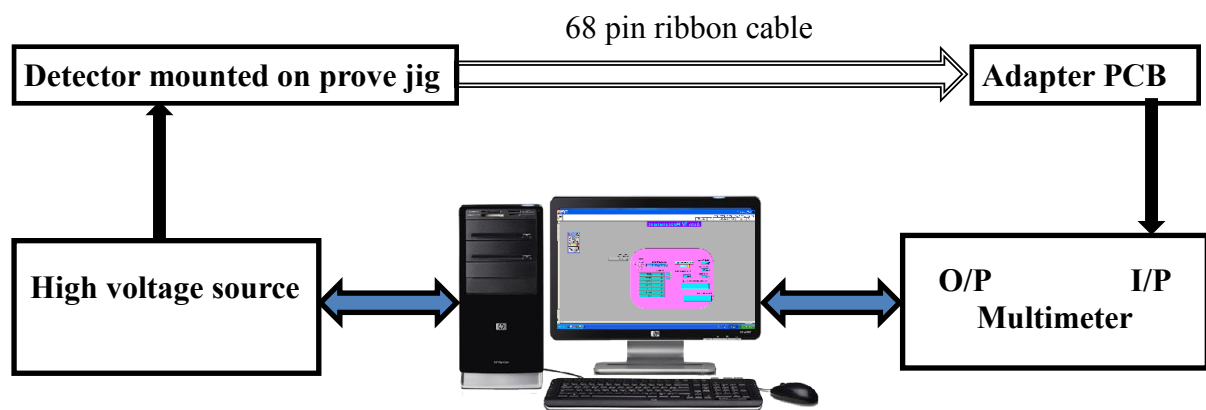


Figure 5.12. The block diagram of the electronic setup used to measure I-V characteristic.

First production batch of double sided silicon strip detector showed high leakage current per strip and several strips showed lower breakdown voltages as can be seen in Figure 5.13 and

Figure 5.14. After careful analysis of first batch results, optimization of process parameters was further carried out to realize the detectors with low leakage currents.

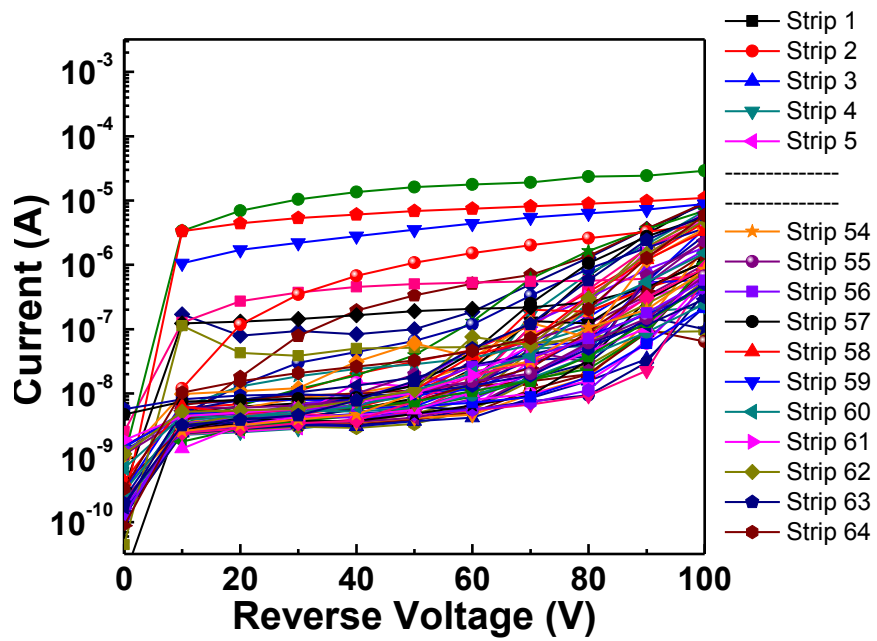


Figure 5.13. Leakage current variation of all 64 strips with reverse voltage for a detector from first batch. Different curves are showing leakage current variation of different strips.

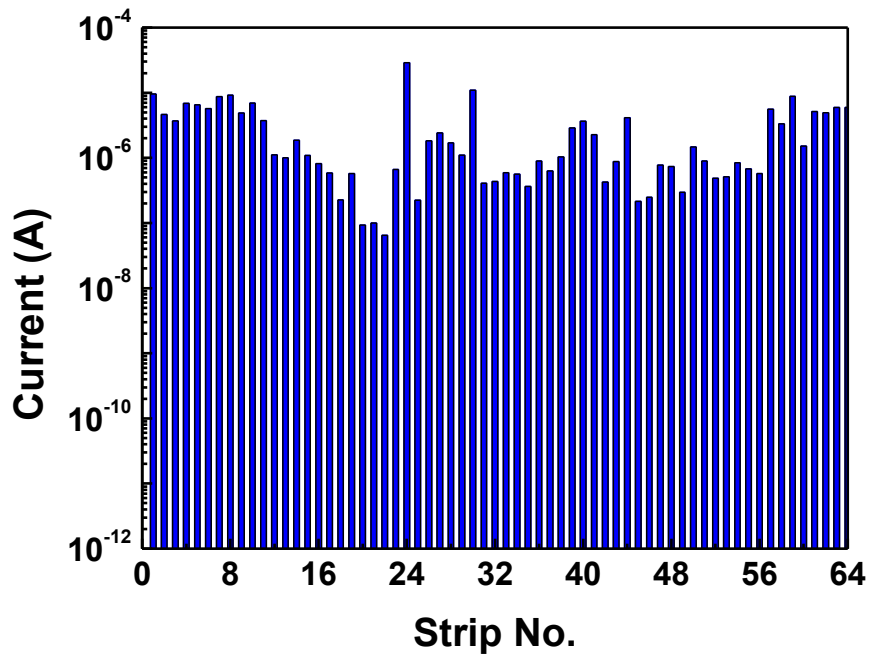


Figure 5.14. Leakage current variation of strips for a detector from first fabrication batch at 100 V reverse voltage.

The final fabrication batch, processed with optimized process parameters, show low leakage currents (less than 10 nA for each strips), higher breakdown voltages exceeding 100 V and better uniformity (Figure 5.15 and Figure 5.16). Baby strip test structure were also evaluated which showed low leakage currents and high breakdown voltages of about 150 V (Figure 5.18).

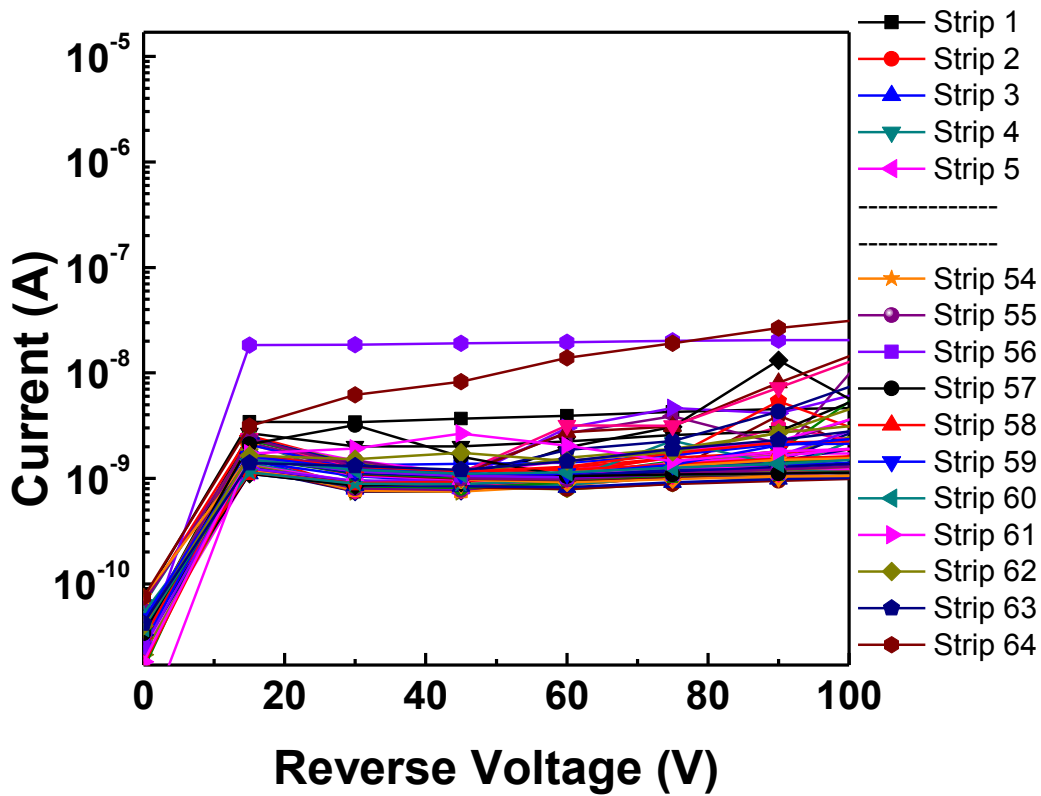


Figure 5.15. Leakage current variation of all 64 strips with reverse voltage for a detector from final fabrication batch. Different curves are showing leakage current variation of different strips.

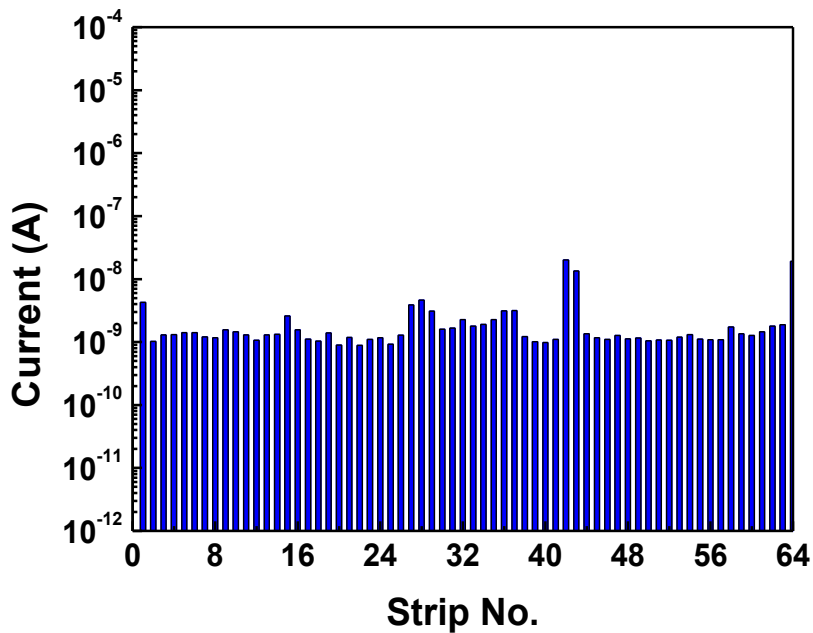


Figure 5.16. Leakage current variation of strips for a detector from final fabrication batch at 100 V reverse voltage.

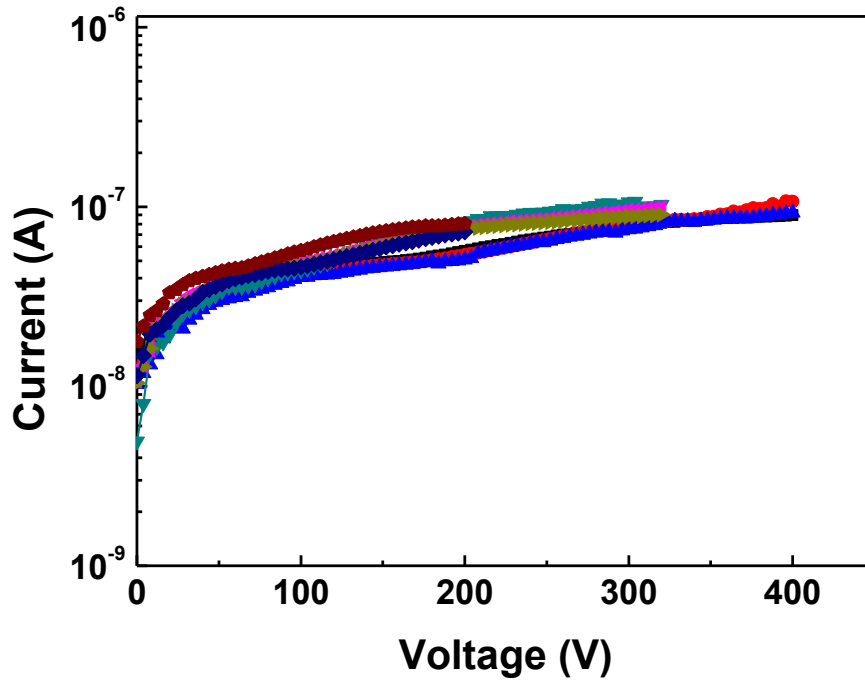


Figure 5.17. Leakage current variation of strips of a baby strip test structure from final fabrication batch.

The C-V characteristics of one of the strips and corresponding $1/C^2$ plot are shown in Figure 5.18. The full depletion voltage estimated from the $1/C^2$ plot is about 70 V. The capacitance measured for all P⁺ side strips of the detector for voltage range 0 to 100 V is as shown in Figure 5.19. The capacitances at 100 V for all the strips are shown in Figure 5.20. These measurements show that the capacitance of all the strips is varying uniformly with the applied reverse voltage. All the strips show uniform capacitance of ~ 23 pF at reverse voltage of 100 V. The I-V and C-V measurements show good uniformity over the area of the detector.

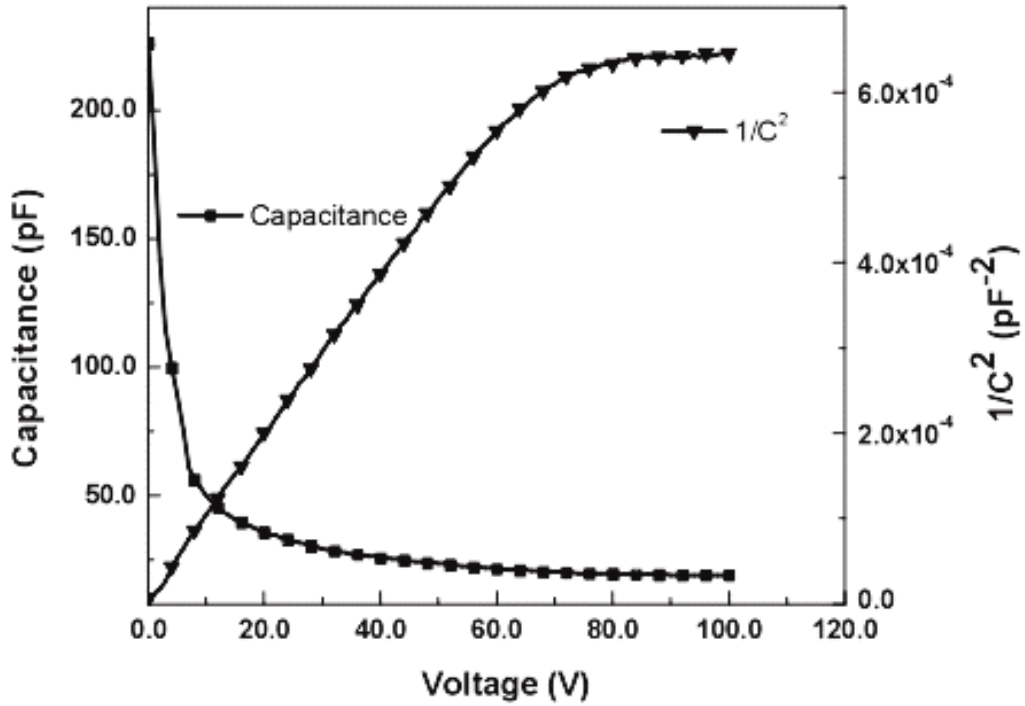


Figure 5.18. C-V and $1/C^2$ -V plots of a strip.

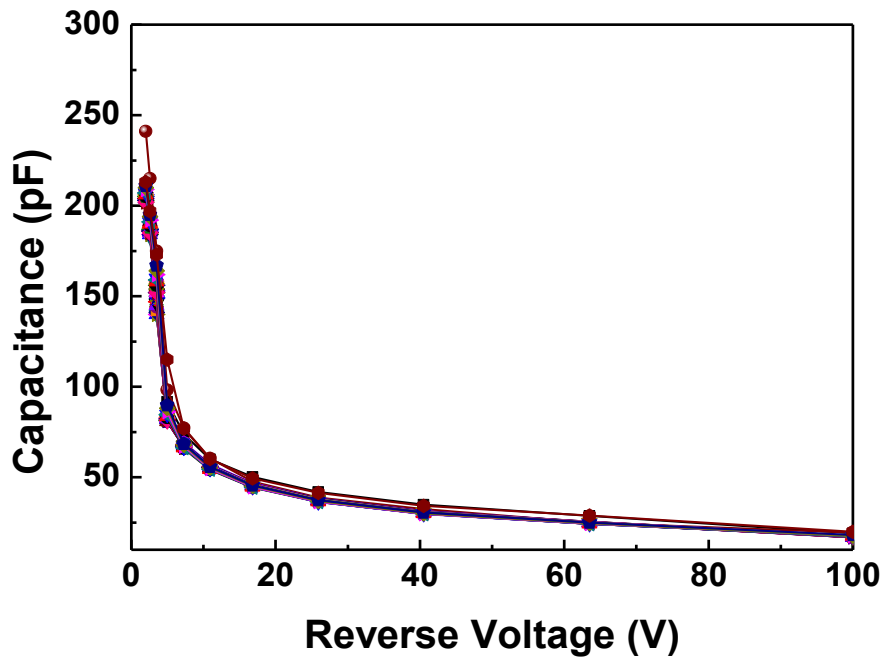


Figure 5.19. C-V characteristics of all 64 P^+ strips of a double-sided strip detector.

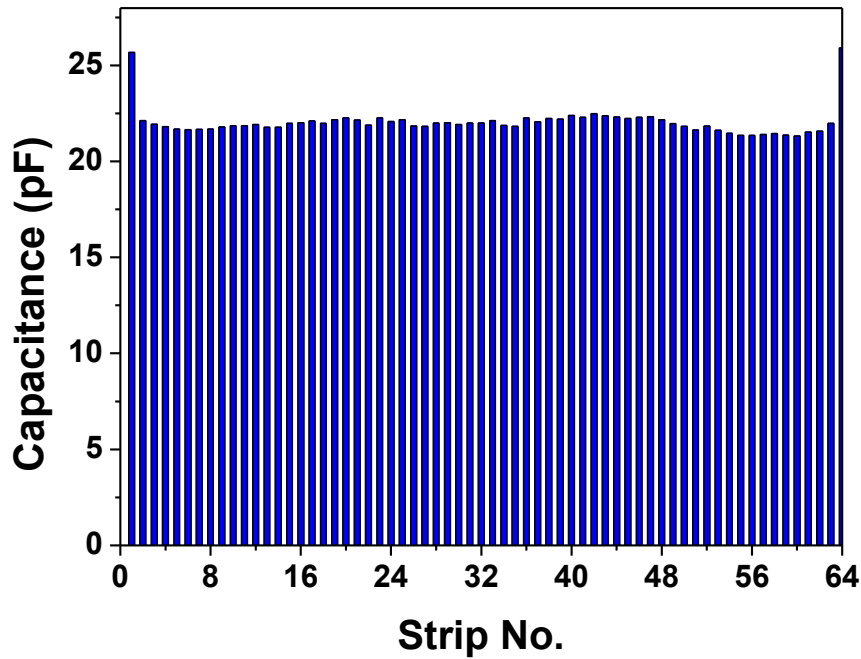


Figure 5.20. Variation of capacitance of P⁺ strips at 100 V reverse voltage.

5.4.3. Evaluation of detector performance by dynamic characterization

Initially, the energy resolution of the detector strips for charged particles was estimated from the alpha response of a PIN pad test structure of 7 mm × 7 mm geometry as measured from the P⁺ side (Figure 5.21) and N⁺ side (Figure 5.22) of the detector. For alpha response measurements, a mixed alpha source having ²³⁸Pu and ²³⁹Pu was used. The measurements were carried out in vacuum (~10⁻³ bar) using standard electronics comprising charge sensitive preamplifier (gain of 44 mV/MeV for silicon), spectroscopy amplifier (gain 50 and shaping time 2.0 μs) and a 4 K channel multichannel analyzer (MCA). As can be seen in Figure 5.21 and Figure 5.22, the pad detector is able to resolve the two alpha peaks of energies 5.156 MeV and 5.499 MeV. In the spectrum obtained from the P⁺ side, the satellite peak of ²³⁸Pu at 5.456 MeV is also clearly visible. The energy resolution obtained from the FWHM of the 5.499 MeV alpha peak is about 23 keV (0.42 %) when P⁺ side of the detector facing the source (P⁺ side

injection) and about 27 keV (0.50 %) when alpha N⁺ side of the detector facing the source (N⁺ side injection).

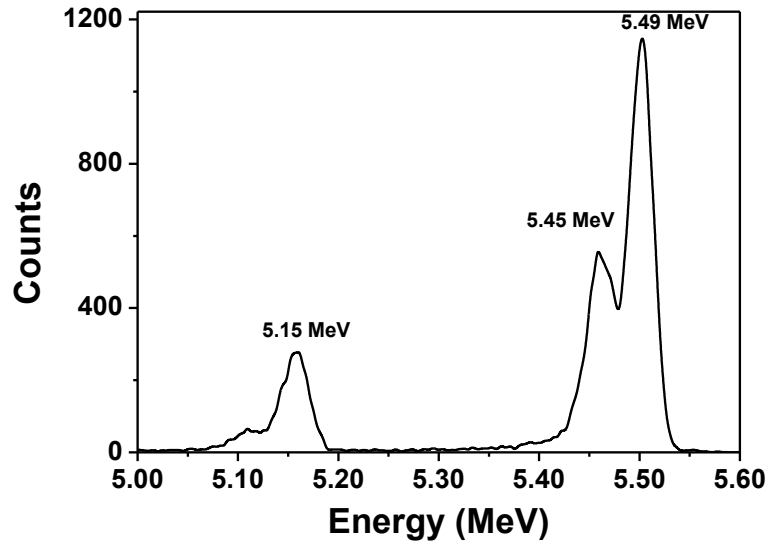


Figure 5.21. Alpha response of pad detector from the P⁺ side injection.

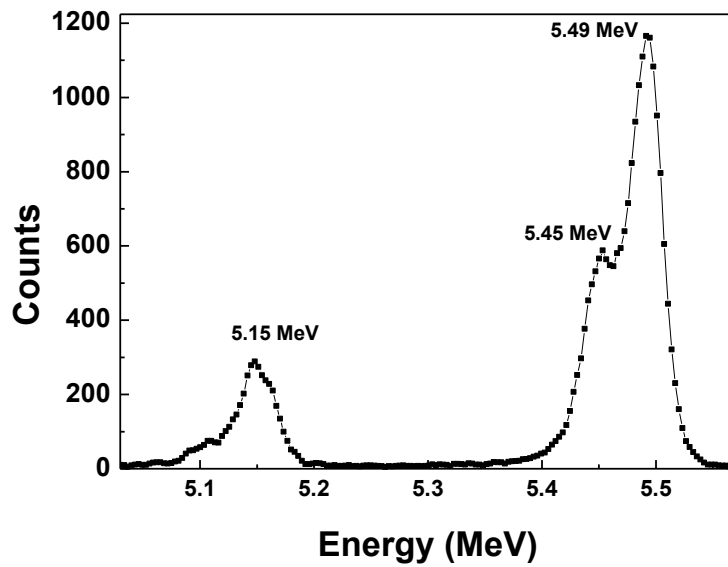


Figure 5.22. Alpha response of the pad detector from N⁺ side injection.

The broadening of the alpha peaks may be attributed to the energy loss straggling in the source and detector dead layer on the P⁺ side or the N⁺ side, not to the electronic noise. To obtain the contributions from the electronic noise, the spectrum was been recorded using a test pulse at the test input of charge sensitive preamplifier. The contribution of electronic noise to the observed FWHM (i.e. 23 keV) is quite small as an electronics noise less than 2 keV FWHM was measured with the test pulse. Since the PIN pad detector is fabricated on the same wafer as the strip detector and has almost the same area as that for P⁺ or N⁺ strips, the strips of the double sided detector were also expected to have similar energy resolution.

In order to verify the estimated energy resolution of the strips of the detector, the detector was characterized for the alpha particle response using Pelletron facility at TIFR, Mumbai. The measurements were carried out in collaboration with NPD, BARC. The detector was mounted in the scattering chamber at a suitable distance from the alpha source. Four multichannel charge sensitive preamplifiers and four multichannel amplifiers each with 16 channels were used to collect the signal from 64 P⁺ strips and another set (four charge sensitive preamplifiers and four amplifiers) were used to measure the signals from 64 N⁺ strips. The detector was placed to face the alpha source from P⁺ side (front side). A negative bias of 85 V was applied to P⁺ strips and back side (N⁺ strips) were grounded through 50 Ω terminator. Initially the detector response was studied for the performance of all strips using 128 channel readout system with ²³⁹Pu + ²⁴¹Am alpha source. The energy deposited by alpha particles in detector was measured in the form of voltage pulses at the amplifier output for each P⁺ and each N⁺ strip. This verified the proper functioning of each strip on the both side of the detector for the charged particles. Further, the output of the amplifiers was digitized using VME based ADCs and recorded in coincidence between front and back strips. All 128 strips were found to be detecting alpha particle. The gains of all the channels were matched by observing the pulse heights. The typical alpha spectra for P⁺ and N⁺ strips acquired using a ²⁴¹Am alpha source are shown in Figure

5.23 to Figure 5.26. The energy resolutions as obtained from the FWHM of Gaussian fitted alpha peaks were ~54 keV and ~58 keV, respectively for the P⁺ and N⁺ strips. The actual energy resolution obtained is found to be lower than the estimated resolution due to the charge collection length (strip length 6 cm) and the collection of charge from the interstrip gaps.

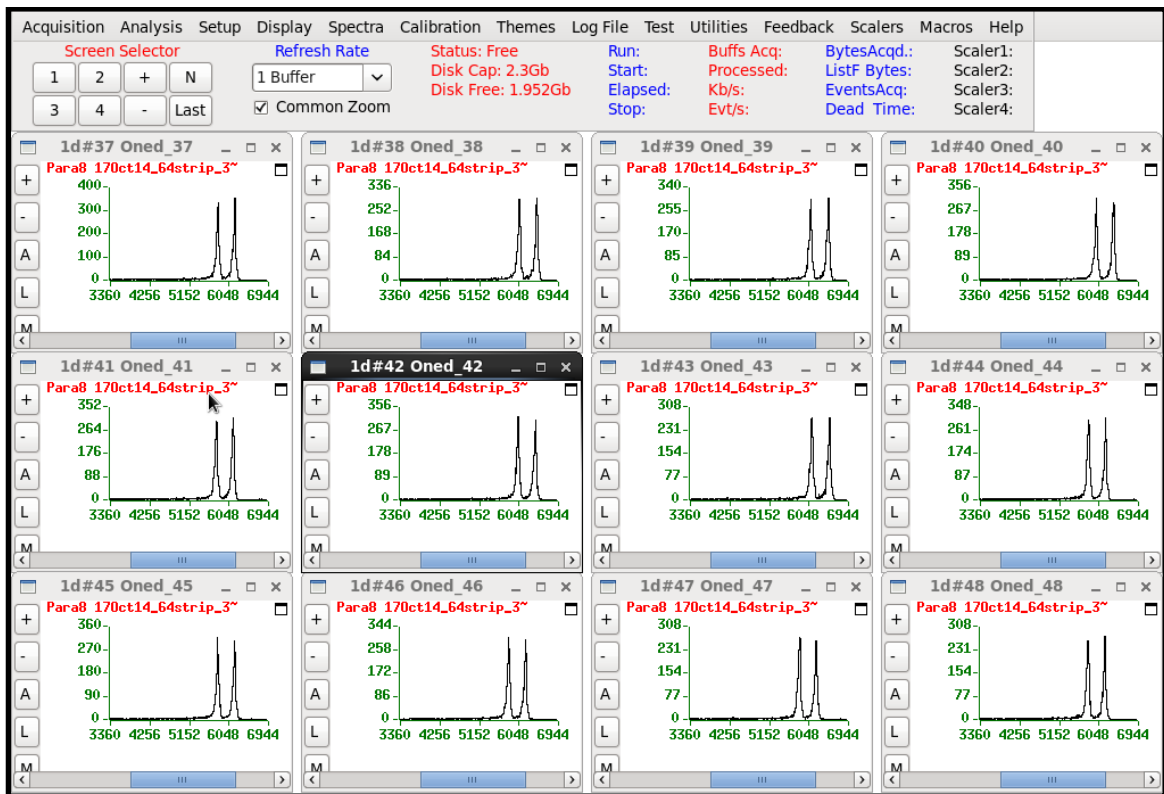


Figure 5.23. 1-D histograms of some of the P⁺ side strips showing alpha particle response.

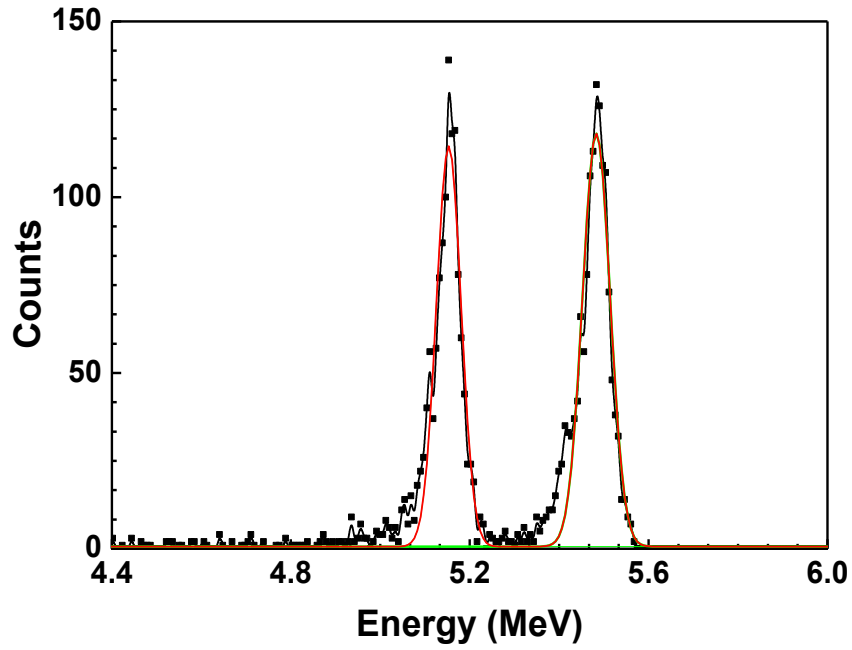


Figure 5.24. Alpha histogram of one of the P^+ strip fitted with a Gaussian function.

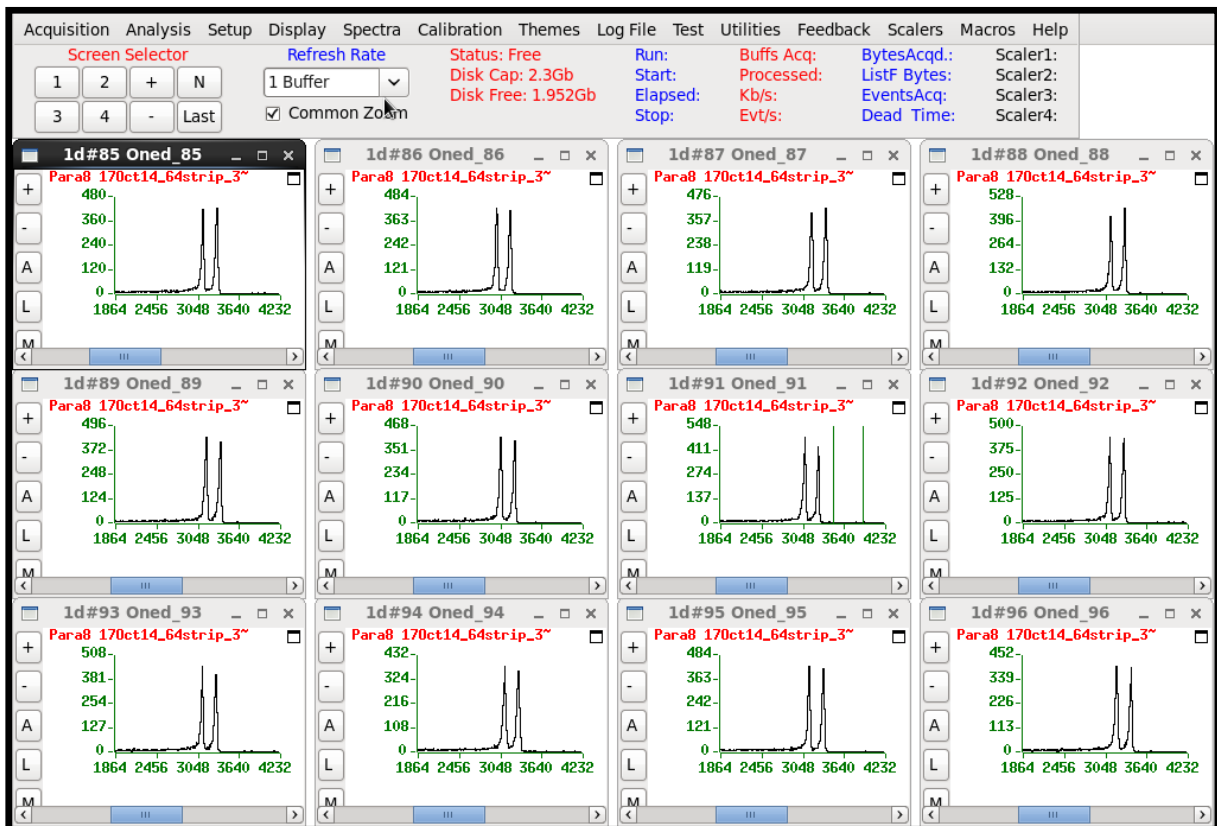


Figure 5.25. 1-D histogram of some of the N^+ side strips showing alpha particle response.

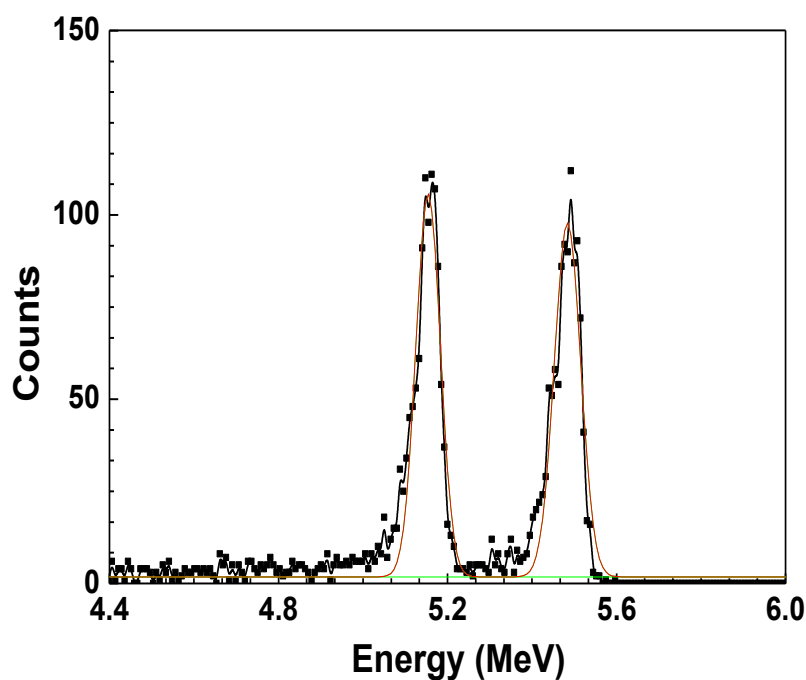
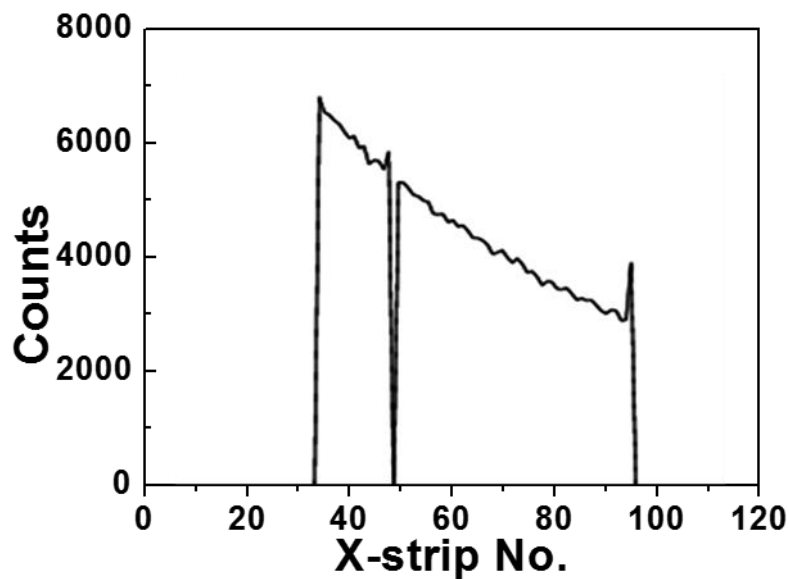


Figure 5.26. Alpha histogram of one of the N^+ strip, fitted with Gaussian function.

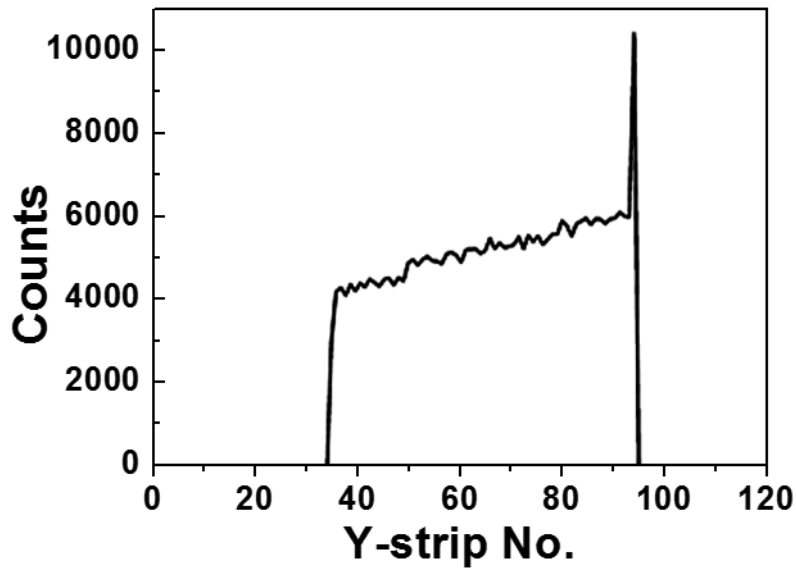
The back-injection performance study is also important as the detector is to be used in pulse shape discrimination mode (PSD). In PSD mode, this single detector can serve for position information, energy information as well as particle identification. The detector was rotated by 180° i.e. N^+ side facing the alpha source, to study the back-injection performance of the detector. No significant degradation in energy resolution was observed in these measurements.

The detector was further characterized in different particle beams with different targets to study the response of detector for a wide range of particles and energies. ^7Li on different targets (^{93}Nb and ^{197}Au) were used for the detector response study. The detector was placed in scattering chamber covering angles from 60° to 80° in forward direction of the beam. The biggest advantage was that the single detector was covering 20° angles at an optimum distance from the detector in a single run and hence the charge distribution evaluation and position evaluation were much simpler. The experiment was completed in two runs. In the first run, ^7Li beam of energy 30 MeV was impinged on Au target. Different contributions from elastic scattering of

^7Li , quasi elastic ^7Li , alpha, proton, deuteron and triton (due to break up of ^7Li) were recorded. Total 128 one dimensional spectra (Count vs. channel No.) corresponding to all 128 strips and two user defined plots (count vs. strip No.) were plotted by acquiring the signals. A monotonic decrease in counts was observed from strip 1 to 64 which was as per the expectation (i.e. approaching towards backward direction of the beam). Figure 5.27 shows the counts recorded in each strip of front side and back side, respectively when ^7Li beam of energy 30 MeV is incident on the gold target of thickness 500 mg/cm^2 and the detector is placed in the forward direction at an angle of 70° . The target was changed to ^{93}Nb and the contributions from ^7Li , ^6Li , alpha, proton, deuteron and triton were observed. The data analysis shows that all the strips are responding uniformly to all the reaction products obtained by different targets and beams.



(a)



(b)

Figure 5.27. The counts recorded in each strip of the detector from (a) front side and (b) back side, when ${}^7\text{Li}$ beam of energy 30 MeV is incident on the gold target of thickness 500 mg/cm^2 .

5.4.4. 2-D image and position resolution

To study the detector performance for position sensing, a mask (Figure 5.28) having nine holes each of diameter of 1cm were fabricated. This mask was placed on the front side of the detector and the detector was mounted in scattering chamber as shown in Figure 5.28. The signals from the detector were acquired and a 2-D plot was generated to construct the image of the mask. In the image, as expected 9 bright holes were observed corresponding to the alpha particles impinged on the detector through the holes in the mask (Figure 5.29).

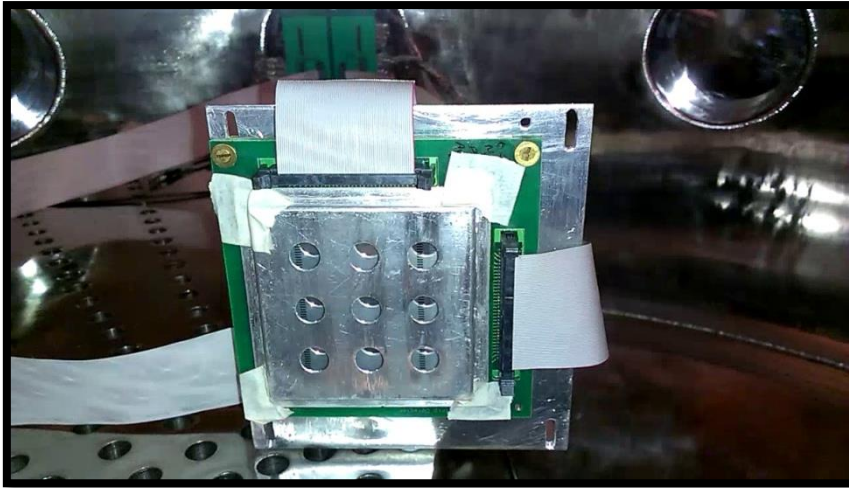


Figure 5.28. Detector with a mask having 9 circular holes mounted in scattering chamber.

Standard read out electronics as described in Section 5.4.3 was used for acquiring the data. The image of the mask was constructed by generating a 2-D plot. A few channels of read out electronics were not working. The mask image obtained verifies the 2-D imaging capability of the detector.

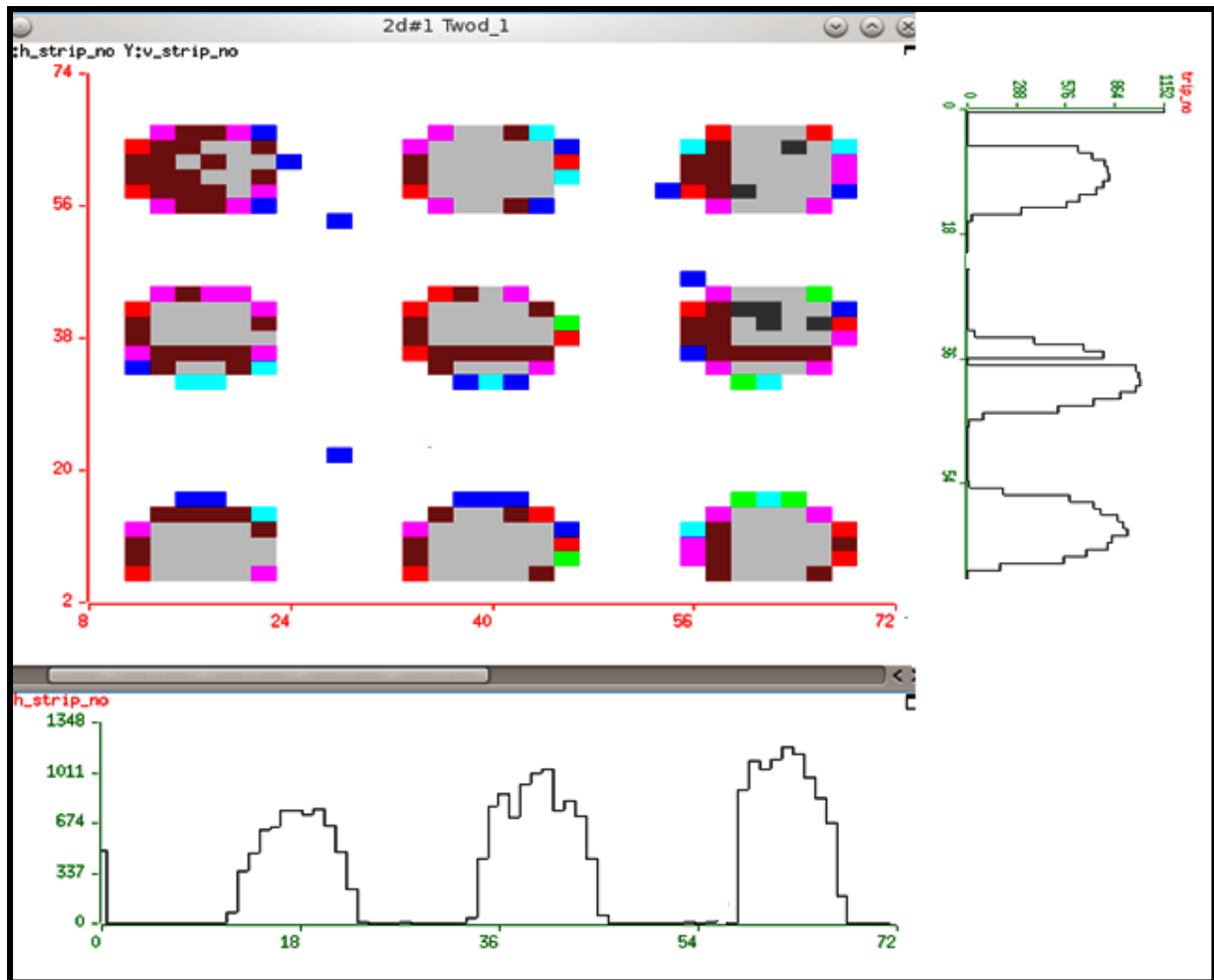


Figure 5.29. 2-D image of mask obtained by the detector.

The mask with 1 cm holes could not be used to obtain the accurate position resolution information of the detector. In order to obtain better position resolution information, a new mask was fabricated having a diagonal line opening of 1mm and holes of diameter of 0.7 mm with a gap of 1.5 mm as shown in Figure 5.30(a). The design of the mask was based on the geometrical parameters of the detectors. The detector with the mask was mounted in scattering chamber and interfaced with the readout electronics. 2-D position image of mask was obtained as shown in Figure 5.30(b).

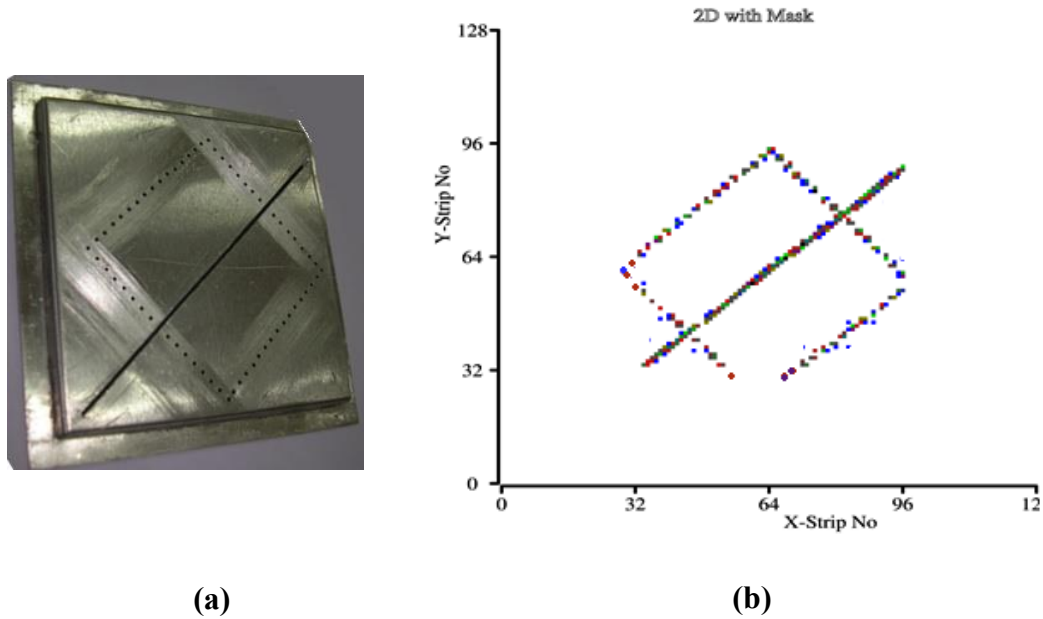


Figure 5.30. (a) The mask designed with a diagonal line opening of 1 mm and holes of diameter 0.7 mm with a gap of 1.5 mm and (b) corresponding image detected by the detector.

5.4.5. Inter-strip cross-talk measurement

The inter-strip cross talk was investigated using 70 MeV ${}^7\text{Li}$ beam incident on 500 mg/cm² thick ${}^{197}\text{Au}$ target. The spectrum was recorded by placing the DSSD at 70° in the forward direction. Figure 5.31 depicts the strip numbers (i, j), which have given coincident signals for two hit events. The diagonal box represents the events corresponding to the signals from adjacent strips (i, i+1). These events are about 8 % of the total events, which matches with the ratio of area of the inter-strip gap to the total active area, implying that these events are inter-strip events. The sum of all off-diagonal events (~500 counts) corresponds to random coincidences, well in agreement with the estimated random rate. It can therefore be concluded that there are almost no cross-talks present for the events, when particle is entering one of the strip. It should be emphasized here that the the meaning of not having inter-strip talk is that any particle incident with in the area of I strip does not create any charge by coupling on the adjacent strips such as i-2, i-1, i+1 or i+2 etc. However, for the particles hitting on the dead

layer between the strips can create charges those are shared by the nearby strips according to the distance of the point where the event took place to the strip. The 8% events as quoted in the text referred to those events occurring only in the dead area of the detector that are 8 %.

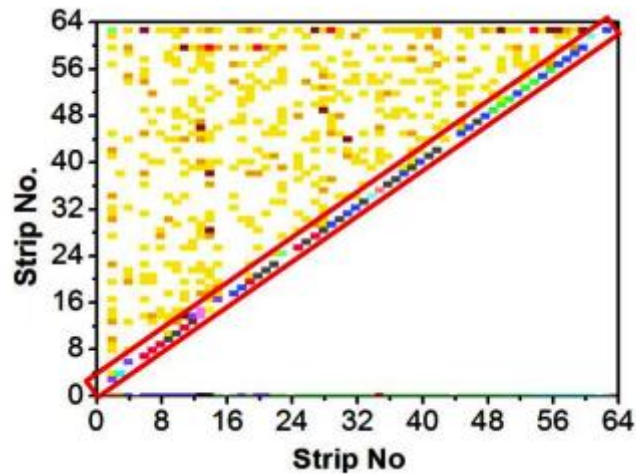


Figure 5.31. The two hit events showing hits in the neighbouring strips and random hits.

5.5. Conclusions

The double-sided strip detectors of geometry of 65 mm x 65 mm on standard wafers were developed. The characterization results show that the detectors have low strip leakage current (~ 10 nA/cm²) and good uniformity over the detector area of about 40 cm². The detector is shown to be able to identify as well as locate the incident particles with precise position sensing and without any inter-strip cross-talk. Development of DSSD has been mainly reported for high energy physics experiments. These detectors are different than the detectors developed in this thesis as these are microstrips with integrated resistors, coupling capacitors, etc. Most of the papers superficially give details of design and fabrication process as the actual process and design are not disclosed. Presently, only Micron Semiconductor, UK is supplying the DSSD which are used for nuclear physics experiments. However, when the work was initiated, the detectors available were 5 cm x 5 cm with only 16 strips on each side. Hence direct comparison

of the detectors could not be done but developed detectors have large size, higher number of strips and hence better position resolution than those available commercially.

Chapter 6

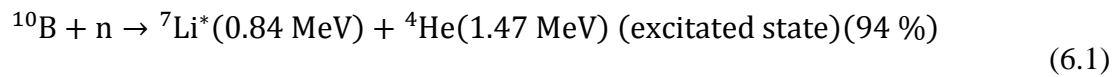
THIN EPITAXIAL SILICON PIN DETECTORS FOR THERMAL NEUTRON MEASUREMENTS WITH IMPROVED n/γ DISCRIMINATION

6.1. Introduction

Neutron detectors are widely used in various physics experiments ranging from studies of nuclear reaction to investigating lattice structure in condensed matter, and for monitoring neutron beams. These detectors also find applications in security applications for the detection of special nuclear materials (SNMs) for preventing proliferation and illegitimate trafficking. Traditionally, ^3He and BF_3 gas filled thermal neutron detectors are mostly used for such applications because of their high efficiencies, in spite of certain issues such as global shortage of ^3He , toxicity of BF_3 , portability, etc. Therefore, in the last decades, there is a significant interest in exploring suitable alternatives to these detectors. In this regard, semiconductor detectors have also attracted attention due to their several advantages, as discussed in Chapter 2.

Thermal neutron detectors developed using various high bandgap materials such as Si, GaN, GaAs, SiC and diamond have already been reported in the literature [69], [70], [108]–[112]. Silicon is the most preferred material due to the availability of high resistivity wafers at much lower costs as compared to other materials as well as established fabrication technology. The silicon based thermal neutron detectors in various configurations such as planar, hetero structure diodes, stacked and 3-D neutron detectors have been investigated earlier [67], [113]–[119]. It has been further shown that by stacking or in 3-D configurations, the neutron detection efficiencies can be improved [67], [117], [119].

As discussed in Chapter 2, neutrons being neutral particles do not cause direct ionization, rather their detection is only possible through nuclear reactions. Therefore, suitable converter materials are needed to generate charged particles through the interaction of thermal neutrons with the converter material. Materials having high neutron cross section such as Boron-10 (^{10}B), Lithium-6 (^6Li), Gadolinium-157 (^{157}Gd) are commonly used as neutron converters [116]. Among these, ^{10}B is the most common converter layer as it has high absorption cross section (3800 barn) for thermal neutrons and relatively high energies of reaction products as given below [120], [121]:



Since, most of the nuclear materials emit almost ten times more gamma rays compared to the neutrons, the gamma sensitivity becomes an important parameter for the neutron detection systems [121], [122]. The silicon detectors being sensitive to both kind of radiations (gamma rays and neutrons), the output signal carries counts from both of them and the resulting information may be misleading in terms of neutron counts. For reducing the signals from gamma rays, the detector operating parameters may be modified to suppress the gamma interaction with active material. The gamma rays interact with the detector material mainly by Compton scattering and/or photoelectric effect depending on the atomic number and thickness of the material (Section 2.2.2). For a standard silicon PIN detector, the detector medium is silicon and the standard thickness is in the range of 300 μm to 500 μm . One approach, to reduce the gamma interaction is by reducing the gamma energy deposition in the detector active volume. This can be done by minimizing the active thickness (depletion layer) by using a low reverse bias voltage. The other way can be setting the lower energy cut off for counting above

the gamma background. However, both of these methods may lead to the significant suppression of neutron counts. It is therefore desirable to design and optimize the detector parameters for reduced gamma sensitivity.

In this Chapter, a novel approach of using thin PIN detectors (thickness of 10-25 μm), for improving n/ γ sensitivity has been investigated. Compared to standard PIN detectors, such thin detectors have improved charge collection due to higher bulk electric fields for a given operating voltage. The detector design and fabrication process, characterization and results demonstrating reduced gamma sensitivity for thin detectors are discussed in this Chapter [42].

6.2. Experimental

6.2.1. Simulation study

The products particles (${}^7\text{Li}$ and 4He) from neutron reaction of neutron with ${}^{10}\text{B}$ have maximum energies of 1.02 MeV and 1.78 MeV for ${}^7\text{Li}$ and 4He respectively. SRIM (Stopping and Range of Ions in Matter) [123] calculations were performed to obtain an estimation of the suitable thickness of silicon to fully stop these charged particles in silicon. The calculated ranges of the ${}^7\text{Li}$ of energies 0.84 MeV and 1.02 MeV are 2.46 μm and 2.80 μm , respectively. For 4He of energies 1.47 MeV and 1.78 MeV, the ranges are 5.16 μm and 6.38 μm , respectively. Therefore, a range of 10–25 μm of detector thickness was chosen for simulation study with gamma radiation. A thick detector having standard thickness of 300 μm was also simulated for comparison. The energy deposited by gamma radiation for different thicknesses of silicon detectors were studied using FLUKA Monte Carlo simulation software. The thin detectors are expected to have much higher electric fields in the active volume (depletion region) compared to thick detectors. The electric fields for different thicknesses (10 μm , 15 μm , 25 μm and 300 μm) of detectors were simulated using a semiconductor process and device simulator. A two

dimensional PIN diode detector structure file was generated by providing the detector process flow as an input to the process simulator. The generated PIN structure file was imported to the device simulator and various device parameters such as potential distribution, electric fields, etc. were obtained. The other critical process parameters such as field oxide thickness, bulk wafer concentration, boron implantation energy and dose for creating the front P⁺ layer, phosphorus implantation energy and dose for creating the back N⁺ layer, etc., were kept same in all cases.

6.2.2. Fabrication of pin detectors

PIN detectors of active area 100 mm² and 50 mm² with thicknesses 10 μm, 15 μm, and 25 μm were fabricated using a custom process as described in Chapter 3. The high purity N type silicon wafers with orientation of <111>, 4" diameter, 300 μm ± 15% thickness and resistivity of 3-5 kΩ-cm were used as a starting material. The process parameters were optimized to fabricate detectors with low leakage currents. The process flow adopted for the fabrication of thin detectors is outlined below:

- (i) Starting N type wafer
- (ii) Field oxidation of 0.3 μm thickness
- (iii) Lithography for back N⁺ contact implantation
- (iv) Implantation of antimony for N⁺ contact
- (v) Epitaxial deposition of silicon for desired thickness (10 μm, 15 μm, 25 μm)
- (vi) Lithography for N⁺ plug (contact to buried layer from the top layer)
- (vii) Diffusion of phosphorus for N⁺ plug

(viii) Lithography for front P⁺ implant

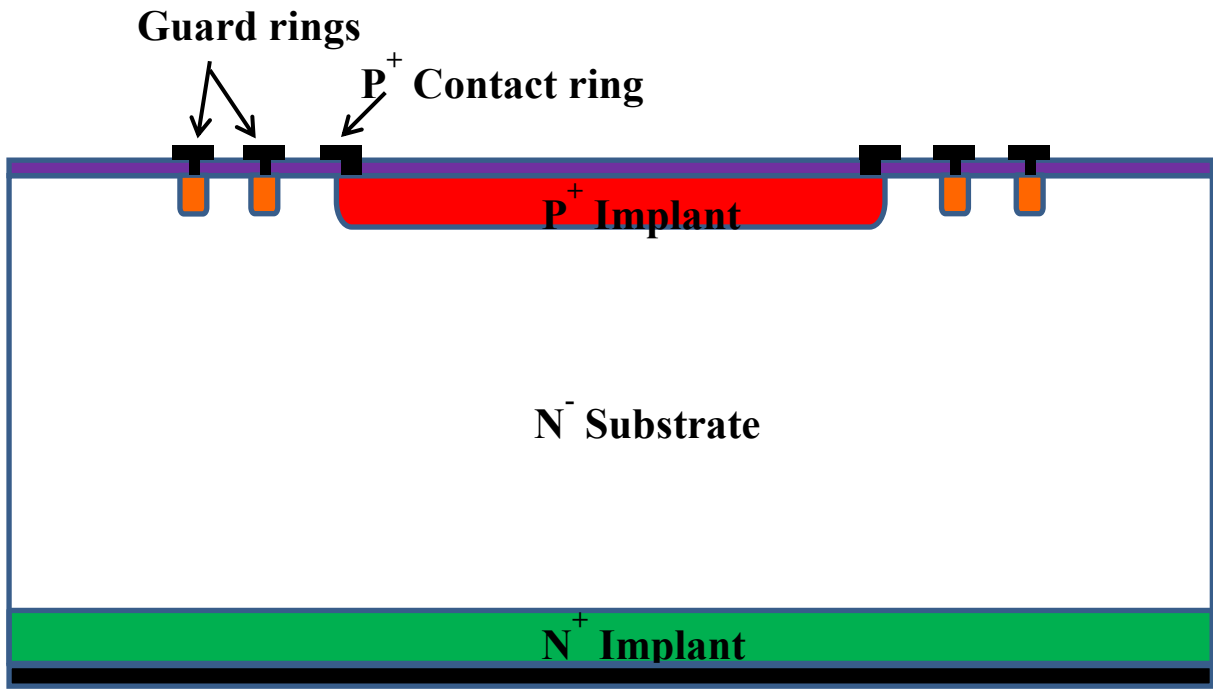
(xi) Boron implant for front P⁺, implant anneal and drive-in

(xii) Lithography for contacts to P⁺ and N⁺ layers

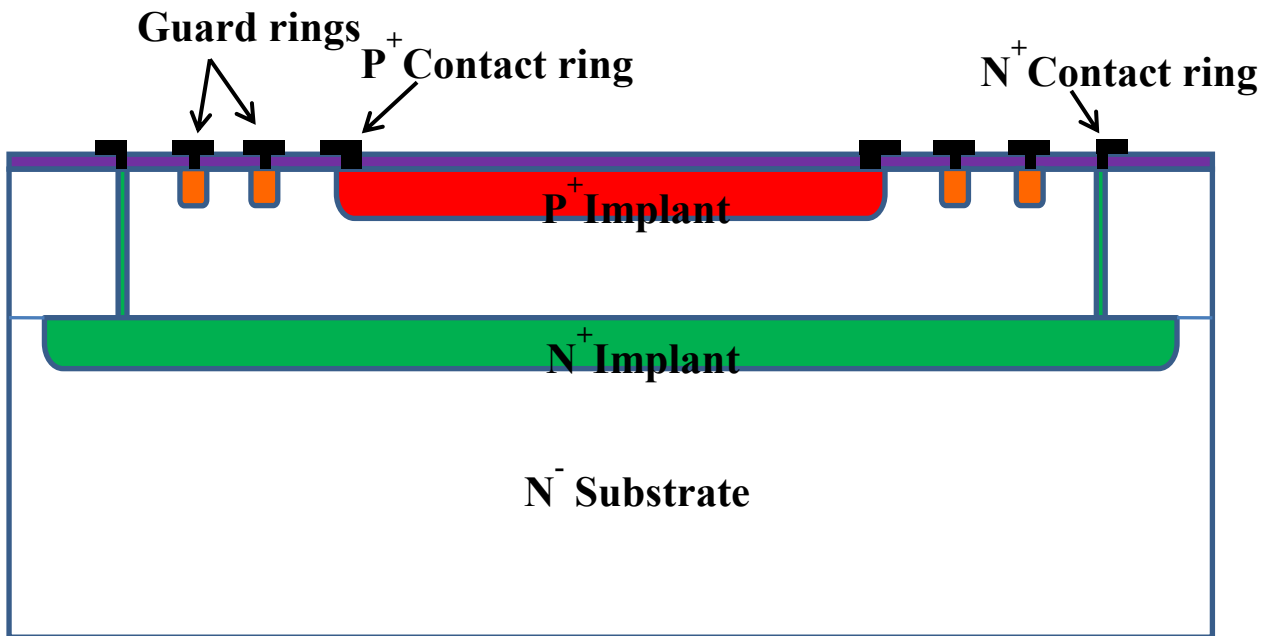
(xiii) Al metallization and lithography for metal

(xiv) Deposition of passivation layer of borophosphosilicate (BPSG) and lithography for opening bond pads.

The process steps from (iii) to (vii) (buried N⁺ contact, epitaxial layer and N⁺ plug) were not required for standard 300 μm thick detectors. Instead, a process involving implantation of phosphorus on the back side of wafer, implant anneal and drive-in was carried out. Al metal was deposited on the backside for realizing back side contact to the N⁺ layer while the front P⁺ and front side processes were same as steps (viii) to (xiv) listed above. From process simulation studies, the front P⁺ layer and the back N⁺ layer were expected to be about 0.75 μm and 2.0 μm respectively. However, these layers cause a decrease in the effective thickness of the detector where the deposited energy is measured only in the depletion layer. The schematics of the cross section of fabricated standard thick and thin PIN detectors are depicted in Figure 6.1 (a) and (b) respectively. After fabrication of wafer, dicing of wafers, die mounting and wire bonding were carried out.



(a)



(b)

Figure 6.1. Schematic cross section of fabricated detectors, (a) Standard thick PIN detector, (b) Thin PIN detector.

6.2.3. Characterization of pin detectors.

The detector leakage currents at different reverse bias voltage were measured using an automated setup having programmable picoammeter with an in built voltage source as described in Chapter 3. The response of detectors to charged particles was studied using a dual energy alpha source of $^{238+239}\text{Pu}$. The alpha response was measured by mounting the detector with an alpha source in a vacuum chamber at $\sim 10^{-3}$ bar. Standard electronics, as discussed in Chapter 3 comprising a charge sensitive preamplifier and a spectroscopy amplifier with a shaping time of 1.0 μs and a 4k channel multichannel analyzer (MCA) were used for obtaining alpha spectra. The response of detectors to gamma radiation was investigated using a ^{137}Cs gamma source of activity 33 μCi . Gamma measurements were carried out in air by enclosing the detector in an aluminum box for shielding against light and electronic noise. The electronics setup used for gamma spectrum was same as that used for alpha spectrum. The detector response to thermal neutrons was measured at multipurpose facility operating at Dhruva reactor (Chapter 3). An enriched ^{10}B film was placed over the detector at front surface to act as a converter layer for thermal neutrons.

6.3. Results and Discussion

6.3.1. Optimization of the parameters using simulation studies

Figure 6.2 shows the simulated gamma spectra (662 keV gamma radiation i.e. ^{137}Cs source) as a function of deposited energy in silicon for different detector thicknesses. For a detector thickness of 300 μm , the Compton edge and a photo peak are seen at about 550 keV and 662 keV respectively. The normalized counts (normalized by the total number of events) obtained from the simulation data are 3.8×10^{-5} , 6.4×10^{-5} , 1.3×10^{-4} , 1.3×10^{-3} , 3.0×10^{-3} and 6.0×10^{-3} for the detectors with thicknesses 10 μm , 15 μm , 25 μm , 100 μm , 200 μm and 300 respectively.

As expected, the gamma energy deposition and hence the total counts decrease with decreasing the thickness, suggesting that the detector (active volume) thickness can be used as tunable parameter to suppress gamma deposition.

The depletion width (d) can be calculated following one sided abrupt junction approximation (Section 3.2.4) which assumes that the concentration of P^+ region is much higher than the N bulk concentration, and neglects the barrier voltage. This yields the following relation (Section 3.2.1):

$$d = \left(\frac{2\varepsilon V}{eN} \right)^{1/2} \quad (6.3)$$

where, ε denotes the permittivity for silicon, V is the applied reverse bias voltage, e is electronic charge and N is the donor concentration in the bulk region. It can be seen from the equation that reverse bias voltage applied to the detector can be used to tune the depletion layer width. For a standard PIN detector operating at a low operating bias of 5 V, the depletion width thus reduces significantly compared to that at a higher operating bias voltage. Moreover, the width of this depletion layer depends on the resistivity of the intrinsic (I) region i.e. substrate wafer resistivity. Even if the depletion layer width is reduced to 100 μm by operating at a low reverse bias voltage, the gamma sensitivity is significant (Figure 6.2). In contrast, a substantial reduction in the gamma sensitivity of the silicon detector is seen for the detectors having thickness of 10–25 μm . This suggests that the gamma sensitivity of detectors can be simply reduced by decreasing the depletion width but this should not lead to a consequent reduction in a major portion of the neutron counts. Therefore, the depletion layer width needs to be adequate for deposition of substantial portion of the energy of charged particles generated by interaction of neutrons with the converter material.

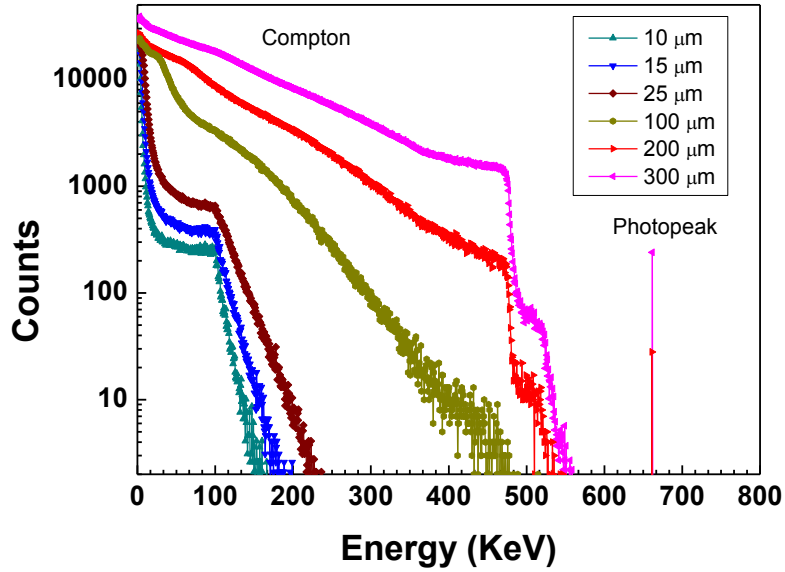


Figure 6.2. Simulated gamma spectra for silicon detectors with different thicknesses.

The semiconductor process and device simulations were further carried out in order to estimate electric fields and depletion widths at lower operating voltages for a standard 300 μm thick detector and for thin detectors. A fabrication process sequence similar to that described in Section 6.2.2 was generated for realizing the two-dimensional (2-D) cross section of the detector by device process simulator. The concentration of N type wafer of $10^{12}/\text{cm}^3$ was used for the simulation. The device structure generated through the process simulation was fed to the device simulator to obtain various parameters such as potential distribution, electric field profile, depletion width, etc. The front P^+ and backside N^+ concentration profiles were kept the same for all detectors irrespective of the thickness. The obtained electric field profiles along the depth of the detector for different thicknesses are compared in Figure 6.3. The results show that the bulk electric field increases with the reduction in the thickness of the detector which might result in an improved charge collection in thin detectors compared to thicker detectors.

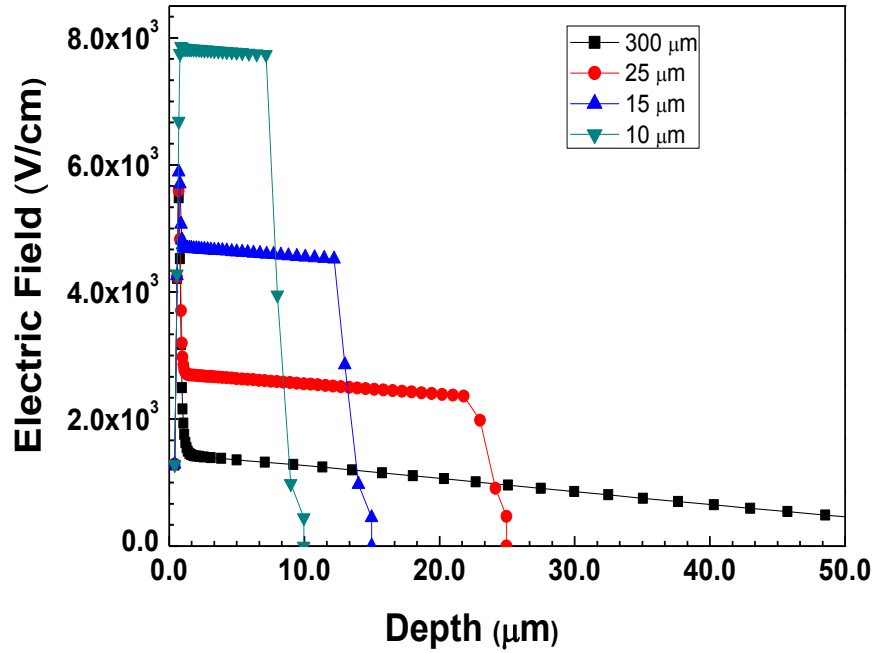


Figure 6.3. Electric field variation along the depth of a silicon PIN detector at a 5 V reverse bias for different detector thicknesses.

The depletion layer width at 5 V is about 75 μm for a 300 μm thick detector, while the thin detectors with thickness of 10 μm , 15 μm and 25 μm are fully depleted at this voltage. This suggests that the choice of operating voltage of 5 V can ensure that the depletion layer width is sufficient for full energy deposition of charged particles released by neutron interaction with ^{10}B converter. Overall, following inferences could be drawn from these simulation studies: (i) The gamma sensitivity can be significantly reduced by decreasing the thickness of the detector, (ii) Even if the detectors are operated at a lower operating voltage of about 5 V, the depletion layer width would be suitable for full energy deposition of neutron reaction products.

6.3.2. Static characterization

Based on conclusions of simulation studies, the thin epitaxial silicon detectors were fabricated and characterized. As a first step, the detectors (thicknesses 10 μm , 15 μm , 25 μm and 300 μm) were examined for current vs voltage (I–V) and capacitance vs voltage (C–V) characteristics.

Typical leakage current and capacitance characteristics at various reverse bias voltages measured for a detector of thickness of 25 μm are depicted in Figure 6.4.

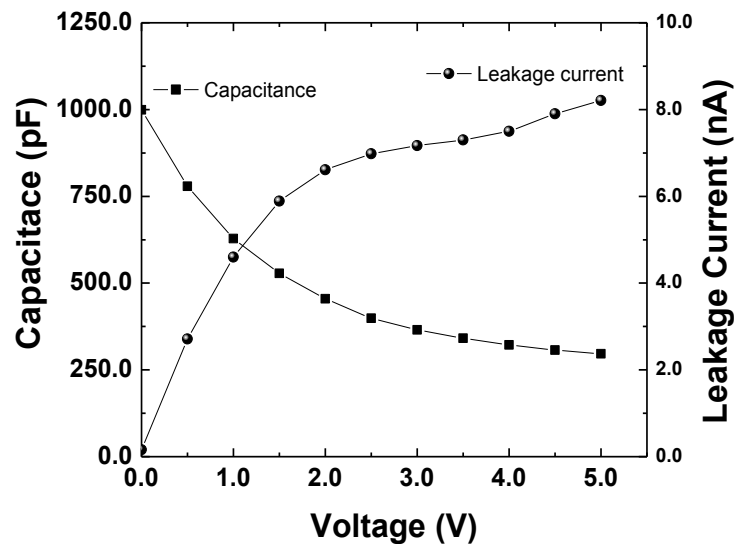


Figure 6.4. Typical I–V and C–V characteristics of a thin PIN detector with thickness of 25 μm , detector area of 50 mm^2 .

The detector is found to have low reverse leakage currents of a few nano-amperes and standard C–V characteristics. As expected, the capacitance of the detector decreases on increasing reverse bias voltage because of the increase in the depletion layer width. The detectors with thicknesses of 15 μm and 10 μm are also found showing similar characteristics with the leakage currents in the range of a few nano-amperes, but the capacitances of these detectors are higher compared to a 25 μm thick detector as they have lower depletion layer widths. It may be mentioned here that though the physical thickness of the detectors is in the range of 10–25 μm , but the actual effective thickness is lower due to the presence of a heavily doped P⁺ and N⁺ regions in the front side and back side, respectively. The I–V and C–V characteristics of thick detector (300 μm) are depicted in Figure 6.5. This detector also shows low leakage currents and full depletion at about ~ 60 V. Considering the fact that thinner detectors have lower active volume, the leakage currents in thin detectors are higher compared to a standard detector of the

thickness of 300 μm . The bulk of the thin detector consists of epitaxial layer whereas that of the standard thick detector is the high purity wafer. Further, epitaxial thin detectors were also subjected to a more complex processing sequence unlike that adapted to the thick detector. The higher leakage current in thin detectors may be attributed to these reasons.

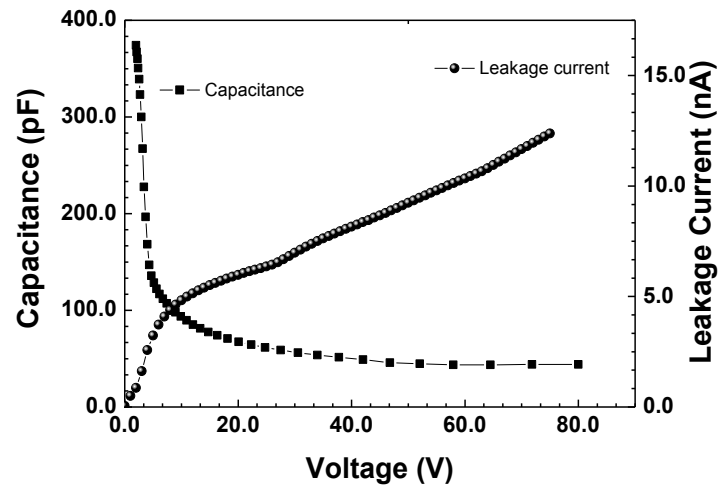


Figure 6.5. Typical I–V and C–V characteristics of a standard PIN detector with thickness of 300 μm , detector area of 100 mm^2 .

6.3.3. Response of the detectors to the charged particles.

The response of thin detectors to charged particles has been examined by recording the alpha spectra from dual energy alpha source and is presented in Figure 6.6.

The bias voltage for thin detectors was 5 V while for thick detector (300 μm) was 60 V (full depletion voltage). The 300 μm thick detector was not only able to resolve the two main peaks of ^{238}Pu (5.499 MeV) and ^{239}Pu (5.156 MeV) but also the satellite peak at 5.456 MeV for ^{238}Pu was resolved. The 25 μm thick detector also has resolved the two peaks corresponding to 5.499 MeV and 5.156 MeV alpha particles, but detectors of smaller thickness (10 and 15 μm) could not do so, in spite of the large difference (343 keV) in the source alpha energies i.e. 5.156 MeV and 5.499 MeV (Figure 6.6). This indicates that the thicknesses of 10 μm and 15 μm are

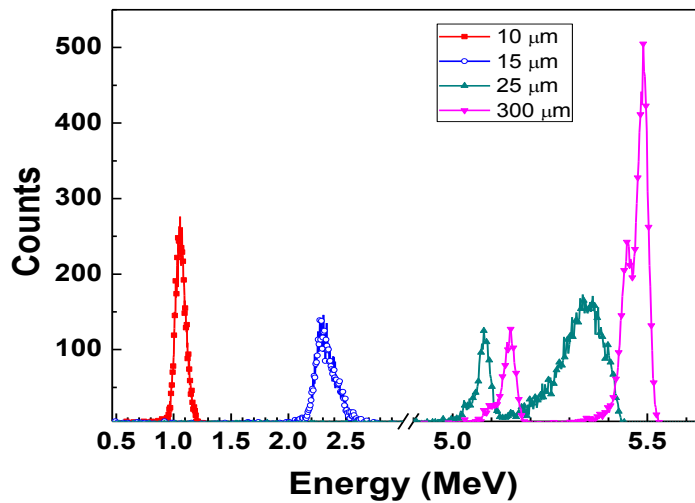


Figure 6.6. Alpha spectra obtained using a dual alpha source ($^{238+239}\text{Pu}$) for PIN detectors of different thicknesses. Thin detectors were biased at 5 V and 300 μm thick detector was biased at 60 V.

not sufficient to fully stop all the alphas. It may further be noted that the 25 μm thin detector has inferior energy resolution compared to the 300 μm thick detector probably because of increased electronic noise due to larger capacitance of the detector. Moreover, the thickness of the detector i.e. 25 μm is close to the thickness required for full energy deposition of 5.499 MeV alpha particles. This could increase energy straggling in the deposited energy causing degradation of the energy resolution.

6.3.4. Gamma sensitivity of the detectors.

It was observed in the simulation results that the gamma sensitivity could be significantly reduced in thin PIN detectors (one to two orders lower). In order to experimentally verify this, the gamma spectra of the different thickness detectors were obtained with a $33\mu\text{Ci}$, 662 keV, ^{137}Cs source (Figure 6.7). The spectra with ^{137}Cs are continuous without showing a photopeak as these are dominated by energy deposition due to Compton scattering in silicon and are also affected by detector noise. Due to low atomic number of silicon, at 662 keV energy, the average

energy deposition in a 300 μm thick silicon layer is a few percent of full energy of 662 keV and is much reduced for the thin detectors.

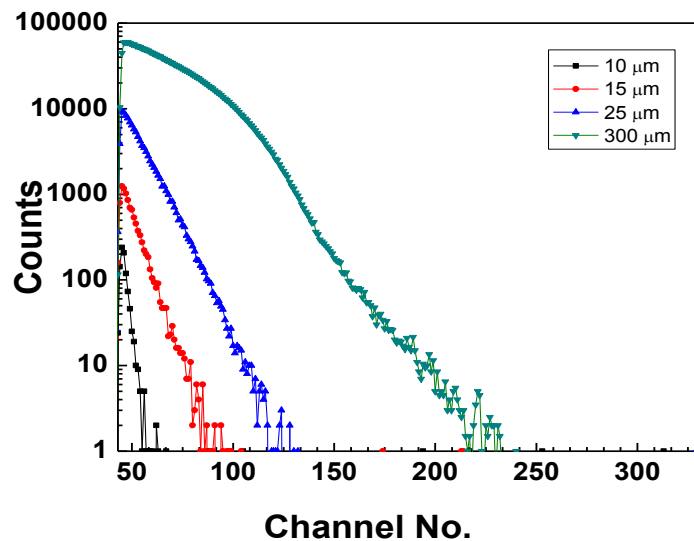


Figure 6.7. Gamma spectra obtained with a ^{137}Cs source for PIN detectors of different thicknesses. All detectors were operated at 5 V bias voltage.

The calibration of the channel numbers in the spectra with respect to the energy could not be carried out using an alpha source because of the fact that the alpha and the gamma radiation deposit significantly different amount of energy in the detector dead layers. The energy calibration using a low energy gamma source such as 60 keV ^{241}Am could also not be done. A clear photo peak separated from the Compton edge could not be observed for the detectors as the total electronic noise was comparable with the deposited energy by 60 keV gamma radiations.

In agreement with the theoretical expectations, the gamma sensitivity of the detectors is observed to be decreasing with the reduction in the detector thickness (Figure 6.7). The count rates calculated from the gamma spectrum for each type of detector are listed in Table 6.1. Since the area (50 mm^2) of the thin detectors is half of that for thick detectors (100 mm^2), therefore, in Table 6.1, the counts for the thick detector are scaled to half of the actual counts

for the comparison of count rates. As can be seen in the figure as well as in table, the gamma count rates for the 10 μm , 15 μm and 25 μm thick detectors are decreased by factors of 1874, 187 and 18 respectively with respect to the gamma count rate of a 300 μm thick detector. Results obtained for 25 μm and 300 μm thick detectors are closely following the trend obtained in simulation data (normalized counts). but the detectors with the thicknesses 10 and 15 μm showing lower count rates which is obvious as the same LLD of 25 channels could not be used for the detectors with thicknesses 10 μm and 15 μm due to the high electronic noise of these detectors. These results demonstrate that the gamma response of the PIN detector could be significantly suppressed by decreasing the thickness of the detector.

Table 6.1. Count rate obtained with a ^{137}Cs gamma source for detectors of different thicknesses

S. No	Thickness of the detector	Counts per second (cps)
1	10 μm	0.3
2	15 μm	3
3	25 μm	30
4	300 μm	562 (obtained by scaling to half of actual counts)

6.3.5. Thermal neutron response of the detectors

In order to examine the other important criteria i.e. low detector thickness should not adversely affect the thermal neutron counts, the detectors were further characterized using a thermal neutron beam at the Guide Tube Laboratory, Dhruva reactor at BARC. The neutron beam of diameter 30 mm, wavelength higher than 4 \AA , mean energy less than 5.1 meV has been made incident on the detectors. The available neutron flux was 5×10^6 n/cm²/s with a gamma

background of about 1 R/h at 90 MW thermal power of Dhruva reactor. The detectors were housed in an aluminium box while measurements, for shielding against light and electronic noise. Since the detector thicknesses of 10 μm and 15 μm were very close, the detectors having thicknesses of 10 μm and 25 μm were investigated for the thermal neutron response.

The neutron spectra were obtained in three conditions: (i) with Cd filter where no neutron beam falls on detector and only gamma detected, (ii) without any Cd filter and ^{10}B neutron converter layer, and (iii) then, subsequently, with an enriched ^{10}B films placed over the detectors and no Cd filter. The acquired spectra are plotted as shown in Figure 6.8, Figure 6.9, and Figure 6.10. The spectra are plotted in terms of counts vs channel numbers, because of the difficulties in the energy calibration of channel numbers for gamma and alpha particles as discussed earlier. Since the aim of the work was counting of thermal neutrons, the spectra plotted in this manner could be very well analyzed to compare for count rates for thermal neutrons.

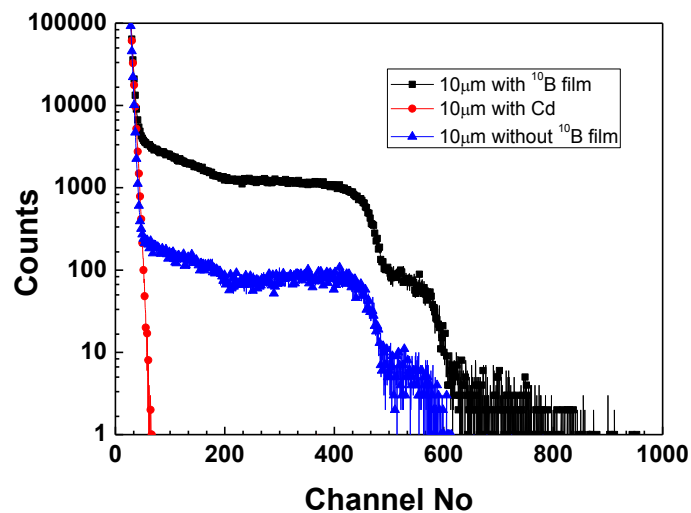


Figure 6.8. Spectra obtained with a thermal neutron beam using a 10 μm thick detector showing response (i) without a ^{10}B film, (ii) with a Cd filter, and (iii) with a ^{10}B film.

The spectra demonstrate detector response due to gamma and due to light charged particles i.e. alpha and ^7Li , released during interaction of neutrons with ^{10}B . Even in the absence of ^{10}B

neutron converter layer, all the detectors exhibit spectra, which have similar characteristics with that observed for a ^{10}B converter, however with lower count rate.

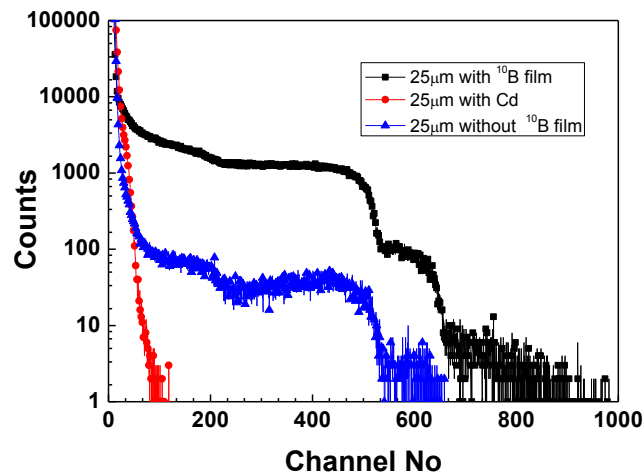


Figure 6.9. Spectra obtained with a thermal neutron beam using a 25 μm thick detector showing response (i) without a ^{10}B film, (ii) with a Cd filter and (iii) with a ^{10}B film.

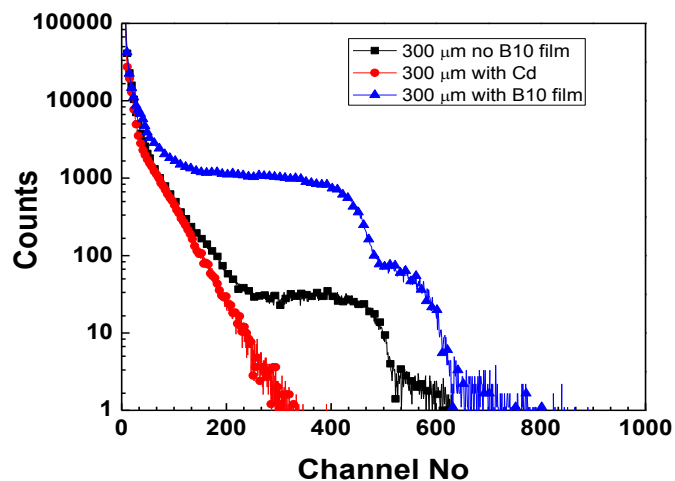


Figure 6.10. Spectra obtained with a thermal neutron beam using a 300 μm thick detector showing response (i) without a ^{10}B film, (ii) with a Cd filter and (iii) with a ^{10}B film.

The detectors were fabricated with a P^+ boron doped layer and a top BPSG passivation layer. Both these layers are expected to have about 18% of ^{10}B as available in natural boron i.e. 11B. Also, the silicon wafer used could have some boron content. Hence, the ^{10}B incorporated in

these layers is expected to give some neutron response. In order to verify this hypothesis, the measurements were recorded with a Cd filter, which significantly reduces the thermal neutron flux. This results in a significant change in the nature of the spectra where the pulses seen at higher channel numbers disappears for all detectors. These measurements therefore confirm that the thermal neutron response without external ^{10}B films emerges due to the presence of ^{10}B in various layers comprising the detector, consistent to the observations reported by others [124]. The actual doping concentration of boron doped P^+ layer and BPSG layer were neither experimentally measured, nor the actual composition of the film was known. Therefore, the quantitative analysis of thermal neutron response due to the boron doped layers in the detector could not be carried out.

The total counts in case of without an external ^{10}B include the counts due to both, the thermal neutrons interacting with internal ^{10}B as well as the gamma. An estimate of gamma sensitivity could be obtained if we consider the counts only with the Cd filter as this filter strongly absorbs thermal neutrons. The noise of 10 μm thick detector was higher i.e. up to about 50 channel numbers. The electronic noises for the 25 μm and 300 μm thick detectors were comparable i.e. up to 25 channel numbers. Considering the lower level discriminator (LLD) of 50 channels for the 10 μm thick detector and 25 channels for the 25 μm and 300 μm thick detectors, the count rates obtained with the Cd filter were 4 cps, 50 cps and 1100 cps for detectors of thicknesses of 10 μm , 25 μm and 300 μm respectively. Consistent to the simulation results, the gamma sensitivity for 10 μm thick detector is found to be negligible and the gamma related pulses are mostly below the electronic noise level (Figure 6.8). The gamma sensitivity of 25 μm thick detector is reduced by a factor of about 20 compared to the 300 μm thick detector.

The spectra obtained with the ^{10}B converter for all the three detectors show similar nature and profile and also same as those were reported for standard silicon detectors, earlier [125]. The

spectra obtained without a ^{10}B converter also have similar shape, but lower counts. The contributions in the overall thermal neutron spectra can be divided in three parts; (i) the counts from the background gamma and 0.84 MeV ^7Li (equation (6.1)), (ii) the counts are mainly from the 1.47 MeV ^4He (equation (6.1)) and (iii) the counts are mainly because of 1.78 MeV ^4He (equation (6.1)). It is further observed that the spectrum for a 300 μm standard detector is shifted slightly towards lower energy side i.e. by 25 channels as compared to the spectrum of a 25 μm thick detector. This could be because of the low electric field in the thicker detector (300 μm) compare to a 25 μm thick detector, as shown in Figure 6.3, resulting in lower charge collection in the thick detector. However, the spectrum of 10 μm thick detector is shifted by about 50 channels to the lower energy side compared to the spectrum of 25 μm thick detector in spite of higher electric field in the former. The possible reason for this could be much larger capacitance of 10 μm detector, the actual current through the feedback capacitor of front-end charge sensitive amplifier is reduced, causing lower pulse height. It may be added here that since, the both detectors were fabricated using the same process for P^+ implantation, front metallization, etc., the front side dead layer is the same for both detectors. The thin detectors were fabricated with a buried N^+ contact created with doping of antimony atoms. Subsequent epitaxial process of deposition of silicon layer is done at high temperature exceeding 1100 $^\circ\text{C}$. This would result in the out-diffusion of antimony into the epitaxial layer resulting in a tail of N^+ region in the thin detectors. This tail region would be significant for the 10 μm thick detector compared to the 25 μm thick detector when normalized to their respective total thicknesses. This leads to the alteration of actual electric field profile in the bulk of the detector. Nevertheless, the causes for the shift of the spectrum to the lower energy side for 10 μm thick detector need further investigation. A comparison of the count rate for detectors with different thicknesses measured with and without ^{10}B film is presented in Figure 6.11.

The count rates in the presence of ^{10}B converter were observed as 1466 cps, 3170 cps and 2980 cps for the detectors of thicknesses of 10 μm , 25 μm and 300 μm respectively. It should be also mentioned here that the total counts for the 300 μm thick detector include a significant portion of counts due to gamma radiation in addition to counts due to thermal neutrons. With respect to the count rate with the ^{10}B converter, the percentage of count rate without a ^{10}B converter is about 4%, 7% and 35% for the detectors of thickness of 10 μm , 25 μm and 300 μm respectively. These count rates are related to the detector response due to the ^{10}B present in the detectors and due to gamma related counts.

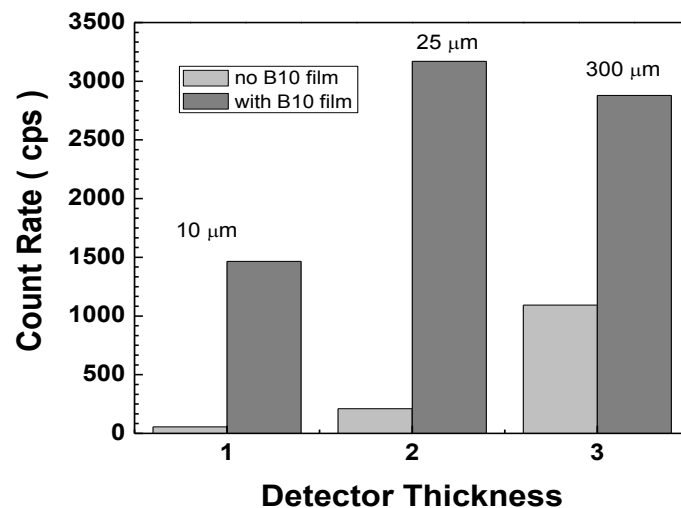


Figure 6.11 Comparison of count rates obtained with or without a ^{10}B film for detectors with thicknesses of; 1 – 10 μm , 2 - 25 μm , 3 - 300 μm .

The data presented in Figure 6.8 to Figure 6.11 demonstrate that the thin detectors can be well used for thermal neutron detection with the significant reduction in the gamma sensitivity, however at the expense of an increase in electronic noise level. The detector with minimum thickness (10 μm) has minimum gamma sensitivity but also shows higher electronic noise due to the increased capacitance, reduced pulse heights and lower count rate for thermal neutrons. The 25 μm thick detector has lower gamma sensitivity and better thermal neutron response

compared to the 300 μm thick detector as well as better electronic noise compared to 10 μm thick detector. The overall comparison of the thermal neutron response and gamma response of different detectors with thickness in the range of 10–300 μm shows that the detector with thickness of 25 μm exhibits the best performance, in terms of thermal neutron count rate and reduction of gamma sensitivity.

6.4. Conclusions

The concept of using epitaxial thin silicon detectors for improving the gamma discrimination has been proposed for the first time. This is validated by fabricating such detectors with different thickness and experiments using these detectors. The epitaxial silicon PIN detectors of different thicknesses (10 μm , 15 μm , 25 μm and 300 μm) were fabricated and examined for their thermal neutron response as well as their gamma sensitivity. The thicknesses were chosen based on the simulation results to optimize the detector performance for higher neutron count with improved n/γ discrimination. The experiments were carried out for evaluating the detectors for I–V, C–V characteristics, their alpha, gamma as well as thermal neutron response. The fabricated detectors had low leakage currents in nanoampere range. The measurements with a ^{137}Cs gamma source showed that there is a substantial reduction in the gamma sensitivity for the compared to a 300 μm thick (300 μm) PIN detector. Further, it has been demonstrated that the thin detectors are better suitable for the thermal neutron measurement with better n/γ discrimination compared to a standard 300 μm detector. The evaluation based on the important detector performance parameters (e.g. electronic noise, pulse heights and gamma sensitivity), the detector with the optimal thickness of 25 μm was found showing the best performance for thermal neutron measurements.

Chapter 7

SUMMARY

The radiation detectors are the instruments used for detecting the presence of specific subatomic particles or energy radiation such as alpha particle, beta particles, various charged particles and gamma rays. These detectors are required for a wide variety of applications ranging from medical, personal, environmental, security purposes to basic science experiments. The detectors are of profound importance in the basic science experiments where the structure and interactions at atomic, sub atomic, nuclear or even at inter-nuclear level are inferred by detecting the outgoing scattered particles/radiations. When a particle/radiation passes through the active medium of the detector, the detector system indicates its presence in the form of some output signal such as current pulse, light flash, etc. The characteristics of the detector, its suitability and applicability majorly depend on active volume of the detector, its design parameters and subsequent electronic arrangement used for collecting the output signal.

A detector is designed and fabricated as per its utility requirements, based on the aim of the experiments, the parameters of the radiation to be measured (e.g. counts, energy, position etc.) as well as the environment where it is to be used. Silicon based semiconductor detectors meet most of the criteria required in majority of the experiments/applications, because of their capabilities to count the particles/radiation, determine their energies, identifying them as well as locating them with high energy and position resolution. In addition to these, silicon detectors possess several other unique advantages, making them useful in any environment e.g. rugged, small in size, low power requirement, high efficiency, batch processing with low cost and better uniformity.

The present thesis deals with design, fabrication, characterization and successful demonstration of the three different silicon detectors:

ΔE -E detector telescope

In the present work, an integrated ΔE -E detector telescope for particle identification has been developed using a novel approach of integrating both the detectors back to back on the same silicon wafer. This approach overcomes the drawbacks of the conventional ΔE -E detector. The detectors are demonstrated to have excellent static parameters (low leakage current and capacitance) and could successfully identify the light charged particles as well as a wide range of heavy fission fragments.

Double sided silicon strip detectors

Prototype of double sided silicon strip detectors are developed as per the requirements of the use in GASPARD Experiment at the upcoming SPIRAL2 facility at GANIL, France. These detectors are designed to have precise position sensing of the charged particles and are shown remarkably doing so without any inter-strip crosstalk.

Thin thermal neutron detectors

Thin epitaxial silicon PIN detectors have been demonstrated for the possibility to use these detectors for thermal neutron detection with significantly improving the n/γ discrimination.

The work carried out in this thesis involves innovative development of silicon detectors, with having design parameters optimized by simulation studies. The thesis also elaborates various characterization methods essential for precise performance evaluation as well as for establishing feedback mechanism for the design improvement.

In future, the integrated detector telescope can be designed with segmentation for measurements of position, in addition to energy measurement and particle identification. The DSSD has been developed using standard high resistivity wafers. For actual use in the GASPARD Experiment, the detectors will be fabricated on NTD wafers for particle identification using PSD technique.

Appendix A

SEMICONDUCTOR PHYSICS

This section is dedicated to some of the important concepts of semiconductor physics and associated phenomenon, required to understand the working principals of silicon detectors and to optimize the design parameters for a particular application [22], [59], [61], [62].

The semiconductors by definition are the solids having resistivity higher than metals and lesser than insulators. In metals, the valence band and conduction bands are overlapping and hence the electrons in the metals are almost free to conduct. On the other hand, the insulators have well separated valance and conduction bands, with a band gap (energy gap between valance and conduction bands) $> 5\text{eV}$. This makes the conduction band in insulators almost empty and hence, a very high resistivity for insulators. In between these two extremes, semiconductors have intermediate band gap ($\sim 1\text{-}5\text{eV}$) leading to an intermediate value of the resistivity. At low temperatures, there is almost no electron present in the conduction band but as the temperature increases, some of the electrons acquire sufficient energy to make a transition from valance band to conduction band. Such transition of electrons leads to a positive entity in the valance band, called holes. The electron-hole (e^- -h) pair generation also takes place when the incident radiation deposits its energy to the semiconductor material, formulating the basis of semiconductor detectors. Following subsections presents some of the important aspects of semiconductor physics governing the performance of the semiconductor detectors.

A.1. Energy gap: direct and indirect band gap

The energy E of a free electron having momentum p and mass m_0 is given by

$$E = \frac{p^2}{m_0} \quad (\text{A.1})$$

In the case of a semiconductor, the electron is not free due to the periodic nuclear potential of lattice. If the effective mass of an electron in semiconductor be m_n then above equation can be modified as

$$E = \frac{p^2}{m_n} = \frac{(\hbar k)^2}{m_n} \quad (\text{A.2})$$

here $\hbar = h/2\pi$ and k is the wave vector. Above equation represents a parabola, known as E-k diagram or dispersion curve (Figure A.1). This E-k diagram constitutes the basis of direct and indirect band gaps in semiconductors and each energy state in valance and conduction bands are characterized by a k -vector in the Brillouin zone (Figure A.1). If the k -vectors for maximal energy state of valance band and minimal energy state of the conduction band are the same, i.e. there is no momentum change for an electron transiting from valance band to conduction band, the band gap is called direct band gap (Figure A.1 (a)) and such semiconductors are known as direct band gap semiconductors (e.g. GaAs, InAs). If the two k -vectors are different, i.e. there is a non-zero change in momentum while electron transition from valance band to conduction band, the band gap is called an indirect band gap (Figure A.1 (b)) and the examples of such semiconductors are Si and Ge. In the direct band gap semiconductors, the electron transition is directly accompanied by emission of a photon while in indirect band gap semiconductors, a photon cannot be emitted because the electron must pass through an intermediate state and transfer momentum to the crystal lattice in the form of a phonon.

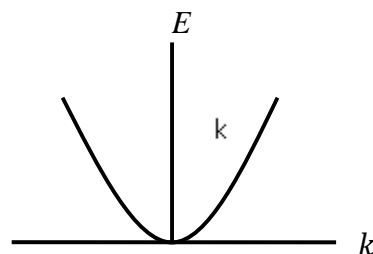


Figure A.1. Basic E-k Band diagram.

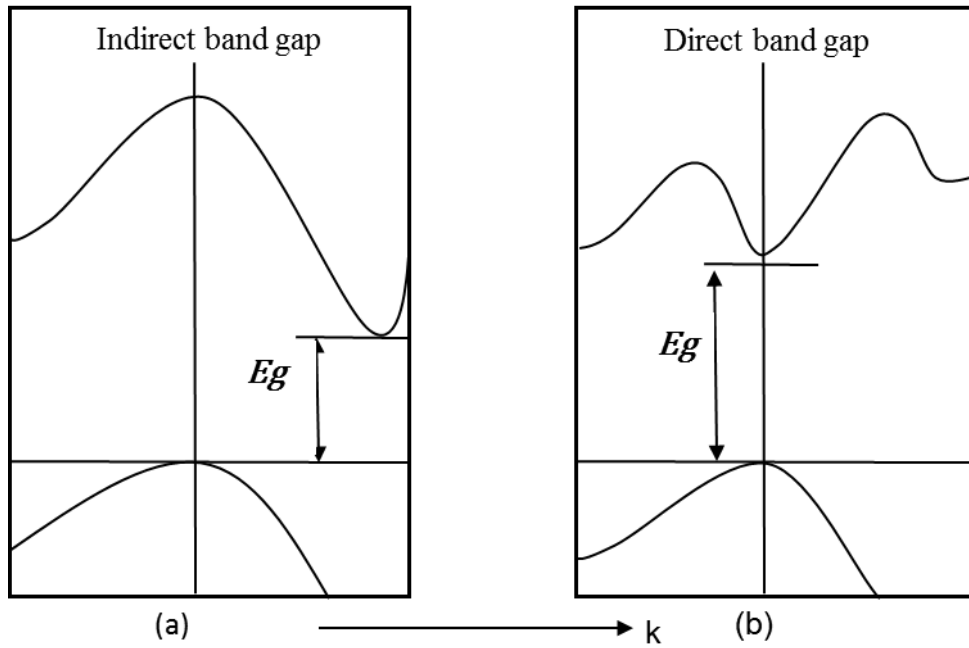


Figure A.2. Energy band diagram of (a) Indirect and (e.g. silicon) and (b) direct band gap (e.g. GaAs) semiconductors.

A.2. Intrinsic semiconductors and extrinsic semiconductors

An intrinsic semiconductor is a pure semiconductor without addition of any external significant impurity. The number of charge carriers in intrinsic semiconductors is therefore governed by the properties of the material itself, and not by the impurities. The electron number density (n_0) in an intrinsic semiconductor is given by

$$n_0 = \int_{E_c}^{E_{max}} n(E) dE = \int_0^{\infty} N(E) F(E) dE \quad (\text{A.3})$$

In this integration, the energies in the conduction band have been referred to the band edge (E_c) taken as $E_c = 0$. $N(E)$ is the density of states and $F(E)$ is occupation probability for an electronic state as given by the following Fermi-Dirac function

$$F(E) = \frac{1}{1 + \exp\left(\frac{E - E_F}{k_B T}\right)} \quad (\text{A.4})$$

where E_F is the Fermi energy, k_B is the Boltzmann constant and T is the absolute temperature. If $E \gg E_F$ (as in intrinsic semiconductor Fermi level lies in the mid of energy gap), then above equation for electrons in conduction band can be approximated as:

$$F_n(E) \approx e^{-\frac{E-E_F}{kT}} \quad (\text{A.5})$$

The density of states in the conduction band is defined as:

$$N(E)dE = 4\pi \left(\frac{2m_n}{h^2} \right)^{3/2} E^{1/2} dE \quad (\text{A.6})$$

where, m_n is the effective mass of electrons in the conduction band.

Using equations (A.1) and (A.2) in equation (2.19)

$$n_0 = 2 \left(\frac{2\pi m_n k_B T}{h^2} \right)^{3/2} e^{-\frac{E_C-E_F}{k_B T}} \quad (\text{A.7})$$

The density of available states, the Fermi function, and the number of electrons and holes occupying available energy states resulting from above equations in the conduction and valence bands at thermal equilibrium are shown in Figure A.3.

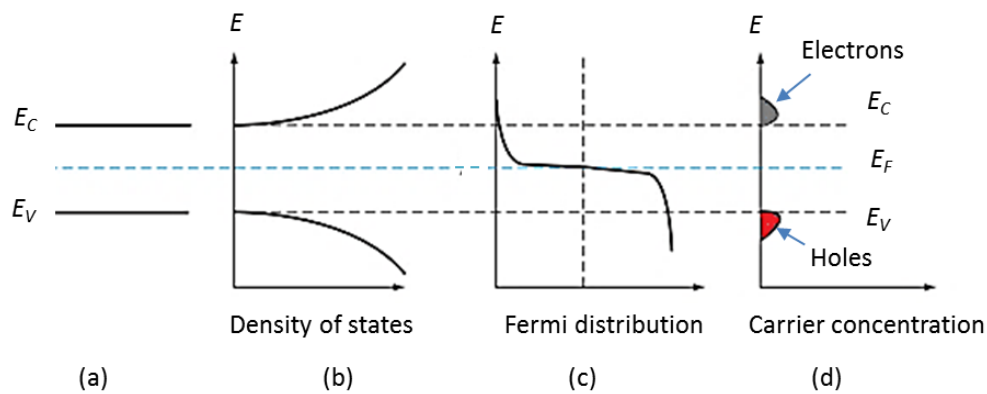


Figure A.3. Intrinsic semiconductor; (a) Schematic band diagram, (b) Density of states, (c) Fermi distribution function, (d) Carrier concentration.

E_C is the lowest energy of conduction band and the effective density of states in conduction band N_C can be defined as:

$$N_C = 2 \left(\frac{2\pi m_n k_B T}{h^2} \right)^{3/2} \quad (\text{A.8})$$

Similarly, if E_V is the maximum energy of valence band, then the number density of holes in valence band can be given as:

$$p_0 = 2 \left(\frac{2\pi m_p k_B T}{h^2} \right)^{3/2} e^{-\frac{E_F - E_V}{k_B T}} \quad (\text{A.9})$$

where, m_p is the effective mass of holes in valence band.

If N_V be the effective density of states in valence band then,

$$N_V = 2 \left(\frac{2\pi m_p k_B T}{h^2} \right)^{3/2} \quad (\text{A.10})$$

In an intrinsic semiconductor, the number of electrons in the conduction band is always equal to the number of holes in valence band. Hence intrinsic carrier density n_i can be given as:

$$n_i = n_0 = p_0, \quad (\text{A.11})$$

$$n_i^2 = n_0 p_0$$

$$n_i = \sqrt{n_0 p_0} = \sqrt{N_C N_V} e^{-\frac{E_g}{2k_B T}} \quad (\text{A.12})$$

where, E_g is the band gap and is equal to the difference between E_C and E_V . Above expression is independent of the Fermi level E_F . The equation (A.11) is known as law of mass action in semiconductors.

The Fermi level for intrinsic semiconductor can be obtained by equations (A.7) & (A.9)

$$E_F = E_i = \frac{E_C + E_V}{2} + \frac{k_B T}{2} \ln \left(\frac{N_V}{N_C} \right) = \frac{E_C + E_V}{2} + \frac{3k_B T}{4} \ln \left(\frac{m_p}{m_n} \right) \quad (\text{A.13})$$

where E_i is the Fermi level close to the middle of the band gap, the deviation being due to the unequal effective masses of electrons and holes.

The properties of the semiconductor materials are altered by intentionally adding some impurity called doping, and the resultant semiconductors are called extrinsic semiconductors.

The doping is done during the growth of the semiconductor or/and after by diffusion or ion implantation. Doping introduces new energy levels in the band gap and hence results in increased probability of excitation of charge carriers in newly introduced energy levels. Figure A.4 shows measured ionization energy for various impurities in silicon. Energy is measured from E_C for levels above the mid line and for the levels below the mid line, energy is measured from E_V .

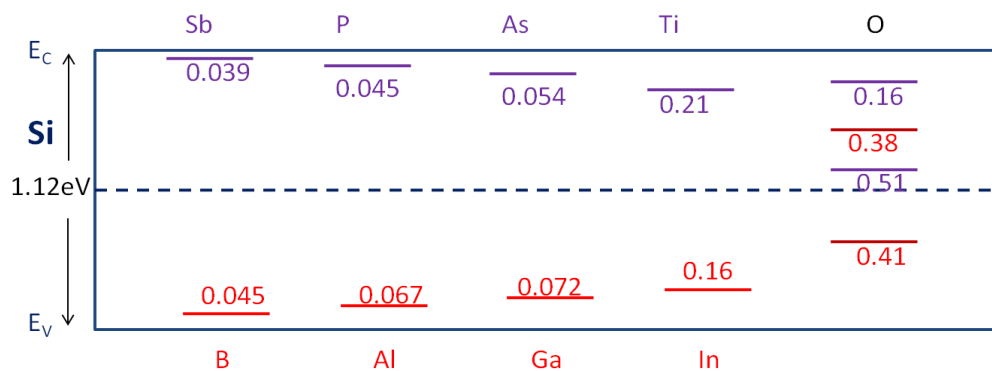


Figure A.4. Ionization energy of various impurities in silicon [61]. For levels above the mid line, the energy is measured from E_C and for those below the mid line, energy is measured from E_V . Acceptor and donor levels are shown in red and violet, respectively.

On the basis of introduced impurities, two types of extrinsic semiconductors can be obtained. When silicon is doped with a pentavalent impurity i.e. of group V (Sb, P and As), then n-type silicon is obtained in which out of five valence electrons, four make covalent bonds with four neighbouring Si atoms and one remains unbound. This fifth electron is free for the conduction. These pentavalent impurities are called donor. When a trivalent impurity atom such as boron replaces a silicon atom, an additional electron is accepted to form four covalent bonds with four neighbouring Si atoms, and a positively charged hole is created in the valence band. This is a p-type silicon, and the trivalent impurity is called an acceptor. If donor levels E_D are close to the conduction band, as is the case for phosphorous ($E_C - E_D = 0.045$ eV) or arsenic ($E_C - E_D = 0.054$ eV) atoms in silicon, these states will be almost completely ionized at room

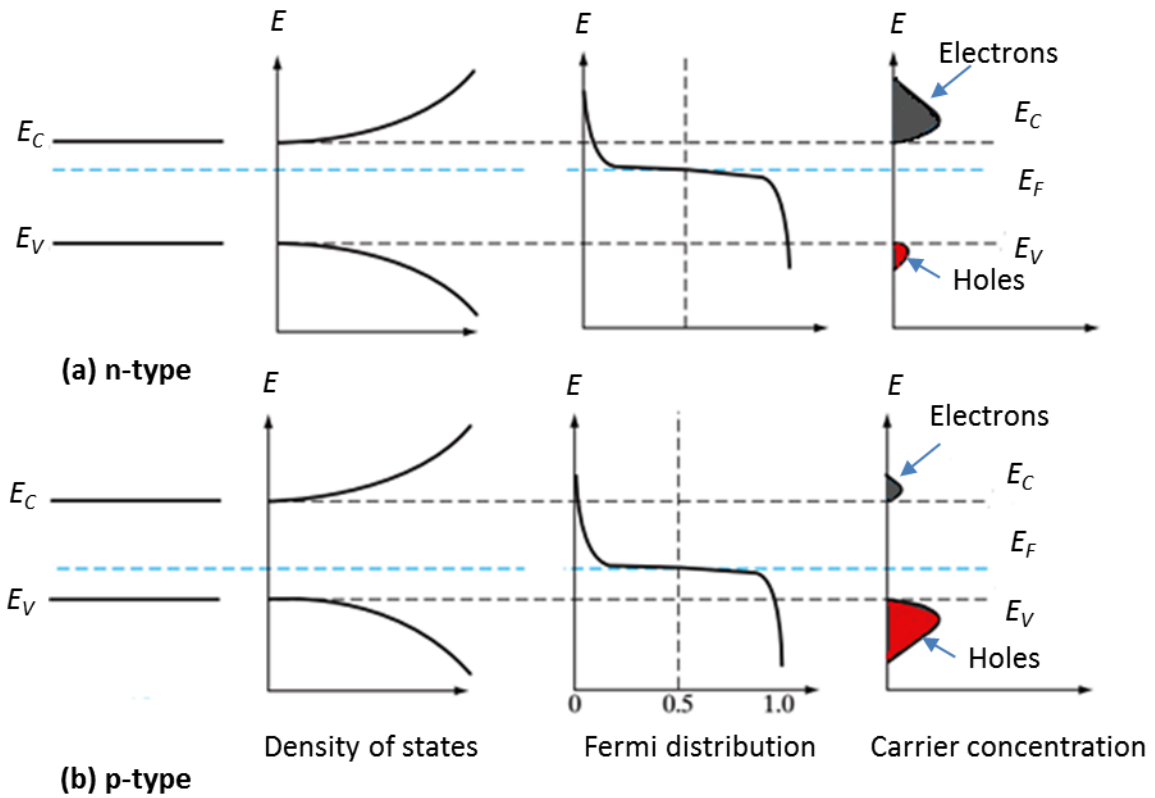


Figure A.6. Schematic band diagram, density of states, Fermi distribution function and carrier concentration of (a) n-type semiconductor, (b) p-type semiconductor [62].

Equations obtained for an intrinsic semiconductor are also true for the extrinsic semiconductor. The product of n_0 and p_0 at equilibrium is a constant for a particular material and temperature, even if the doping is varied (equation (A.11)). Therefore, the generalized expression for law of mass action for extrinsic semiconductor can be written as:

$$n \cdot p = n_i^2 = N_C N_V e^{-\frac{E_g}{k_B T}} \quad (\text{A.14})$$

where n and p represent the number of electrons and holes in the extrinsic semiconductor at equilibrium. The material remains neutral, irrespective of the kind and amount of the doping.

Therefore,

$$N_A + n = N_D + p \quad (\text{A.15})$$

where N_A and N_D are donor and acceptor concentrations respectively.

For n-type material, the dopant density is always far higher than the intrinsic carrier density $N_D \gg p$ and $N_A = 0$. Hence, the majority charge carrier density n_n and minority charge carrier density p_n in n-type material can be given as:

$$n_n = N_D \quad (\text{A.16})$$

from equations (A.14), (A.15) and (A.16)

$$n_n = n_i e^{\frac{E_F - E_i^n}{k_B T}} \quad (\text{A.17})$$

where E_i is the intrinsic Fermi level.

$$p_n = \frac{n_i^2}{N_D} \quad (\text{A.18})$$

The Fermi level for n-type material,

$$E_{Fn} = E_C - k_B T \ln \frac{N_c}{N_D} \quad (\text{A.19})$$

Similar expressions can be obtained for p-type materials as

$$n_p = N_A \quad (\text{A.20})$$

$$n_p = n_i e^{\frac{E_i^p - E_F}{k_B T}} \quad (\text{A.21})$$

$$p_n = \frac{n_i^2}{N_D} \quad (\text{A.22})$$

and the fermi level for p- type material,

$$E_{Fp} = E_C + k_B T \ln \frac{N_c}{N_D} \quad (\text{A.23})$$

The equations described above govern the density of the charge carries present and/or generated in the detector material by interaction with radiation and hence dictates many of the parameters related to the detector capabilities.

A.3. Generation & recombination of charge carriers

When the charge carriers are generated in the semiconductor by external means, then the relation $np = n_i^2$ is no more valid until equilibrium maintained. This process of generating charge carrier is called charge injection. In the situation, $p > n_i$, recombination of charge carriers starts to restore the equilibrium. When semiconductor is energised, some electrons are excited in conduction band and holes are left behind in valence band. This is followed by the de-excitation i.e. recombination. The charge carrier generation in semiconductors can take place mainly through following ways [22], [62]

A.3.1. Thermal generation

Due to quite low band gap, a small rise in the temperature may provide sufficient energy to the electrons in the valence band of the semiconductor to make a transition to conduction band and hence creating an electron-hole (charge carrier) pair. Such creation of the charges is possible even at room temperatures in semiconductors having sufficiently low band gap, such as Ge (band gap $\sim 0.74\text{eV}$), resulting in an undesired source of noise, when utilized as detector materials. To avoid this, the Ge based detectors (e.g, high purity germanium detectors) are usually operated at low temperatures or even at liquid nitrogen temperatures. However, in the case of silicon (band gap $\sim 1.1\text{eV}$), the probability of excitation of electron at room temperature is very low. It may happen with the help of intermediate states present due to lattice defects and impurities. In this process, excitation due to thermal agitation takes place from valence band to such intermediate state and from that state to final conduction band.

A.3.2. Generation by radiation

The charged particles and electromagnetic radiation lose their energies in the semiconductor material by different means as described in the Section 2.1. In all the cases, the deposition of

the energy leads to the formation of the electron-hole pairs (charge carriers) which thereby are collected for signalling the passage of the radiation. In semiconductors, because of the quite low band gap, only a small fraction of the energy is required to generate electron-hole pairs. For example, the average energy used to produce a single electron-hole pair is only 3.6 eV, three times larger than the band gap of 1.12 eV and much less than the energies of the charged particles/radiation, usually targeted for the detection.

A.3.3. Impact ionization process

Another way to create charge carriers in a semiconductor detector is by applying electric field. The sufficiently high electric field pulls electrons directly out from the atoms. The charge carriers produced this way or through other ways acquire sufficient kinetic energy between the collisions. These high energetic charge carriers further transfer their energy to atoms to create more electron-hole pairs (avalanche) by collision. The generation rate in this process is proportional to drift current densities (equation (A.34)).

When the charge injection or excess carriers are introduced in the semiconductor, the thermal equilibrium gets disturbed i.e. $pn \neq n_i^2$. In order to restore equilibrium, electrons and hole recombination occurs. In recombination process energy is released either by emitting photon (radiative recombination) or by dissipation to lattice (non-radiative recombination). Radiative recombination dominates in direct band gap semiconductors (GaAs) and non-radiative recombinations are prominent mostly in indirect band gap semiconductors (Si, Ge, etc.). In indirect band gap semiconductors, there is a change in momentum when electrons transit from valence band to conduction band. Therefore, non-radiative recombination usually takes place with assistance of intermediate levels (recombination centers due to presence of impurity and crystal defects).

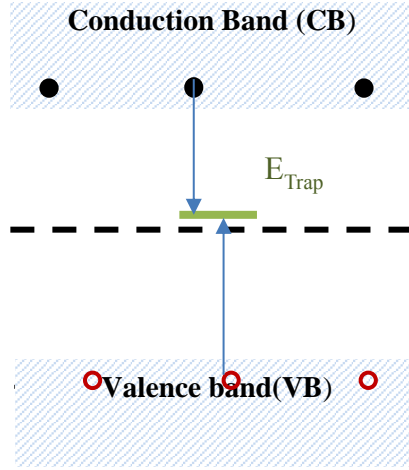


Figure A.7. Typical energy band diagram presenting indirect recombination.

The recombination can be classified in following processes

Direct recombination: This process is a radiative recombination in which band to band transition takes place along with the emission of photon and dominates in the direct band gap semiconductors such as GaAs. The net recombination rate U_D can be given as [22]

$$U_D = R - R_{th} = \beta(np - n_i^2) \quad (A.24)$$

where R is recombination rate, R_{th} is recombination rate at thermal equilibrium and β is recombination coefficient.

Shockley-Hall-Read recombination: In this process the recombination takes place with the assistance of trapping centres present in the band gap due to crystal defects and impurity. The net recombination rate for trap-assisted recombination is given by [22]

$$U_{SHR} = \frac{pn - n_i^2}{p + n + 2n_i \cosh\left(\frac{E_i - E_t}{k_B T}\right)} N_t v_{th} \sigma \quad (A.25)$$

where, E_t is the trap energy level, v_{th} thermal velocity, N_t the defect concentration and σ generation cross section.

This expression can be further simplified for p-type ($p \gg n$) to

$$U_{SHRp} = \frac{n_p - n_{p0}}{\tau_n} \quad (A.26)$$

and for n-type ($n \gg p$) to

$$U_{SHRn} = \frac{p_n - p_{n0}}{\tau_p} \quad (A.27)$$

where, τ_p and τ_n are generation life time of the minority charge carriers and given by

$$\tau_n = \tau_p = \frac{1}{N_t v_{th} \sigma} \quad (A.28)$$

A.3.4. Surface recombination

Semiconductor crystal surfaces and interfaces abruptly terminated have a large number of recombination centres due to dangling bonds. Also, during the fabrication process, defects and impurity concentrations at the surface and interfaces are increased. The net recombination rate in this process can be given by replacing defect concentration N_t with surface defect concentration N_{ts} in equation (A.28).

A.3.5. Auger recombination:

In this process, electron and hole recombine in a band-to-band transition and energy is transferred to another electron or hole.

The net recombination rate (U_{Auger}) can be given as[22]

$$U_{Auger} = A_n n(np - n_i^2) - A_p p(np - n_i^2) \quad (A.29)$$

Above expression is similar to a net recombination rate for direct recombination with an extra term for electrons or holes which receive the energy released in Auger recombination.

A.4. Carrier transport

The electrons in the conduction band have three degree of freedom and energy $\frac{1}{2}k_B T$ (equipartition of energy) is associated with each degree of freedom. Therefore, the kinetic energy of electron in conduction band can be given as

$$\frac{1}{2}m_n v^2 = \frac{3}{2}k_B T \quad (\text{A.30})$$

where m_n is the effective mass of electron and v is the thermal velocity ($\sim 10^7$ cm/s for silicon). The electron in the crystal lattice moves randomly with this velocity and collides with the lattice atoms. The mean free path between collisions is about 10^{-5} cm and mean free time τ is about 10^{-12} s. The carrier transport processes take place through different mechanisms such as drift (application of an external electric field), diffusion (due to concentration gradient), recombination, generation, space charge effect, tunnelling, and impact ionization.

A.4.1. Drift

The average displacement of a charge in a semiconductor due to thermal velocity is zero. When a small electric field E is applied, a force qE is experienced by charge (q) carrier, resulting in an additional drift component in velocity along the field during the time between collisions. This additional component is called drift velocity due to which a net displacement along the applied field is obtained. The drift velocity is related to applied field according to following relation [61], [62]:

for electrons,

$$v_n = -\left(\frac{q \cdot \tau}{m_n}\right) E = -\mu_n E \quad (\text{A.31})$$

for holes,

$$v_p = \left(\frac{q \cdot \tau}{m_p} \right) E = \mu_p E \quad (\text{A.32})$$

where μ_n and μ_p are the mobilities of electron and hole respectively which depend on temperature and scattering by lattice and impurity atoms. The mobility of electrons is greater than the mobility of holes due to smaller effective mass. Above equations are only valid for low external electric fields, which provide the drift velocity low enough in comparison with the thermal velocity. As for higher electric fields, drift velocity attains the saturation value and approaches thermal velocity.

Let us consider a voltage V is applied across the thickness t of a semiconductor slab with surface area A , then the total current flowing through the slab is given by

$$I = I_e + I_h = eA(nv_n + pv_h) \quad (\text{A.33})$$

The current density is therefore given as

$$\begin{aligned} J &= \frac{I}{A} = J_n + J_p = e(nv_n + pv_h) = e(n\mu_n + p\mu_h)E \\ &= e(n\mu_n + p\mu_h) \frac{V}{t} \end{aligned} \quad (\text{A.34})$$

but the resistivity $\rho = \frac{V}{Jt}$

It is the mobility of these electron and holes which governs the resistivity of the material, as given by

$$\rho = \frac{1}{e(n\mu_n + p\mu_h)} \quad (\text{A.35})$$

or n-type semiconductor $n \gg p$

$$\rho = \frac{1}{en\mu_n}$$

for p-type semiconductor $p \gg n$

$$\rho = \frac{1}{en\mu_p}$$

A.4.2. Carrier diffusion

If there is a spatial variation of charge carrier concentration, then diffusion of charges starts from high concentration region to low concentration region, causing a so-called diffusion current. It can be described by the following diffusion equation:

$$\varphi_n(x) = -D_n \frac{dn(x)}{dx} \quad (\text{A.36})$$

$$\varphi_p(x) = -D_p \frac{dp(x)}{dx} \quad (\text{A.37})$$

where $\varphi_n(x)$ is electron flux, D_n is the diffusion coefficient for electron and $dn(x)/dx$ represents electron concentration gradient. All the quantities with suffix p denote the same quantities for hole. If electric field and concentration gradient both are present, the total current density of for the electron and holes can be expressed as [22]

$$J_n = en\mu_n E + eD_n \frac{dn(x)}{dx} \quad (\text{A.38})$$

$$J_p = en\mu_p E - eD_p \frac{dp(x)}{dx} \quad (\text{A.39})$$

Mobility and diffusion are related to each other by the following equations:

$$D_n = \frac{k_B T}{q} \mu_n \quad (\text{A.40})$$

$$D_p = \frac{k_B T}{q} \mu_p \quad (\text{A.41})$$

Total conduction density is the sum of both J_n and J_p .

References

- [1] W. R. Leo, *Techniques for Nuclear and Particle Physics Experiments : a How-to Approach*. Springer Berlin Heidelberg, 1994.
- [2] H. R. Vega-Carrillo, “TLD pairs, as thermal neutron detectors in neutron multisphere spectrometry,” *Radiat. Meas.*, vol. 35, no. 3, pp. 251–254, Jun. 2002.
- [3] M. Assié *et al.*, “New methods to identify low energy ^3He with Silicon-based detectors,” *Nucl. Instr. and Meth. A*, vol. 908, pp. 250–255, Nov. 2018.
- [4] G. Aad *et al.*, “ATLAS pixel detector electronics and sensors,” *J. Instrum.*, vol. 3, no. 07, pp. P07007–P07007, Jul. 2008.
- [5] E. Aprile and T. Doke, “Liquid xenon detectors for particle physics and astrophysics,” *Rev. Mod. Phys.*, vol. 82, no. 3, pp. 2053–2097, Jul. 2010.
- [6] The ATLAS Collaboration *et al.*, “Expected Performance of the ATLAS Experiment - Detector, Trigger and Physics,” Dec. 2008.
- [7] N. A. Graf, “The Silicon Detector Concept,” *Phys. Procedia*, vol. 37, pp. 143–150, Jan. 2012.
- [8] G. Casse, “Recent developments on silicon detectors,” *Nucl. Instr. and Meth. A*, vol. 732, pp. 16–20, Dec. 2013.
- [9] D. Renker and E. Lorenz, “Advances in solid state photon detectors,” *J. Instrum.*, vol. 4, no. 04, pp. P04004–P04004, Apr. 2009.
- [10] A. Owens and A. Peacock, “Compound semiconductor radiation detectors,” *Nucl. Instr. and Meth. A*, vol. 531, no. 1–2, pp. 18–37, Sep. 2004.
- [11] G. Lindström *et al.*, “Radiation hard silicon detectors—developments by the RD48 (ROSE) collaboration,” *Nucl. Instr. and Meth. A*, vol. 466, no. 2, pp. 308–326, Jul. 2001.
- [12] “High resolution amorphous silicon radiation detectors,” Dec. 1989.
- [13] L. Arnold *et al.*, “The STAR silicon strip detector (SSD),” *Nucl. Instr. and Meth. A*, vol. 499, no. 2–3, pp. 652–658, Mar. 2003.
- [14] S. Takeda *et al.*, “Development of double-sided silicon strip detectors (DSSD) for a Compton telescope,” *Nucl. Instr. and Meth. A*, vol. 579, no. 2, pp. 859–865, Sep. 2007.
- [15] H. F.-W. Sadrozinski, “Applications of silicon detectors,” *IEEE Trans. Nucl. Sci.*, vol. 48, no. 4, pp. 933–940, 2001.
- [16] H. Bornefalk and M. Danielsson, “Photon-counting spectral computed tomography using silicon strip detectors: a feasibility study,” *Phys. Med. Biol.*, vol. 55, no. 7, pp. 1999–2022, Apr. 2010.
- [17] H. O. Pritchard, R. W. Nicholls, and A. Lakshmi, “Ultraviolet sensitization of silicon

- detectors for space astronomical applications,” *Appl. Opt.*, vol. 18, no. 13, p. 2085, Jul. 1979.
- [18] P. R. Granfors and R. Aufrichtig, “Performance of a 41×41-cm² amorphous silicon flat panel x-ray detector for radiographic imaging applications,” *Med. Phys.*, vol. 27, no. 6, pp. 1324–1331, Jun. 2000.
- [19] Y. K. Akimov, “Silicon radiation detectors (Review),” *Instruments Exp. Tech.*, vol. 50, no. 1, pp. 1–28, Feb. 2007.
- [20] G.-F. DALLA BETTA and M. BOSCARDIN, “SILICON RADIATION DETECTORS: REVIEW OF PRODUCTION AND R&D ACTIVITIES AT ITC-IRST,” in *Sensors and Microsystems*, 2004, pp. 32–41.
- [21] P. Rehak, “Silicon radiation detectors,” *IEEE Trans. Nucl. Sci.*, vol. 51, no. 5, pp. 2492–2497, Oct. 2004.
- [22] G. Lutz, *Semiconductor Radiation Detectors*. Berlin, Heidelberg: Springer Berlin Heidelberg, 2007.
- [23] E. Steinbauer, P. Bauer, M. Geretschläger, G. Bortels, J. P. Biersack, and P. Burger, “Energy resolution of silicon detectors: approaching the physical limit,” *Nucl. Instr. and Meth. B*, vol. 85, no. 1–4, pp. 642–649, Mar. 1994.
- [24] E. Sciacca *et al.*, “Silicon planar technology for single-photon optical detectors,” *IEEE Trans. Electron Devices*, vol. 50, no. 4, pp. 918–925, Apr. 2003.
- [25] G. Lutz, “Silicon radiation detectors,” *Nucl. Instr. and Meth. A*, vol. 367, no. 1–3, pp. 21–33, Dec. 1995.
- [26] T. Maisch, R. Günzler, M. Weiser, S. Kalbitzer, W. Welser, and J. Kemmer, “Ion-implanted Si pn-junction detectors with ultrathin windows,” *Nucl. Instr. and Meth. A*, vol. 288, no. 1, pp. 19–23, Mar. 1990.
- [27] C. Kenney, S. Parker, J. Segal, and C. Storment, “Silicon detectors with 3-D electrode arrays: fabrication and initial test results,” *IEEE Trans. Nucl. Sci.*, vol. 46, no. 4, pp. 1224–1236, 1999.
- [28] G. Pellegrini, M. Lozano, M. Ullán, R. Bates, C. Fleta, and D. Pennicard, “First double-sided 3-D detectors fabricated at CNM-IMB,” *Nucl. Instr. and Meth. A*, vol. 592, no. 1–2, pp. 38–43, Jul. 2008.
- [29] S. E. Holland, D. E. Groom, N. P. Palaio, R. J. Stover, and Mingzhi Wei, “Fully depleted, back-illuminated charge-coupled devices fabricated on high-resistivity silicon,” *IEEE Trans. Electron Devices*, vol. 50, no. 1, pp. 225–238, Jan. 2003.
- [30] A. Fujiwara and Y. Takahashi, “Manipulation of elementary charge in a silicon charge-coupled device,” *Nature*, vol. 410, no. 6828, pp. 560–562, Mar. 2001.
- [31] M. Y. Kim *et al.*, “Development of a large area silicon pad detector for the identification of cosmic ions,” *Nucl. Phys. B - Proc. Suppl.*, vol. 172, pp. 162–164, Oct. 2007.

- [32] B. Perea Solano *et al.*, “Edgeless silicon pad detectors,” *Nucl. Instr. and Meth. A*, vol. 560, no. 1, pp. 135–138, May 2006.
- [33] G. Silvestre, “Evaluation of double-sided silicon microstrip sensor for the FOOT experiment,” *Nucl. Instr. and Meth. A*, Nov. 2018.
- [34] G. Casse, P. P. Allport, S. Martí i Garcia, M. Lozano, and P. R. Turner, “First results on charge collection efficiency of heavily irradiated microstrip sensors fabricated on oxygenated p-type silicon,” *Nucl. Instr. and Meth. A*, vol. 518, no. 1–2, pp. 340–342, Feb. 2004.
- [35] L. T. Tran *et al.*, “Development of a large-area silicon α -particle detector,” *Appl. Radiat. Isot.*, vol. 92, pp. 96–101, Sep. 2014.
- [36] N. Zorzi, M. Melchiorri, A. Piazza, C. Piemonte, and A. Tarolli, “Development of large-area silicon photomultiplier detectors for PET applications at FBK,” *Nucl. Instr. and Meth. A*, vol. 636, no. 1, pp. S208–S213, Apr. 2011.
- [37] M. Bruzzi, “Radiation damage in silicon detectors for high-energy physics experiments,” *IEEE Trans. Nucl. Sci.*, vol. 48, no. 4, pp. 960–971, 2001.
- [38] G. Casse, P. P. Allport, and M. Hanlon, “Improving the radiation hardness properties of silicon detectors using oxygenated n-type and p-type silicon,” *IEEE Trans. Nucl. Sci.*, vol. 47, no. 3, pp. 527–532, Jun. 2000.
- [39] A. Topkar *et al.*, “Development of integrated ΔE silicon detector telescope using silicon planar technology,” *Nucl. Instr. and Meth. A*, vol. 654, no. 1, pp. 330–335, Oct. 2011.
- [40] A. Singh, A. Topkar, U. Köster, P. K. Mukhopadhyay, and C. K. Pithawa, “Performance study of an integrated ΔE -E silicon detector telescope using the lohengrin fission fragment separator at ILL, Grenoble,” *IEEE Trans. Nucl. Sci.*, vol. 62, no. 1, pp. 264–271, Feb. 2015.
- [41] A. Topkar *et al.*, “Development, prototyping and characterization of double sided silicon strip detectors,” *Nucl. Instr. and Meth. A*, vol. 834, pp. 205–210, 2016.
- [42] A. Singh, S. Desai, A. Kumar, and A. Topkar, “Performance study of thin epitaxial silicon PIN detectors for thermal neutron measurements with reduced γ sensitivity,” *Nucl. Instr. and Meth. A*, vol. 890, pp. 28–34, Feb. 2018.
- [43] B. Schmidt, J. von Borany, and D. Schubert, “Application of wet chemical selective etch techniques to the fabrication of thin silicon detectors,” *Nucl. Instr. and Meth. A*, vol. 326, no. 1–2, pp. 21–26, Mar. 1993.
- [44] J. Pouthas *et al.*, “INDRA, a 4π charged product detection array at GANIL,” *Nucl. Instr. and Meth. A*, vol. 357, no. 2–3, pp. 418–442, Apr. 1995.
- [45] A. Rashevsky *et al.*, “Characteristics of the ALICE Silicon Drift Detector,” *Nucl. Instr. and Meth. A*, vol. 461, no. 1–3, pp. 133–138, Apr. 2001.
- [46] A. Rivetti *et al.*, “The front-end system of the silicon drift detectors of ALICE,” *Nucl.*

- Instr. and Meth. A*, vol. 541, no. 1–2, pp. 267–273, Apr. 2005.
- [47] C. Cavicchioli, “Detector performance of the ALICE silicon pixel detector,” *Nucl. Instr. and Meth. A*, vol. 628, no. 1, pp. 77–80, Feb. 2011.
- [48] T. T. Collaboration *et al.*, “The TOTEM Experiment at the CERN Large Hadron Collider,” *J. Instrum.*, vol. 3, no. 08, pp. S08007–S08007, Aug. 2008.
- [49] G. F. Knoll, “Radiation Detection and Measurement,” in *Radiation Detection and Measurement*, 3rd ed., John Wiley & Sons, Inc., New York, 2000.
- [50] S. Reza and K. Iniewski, *Semiconductor radiation detectors, technology, and applications*. .
- [51] C. Grupen, B. Shwartz, and Cambridge University Press., *Particle Detectors*. Cambridge: Cambridge University Press, 2008.
- [52] C. M. DAVISSON, “INTERACTION OF γ -RADIATION WITH MATTER,” *Alpha-, Beta- Gamma-Ray Spectrosc.*, pp. 37–78, Jan. 1968.
- [53] N. Tsoulfanidis and S. Landsberger, *Measurement and detection of radiation*. .
- [54] H. Spieler, *Semiconductor detector systems*. Oxford University Press, 2005.
- [55] U. Fano, “On the Theory of Ionization Yield of Radiations in Different Substances,” *Phys. Rev.*, vol. 70, no. 1–2, pp. 44–52, Jul. 1946.
- [56] U. Fano, “Ionization Yield of Radiations. II. The Fluctuations of the Number of Ions,” *Phys. Rev.*, vol. 72, no. 1, pp. 26–29, Jul. 1947.
- [57] D. Pitzl *et al.*, “Type inversion in silicon detectors,” *Nucl. Instr. and Meth. A*, vol. 311, no. 1–2, pp. 98–104, Jan. 1992.
- [58] C. Niebuhr, “Aging effects in gas detectors,” *Nucl. Instr. and Meth. A*, vol. 566, no. 1, pp. 118–122, Oct. 2006.
- [59] C. Kittel, *Introduction to solid state physics*. Wiley, 2005.
- [60] R. C. Alig, S. Bloom, and C. W. Struck, “Scattering by ionization and phonon emission in semiconductors,” *Phys. Rev. B*, vol. 22, no. 12, pp. 5565–5582, Dec. 1980.
- [61] S. M. Sze, *Semiconductor devices : Physics and technology*. Wiley India, 2009.
- [62] B. G. Streetman and S. Banerjee, *Solid state electronic devices*. Pearson/Prentice Hall, 2006.
- [63] F. J. Ramírez-Jiménez, E. F. Aguilera, R. López-Callejas, J. S. Benítez-Read, and J. Pacheco-Sotelo, “A novel application of a PIN diode-preamplifier set for the measurement of charged particles,” *Nucl. Instr. and Meth. A*, vol. 545, no. 3, pp. 721–726, Jun. 2005.
- [64] G. Pellegrini *et al.*, “Technology of p-type microstrip detectors with radiation hard p-

- spray, p-stop and moderated p-spray insulations,” vol. 579, pp. 599–603, Sep. 2007.
- [65] M. Alderighi *et al.*, “Charge identification in large area planar silicon detectors, using digital pulse shape acquisition,” *IEEE Trans. Nucl. Sci.*, vol. 53, no. 1, pp. 279–285, Feb. 2006.
- [66] Y. Liu *et al.*, “Uniform design and regression analysis of LPCVD boron carbide from BCl₃–CH₄–H₂ system,” *Appl. Surf. Sci.*, vol. 255, no. 11, pp. 5729–5735, Mar. 2009.
- [67] R. J. Nikolić *et al.*, “6:1 aspect ratio silicon pillar based thermal neutron detector filled with ¹⁰B,” *Appl. Phys. Lett.*, vol. 93, no. 13, p. 133502, 2008.
- [68] N. LiCausi, J. Dingley, Y. Danon, J.-Q. Lu, and I. B. Bhat, “A novel solid state self-powered neutron detector,” *Proc. SPIE*, vol. 7079, pp. 707908-1-707908–12, 2008.
- [69] P. Chaudhari, A. Singh, A. Topkar, and R. Dusane, “Hot wire chemical vapor deposited boron carbide thin film/crystalline silicon diode for neutron detection application,” *Solid. State. Electron.*, vol. 78, pp. 156–158, 2012.
- [70] P. Chaudhari, A. Singh, A. Topkar, and R. Dusane, “Fabrication and characterization of silicon based thermal neutron detector with hot wire chemical vapor deposited boron carbide converter,” *Nucl. Instr. and Meth. A*, vol. 779, pp. 33–38, 2015.
- [71] P. Kandlakunta and L. Cao, “Gamma-ray rejection, or detection, with gadolinium as a converter,” *Radiat. Prot. Dosimetry*, vol. 151, no. 3, pp. 586–590, Sep. 2012.
- [72] P. Kandlakunta, “A Proof-of-Principle Investigation for a Neutron-Gamma Discrimination Technique in a Semiconductor Neutron Detector,” 2012.
- [73] L. Bardelli *et al.*, “Progresses in the pulse shape identification with silicon detectors within the FAZIA Collaboration,” *Nucl. Instr. and Meth. A*, vol. 654, no. 1, pp. 272–278, Oct. 2011.
- [74] L. Bardelli, G. Poggi, G. Pasquali, and M. Bini, “A method for non-destructive resistivity mapping in silicon detectors,” *Nucl. Instr. and Meth. A*, vol. 602, no. 2, pp. 501–505, Apr. 2009.
- [75] L. Bardelli *et al.*, “Influence of crystal-orientation effects on pulse-shape-based identification of heavy-ions stopped in silicon detectors,” *Nucl. Instr. and Meth. A*, vol. 605, no. 3, pp. 353–358, Jul. 2009.
- [76] L. Evensen, A. Hanneborg, B. S. Avset, and M. Nese, “Guard ring design for high voltage operation of silicon detectors,” *Nucl. Inst. Methods Phys. Res. A*, vol. 337, no. 1, pp. 44–52, Dec. 1993.
- [77] G. Casse, “Overview of the recent activities of the RD50 collaboration on radiation hardening of semiconductor detectors for the sLHC,” *Nucl. Instr. and Meth. A*, vol. 598, no. 1, pp. 54–60, Jan. 2009.
- [78] L. Andricek *et al.*, “Design and test of radiation hard p+n silicon strip detectors for the ATLAS SCT,” *Nucl. Instr. and Meth. A*, vol. 439, no. 2–3, pp. 427–441, Jan. 2000.

- [79] S. Coffa, *Ion implantation technology-94 : proceedings of the Tenth International Conference on Ion Implantation Technology, Catania, Italy, June 13-17, 1994*. North-Holland, 1995.
- [80] D. Passeri, P. Ciampolini, G. M. Bilei, M. Angarano, and F. Moscatelli, "Optimization of overhanging-metal microstrip detectors: test and simulation," *IEEE Trans. Nucl. Sci.*, vol. 48, no. 3, pp. 249–253, Jun. 2001.
- [81] P. Singh *et al.*, "Status report on the folded tandem ion accelerator at BARC," *Pramana*, vol. 59, no. 5, pp. 739–744, Nov. 2002.
- [82] S. K. Gupta, "6 MV FOLDED TANDEM ION ACCELERATOR FACILITY AT BARC S . K . Gupta * LEHIPA , Physics Group , Bhabha Atomic Research Centre , Mumbai 400085 Abstract," pp. 1–4.
- [83] S. Santra and P. Singh, "Beam optics of the folded tandem ion accelerator at BARC," *Pramana*, vol. 59, no. 1, pp. 53–68, Jul. 2002.
- [84] P. Armbruster *et al.*, "The recoil separator Lohengrin: Performance and special features for experiments," *Nucl. Instruments Methods*, vol. 139, pp. 213–222, Dec. 1976.
- [85] U. Köster, H. Faust, T. Materna, and L. Mathieu, "Experience with in-pile fission targets at LOHENGRIN," *Nucl. Instr. and Meth. A*, vol. 613, no. 3, pp. 363–370, Feb. 2010.
- [86] L. Mathieu *et al.*, "New neutron long-counter for delayed neutron investigations with the LOHENGRIN fission fragment separator," *J. Instrum.*, vol. 7, no. 08, pp. P08029–P08029, Aug. 2012.
- [87] K. G. Prasad, "Medium energy heavy ion accelerator at TIFR," *Nucl. Instr. and Meth. B*, vol. 40–41, pp. 916–920, Apr. 1989.
- [88] A. Chatterjee *et al.*, "A 150 cm diameter scattering chamber for Pelletron-LINAC facility at Mumbai," in *Proceedings of the International Symposium on Nuclear Physics*, 2009, pp. 700–701.
- [89] S. L. Chaplot and R. Mukhopadhyay, "Neutron Beam Research at Dhruva Reactor," *Neutron News*, vol. 25, no. 1, pp. 15–17, Jan. 2014.
- [90] G. Thungström, E. J. van Veldhuizen, L. Westerberg, L.-O. Norlin, and C. S. Petersson, "Fabrication of an integrated ΔE -E-silicon detector by wafer bonding using cobalt disilicide," *Nucl. Instr. and Meth. A*, vol. 391, no. 2, pp. 315–328, Jun. 1997.
- [91] S. Tudisco *et al.*, "A new large area monolithic silicon telescope," *Nucl. Instr. and Meth. A*, vol. 426, no. 2–3, pp. 436–445, May 1999.
- [92] A. J. Kordyasz *et al.*, "Response to heavy ions and fission fragments of the monolithic silicon E– ΔE telescopes produced by the Quasi-Selective Epitaxy," *Nucl. Instr. and Meth. A*, vol. 530, no. 1–2, pp. 87–91, Sep. 2004.
- [93] V. V. Parkar *et al.*, "Fusion cross sections for ${}^7\text{Li} + {}^{12}\text{C}$ system at near barrier

- energies,” *Nucl. Phys. A*, vol. 792, no. 3–4, pp. 187–200, Aug. 2007.
- [94] H. W. Schmitt, W. E. Kiker, and C. W. Williams, “Precision Measurements of Correlated Energies and Velocities of ^{252}Cf Fission Fragments,” *Phys. Rev.*, vol. 137, no. 4B, pp. B837–B847, Feb. 1965.
- [95] E. Weissenberger, P. Geltenbort, A. Oed, F. Gönnerwein, and H. Faust, “Energy calibration of surface barrier detectors for fission fragments,” *Nucl. Instr. and Meth. A*, vol. 248, no. 2–3, pp. 506–515, Aug. 1986.
- [96] J. N. Neiler, F. J. Walter, and H. W. Schmitt, “Fission-Fragment Energy-Correlation Measurements for the Thermal-Neutron Fission of ^{239}Pu and ^{241}Pu ,” *Phys. Rev.*, vol. 149, no. 3, pp. 894–905, Sep. 1966.
- [97] J. Elseviers *et al.*, “ β -delayed fission of ^{180}Tl ,” *Phys. Rev. C*, vol. 88, no. 4, p. 044321, Oct. 2013.
- [98] G. Siegert *et al.*, “Direct determination of the nuclear charge distribution of mass separated fission products from $^{235}\text{U}(\text{nth},f)$,” *Phys. Lett. B*, vol. 53, no. 1, pp. 45–47, Nov. 1974.
- [99] Blanc, A. *et al.*, “Spectroscopy of neutron rich nuclei using cold neutron induced fission of actinide targets at the ILL: The EXILL campaign,” *EPJ Web Conf.*, vol. 62, p. 1001, 2013.
- [100] E. Belau *et al.*, “Charge collection in silicon strip detectors,” *Nucl. Instruments Methods Phys. Res.*, vol. 214, no. 2–3, pp. 253–260, Sep. 1983.
- [101] “The GASPARD project,” *Nucl. Instr. and Meth. B*, vol. 317, pp. 661–663, 2013.
- [102] S. Carboni, “FAZIA: a new detector for nuclear physics.”
- [103] A. Topkar, B. Aggarwal, S. Praveenkumar, S. K. Kataria, and Y. P. Prabhakar Rao, “The CMS preshower silicon sensors: Technology development and production in India,” *Nucl. Instr. and Meth. A*, vol. 585, no. 3, pp. 121–127, Feb. 2008.
- [104] A. Singh *et al.*, “Performance study of indigenously developed double sided silicon strip detector with charged particles,” vol. 62, pp. 1044–1045, 2017.
- [105] A. Topkar, A. Singh, A. Bharti, A. Kumar, A. Kumar, and C. K. Pithawa, “Development of double-sided silicon strip detector,” in *Proceedings of the DAE Symp. on Nucl. Phys.*, 2013, vol. 58, no. 2, pp. 856–857.
- [106] Y. Unno *et al.*, “Optimization of surface structures in n-in-p silicon sensors using TCAD simulation,” *Nucl. Instr. and Meth. A*, vol. 636, no. 1 SUPPL., pp. S118–S124, 2011.
- [107] N. Bacchetta *et al.*, “Improvement in breakdown characteristics with multiguard structures in microstrip silicon detectors for CMS,” *Nucl. Instr. and Meth. A*, vol. 461, no. 1–3, pp. 204–206, Apr. 2001.
- [108] D. S. McGregor, R. T. Klann, H. K. Gersch, and Y. H. Yang, “Thin-film-coated bulk

- GaAs detectors for thermal and fast neutron measurements,” *Nucl. Instr. and Meth. A*, vol. 466, no. 1, pp. 126–141, 2001.
- [109] A. Melton, E. Burgett, M. Jamil, T. Zaidi, N. Hertel, and I. Ferguson, “GaN as a neutron detection material,” *Proceedings of the IEEE SoutheastCon 2010 (SoutheastCon)*. pp. 402–403, 2010.
- [110] R. T. Kouzes, J. R. Ely, A. T. Lintereur, and D. L. Stephens, “Neutron Detector Gamma Insensitivity Criteria,” *Pacific Northwest Natl. Lab.*, vol. PNNL-18903, pp. 1–18, 2009.
- [111] M. Angelone *et al.*, “Neutron detection and dosimetry using polycrystalline CVD diamond detectors with high collection efficiency,” *Radiat. Prot. Dosimetry*, vol. 120, no. 1–4, pp. 345–348, 2006.
- [112] M. Angelone *et al.*, “Neutron detectors based upon artificial single crystal diamond,” *IEEE Transactions on Nuclear Science*, vol. 56, no. 4. pp. 2275–2279, 2009.
- [113] A. B. Rosenfeld *et al.*, “Neutron Dosimetry with Planar Silicon p-i-n Diodes,” *IEEE Transactions on Nuclear Science*, vol. 50, no. 6 I. pp. 2367–2372, 2003.
- [114] A. Affolder, P. Allport, and G. Casse, “Charge collection efficiencies of planar silicon detectors after reactor neutron and proton doses up to 1.6×10^{16} neq cm⁻²,” *Nucl. Instr. and Meth. A*, vol. 612, no. 3, pp. 470–473, Jan. 2010.
- [115] A. N. Caruso *et al.*, “The all boron carbide diode neutron detector: Comparison with theory,” *Mater. Sci. Eng. B*, vol. 135, no. 2, pp. 129–133, Nov. 2006.
- [116] A. N. Caruso, “The physics of solid-state neutron detector materials and geometries.,” *J. Phys. Condens. Matter*, vol. 22, no. 44, p. 443201, 2010.
- [117] S. L. Bellinger, R. G. Fronk, W. J. McNeil, T. J. Sobering, and D. S. McGregor, *High efficiency dual-integrated stacked microstructured solid-state neutron detectors*. IEEE, 2010, pp. 2008–2012.
- [118] R. G. Fronk *et al.*, “Dual-sided microstructured semiconductor neutron detectors (DSMSNDs),” *Nucl. Instr. and Meth. A*, vol. 804, pp. 201–206, Dec. 2015.
- [119] S. L. Bellinger, R. G. Fronk, T. J. Sobering, and D. S. McGregor, “High-efficiency microstructured semiconductor neutron detectors that are arrayed, dual-integrated, and stacked,” *Appl. Radiat. Isot.*, vol. 70, no. 7, pp. 1121–1124, 2012.
- [120] G. F. Knoll, *Radiation detection and measurement / Glenn F. Knoll*. New York: Wiley, 1989.
- [121] Q. Shao *et al.*, “Gamma discrimination in pillar structured thermal neutron detectors,” *Proc. SPIE*, vol. 8358. pp. 83581N–83581N–9, 2012.
- [122] Q. Shao *et al.*, “Experimental determination of gamma-ray discrimination in pillar-structured thermal neutron detectors under high gamma-ray flux,” *Nucl. Instr. and Meth. A*, vol. 799, pp. 203–206, 2015.

- [123] J. F. Ziegler, M. D. Ziegler, and J. P. Biersack, “SRIM – The stopping and range of ions in matter (2010),” *Nucl. Instr. and Meth. B*, vol. 268, no. 11, pp. 1818–1823, 2010.
- [124] R. Bedogni *et al.*, “Experimental characterization of semiconductor-based thermal neutron detectors,” *Nucl. Instr. and Meth. A*, vol. 780, pp. 51–54, Apr. 2015.
- [125] M. Wielunski *et al.*, “Study of the sensitivity of neutron sensors consisting of a converter plus Si charged-particle detector,” *Nucl. Instr. and Meth. A*, vol. 517, no. 1–3, pp. 240–253, 2004.